Compact Laser-Driven Electron Acceleration, Bunch Compression and Coherent Nonlinear Thomson Scattering

ARCHIVES
MASSACHUSETTS INSTITUTE OF TECHNOLOGY
OCT 0 2 2013
LIBRARIES

by

Liang Jie Wong

B.S., University of California, Berkeley (2008)
S.M., Massachusetts Institute of Technology (2011)

Submitted to the Department of Electrical Engineering and Computer Science
in Partial Fulfillment of the Requirements for the Degree of

Doctor of Philosophy

at the

MASSACHUSETTS INSTITUTE OF TECHNOLOGY

September 2013

© 2013 Liang Jie Wong. All rights reserved.

The author hereby grants to MIT permission to reproduce and to
distribute publicly paper and electronic copies of this thesis document in whole or in part
in any medium now known or hereafter created.

Author.....
Department of Electrical Engineering and Computer Science
August 29, 2013

Certified by.....
Franz X. Kärtner
Adjunct Professor of Electrical Engineering
Thesis Supervisor

Certified by.....
Erich P. Ippen
Elihu Thomson Professor of Electrical Engineering
Professor of Physics
Thesis Supervisor

Accepted by.....
Leslie A. Kolodziejski
Professor of Electrical Engineering
Chair, Department Committee on Graduate Students

Compact Laser-Driven Electron Acceleration, Bunch Compression and Coherent Nonlinear Thomson Scattering

by

Liang Jie Wong

Submitted to the Department of Electrical Engineering and Computer Science
on August 29, 2013, in partial fulfillment of the requirements for the Degree of
Doctor of Philosophy

Abstract

Coherent hard x-rays have many medical, commercial and academic research applications. To facilitate the design of a table-top coherent hard x-ray source, this thesis studies the linear acceleration of electrons by optical lasers in unbounded vacuum, the linear acceleration and compression of electron bunches by coherent terahertz pulses in cylindrical waveguides, and the generation of coherent hard x-ray radiation by nonlinear Thomson scattering of compressed electron bunches.

The Lawson-Woodward theorem describes conditions prohibiting net electron acceleration in laser-electron interactions. We point out how the Lawson-Woodward theorem permits net linear acceleration of a relativistic electron in unbounded vacuum and verify this with electrodynamic simulations. By hypothesizing that substantial net linear acceleration is contingent on the field's ability to bring the particle to a relativistic energy in its initial rest frame, we derive a general formula for the acceleration threshold, which is useful as a practical guide to the laser intensities that linear vacuum acceleration requires.

We characterize the scaling laws of linear acceleration by a pulsed radially-polarized beam in infinite vacuum, showing that greater energy gain is achievable with tighter focusing and the use of pre-accelerated electrons. We propose a two-color linear acceleration scheme that exploits changes in the interference pattern caused by the Gouy phase shift to achieve over 90% the one-color theoretical gain limit, more than twice the 40% achievable with a one-color paraxial beam.

Interested in capitalizing on the larger wavelengths of coherent terahertz radiation to accelerate larger electron bunches, we study electron acceleration and bunch compression in a cylindrical metal-coated dielectric waveguide. We numerically predict an achievable acceleration gradient of about 450 MeV/m using a 20 mJ terahertz pulse, and separately achieve a 50 times compression to a few-femtosecond duration of a 1.6 pC relativistic electron bunch.

Finally, we numerically study the production of coherent hard x-rays via nonlinear Thomson scattering for different degrees of laser focusing. We derive an approximate analytical formula for the optimal incident field intensity that maximizes the radiation intensity spectral peak for a given output and input frequency.

Thesis Supervisor: Franz X. Kärtner
Title: Adjunct Professor of Electrical Engineering

Thesis Supervisor: Erich P. Ippen
Title: Elihu Thomson Professor of Electrical Engineering
Professor of Physics

Acknowledgments

First and foremost, I would like to thank Prof. Franz Kärtner for his guidance, advice and constant support throughout my PhD journey. His drive and vision were very inspiring, and I benefited greatly from his vast experience and deep insights.

I am also very grateful to Prof. Erich Ippen for his constant support and mentorship. My discussions with Prof. Kärtner and Prof. Ippen have fructified my research and opened my eyes further to the world of physics.

Many thanks is due to Prof. Peter Hagelstein and Dr. Luis Velásquez-García. They were very helpful and responsive, and gave me much advice on my research.

I have had the privilege of working with Dr. Arya Fallahi of CFEL, DESY, from whom I learned a great deal through our discussions and collaboration.

I am also grateful for the many discussions I have had with Dr. William Graves, Dr. Guoqing Chang, Dr. Eduardo Granados, Dr. Kyung-Han Hong, Dr. Shu-Wei Huang, Dr. Jeffery Moses, Dr. Emilio Nanni, Dr. Damian Schimpf, Dr. Alexander Sell, Ronny Huang and many others.

My studies were financially supported by the Agency for Science, Technology and Research in Singapore.

Last but not least, I am indebted to my family for their encouragement and unwavering support.

Contents

Chapter 1

Introduction

This work treats the acceleration and compression of electron bunches by coherent optical and terahertz light, as well as the generation of coherent x-ray radiation via nonlinear Thomson scattering. One of the main motivations of our study is to facilitate the design of a table-top coherent hard x-ray source, for which compact acceleration, compression and nonlinear Thomson scattering stages are essential.

1.1 Background

Beginning with light in the visible spectrum, the photon has been indispensable to mankind in its investigation and exploration of the physical universe. The progress of science in recent centuries has widened the useful range of the electromagnetic spectrum to include frequencies as high as those of x-rays and gamma rays, which have become essential to further progress. The multiplicity of commercial, medical and academic research applications requiring brilliant x-ray sources is reflected in the high demand for beam-time at x-ray laser facilities like the Linac Coherent Light Source (LCLS) in the U.S.A., the SPring-8 Angstrom Compact Free Electron Laser (SACLA) in Japan, and the Free-Electron Laser in Hamburg (FLASH) in Germany. In spite of this high demand, however, such facilities remain few, often distant and challenging to

access. The beam-time application process at the LCLS, for instance, is so competitive that only one out of four experimental proposals is approved [L12]. It is unfortunate that the size and efficiency of x-ray lasers have not scaled with the burgeoning potentials of the technology to make supply commensurate with demand.

The advent of high-intensity lasers in the optical and terahertz frequency ranges may hold the key to easing this discrepancy. As early as the 1970s, scientists have considered the use of lasers to accelerate charged particles [Cha71]. However, it was not until the invention of chirped pulse amplification by Strickland and Mourou in 1985 [SM85] that laser-driven particle acceleration began to attract widespread attention. In the decades that followed, demonstrated optical laser intensities have rapidly soared [MU92, PM94, PPS+99, TM02, BPP+04] to values as high as 10^{22} W/cm^2 [BPP+04]. This corresponds to electric fields on the order of 10^{14} V/m, six orders of magnitude above the approximate 10^8 V/m in conventional radiofrequency (RF) accelerator structures.

More recently on the terahertz front, THz pulses with electric fields as strong as 10^{10} V/m have been generated in GaSe from 30 fs laser pulses via birefringent phase-matching [SLH08], with the highest field achieved at 30 THz. THz pulses centered at 0.2-1.0 THz can be efficiently generated in $LiNbO_3$ [HYH+08] via tilted-pulse-front pumping (TPFP) phase-matching. Such high fields can accelerate electron bunches to the desired energy and compress them to the desired bunch length over much smaller interaction distances than what is permitted by traditional RF accelerator technology, where the damage threshold of RF cavities limits the acceleration gradient to a value on the order of 100 MeV/m. Coherent x-rays are useful in biomedical imaging [Lew04], in analyzing the structure of proteins [CFB+11] and viruses [SEM+11], and in producing real-time movies of molecular interactions during chemical reactions [Zew00]. In particular, phase contrast x-ray imaging, which requires coherent x-rays in many implementations, produces much better image quality than conventional absorption techniques since the refractive index decrement of tissues is typically more than three orders of magnitude greater than their absorption index in the diagnostic x-ray energy range [Lew04]. The widespread availability of compact electron accelerators and coherent x-ray sources is thus highly desirable.

Methods under investigation for compact electron acceleration include the inverse free electron laser, the inverse Cherenkov effect, plasma acceleration, dielectric-based acceleration

and vacuum acceleration. These approaches typically involve optical lasers, but forays have also been made into the acceleration of electrons in vacuum [HFM+11] and in waveguides [YR05] by coherent THz light.

The inverse free electron laser [Pal72, CPZ85, KSB+01] and the inverse Cherenkov effect [FP83, SEK96] are respectively, as their names suggest, the reverse of the free electron laser and Cherenkov radiation processes, so that the electrons gain energy instead of radiating it. Plasma-based electron acceleration, first proposed by Tajima and Dawson in 1979 [TD79] and experimentally demonstrated as early as 1995 (e.g. [MZD+95]), involves using optical laser pulses to excite waves in plasma. The charge separation of the plasma waves creates electric fields that accelerate electrons. Plasmas can sustain fields that scale as $96(n_0[\mathrm{cm}^{-3}])^{1/2}$ V/m, n_0 ambient electron number density, so $n_0 = 10^{18}\mathrm{cm}^{-3}$ yields an acceleration gradient of 96 GeV/m. Plasma acceleration comes in several varieties [ESL09]. In plasma beat-wave acceleration [KD83, JMK+84, CMD+93], for instance, two laser pulses of frequencies differing by the plasma frequency are used to excite the plasma wave. Laser wakefield acceleration [ESK+96, SET+88, SEK+92], on the other hand, uses a single laser pulse of wavelength equal to or smaller than the plasma wavelength. In the "blow-out" or "bubble" regime, a high-enough laser intensity expels all electrons from the axis, leading to the formation of a vacuum bubble, self-injection of electrons into this bubble and subsequent acceleration of these electrons to high energies. In 2004, three groups ([CTT+04, MMN+04, FGP+04]) achieved electron bunches with an energy spread of a few percent and a low divergence of several milliradians by operating in the blow-out regime. Since then, many methods to obtain greater stability, reproducibility and higher electron energies in electron acceleration experiments have been proposed and demonstrated (see references in [ESL09]). These include controlled injection of electrons with colliding laser pulses, the use of negative plasma density gradients and the use of plasma-channel-guided lasers.

Dielectric-based acceleration may be driven by an external optical laser source or by the wakefields of another electron bunch (i.e. dielectric wakefield accelerator) [GSC+88, ASB+12, AJK+12]. Laser-driven dielectric structures for electron acceleration include two-dimensional photonic crystals [Cow03], three-dimensional photonic crystals [Cow08], photonic crystal fibers [Lin01, MS04, NSK11] and transmission grating structures [PLB06]. These structures are expected to sustain an acceleration gradient in the vicinity of 400-800 MeV/m. However, the

total charge is not expected to exceed 10-20 fC, so the technology is probably best suited for niche applications that require fewer coherent x-rays [CCE+10].

Vacuum acceleration -- the name we use here for laser-driven particle acceleration in unbounded vacuum (i.e. no physical structures to guide or block light) -- occurs through either the ponderomotive force associated with the transverse electric and magnetic field components (ponderomotive acceleration) [CPZ85, KSB+01, Hor88, ESK95, HFS+95, QM98, MLM97, SZ01, WHY+01, SK02, HS02, PBR08], or the force exerted by the longitudinal electric field component (linear acceleration) [PBC+05, HZT+96, SZ91, Sal07, FPV10, VPP05, KP07]. Ponderomotive acceleration schemes include vacuum beat wave acceleration [Hor88], in which the wiggler field of the inverse free electron laser scheme is simply replaced by a second laser; high-intensity ponderomotive scattering [ESK95, HFS+95, QM98], in which the electron is scattered away from the laser focus with a high escape energy; the capture and acceleration scenario [SZ01], in which relativistic electrons are injected at an angle into the laser focus; and ionization of highly-charged ions near the laser pulse peak [SK02]. Experiments [KSB+01, QM98, HS02] have demonstrated that ponderomotive acceleration may be achieved in reality. Linear vacuum acceleration schemes typically involve the use of a beam or beam configuration such that only the z-directed electric field exists on axis. A number of linear acceleration schemes [PBC+05, HZT+96] that involve terminating the laser field before the accelerated electron starts losing energy to the field -- so they are not strictly "vacuum acceleration" schemes according to our usage, but have nevertheless been referred to by that term -- have also been proposed.

Because of the numerous trade-offs involved, no approach has emerged as a clear winner. The use of a plasma medium is an attractive way of achieving laser-driven electron acceleration, for instance, but faces problems like the inherent instability of laser-plasma interactions, which limits the laser propagation distance and degrades accelerator performance [ESL09]. Schemes that use guiding structures benefit from light confinement, which decreases the required driving energy and increases the interaction distance, compared to schemes that take place in (effectively) unbounded vacuum, but suffer from intensity limitations imposed by thermal damage and dielectric breakdown of the guiding structures. Linear acceleration schemes that use optical wavelengths instead of THz or RF wavelengths tend to enjoy a higher acceleration gradient, which favors greater bunch compression and acceleration, but space-charge effects make it

difficult to confine a bunch of substantial charge within a half-cycle if the wavelength is too small.

To produce coherent x-rays, it is necessary to compress the longitudinal dimension of the electron bunches to a value on the order of the desired x-ray wavelength. It is possible to achieve simultaneous acceleration and compression of an electron bunch with the z-directed electric field of a transverse-magnetic electromagnetic field at optical and THz frequencies. This is akin to the idea of velocity bunching scheme [SF01, FBC+11] proposed for use at RF frequencies to enable compression of the electron beam at early stages of the accelerator chain when beam energy is low, which avoids problems related to magnetic compression like beam filamentation, emittance dilution and coherent synchrotron radiation [FBC+11]. Compressed electron bunches at energies no more than a few MeV are also interesting for electron beam diffraction (e.g.: [BZ07, WG12]), although in the case of a velocity-bunching-type scheme, a method may have to be devised to separate the compressed electron bunch from the compressing laser pulse (this may be done with bending magnets if the interaction were in vacuum but the solution here is less straightforward since the electrons are in a waveguide).

A suitably accelerated and compressed electron bunch may be sent into a counterpropagating laser pulse to generate coherent x-rays via nonlinear Thomson scattering (or inverse Compton scattering, as it is sometimes referred to in the literature) [GBK+09], a process involving the emission of upshifted photons from the transverse oscillations of a relativistic electron in an electromagnetic pulse [Vac62]. The dynamics and radiation of an electron in an arbitrarily intense, elliptically polarized plane electromagnetic wave were studied by Sarachik and Schappert [SS70] for the case of an electron initially at rest, and later generalized to arbitrary initial electron velocities by Salamin and Faisal [SF96]. The nonlinear Thomson scattering of continuous intense linearly and circularly-polarized plane waves with electron beams and plasmas was studied by Esarey et al. [ERS93]. The spatial and spectral characteristics of the nonlinear Thomson scattering were also analyzed theoretically by many other authors (e.g. [REB95, Kra04, Gao04, Pop11]). Experiments have been performed demonstrating the features predicted by nonlinear Thomson scattering theory (e.g.: [CMU98, SLC+96, TRP+03]). All-optical setups for x-ray and gamma ray generation involving the nonlinear Thomson scattering of laser-accelerated electrons have also been proposed [CEL01, HLK+03] and demonstrated

[SLS+06, TCT+12]. At such a pace of progress, table-top temporally-coherent hard x-ray and gamma-ray sources may well be within reach in the near future.

1.2 Overview

In Chapter 2, we investigate the idealized scenario in which an electron interacts with a propagating z-directed electric field. This scenario is highly relevant to the rest of this work because a propagating z-directed electric field approximates the electromagnetic profile close to the axis of a cylindrically symmetric transverse-magnetic mode (e.g.: a radially-polarized beam or the TM_{01} mode of a cylindrical waveguide). General analytical formulas covering almost all aspects of the single-particle case are derived. We introduce the phase contour diagram and use it to illustrate various scenarios that can occur depending on the field intensity, the field's phase velocity and the initial electron energy. We discuss a phenomenon we call "asymptotic trapping", which can lead to phase-matching over arbitrarily long distances, so long as the driving laser field is not depleted. We also present an injection and extraction strategy to maximize energy gain for a single electron of a certain kinetic energy given the vector potential and phase velocity of the driving wave.

In Chapter 3, we study the acceleration of a free electron in infinite vacuum along the axis of a pulsed radially-polarized laser beam. We extend the results of previous studies to include the case of electrons with non-zero initial velocities. These electrons (which we call "pre-accelerated electrons") are injected into the laser beam ahead of the pulse and may be the output of a preceding acceleration stage. We show that net energy gain can be much greater for a pre-accelerated electron than for an initially stationary one. In particular, the net energy gain of an initially relativistic electron may exceed more than half the theoretical energy gain limit (derived in [FPV10]), which is not possible with an initially stationary electron in the parameter space studied. The *de facto* energy gain limit (of half the theoretical energy gain limit) argued by Fortin et. al. [FPV10] for the initially stationary electron may thus be surpassed with the pre-accelerated electron.

By extending our parameter space to include powers as low as 5 TW, we show that substantial acceleration can already be achieved with laser peak powers of a few terawatts. Finally, we propose and study the direct acceleration of an electron in infinite vacuum by a two-color pulsed radially-polarized laser beam. This scheme exploits the presence of the Gouy phase

shift to accelerate a stationary electron by over 90% of the one-color theoretical energy gain limit, more than twice of what is possible with a one-color paraxial beam of equal total energy and pulse duration. It is worth noting that sub-wavelength focusing of a single beam can achieve only about 80% of the theoretical gain limit [MVA+12].

Our studies are conducted using Gaussian beam solutions of the paraxial wave equation. Recently, it has been pointed out that higher-order corrections in the electromagnetic field are necessary even when focusing is not tight (i.e. even in the paraxial regime) to accurately model the electrodynamics of off-axis particles [MVP13]. To ensure that our simulations were accurate, we compare the on-axis fields of our paraxial solution with those of an exact beam-like solution of Maxwell's equations and verify that there are no major discrepancies even in the case of tight focusing. Note that throughout this work, we are careful to use the paraxial beam solution only for on-axis electrodynamic simulations.

In Chapter 4, we recapitulate the derivation of the Lawson-Woodward theorem, a theorem which forbids electron acceleration in vacuum under a certain set of conditions. Whenever the topic of vacuum linear acceleration is broached In the literature (e.g.: in [ESL09]), it is common to read about the need for physical boundaries to violate the Lawson-Woodward theorem, without any mention of the fact that an initially relativistic electron is capable of gaining net energy from a laser beam in vacuum even in the absence of physical boundaries. We point out how this phenomenon is in full accord with the Lawson-Woodward theorem. By hypothesizing that substantial net linear acceleration is contingent on the accelerating field's ability to bring the particle to a relativistic energy in its initial rest frame during the interaction, we go on to derive a general formula for the acceleration threshold, which is useful as a practical guide to the laser intensities that unbounded linear acceleration requires under various scenarios.

In Chapter 5, we study the ability of terahertz pulses to accelerate and compress electron bunches in a cylindrically symmetric, metal-coated dielectric waveguide. We are interested in this scheme because, compared to optical pulses, terahertz pulses are able to accelerate a larger number of electrons per bunch by virtue of the longer wavelength of terahertz radiation. We numerically demonstrate the acceleration of a 1.6 pC electron bunch from a kinetic energy of 1 MeV to one of 10 MeV over an interaction distance of about 20 mm, using a 20 mJ pulse centered at 0.6 THz in a dielectric-loaded metallic waveguide. We also investigate the acceleration of 16 pC and 160 pC 1 MeV electron bunches, observing that performance does not

change significantly for a 16 pC-bunch, but deteriorates prohibitively for a 160pC-bunch due to the overwhelming Coulomb repulsion. Finally, we optimize the dielectric-loaded metal waveguide design for simultaneous acceleration and bunch compression, achieving a 50 times (100 fs 1.6 pC electron bunch compressed to 2 fs over an interaction distance of about 18mm) and 62 times (100 fs to 1.61 fs over an interaction distance of 42 cm) compression for a 1 MeV and 10 MeV electron bunch respectively. These results were achieved with a 20 mJ laser pulse centered at 0.6 THz, and encourage the exploration of THz-laser-driven electron acceleration as a path to compact electron acceleration and bunch compression schemes.

In Chapter 6, we present the classical theory of nonlinear Thomson scattering and derive an approximate analytical formula for the on-axis intensity spectrum of a single relativistic particle traveling into a counterpropagating linearly-polarized electromagnetic pulse. From this formula, we deduce that if we restrict ourselves to the first harmonic and are free to choose any combination of normalized vector potential and electron energy we like, there is an optimal incident field intensity that gives the maximum spectral intensity peak for a given output and input frequency. Beyond a certain point, it is futile to obtain greater monochromatic output by increasing the intensity of the incident laser pulse. Instead, the amount of charge in the bunch or the number of cycles in the laser-electron interaction must be increased.

We discuss the algorithms we have implemented to compute the nonlinear Thomson scattering temporal and spectral profiles. In particular, we describe a method that solves the electrodynamic equation in advanced time to compute the radiation spectrum via the fast Fourier transform without the use of any interpolation techniques. We benchmark our code with analytical formulas for synchrotron radiation and inverse Compton scattering. With our code, we study the scattering of an optical laser pulse off an electron bunch under different degrees of laser focusing, comparing the results obtained using the exact pulsed solution (i.e. a pulsed beam-like electromagnetic field that exactly solves Maxwell's equations) with those obtained using an ideal pulsed plane wave of the same peak intensity. Features of the radiation observed and discrepancies between the plane wave and exact pulse results are discussed and explained.

Chapter 2

Electrodynamics in a longitudinal electric field

Along the beam axis of a cylindrically symmetric transverse-magnetic mode (TM_{0p} mode, p a non-negative integer) propagating in the z-direction in vacuum or in a waveguide, a particle sees only a z-directed traveling electric field. The transverse electromagnetic fields vanish on axis and increase in amplitude until a certain point as one moves away from the axis. This makes acceleration schemes employing TM_{0p} modes very attractive for the linear acceleration of electrons. In this chapter, we examine the idealized case of a particle subjected to a continuous-wave (CW) z-directed planar electric field, with the goal of obtaining physical intuition about the electrodynamics in linear acceleration schemes based on TM_{0p} modes.

When a charged particle is subjected to a CW z-directed planar electric field, exactly one of three things will happen: (a) the particle will slip continuously through successive accelerating and decelerating half-cycles, (b) the particle will be borne along with the wave, slipping asymptotically towards a certain phase in an accelerating cycle (a phenomenon we call "asymptotic trapping") or (c) the particle will be borne along with the wave, oscillating about its injection phase in the frame of the field. We introduce and use the phase contour diagram to investigate the conditions under which each of these scenarios take place. In the process, we also derive analytical formulas and obtain semi-analytical solutions related to the energy and displacement of a single particle as a function of its injection energy, injection phase and extraction phase, as well as the amplitude and phase velocity of the driving field.

Finally, we use the phase contour diagram to devise a general scheme for maximum acceleration, given an initial electron energy and CW z-directed electric field. Our results show that for a given initial electron energy, there is a certain field intensity below which maximum acceleration is achieved with a subluminal wave, and above which maximum acceleration is achieved with a phase velocity exactly equal to the speed of light in vacuum. The mechanism that applies in the latter case is asymptotic trapping, which keeps a particle from ever slipping out of the first accelerating half-cycle the particle encounters, and accelerates the particle with a practically constant acceleration gradient. We also discuss the limitations of studying electron acceleration under such idealized conditions. Although the study of an electron in a z-directed traveling electric field is not new (e.g.: [SF01], [EP95]), the concept of asymptotic trapping, the study of superluminal phase velocities and the study of how maximum energy gain scales with field amplitude and phase velocity in such a model have not been presented elsewhere as of the writing of this thesis, to the best of our knowledge.

2.1 Equations of motion

Close to the axis of a hollow cylindrical waveguide containing a TM_{0p} mode (p a non-negative integer), the electromagnetic field is well-approximated by a z-directed electric field of amplitude $E_0 > 0$:

$$\vec{E} = E_z \hat{z} = E_0 \cos(\omega t - \kappa z + \psi_0)\hat{z}\,. \tag{2.1}$$

Note that such a field is also exactly sustained by a sea of charge in vacuum where the charge density $\rho = \varepsilon_0(\nabla \cdot \vec{E}) = \kappa\varepsilon_0 E_0 \sin(\omega t - \kappa z + \psi_0)$, ε_0 being the permittivity of free space. Without loss of generality, we will consider only the case of $\kappa \geq 0$, since we are always free to define our coordinate system so that this is true.

Consider the action of such a field upon a charged particle of (rest) mass m and charge q, according to the Lorentz force equation. The charged particle is modeled as a point charge. Let z denote the particle's displacement in z and t denote time. Clearly, the particle will move only

along the z direction, so its velocity $\vec{v}(t) = c\beta(t)\hat{z}$, where c is the speed of light in vacuum. We thus obtain a set of coupled differential equations:

$$\begin{aligned} \frac{d}{dt}(\gamma\beta) &= \frac{qE_z}{mc} = \frac{qE_0}{mc}\cos\psi \\ \frac{dz}{dt} &= \beta c, \end{aligned} \tag{2.2}$$

where $\gamma = 1/(1-\beta^2)^{1/2}$ is the relativistic Lorentz factor and $\psi \equiv \omega t - \kappa z + \psi_0$. Note that

$$\frac{d\psi}{dt} = \omega\left(1 - \frac{\beta}{\beta_{ph}}\right), \tag{2.3}$$

where $\beta_{ph} = \omega/\kappa c > 0$ is the normalized phase velocity of the continuous wave z-directed electric field. There is no loss of generality in the physics of the problem by requiring $\beta_{ph} > 0$, since there is no restriction on the sign of $\beta(0)$. Combining (2.2) and (2.3) by the chain rule gives us

$$\begin{aligned} \frac{d}{d\psi}(\gamma\beta) &= \frac{-a_0}{1-\beta/\beta_{ph}}\cos\psi \\ \frac{dz}{d\psi} &= \frac{\beta/k}{1-\beta/\beta_{ph}}, \end{aligned} \tag{2.4}$$

where $a_0 \equiv -qE_0/mc\omega$ and $k = \omega/c$. The first line of (2.4) may be solved to give

$$\gamma - \gamma\beta\beta_{ph} = a_0\beta_{ph}(\sin\psi - \sin\psi_s) + (\gamma - \gamma\beta\beta_{ph})_s \equiv G(\psi), \tag{2.5}$$

where subscript s appended to any variable or expression simply denotes the same variable or expression evaluated at any particular reference point in phase space (i.e. ψ- $\gamma\beta$ space). In the literature, one often finds (2.5) written in the form

$$H = \gamma - \gamma\beta\beta_{ph} - a_0\beta_{ph}\sin\psi \tag{2.6}$$

H is a constant of motion traditionally referred to as the Hamiltonian [SF01]. (2.5) is readily solved for $\gamma\beta$ to give

$$(\gamma\beta)(\psi) = \begin{cases} \left(G(\psi)\beta_{\text{ph}} \pm \sqrt{\beta_{\text{ph}}^2 + G^2(\psi) - 1}\right)\gamma_{\text{ph}}^2, & \beta_{\text{ph}} < 1 \\ \dfrac{1 - G^2(\psi)}{2G(\psi)}, & \beta_{\text{ph}} = 1 \\ \left(G(\psi)\beta_{\text{ph}} - \sqrt{\beta_{\text{ph}}^2 + G^2(\psi) - 1}\right)\gamma_{\text{ph}}^2, & \beta_{\text{ph}} > 1 \end{cases} \tag{2.7}$$

where $\gamma_{\text{ph}} = 1/(1 - \beta_{\text{ph}}{}^2)^{1/2}$. Equivalently, (2.7) may be written as

$$\beta(\psi) = \begin{cases} \dfrac{\beta_{ph} \pm G(\psi)\sqrt{\beta_{ph}^2 + G^2(\psi) - 1}}{\beta_{ph}^2 + G^2(\psi)}, & \beta_{\text{ph}} < 1 \\ \dfrac{\beta_{ph} - G(\psi)\sqrt{\beta_{ph}^2 + G^2(\psi) - 1}}{\beta_{ph}^2 + G^2(\psi)}, & \beta_{\text{ph}} \geq 1 \end{cases} \tag{2.8}$$

Note that the choice of sign in (2.7) corresponds to that in (2.8). The validity of these results may be ascertained by inserting (2.7) into the leftmost side of (2.5) and checking that it evaluates to G. The following summarizes a few salient properties of (2.5) as an equation with $\gamma\beta$ as the unknown:

1. Parameters a_0, ψ, ψ_s, β_{ph} and β_s must be specified before we can solve (2.5) for $\gamma\beta$. For $\beta_{\text{ph}} \leq 1$, $G \geq (1 - \beta_{\text{ph}}{}^2)^{1/2}$ will be true if (but not only if) a physically valid combination of parameters is chosen. For $\beta_{\text{ph}} > 1$, G may take on any real value. Note that for given a_0, β_{ph} and β_s, not every combination of ψ and ψ_s may be physically valid.
2. For $\beta_{\text{ph}} < 1$, no solutions exist if $\beta_{\text{ph}}{}^2 + G^2 - 1 < 0$. Exactly one solution exists if $\beta_{\text{ph}}{}^2 + G^2 - 1 = 0$, and two distinct solutions exist if $\beta_{\text{ph}}{}^2 + G^2 - 1 > 0$. Of course, where two solutions exist, only one of them can be correct for a given combination of a_0, ψ, ψ_s, β_{ph} and β_s, assuming the combination is physically valid.
3. Where two (distinct) solutions exist for $\beta_{\text{ph}} < 1$, we invariably have $\beta > \beta_{\text{ph}}$ for the choice of "+" and $\beta < \beta_{\text{ph}}$ for the choice of "–" in (2.7) (hence, we can immediately determine

the correct solution if we know in advance which side of β_{ph} the correct solution must lie on). Where one solution exists for $\beta_{ph} < 1$, we invariably have $\beta = \beta_{ph}$.

4. For $\beta_{ph} \geq 1$, we always have a solution since $\beta_{ph}^2 + G^2 - 1 \geq 0$. We always have exactly one solution since only the choice of "–" yields a result satisfying (2.5).

These properties are derived (where applicable) and discussed in greater detail in Appendix A.

With (2.8), we may solve for $t(\psi)$ and $z(\psi)$ by numerical integration since (2.3) and the second line of (2.4) give

$$\begin{aligned} \frac{dt(\psi)}{d\psi} &= \frac{1/\omega}{1-\beta(\psi)/\beta_{ph}} \\ \frac{dz(\psi)}{d\psi} &= \frac{\beta(\psi)/k}{1-\beta(\psi)/\beta_{ph}} \end{aligned} \tag{2.9}$$

The partially-analytical nature of the problem thus enables us to fully solve the coupled ordinary differential equations in (2.2) with only numerical quadrature methods, instead of ordinary differential equation algorithms that are generally more complicated. In general, there are three types of solutions: trapped orbital trajectories (or trapped orbits), in which the particle oscillates about a particular zero-crossing of the wave (possible only if $\beta_{ph} < 1$); trapped asymptotic trajectories, in which the particle slips asymptotically towards a certain phase within a cycle of the wave (possible only if $\beta_{ph} = 1$); and untrapped trajectories, in which the particle slips continuously through the cycles of the wave. Note that care must be taken when integrating (2.9) for trapped orbits since $t(\psi)$ and $z(\psi)$ are then not, strictly speaking, functions of ψ (i.e. multiple values of t and z may correspond to a single value of ψ). Also, different choices of the ± sign in (2.8) must be chosen for different portions of the orbit.

The integration of (2.9) is much more straightforward in the case of trapped asymptotic trajectories and untrapped trajectories. In these cases, $t(\psi)$ and $z(\psi)$ are functions of ψ and only one choice of the ± sign in (2.8) is applicable, depending on whether $\beta(t) > \beta_{ph}$ $\forall t$ or $\beta(t) < \beta_{ph}$ $\forall t$ (one of these must be true if the particle is asymptotically trapped or untrapped), throughout the entire integration.

2.2 The phase contour diagram and the separatrix

Since we are primarily interested in electrons, we will restrict our discussion to the case of $q < 0$ hereafter. Nevertheless, all results and conclusions may be translated to the case of $q > 0$ simply by replacing ψ by $\psi + \pi$. In a sense, the restriction $q < 0$ does not lead to any loss of generality because $q > 0$ in (2.1) is mathematically equivalent to the case of $q < 0$ with a different value of ψ_0. Note of course that assuming $E_0 > 0$ (which we stated earlier) and $q < 0$ is equivalent to simply assuming $a_0 > 0$, as far as the mathematics of (2.2) is concerned.

Equation (2.7) may be used to plot the various possible trajectories of a single particle (or the trajectories of multiple non-interacting particles) in the ψ- $\gamma\beta$ phase space. An example of such a phase contour diagram is shown in Fig. 2-1, which was made for the case of an electron injected into a wave travelling at a subluminal phase velocity. The phase contour diagram is periodic in ψ with a period of 2π. As such, we restrict its domain to $-\pi/2 < \psi \leq 3\pi/2$.

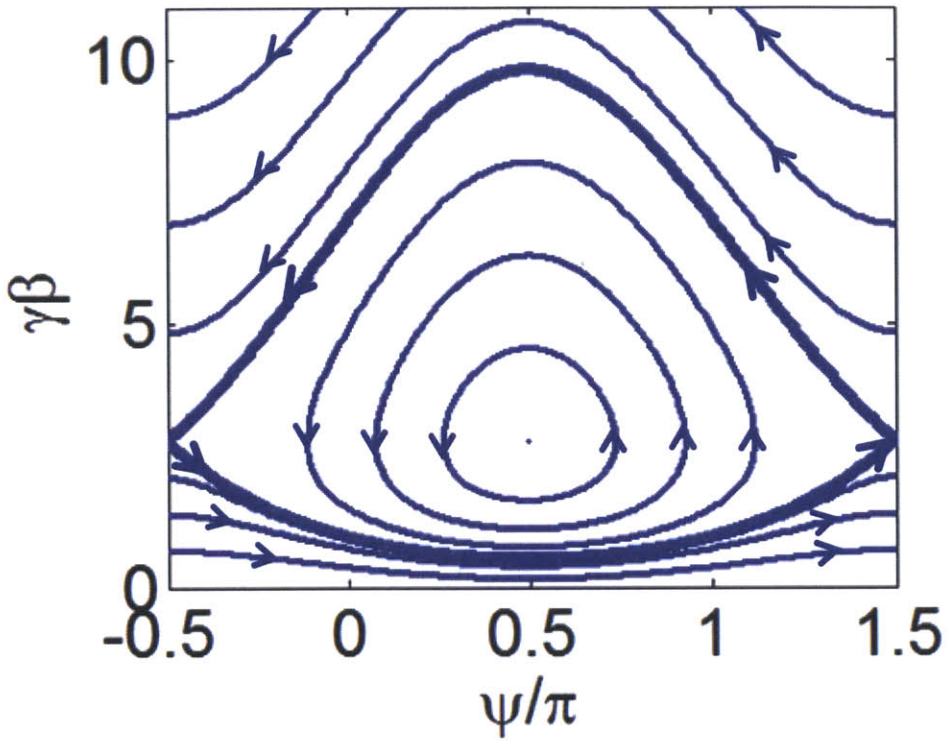

Fig. 2-1: A phase contour diagram, showing various possible trajectories of an electron in a given z-directed CW electric field. Arrows indicate the direction of electron motion in time along the phase contour lines. The separatrix, a boundary separating trapped orbits from untrapped trajectories, is drawn in thicker lines. This phase contour plot was made for the case of $a_0 = 0.1553$ and $\beta_{ph} = 0.9409$.

2.2.1 Subluminal phase velocities

In this section, we restrict our discussion to the case of $\beta_{ph} < 1$. If an electron were to begin in the field at $\psi = \pi/2$, moving in the direction of wave propagation with velocity $\beta = \beta_{ph}$, one can see readily from (2.1) and (2.2) that the electron's velocity would never change since the electron would never experience any force. The trajectory of such an electron is represented by the single-point "contour" at $(\pi/2, \gamma_{ph}\beta_{ph})$ in Fig. 2-1 (i.e. where $\gamma_{ph}\beta_{ph}$ is approximately 2.78).

If the electron were to start at any point in phase space other than $(\pi/2 + n\pi, \gamma_{ph}\beta_{ph})$, n any integer, the electron's position in phase space would vary with time. The electron would move along the phase contour line determined by its initial momentum and phase. Fig. 2-1 shows some

of these phase contour lines. Arrows indicate the direction along the contour in which the electron moves as time progresses.

To foster familiarity with phase contour diagrams, we present in Fig. 2-2 schematic illustrations of electron motion (relative to the CW wave) and corresponding phase contour lines for three general scenarios. Fig. 2-2(a) and (d) deal with the case of a trapped orbit, for which $\psi_s - 2\pi < \psi(t) < \psi_s + 2\pi$, $\forall t$ (ψ_s being the initial value of ψ). In this case, the electron is carried along by the wave and always oscillates about $\psi = \pi/2$. This oscillation can be made so large (by increasing the magnitude of a_0, for instance) that the turning points of the electron's motion relative to the CW wave occur arbitrarily close to $\psi = -\pi/2$ and $\psi = 3\pi/2$. Physically, what happens is that the electron gains just enough energy by the time it arrives close to $\psi = 3\pi/2$ to be just slightly faster than the wave, and the electron loses just enough energy by the time it arrives close to $\psi = -\pi/2$ to be just slightly slower than the wave. As the electron's turning points in Fig. 2-2(a) approach $\psi = -\pi/2$ and $\psi = 3\pi/2$, the electron's phase space orbit in Fig. 2-2(d) approaches the separatrix. The separatrix is a boundary that separates trapped orbits from untrapped trajectories. An electron moving exactly on the separatrix will stop at the first point it encounters that is of the form $(3\pi/2 + 2n\pi, \gamma_{ph}\beta_{ph})$, n any integer, and remain there for all time. Physically, what happens is that the electron arrives at a point where the electric field is zero with a velocity that matches the wave's phase velocity exactly. Henceforth, the electron moves with the wave but never experiences any force.

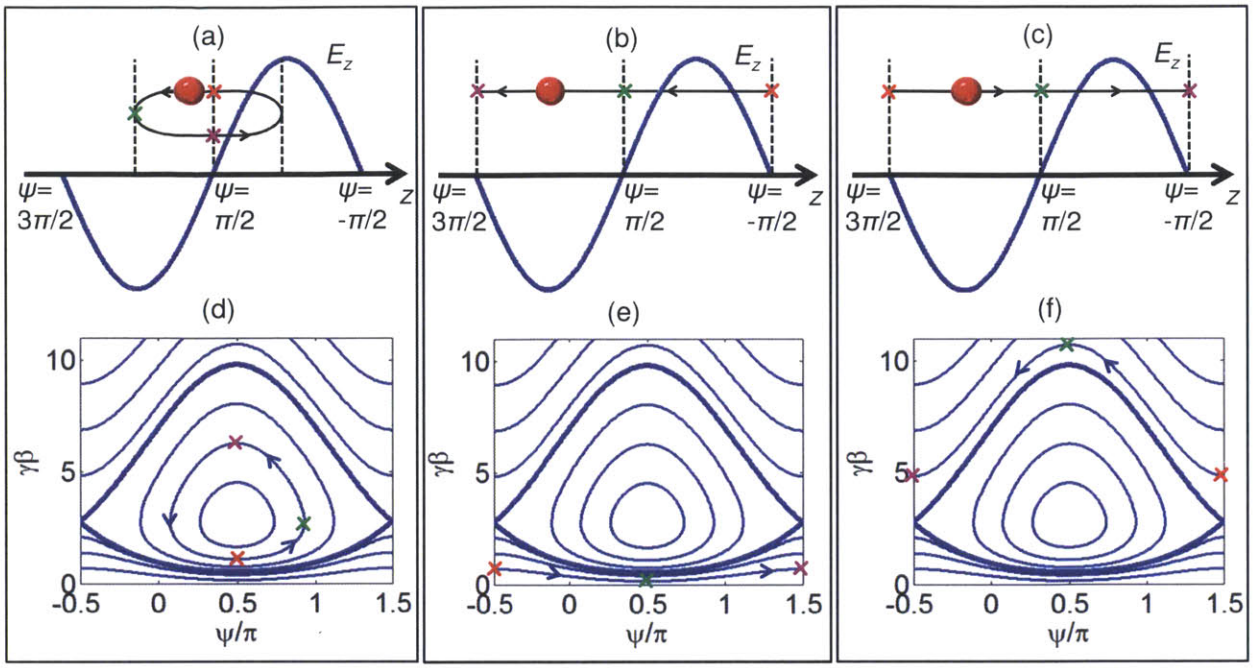

Fig. 2-2: Visualization of the electron motion represented by phase contour lines. Schematic illustrations of electron motion relative to the CW wave $E_z = E_0\cos(\psi)$ are shown corresponding to (a) a trapped orbit, (b) an untrapped path below the separatrix (injected electron too slow to be trapped), and (c) an untrapped path above the separatrix (injected electron too fast to be trapped). Arrows and crosses in (d), (e) and (f) mark the phase contour lines corresponding to the cases in (a), (b) and (c) respectively. Arrows (excluding those on axes, of course) indicate direction of electron motion with time. Colored crosses have been inserted to improve ease of identifying corresponding electron positions in schematic diagram and phase space. The phase contour plots were made for the case of $a_0 = 0.1553$ and $\beta_{ph} = 0.9409$.

Fig. 2-2(b) and (e) correspond to the case of an untrapped trajectory, with the electron slipping backward continuously relative to the CW wave because the electron never gains enough energy from each accelerating half-cycle to stay within the cycle. In this case, $\beta(t) < \beta_{ph}\ \forall t$. Fig. 2-2(c) and (f) also correspond to an untrapped trajectory, but with the electron slipping forward continuously relative to the CW wave. Here, $\beta(t) > \beta_{ph}\ \forall t$. Note that for a given initial electron energy, the choice of injection (i.e. initial) phase can determine if the electron will be trapped or untrapped. For initial energies below the minimum or above the maximum of the separatrix, however, the choice of any injection phase will result in an untrapped trajectory.

2.2.2 Luminal and superluminal phase velocities

If the phase velocity is luminal ($\beta_{ph} = 1$) or superluminal ($\beta_{ph} > 1$), orbital trapping, which involves the particle velocity exceeding the phase velocity at some point, is no longer possible. $\beta(t) < \beta_{ph}\ \forall t$ must be true under any circumstances, so the particle will always be slipping backward with respect to the wave. For $\beta_{ph} = 1$, trapping is still possible in the form of a trapped asymptotic trajectory. For $\beta_{ph} > 1$, only untrapped trajectories are possible and the separatrix does not exist.

Fig. 2-2.1 (a) and (d) illustrate the case of asymptotic trapping in a luminal wave. Because $\beta < \beta_{ph} = 1$ for all finite particle energies, the particle is in fact always slipping with respect to the wave, but it slips asymptotically towards a certain phase value in the accelerating half-cycle, and never slips out of the first accelerating half-cycle it encounters. Hence, the phase slippage of such a trapped particle becomes increasingly negligible with time (although the slippage never stops) and after some time the particle effectively experiences a constant accelerating gradient forever, assuming an electromagnetic beam of infinite length and energy, Note from Fig. 2-2.1 (d) and (e) that the phase contour diagram in the luminal case resembles that in the subluminal case, except here only the portion below $\gamma\beta = \gamma_{ph}\beta_{ph}$ is valid (since in the luminal case $\gamma\beta = \gamma_{ph}\beta_{ph}$, the widest portion of the separatrix, occurs at infinity). As such, the separatrix for the luminal case consists only of a bottom arc running to the right, without a top arc running to the left. Any particle placed in the phase space above this bottom arc will be asymptotically trapped, whereas any particle placed in the phase space below it will be untrapped. The phase contour lines lying within the separatrix in the luminal case all run to infinity (in $\gamma\beta$), asymptotically approaching constant phase values.

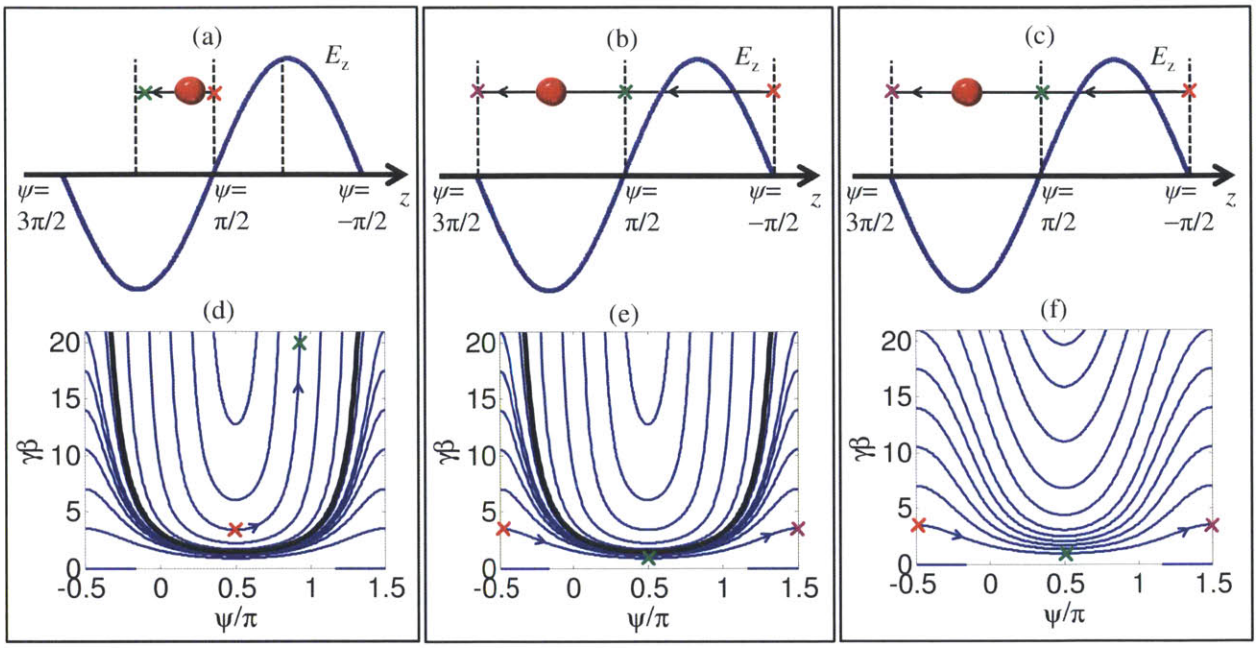

Fig. 2-2.1: Visualization of the electron motion represented by phase contour lines. Schematic illustrations of electron motion relative to the CW wave $E_z = E_0\cos(\psi)$ are shown corresponding to (a) a trapped asymptotic trajectory in a luminal wave, (b) an untrapped path in a luminal wave (injected electron too slow to be trapped), and (c) an untrapped path in a superluminal wave. Arrows and crosses in (d), (e) and (f) mark the phase contour lines corresponding to the cases in (a), (b) and (c) respectively. Arrows (excluding those on axes, of course) indicate direction of electron motion with time. Colored crosses have been inserted to improve ease of identifying corresponding electron positions in schematic diagram and phase space. The separatrices in (d) and (e) are not only thicker but also of a different color (black) for extra distinctiveness since many other phase contours run close by it. The phase contour plots were made for $a_0 = 0.1553$, with $\beta_{ph} = 1$ in the luminal cases and $\beta_{ph} = 1.01$ in the superluminal case.

Untrapped trajectories for the luminal and superluminal cases are illustrated schematically in Fig. 2-2.1 (b) and (c) (they are identical to each other and identical to Fig. 2-2(b)) respectively, with the corresponding trajectories shown in Fig. 2-2.1 (e) and (f) respectively. The separatrix does not exist in the superluminal case because there is no possibility of trapping.

Because asymptotic trapping can ideally keep a particle from ever slipping out of the first accelerating half-cycle the particle encounters, and accelerate the particle at a practically

constant acceleration gradient, one intuitively feels that it may be a promising strategy to pursue for accelerating particles, if the right beam is readily available.

2.2.3 Evolution of phase contour diagrams with field strength and phase velocity

In this sub-section, we discuss qualitatively how the phase contour diagram and the separatrix changes from one set of values for normalized field strength a_0 and normalized phase velocity β_{ph} to another. A fairly comprehensive overview is given by the collection of phase contour plots in Fig. 2-2.2, which is organized as follows: All plots in the first column were made for $a_0 = 0.1$, all plots in the second column for $a_0 = 1$ and all plots in the third column for $a_0 = 10$. All figures in the same row share the same β_{ph}, which increases from top to bottom and include subluminal, luminal and superluminal phase velocities.

When $a_0 = 0.1$ and β_{ph} is very non-relativistic, the separatrix is "eye-like" and approximately symmetric in $\gamma\beta$ about $\gamma\beta = \gamma_{ph}\beta_{ph}$. As β_{ph} increases (keeping a_0 constant), the "eye" rises and widens, but the upper arc swells disproportionately and appears increasingly "mountain-like", which also encourages one to fancy the lower arc as a "valley" (imagine looking at a mountain through a valley between two hills). This widening of the separatrix reflects the increasing range of velocities an orbitally trapped particle can possess as the phase velocity of the driving field increases. The disproportionate widening (i.e. the upper arc swells more than the lower arc) is simply a result of choosing $\gamma\beta$ for the ordinate of the phase contour diagram; if we had chosen β instead for the ordinate, it would have been the lower arc that swells more as the "eye" rises and the upper arc is increasing squished flat against $\beta = 1$. The widest part of the separatrix always occurs at $\gamma\beta = \gamma_{ph}\beta_{ph}$.

When $\beta_{ph} = 1$, $\gamma_{ph}\beta_{ph}$ is infinite and the widest part of the separatrix occurs at infinity ($\psi = -\pi/2, 3\pi/2$), so the phase contour diagram becomes entirely "valley-like". Although in Fig. 2-2.2 the phase contour diagram appears to change abruptly from the $K_{ph} = 100$ MeV cases (where $K_{ph} \equiv (\gamma_{ph} - 1)mc^2$) to the $\beta_{ph} = 1$ cases, this is only because we chose to show the entire separatrix in the $K_{ph} = 100$ MeV cases. If we had restricted our range of $\gamma\beta$ to values within the bottom arc of

the separatrix, the visual transition in the diagrams from K_{ph} = 100 MeV to the β_{ph} = 1 would probably be more continuous.

For $\beta_{ph} > 1$, the separatrix does not exist because trapping is impossible. The diagrams continue to look "valley-like", with the "valleys" becoming shallower as β_{ph} increases. This simply reflects the increasing velocity mismatch between the particle and the wave, and hence a diminished ability of the wave for particle acceleration.

The trend with which the phase contour diagrams evolve as β_{ph} is varied from nonrelativistic to relativistic to luminal to superluminal velocities is essentially the same for other values of a_0. We can see from the $a_0 = 1$ and $a_0 = 10$ cases in Fig. 2-2.2 that for larger a_0, the subluminal diagrams become "mountain-like" sooner and the separatrix minimum in the luminal diagram is lower, which accords with the increased acceleration capability one would expect from a wave with larger a_0. Also, the contours in the diagrams become steeper, which accords with the fact that the acceleration gradient at every point in phase (where the field is not zero) is now higher.

With some mathematical rigor, we can make even more precise statements about the separatrix minimum and maximum that may not be obvious from simply studying Fig. 2-2.2:

1. If we keep β_{ph} constant, the separatrix maximum increases and the separatrix minimum decreases as a_0 increases.
2. If we keep a_0 constant, the separatrix maximum increases as β_{ph} increases. The separatrix minimum decreases as β_{ph} increases for $0 < \gamma_{ph}\beta_{ph} < a_0$, and increases as β_{ph} increases for $\gamma_{ph}\beta_{ph} > a_0$. For given a_0, the least separatrix minimum possible thus occurs when $\gamma_{ph}\beta_{ph} = a_0$.

Through all this, bear in mind that we have been assuming without loss of generality that $\beta_{ph} > 0$, $a_0 > 0$. We will elaborate upon this behavior of the separatrix in Section 2.3.2.

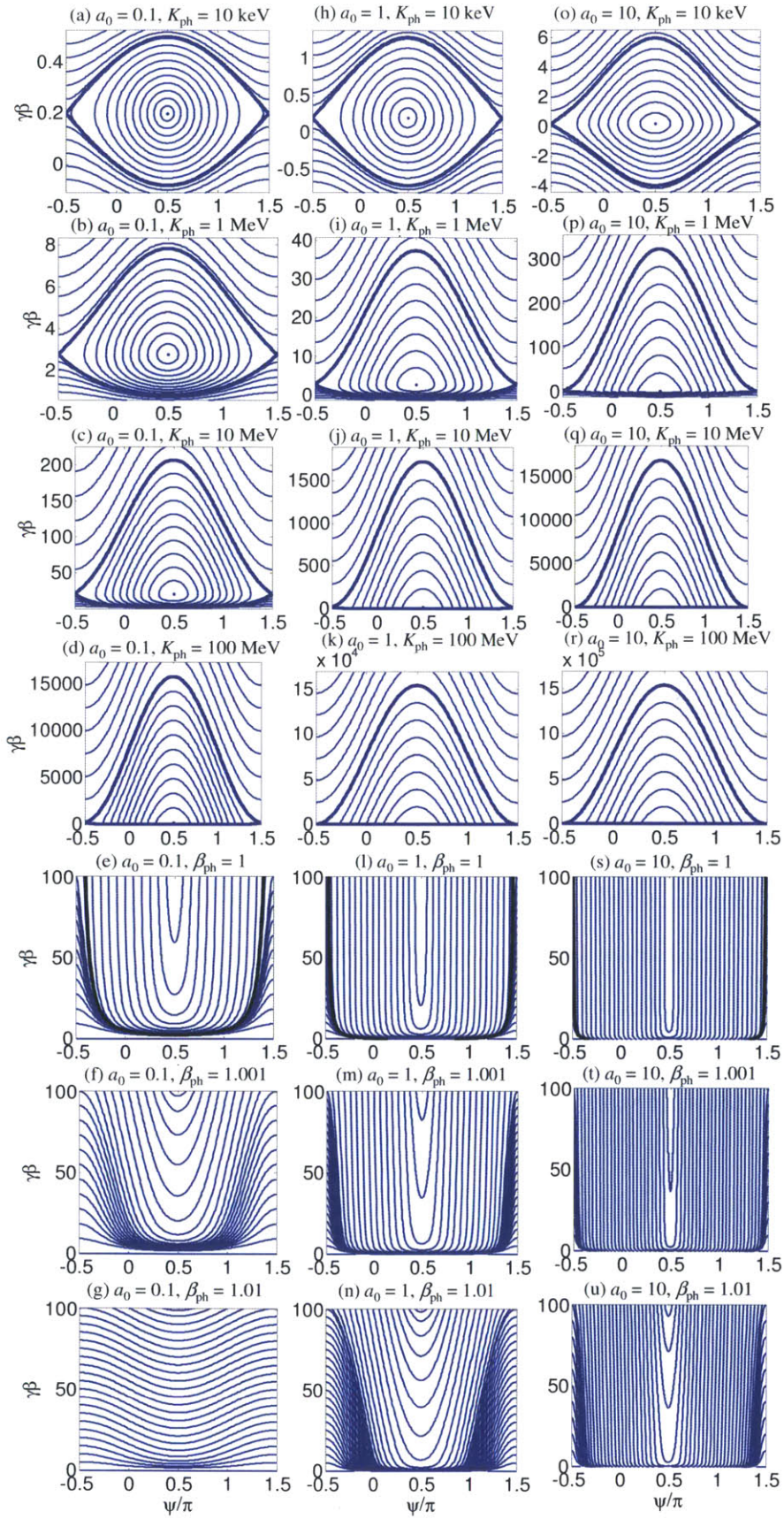

Fig. 2.2: Phase contour diagrams for various values of a_0 and β_{ph}. The first column of figures ((a) to (g)) correspond to $a_0 = 0.1$, the second ((h) to (n)) to $a_0 = 1$, and the third ((o) to (u)) to $a_0 = 10$. Subluminal phase velocities considered are $K_{ph} = 0.01, 1, 10, 100$ MeV. Superluminal phase velocities considered are $\beta_{ph} = 1.01, 1.001$. The separatrix is plotted as a thicker line in the subluminal diagrams. For the luminal ($\beta_{ph} = 1$) case, the separatrix is not only thicker but also of a different color (black) for extra distinctiveness since many other phase contours run close by it.

2.3 Properties of the phase contour diagram

The objective of this section is to present mathematical formulas for a few important features of the phase contour diagram.

2.3.1 The widest portion of trapped trajectories

The widest portion of the trapped trajectories (as well as that of the separatrix) occurs at $\gamma\beta = \gamma_{ph}\beta_{ph}$ (for $\beta_{ph} = 1$, this implies $\gamma\beta \rightarrow \infty$). This is evident from the fact that (2.7) applied to a general trapped trajectory has exactly one solution for a given ψ (and is hence at the widest portion of the trapped trajectory) when

$$\beta_{ph}^2 + G^2(\psi) = 1. \tag{2.10}$$

This gives

$$(\gamma\beta)(\psi) = G(\psi)\beta_{\mathrm{ph}}\gamma_{\mathrm{ph}}^2 = \gamma_{\mathrm{ph}}\beta_{\mathrm{ph}}, \tag{2.11}$$

where the second equality was made by noting that (2.10) gives $G(\psi) = (1-\beta_{\mathrm{ph}}^2)^{1/2} = 1/\gamma_{\mathrm{ph}}$ (positive sign chosen for square root because, as seen from (2.5), $G(\psi) > 0$ if $\beta_{\mathrm{ph}} \leq 1$, which is in turn necessary for the possibility of trapped trajectories and the existence of a separatrix). By solving (2.10) for ψ, one can also determine the two values of ψ corresponding to the widest portion of a phase contour line containing the point $(\psi_s, (\gamma\beta)_s)$. Combining (2.5) and (2.10), and considering only the domain $-\pi/2 < \psi \leq 3\pi/2$, we find that the values of ψ, ψ_l on the left and ψ_r on the right, are given by

$$\psi_l = \arcsin\left[\frac{1}{a_0\beta_{\mathrm{ph}}}\left(\frac{1}{\gamma_{\mathrm{ph}}} - G(\psi_s)\right) + \sin\psi_s\right], \qquad -\frac{\pi}{2} < \psi_l \leq \frac{\pi}{2} \tag{2.12}$$

$$\psi_r = \pi - \psi_l$$

Recall from (2.5) that $G(\psi_s) = (\gamma - \gamma\beta\beta_{ph})_s$. For $\beta_{ph} = 1$, simply set $1/\gamma_{ph} = 0$. Equation (2.12) is a convenient way of determining ψ_l and ψ_r because many calculators and computational programs (e.g. Matlab R2011b) return a value between $-\pi/2$ and $\pi/2$ by default when the arcsine function is called with a single argument.

2.3.2 The maximum and minimum of the separatrix

Equation (2.7) may be used to solve for the maximum and minimum of the separatrix, which both occur at $\psi = \pi/2$. For $\beta_{ph} < 1$, we find that

$$\begin{aligned}(\gamma\beta)_{\text{sep max,min}} &= \left(G_1\beta_{ph} \pm \sqrt{\beta_{ph}^2 + G_1^2 - 1}\right)\gamma_{ph}^2 \\ &= \gamma_{ph}\beta_{ph}\left(2\gamma_{ph}\beta_{ph}a_0 + 1\right) \pm \gamma_{ph}\sqrt{4\gamma_{ph}\beta_{ph}a_0}\sqrt{\gamma_{ph}\beta_{ph}a_0 + 1} \\ &\approx \begin{cases} (\gamma\beta)_{ph} \pm \sqrt{4a_0(\gamma\beta)_{ph}}, & \gamma_{ph} \approx 1,\ 2\gamma_{ph}\beta_{ph}a_0 << 1 \\ 2(\gamma\beta)_{ph}^2 a_0 \pm 2(\gamma\beta)_{ph}^2 a_0 + \dfrac{1-(2a_0)^2}{4a_0}, & \beta_{ph} \approx 1,\ \gamma_{ph}\beta_{ph}a_0 >> 1 \end{cases}\end{aligned} \tag{2.13}$$

where $G_1 = 2\beta_{ph}a_0 + 1/\gamma_{ph}$ and $(\gamma\beta)_{ph} \equiv \gamma_{ph}\beta_{ph}$. Choosing the "+" sign in (2.13) gives the maximum of the separatrix, whereas choosing the "–" sign gives the minimum. When the phase velocity is very non-relativistic, the final approximate equality in (2.13) tells us that the separatrix maximum and minimum are located at approximately equal distances in $\gamma\beta$ from $\gamma_{ph}\beta_{ph}$, with this distance approximately proportional to $(a_0(\gamma\beta)_{ph})^{1/2}$, so scaling a_0 or $\gamma_{ph}\beta_{ph}$ by a given factor tunes this distance by approximately the same amount. When the phase velocity is very relativistic, the maximum of the separatrix occurs at approximately $\gamma\beta = 4(\gamma\beta)_{ph}^2 a_0$, and scaling a_0 by a factor of 4, for instance, affects the separatrix maximum in roughly the same way that scaling $(\gamma\beta)_{ph}$ by a factor of 2 does. Note that the third term in the relativistic approximation has been included for a more accurate approximation of the separatrix minimum, since when the "–" sign is chosen the first two terms subtract to 0.

When $\beta_{ph} = 1$, only the bottom arc of the separatrix exists and the minimum is given by

$$(\gamma\beta)_{\text{sep min}} = \frac{1-(2a_0)^2}{4a_0}, \quad \beta_{\text{ph}} = 1 \tag{2.14}$$

Not surprisingly, this is also the expression we obtain for the separatrix minimum in (2.13) in the limit of a very relativistic phase velocity.

In Section 2.2.3, we pointed out that the separatrix maximum increases as a_0 and/or β_{ph} increases. This is immediately apparent just from looking at (2.13) with the '+' sign chosen.

We also noted that for given β_{ph}, the separatrix minimum decreases as a_0 increases; that for given a_0, the separatrix minimum decreases as β_{ph} increases when $0 < \gamma_{\text{ph}}\beta_{\text{ph}} < a_0$, and increases as β_{ph} increases when $\gamma_{\text{ph}}\beta_{\text{ph}} > a_0$; and finally that for given a_0, the lowest possible separatrix minimum occurs when $\gamma_{\text{ph}}\beta_{\text{ph}} = a_0$. Its value is

$$(\gamma\beta)_{\text{sep min min}} = -a_0. \tag{2.15}$$

These statements on the separatrix minimum are proven in Appendix B.

2.3.3 Asymptotic trapping with maximum acceleration gradient

We have already noted that asymptotic trapping can keep a particle from ever slipping out of the first accelerating half-cycle the particle encounters, and accelerate the particle with a practically constant acceleration gradient. For a particle of injected momentum $\gamma_s\beta_s$ to be asymptotically trapped, we must have (in addition to $\beta_{\text{ph}} = 1$)

$$a_{0,\text{trap}} \geq \frac{\gamma_s}{2}(1-\beta_s). \tag{2.16}$$

If $a_0 = \gamma_s(1-\beta_s)/2$, the particle's momentum is exactly equal to the momentum of the separatrix minimum (which occurs at $\psi = \pi/2$). The particle will be asymptotically trapped and accelerated, asymptotically slipping towards $\psi = 3\pi/2$ as its energy grows more and more relativistic. The travelling wave has a node at $\psi = 3\pi/2$, however. Close to this asymptote, the

acceleration gradient is likely to be very small, and the particle may have to propagate in the field over a substantial amount of physical distance to obtain a certain desired energy gain.

A better strategy, as far as single-particle energy gain is concerned, would be to asymptotically trap the particle at or close to $\psi = \pi$, where the acceleration gradient is maximum. Note that the minimum of the trapped orbits always occur at $\psi = \pi/2$. Therefore, the smallest a_0 (which involves injecting the particle at $\psi = \pi/2$) required to asymptotically trap a particle of injected momentum $\gamma_s\beta_s$ such that the particle slips asymptotically towards $\psi = \psi_\infty$, is

$$a_{0,\min} = \frac{\gamma_s(1-\beta_s)}{1-\sin\psi_\infty}. \tag{2.17}$$

For $\psi_\infty = \pi$, we simply have $a_{0,\min} = \gamma_s(1-\beta_s)$. exactly twice the smallest a_0 required to trap the same particle at $\psi_\infty = 3\pi/2$.

A larger a_0 is always more desirable because it corresponds to a higher acceleration gradient. To attain asymptotic trapping at $\psi = \psi_\infty$ when $a_0 > a_{0,\min}$, we need to start our particle of given injection momentum $\gamma_s\beta_s$ at the starting phase

$$\psi_{s0} = \pi - \arcsin\left[\frac{\gamma_s(1-\beta_s)}{a_0} + \sin(\psi_\infty)\right],\ a_0 \geq a_{0,\min},\ \frac{\pi}{2} \leq \psi_{s0} \leq \frac{3\pi}{2}, \tag{2.18}$$

where, as in (2.12), we define our arcsine function as one that returns a value between $-\pi/2$ and $\pi/2$.

In practice, the energy gain from asymptotic trapping will be limited by factors like slippage of the pulse envelope (since true CW operation is unlikely in reality) relative to its carrier and the depletion of the driving laser, which is not modeled here.

2.4 Maximum energy gain of a single particle

Given a wave of the form of (2.1) with a specified a_0 and β_{ph}, and assuming we have complete freedom to choose the points at which to inject and extract a particle, we can use the phase

contour diagram to devise a general scheme for maximum acceleration of an electron of initial velocity β_s. Allow ψ_s to denote the injection phase and ψ_e the extraction phase. Our strategy, which one obtains simply by studying phase contour diagrams like Fig. 2-1, may be divided into three scenarios:

1. If $\beta_s < \beta_{sep\ min}$, we choose $\psi_s = \pi/2$ and $\psi_e = 3\pi/2$. In this scenario, the particle can never be captured, so we inject it at the start of an accelerating half-cycle and extract it as soon as it has slipped through the entire half-cycle. For $\beta_{ph} > 1$, the particle can only slip backward relative to the wave so only this scenario is applicable.
2. If $\beta_{sep\ min} < \beta_s < \beta_{ph}$, we achieve maximum acceleration by allowing the particle to ride the trapped orbit just inside the separatrix, up to an energy that is arbitrarily close to the maximum of the separatrix. Hence, we choose $\psi_s \approx \pi - \psi_s'$ (we use "≈" here to indicate that we do not want a point on the separatrix, but one on a trapped orbit close to the separatrix), where

$$\psi_s' = \arcsin\left[\frac{1}{a_0\beta_{ph}}\left(G(\psi_s) - \frac{1}{\gamma_{ph}}\right) - 1\right], \qquad -\frac{\pi}{2} < \psi_s' \leq \frac{\pi}{2}. \tag{2.19}$$

   ψ_s' is simply the value of ψ corresponding to β_s along the lower arc of the separatrix, between $-\pi/2$ and $\pi/2$. Once again, $G(\psi_s) = (\gamma - \gamma\beta\beta_{ph})_s$. Using an injection phase of about ψ_s' also leads to the same energy gain, but the distance the particle has to travel is longer. The extraction phase is simply $\psi_e = \pi/2$, the energy peak of all trapped orbits.

   In the special case $\beta_{ph} = 1$, the choice of any starting phase within the separatrix will lead to arbitrarily large energy gain, since the particle is asymptotically trapped and never slips from the accelerating half-cycle.
3. If $\beta_s > \beta_{ph}$, we choose $\psi_s = 3\pi/2$ and $\psi_e = \pi/2$. Although it may be possible to trap the particle, it is invariably possible to obtain higher energy gain by using an untrapped trajectory.

This strategy is summarized in Fig. 2-3.

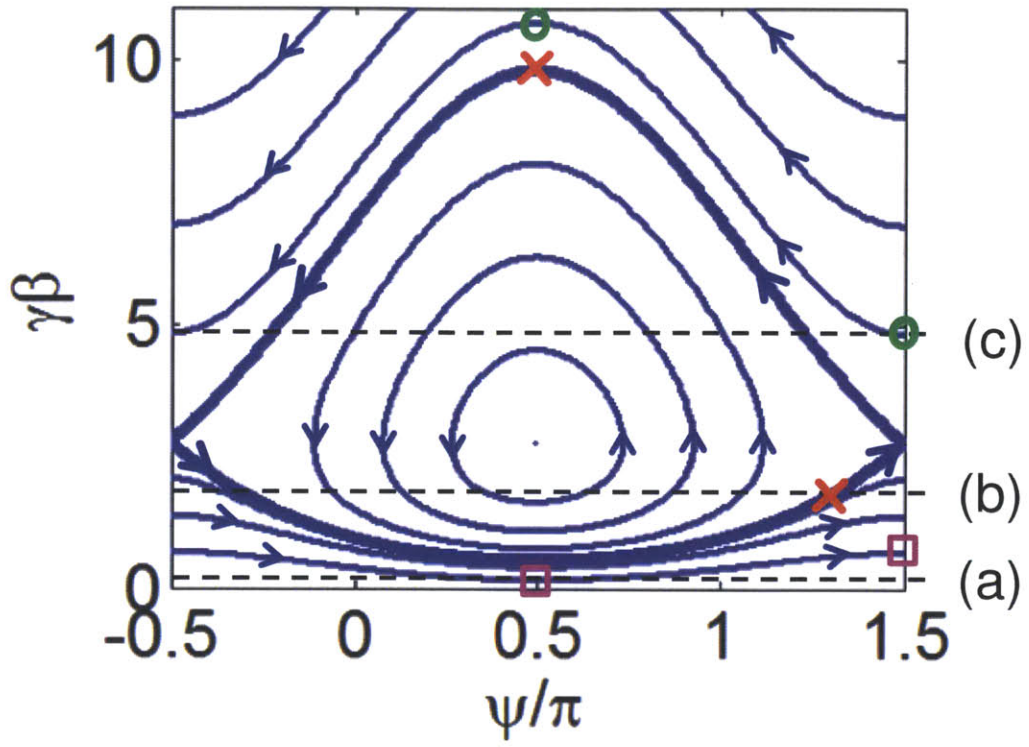

Fig. 2-3: Illustration of optimal acceleration scheme for a single electron of given initial velocity β_s such that (a) $\beta_s < \beta_{sep\,min}$, for which magenta squares mark injection and extraction points; (b) $\beta_{sep\,min} < \beta_s < \beta_{ph}$, for which red crosses mark injection and extraction points (note that the crosses are not exactly on the separatrix, but on a trapped orbit arbitrarily close to the separatrix); and (c) $\beta_s > \beta_{ph}$, for which green circles mark injection and extraction points. Injection points in the various scenarios are the points through which the corresponding dotted line passes.

By using (2.7), and the injection and extraction phases we have determined for various scenarios, we find that the momentum of the particle upon extraction is

$$(\gamma\beta)_e = \left(G\beta_{ph} + S\sqrt{\beta_{ph}^{\,2} + G^2 - 1} \right)\gamma_{ph}^{\,2} \tag{2.20}$$

where $G = -2\beta_{ph}a_0 + G(\psi_s)$, $S = -1$ for Scenario 1; $G = 2\beta_{ph}a_0 + 1/\gamma_{ph}$, $S = +1$ for Scenario 2 (so (2.20) gives the same solution as (2.13) with the "+" sign); and $G = 2\beta_{ph}a_0 + G(\psi_s)$, $S = +1$ for Scenario 3. As before, $G(\psi_s) = (\gamma - \gamma\beta\beta_{ph})_s$.

To give an idea of how the maximum energy gain of a single particle, as obtained via the strategy outlined above, scales with various a_0 and β_{ph}, we plot color maps of maximum final kinetic energy as a function of a_0 and $K_{ph} \equiv (\gamma_{ph} - 1)mc^2$ for electrons of various injected kinetic energies in Fig. 2-4. The range of β_{ph} in this figure is confined to the subluminal regime. Below each color map of maximum final kinetic energy, we have also plotted a corresponding map showing which optimization scenario the maximum energy gain at each point corresponds to. We observe that Scenario 2 (riding a trapped orbit close to the separatrix) corresponds to the regime (green) containing the most promising final electron energies, and that within Scenario 2 energy gain improves dramatically with more luminal β_{ph} and larger a_0. Also, at small values of a_0, we observe that the phase velocity β_{ph} most suitable for accelerating a particle injected with a velocity of β_s is one slightly above β_s (this once again takes place in Scenario 2).

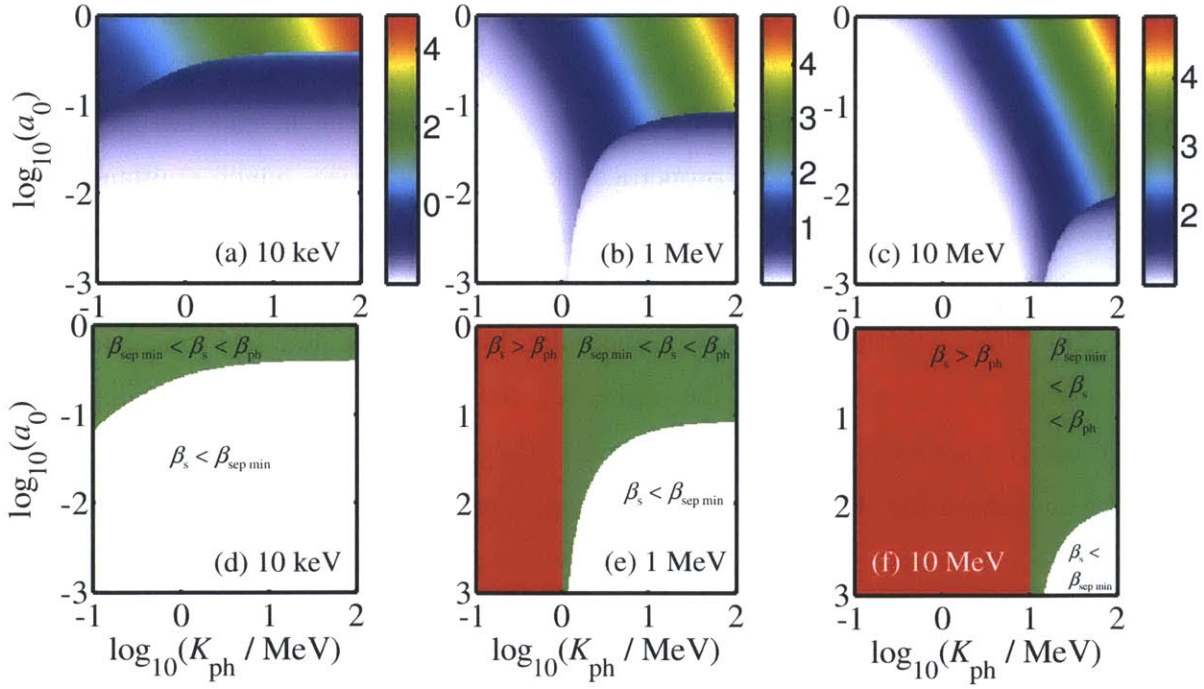

Fig. 2-4: Color maps of maximum $\log_{10}(K_e$ / MeV) as function of a_0 and $K_{ph} \equiv (\gamma_{ph} - 1)mc^2$, K_e being the kinetic energy of the particle (an electron in this case) upon extraction, for an injected kinetic energy K_s (with $\beta_s > 0$) of (a) 10 keV, (b) 1 MeV and (c) 10 MeV. (d), (e) and (f) correspond to (a), (b) and (c) respectively, and show the optimization scenario at each point: white indicates $\beta_s < \beta_{sep\,min}$, green $\beta_{sep\,min} < \beta_s < \beta_{ph}$ and red $\beta_s > \beta_{ph}$.

Before going any further, there are two important points to be made about how figures in this section like Fig. 2-4 should be understood and the realism of the energy gains presented. Firstly, note that Fig. 2-4(a) predicts electron acceleration from 10 keV to over 10 GeV with a wave of $a_0 = 1$, $K_{ph} = 100$ MeV. Although such a result may seem incredible, recall that with (2.2) we have assumed a CW beam of infinite length and energy. We have also assumed that the electron may be allowed to travel an arbitrarily long distance in the wave (in other words, we have assumed an acceleration facility of potentially infinite length, channeling a single-frequency TM_{0p} traveling wave of infinite energy). In reality, we would not have a CW beam but at best a narrowband pulse of finite energy and group velocity, and even if our waveguide continues indefinitely, the pulse is likely to slip from the electron before the electron has arrived at the separatrix peak in Scenario 2. Pulse-spreading due to dispersion is also an issue we have not considered at this point. The design of a waveguide strong enough to withstand fields corresponding to $a_0 = 1$ is yet another challenge.

Secondly, we have optimized only for the energy gain of a single particle. In reality we are interested in accelerating an electron bunch instead of a single electron. In addition to energy gain, we would also be concerned about properties like final bunch size, bunch emittance and energy spread of our accelerated bunch. Since the phase spread of a bunch tends to be larger at the peak of a trapped orbit than at its side (widest part), extracting the bunch at the peak is not likely to be optimal if a small phase spread is important. It is also not practical to accelerate a bunch along a trapped orbit too close to the separatrix, since all particles that fall outside the separatrix will not be trapped. Non-idealities like space charge, radiation reaction and wakefields should also be accounted for. The final optimization parameters for a realistic implementation involving multiple interacting particles are thus likely to be different from what was obtained here.

With these two points in mind, we nevertheless find that Fig. 2-4 gives a very useful overview of what kind of a_0 and β_{ph} must be achieved for physics to even permit at all a certain electron energy gain desired, under the most idealized conditions. This idealized analysis is only the first step, but an important one, towards an engineering solution. In the upcoming chapters, we will work with electrodynamic models that are less analytically tractable but closer to reality.

Fig. 2-4 is also instructive in showing us the sensitivity of maximum final kinetic energy to changes in phase velocity when the latter is close to c. A waveguide designer used to thinking of

phase velocity in terms of β_{ph} (instead of γ_{ph}) may be tempted to make the approximation β_{ph} = 0.995 ≈ 0.9995 ≈ 1 for a waveguided travelling field, but this is an egregious assumption where the acceleration of relativistic particles is concerned: β_{ph} = 0.995 corresponds to $\log_{10}(K_{ph}/\text{MeV})$ = $\log_{10}(4.62)$ = 0.665, whereas β_{ph} = 0.9995 corresponds to $\log_{10}(K_{ph}/\text{MeV})$ = $\log_{10}(15.7)$ = 1.20, and β_{ph} = 1 corresponds to $K_{ph} = \infty$. From Fig. 2-4 one can tell that these values of K_{ph} have very different maximum acceleration profiles as a function of a_0 (in fact $K_{ph} = \infty$ lies beyond the plotted range). Extreme precision in phase velocity is therefore paramount in an optimal waveguide design.

Fig. 2-4 may be more directly useful for low a_0. In this case, waveguide damage becomes less of a concern and the electron is likely to slip from the accelerating half-cycle (whereupon we would want to extract the electron) before the pulse slips from the electron.

We have already noted that for a given $K_{ph} > K_s$, the energy gain profile is significantly better for values of a_0 that fall in Scenario 2 (green) than for those that fall in Scenario 1 (white). The formula for the boundary between the two regimes may be obtained as

$$a_{0,bd} = \left(\gamma_s - \gamma_s \beta_s \beta_{ph} - \frac{1}{\gamma_{ph}} \right) \frac{1}{2\beta_{ph}}, \tag{2.21}$$

with "=" replaced by "≥" (and "$a_{0,bd}$" replaced by "a_0") if we wish to refer to the regime corresponding to Scenario 2. Note that as β_{ph} approaches 1, $a_{0,bd}$ approaches a constant value: $\beta_{ph} \rightarrow 1 \Rightarrow a_{0,bd} \rightarrow \gamma_s(1-\beta_s)/2$. This expression for $a_{0,bd}$ is the same as what we calculated in (2.16) for the minimum a_0 required to asymptotically trap a particle of a given injected momentum when the phase velocity is luminal.

Fig. 2-5 presents the maximum energy gain for superluminal phase velocities. As noted before, the optimization regime always corresponds to Scenario 1 in this case. Since β can never exceed 1, and $\beta_{ph} > 1$, increasing β_{ph} (or decreasing β_s) for a given a_0 leads to increasing phase velocity mismatch and hence a smaller absolute maximum energy gain.

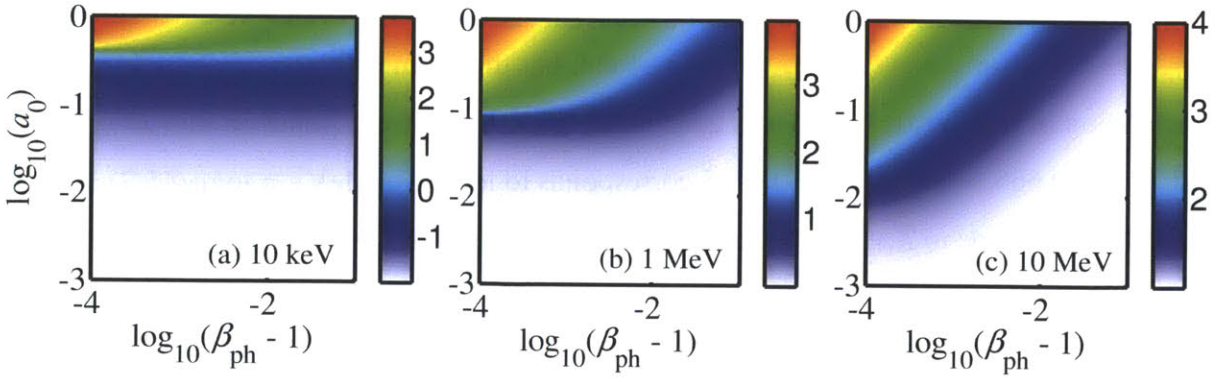

Fig. 2-5: Color maps of maximum $\log_{10}(K_e$ / MeV) as function of a_0 and superluminal β_{ph}, K_e being the kinetic energy of the particle (an electron in this case) upon extraction, for an injected kinetic energy ($\beta_s > 0$) of (a) 10 keV, (b) 1 MeV and (c) 10 MeV.

Fig. 2-4 and Fig. 2-5 support the conclusion that optimal acceleration of any injected particle is achieved by using a wave traveling exactly at the vacuum speed of light ($\beta_{ph} = 1$) with $a_0 > \gamma_s(1-\beta_s)/2$. This agrees with our previous observation that an asymptotically trapped particle stands to gain infinite energy from a CW beam of infinite length and energy.

Fig. 2-6 and Fig. 2-7 present the same kind of information as Fig. 2-4 and Fig. 2-5 respectively from a different perspective. Instead of plotting final kinetic energy as a function of a_0 and β_{ph} for several values of β_s, we plot fractional kinetic energy gain as a function of a_0 and β_{ph} for several values of β_{ph} in Fig. 2-6 and Fig. 2-7. These figures lead us to essentially the same conclusions as before. We have chosen to plot fractional kinetic energy gain instead of final kinetic energy in this case because β_s is no longer constant within each plot. In Fig. 2-7, it is interesting to note that for given a_0 and β_{ph}, the fractional kinetic energy gain *tends* to decrease with increasing β_s, although the decreasing phase mismatch (β_s is moving closer to β_{ph}) is in fact causing the absolute energy gain to increase.

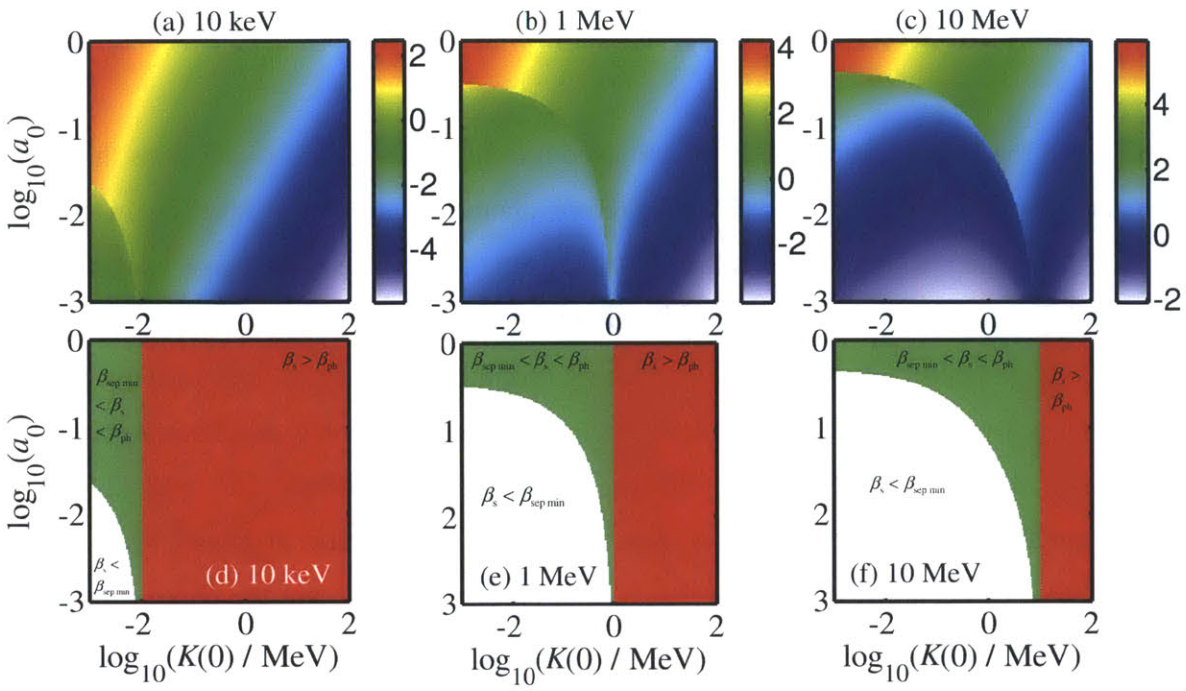

Fig. 2-6: Color maps of maximum $\log_{10}((K_e - K(0))/ K(0))$ as function of a_0 and $K(0) \equiv (\gamma_s - 1)mc^2$ (with $\beta_s > 0$), K_e being the kinetic energy of the particle (an electron in this case) upon extraction, for various phase velocities that correspond to electrons of kinetic energy $K_{ph} \equiv [1/(1 - \beta_{ph}^2)^{1/2} - 1]mc^2$ (a) 10 keV, (b) 1 MeV and (c) 10 MeV. (d), (e) and (f) correspond to (a), (b) and (c) respectively, and show the optimization scenario at each point: white indicates $\beta_s < \beta_{sep\ min}$, green $\beta_{sep\ min} < \beta_s < \beta_{ph}$ and red $\beta_s > \beta_{ph}$.

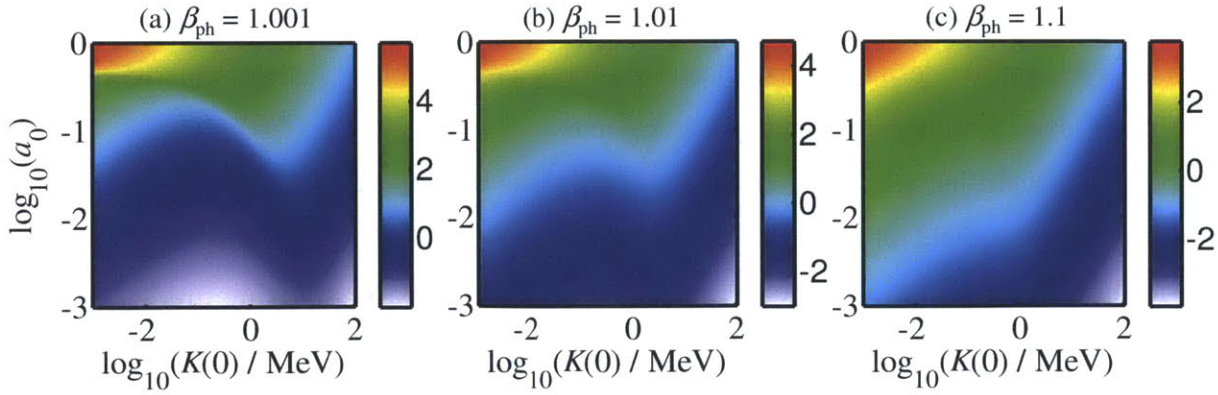

Fig. 2-7: Color maps of maximum $\log_{10}((K_e - K(0))/ K(0))$ as function of a_0 and $K(0) \equiv (\gamma_s - 1)mc^2$ (with $\beta_s > 0$) for various superluminal β_{ph}.

2.5 Summary and future work

We introduced the phase contour diagram and used it to illustrate the three scenarios that can occur when an electron is subject to a CW z-directed planar electric field traveling in the z-direction: (a) slippage, wherein the particle will slip continuously through successive accelerating and decelerating half-cycles, (b) asymptotic trapping, wherein the particle is borne along with the wave, slipping asymptotically towards a certain phase in an accelerating cycle and (c) orbital trapping, wherein the particle will be borne along with the wave, oscillating about its injection phase in the frame of the field. We derived analytical solutions (2.7) and (2.8) for normalized momentum and normalized velocity respectively as a function of phase. From (2.7) and (2.8), we may obtain momentum and velocity as a function of time via the chain rule after solving (2.9) with an appropriate numerical quadrature method.

Asymptotic trapping is an attractive scenario because it can lead to phase-matching over arbitrarily long distances, so long as the driving laser field is not depleted. In practice, the energy gain from asymptotic trapping will be limited by factors like slippage of the pulse envelope (since true CW operation is unlikely in reality) relative to its carrier and dispersive effects introduced by the guiding structure. Finally, in Section 2.4, we presented an injection and extraction strategy to maximize energy gain for a single electron of a certain kinetic energy given a_0 and β_{ph} of the driving wave. A study of the optimized results shows us that, if allowed to choose phase velocity (which in reality may be controlled by waveguide design or operation frequency) for a given field amplitude and initial electron energy, a luminal phase velocity is optimum if field amplitude and initial electron energy are sufficiently high, otherwise final energy is maximized at some subluminal phase velocity.

Future work would include the study of optimum trade-off between the group velocity and the z-directed electric field of actual electromagnetic fields to realize conditions as close as possible to those required for asymptotic trapping. One could consider studying this scheme in vacuum, in dielectric/metal waveguides or in plasma channels.

Chapter 3

Linear acceleration by radially-polarized laser beams

In the previous chapter, we dealt with an electron in a CW planar z-directed electric field. Such an idealization enabled us to derive analytical and semi-analytical solutions that gave us insight into the potentials and limitations of laser-driven linear acceleration schemes (for instance, we found in the asymptotic trapping scenario that it is possible to phase-match particle and field indefinitely if our z-directed planar electric field travels at the speed of light in vacuum, assuming the field does not deplete substantially). A CW planar z-directed electric field, however, is not a solution to Maxwell's equations and was studied only because it approximates the electric field on the beam axis of a weakly-focused TM_{0p} mode in vacuum or in a waveguide. In this chapter, we study the electrodynamics on the beam axis of an actual pulsed TM_{01} mode in vacuum where the focusing may be tight enough to cause substantial variations in phase velocity along the beam axis. Our goal is to understand how the electron energy gain scales as a function of beam focusing, pulse duration, pulse energy and peak power.

The vacuum TM_{01} mode is often referred to as the "radially-polarized laser beam" in the literature. It is attractive for linear acceleration because the z-directed electric field peaks on the beam axis, where the transverse electromagnetic fields vanish. As a result, particles on or near the beam axis are subjected primarily to an electric field parallel to the direction in which they are accelerated, and tend to experience a minimal of transverse wiggling that tends increase radiative losses. Our discussion follows the analyses

presented in [WK10] and [WK11a]. In those works, we performed our simulations using paraxial electromagnetic beam solutions. To verify that these paraxial solutions do indeed closely approximate the exact beam solution on the beam axis in the regime of interest, we will also present the exact solution for the pulsed radially-polarized beam – derived in Appendix E according to the steps in [Apr10] – and compare the two solutions.

In this chapter, all optimizations are carried out in view of maximizing net energy transfer from laser pulse to electron. We begin by studying the initially stationary electron. There has been some interest [Sal06, Sal07, FPV10, VPP05, KP07] in the scenario of electrons born (for instance, by ionization) in the path of the laser pulse, and a previous study by Fortin et. al. [FPV10] showed that an electron can reach the high-intensity cycles of the pulse without having been released by photoionization near the pulse peak. The study also concluded that the optimal beam waist at petawatt peak powers lies well within the paraxial wave regime. The latter conclusion, however, is true only for an initially stationary electron required to start at the laser focus. We show that after including the electron's initial position in the optimization space, we in fact achieve maximum acceleration with the most tightly-focused laser.

Next, we study acceleration of electrons moving with non-zero initial velocities. These electrons, the output of perhaps an RF gun or a preceding acceleration stage, are injected into the laser beam ahead of the pulse. We show that the net energy gain can be much greater for a pre-accelerated electron than for an initially stationary one. Our parameter space includes powers as low as 5 TW, and we will see that substantial acceleration can already be achieved with laser peak powers of a few terawatts. In particular, we give an example in which a 5 TW pulse, either 7.5 fs or 15 fs in pulse duration, accelerates an electron from a kinetic energy of 10 MeV to a kinetic energy of about 50 MeV; and another example in which a two-stage accelerator employing a 10 TW, 10 fs pulse in each stage accelerates an initially stationary electron to a final kinetic energy of about 36 MeV. These electron energies are already sufficient for applications like the production of hard x-rays via inverse Compton scattering [GBK+09].

Finally, we consider the linear acceleration of charged particles with a superposition of two radially-polarized laser beams. While a one-color pulsed paraxial beam can accelerate an initially-stationary electron up to only 40% of the theoretical energy gain limit, a two-color pulsed paraxial beam can accelerate the electron by over 90% of the one-color beam's theoretical gain limit, for a given total energy and pulse duration. The scheme succeeds by exploiting how the Gouy phase shift varies the interference pattern of the on-axis electric field with position along the beam axis. It is worth noting that sub-

wavelength focusing of a single beam can achieve only about 80% of the theoretical gain limit [MVA+12].

3.1 Exact and paraxial on-axis electric field formulas for the radially-polarized laser beam

Our original simulations were performed using the vector fields derived from the paraxial Gaussian beam according to the procedure presented in Appendix C (Appendix D discusses how to convert beam to pulse). Before launching into a discussion of our results proper, it is important to ascertain that the on-axis fields predicted by the paraxial solution closely approximate those predicted by the exact solution, which we derive in Appendix E.

As discussed in Appendix C, the wave equation for the vector wave

$$\nabla^2 \vec{A} - \frac{1}{c^2}\frac{\partial^2 \vec{A}}{\partial t^2} = 0, \tag{3.1}$$

reduces to the paraxial wave equation

$$\left(\frac{\partial^2}{\partial x^2} + \frac{\partial^2}{\partial y^2}\right) A_{0z} - 2ik\frac{\partial A_{0z}}{\partial z} = 0 \tag{3.2}$$

under the paraxial wave approximation [Hau84]

$$\left|\frac{\partial^2 A_{0z}}{\partial z^2}\right| << \left|2k\frac{\partial A_{0z}}{\partial z}\right|, \tag{3.3}$$

where $\vec{A} = A\hat{z} = A_{0z}e^{i\eta}\hat{z}$ and $\eta \equiv \omega t - kz + \psi_0$. (3.2) is simply a two-dimensional Schrodinger equation (with z in place of t) that has the well-known Gaussian beam solution

$$A_{0z} = A_0 f e^{-f\rho^2}, \tag{3.4}$$

where $f = \mathrm{i}/(\mathrm{i} + z/z_0)$, $\rho = r/w_0$, $z_0 = kw_0^2/2$ and A_0 is a normalization constant. For (3.4) to be valid under the paraxial wave approximation it has to satisfy (3.3) at all points in space-time. The derivatives of A_{0z} are

$$\begin{aligned} \frac{\partial A_{0z}}{\partial z} &= \frac{\mathrm{i}}{z_0}(1 - f\rho^2) f A_{0z} \\ \frac{\partial^2 A_{0z}}{\partial z^2} &= -\frac{\mathrm{f}^2}{z_0^2}\left[(1 - f\rho^2)(2 - f\rho^2) - 2\right] A_{0z} \end{aligned} \tag{3.5}$$

As a result, we have

$$\left|\frac{\partial^2 A_{0z}/\partial z^2}{2k\partial A_{0z}/\partial z}\right| = \left|\frac{\varepsilon_d^{\,2} f\left[(1 - f\rho^2)(2 - f\rho^2) - 2\right]}{4(1 - f\rho^2)}\right|, \tag{3.6}$$

where $\varepsilon_d = 2/(kw_0)$ is the divergence angle of the beam. From (3.5) or (3.6), one can see that (3.4), which has been a popular choice for modeling laser beams, does not satisfy the paraxial wave approximation (3.3) for all points in space-time, regardless of the amount of focusing. Specifically, when $z = 0$, $r = w_0$, $\partial A_{0z}/\partial z = 0$ but $\partial^2 A_{0z}/\partial z^2 \neq 0$, and (3.6) becomes a singularity. Fig. 3-1 shows the values of (3.6) in r-z space for different divergence angles.

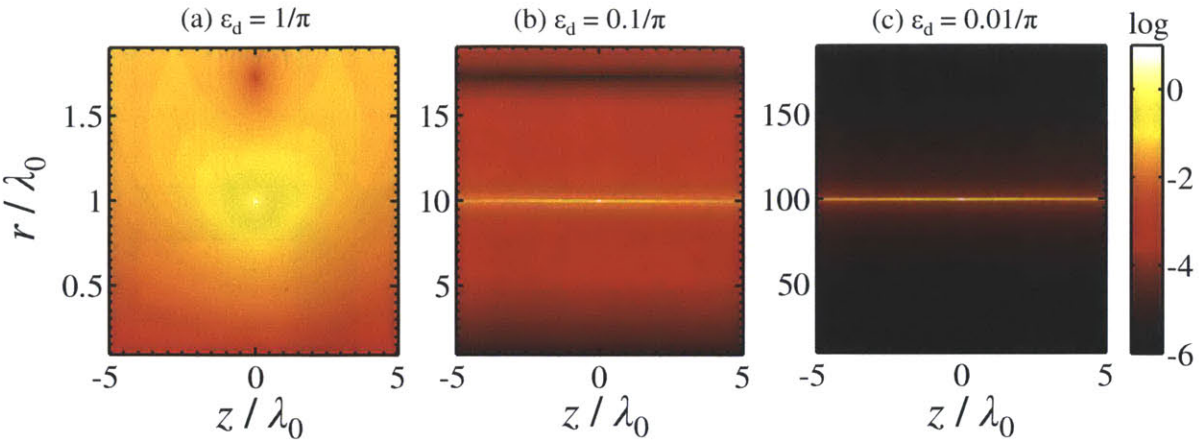

Fig. 3-1: Color maps of the logarithm (base 10) of the ratio (3.6) for various divergence angles. In each case we have plotted z from -5λ to 5λ and r from $0.1w_0$ to $1.9w_0$. For better contrast, we have artificially limited the color axis from -6 to 1 (i.e. we have color variations only for values of (3.6) between 10^{-6} and 10). Notice that the singularity at $z = 0$, $r = w_0$ does not disappear regardless of focusing. These plots show that the Gaussian beam grossly violates the paraxial wave approximation (3.3) at certain points in space, even for a nominally paraxial beam.

As shown in Fig. 3-1, the Gaussian beam violates the paraxial wave approximation (3.3) at certain off-axis points in space no matter how small we make the divergence angle. Note, however, that (3.6) is 0 on the beam axis everywhere. This suggests that the Gaussian beam formulation, in spite of its deficiencies, may provide an accurate prediction of the on-axis fields. We now proceed to verify this by comparing the paraxial and exact formulas for the on-axis electric field of the fundamental radially-polarized beam. The paraxial formulas are derived in detail in Appendices C and D. The exact formulas are derived in detail in Appendix E.

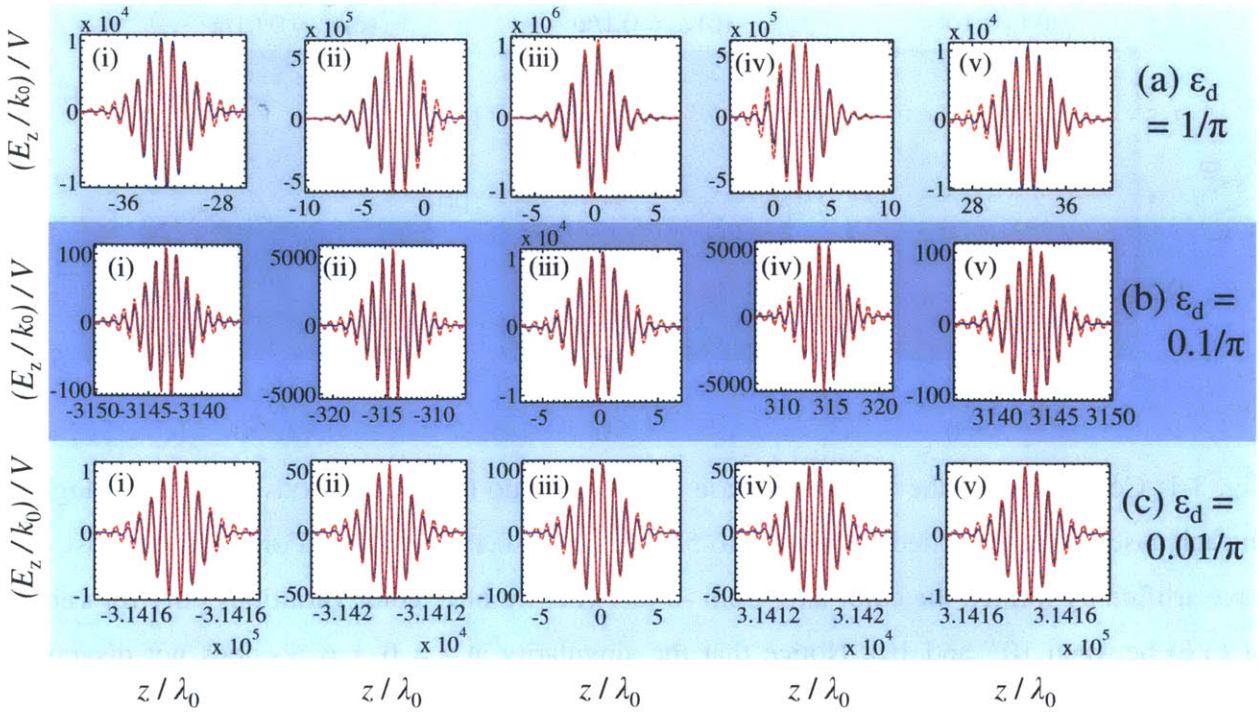

Fig. 3-2: Plots of z-directed on-axis ($r = 0$) electric field E_z of the fundamental radially polarized pulsed beam corresponding to the paraxial solution (red dotted line) and exact solution (blue solid line), for various values of divergence angle. For each divergence angle the pulse is shown at five different times: (i) $t = -10a/c$, (ii) $t = -a/c$, (iii) $t = 0$, (iv) $t = a/c$ and (v) $t = 10a/c$, with initial pulse position $z_i = 0$ and peak power $P = 10^{12}$ W. Note that all other electromagnetic field components are zero on axis.

From Fig. 3-2, we see that on the beam axis, E_z of the exact case is very well approximated by the solution obtained from the paraxial beam. In Fig. 3-2(b) and (c), where the beam is relatively paraxial, differences in the wings of the pulse are likely due to choice of pulse spectrum (recall that we use a Poisson spectrum in the exact beam case but a sech pulse in the paraxial beam case) rather than any fundamental discrepancy. Fig. 3-2(a) shows that the paraxial solution remains surprisingly accurate on axis even when the beam is focused as tightly as $w_0 = \lambda_0$. Most telling of all, the close match between the power scaling results computed using fields derived from the paraxial beam [WK10] and the results computed using fields derived from the exact beam [FPV10] assure us that our model is accurate enough for this problem.

3.2 Theory of direct acceleration by a pulsed radially-polarized laser beam

The physical scenario we study is the following: A free electron, initially at rest or moving in field-free vacuum, is overtaken by the pulse of a radially-polarized laser beam that exchanges energy with the electron purely via the laser's on-axis, longitudinal electric field (i.e. via direct acceleration). The pulse eventually overtakes the electron, leaving the electron once again in field-free vacuum, with a velocity generally different from what it had before. The free electron may have been introduced either by ionization of a target in the path of the pulse, as in [KP07], or by a preceding acceleration stage. To compute the net energy gain of the electron, we need a description of the laser pulse and equations to model the electron's motion.

As discussed in detail in Appendices C and D, we may derive the electric field $\vec{E}$ and magnetic flux density $\vec{B}$ for a pulsed radially-polarized laser beam in vacuum under the paraxial wave approximation:

$$\vec{E}(r,z,t) = \mathrm{Re}\left\{\tilde{E}(r,z)e^{j(\xi+\psi_0)}\mathrm{sech}\left(\frac{\xi+kz_i}{\xi_0}\right)\right\}, \quad \vec{B}(r,z,t) = \hat{\phi}\frac{1}{c}\vec{E}(r,z,t)\cdot\hat{r}, \tag{3.7}$$

where

$$\tilde{E}(r,z) \equiv f^2\rho e^{-f\rho^2}\sqrt{\frac{8\eta_0 P}{\pi w_0{}^2}}\left[\hat{r} - \hat{z}\frac{2j}{kr}\left(1-f\rho^2\right)\right], \quad \tilde{B}(r,z) \equiv \hat{\phi}\frac{1}{c}\tilde{E}(r,z)\cdot\hat{r}, \tag{3.8}$$

r,ϕ,z are the cylindrical coordinates and $\hat{r},\hat{\phi},\hat{z}$ the corresponding unit vectors; $j \equiv \sqrt{-1}$; $f \equiv j/(j+(z/z_0))$; $\rho \equiv r/w_0$; $\xi \equiv \omega t - kz$; $z_0 \equiv \pi w_0{}^2/\lambda$ is the Rayleigh range; w_0 is the beam waist radius; λ is the carrier wavelength (i.e. the central wavelength of the pulse); $k \equiv 2\pi/\lambda$; $\omega = kc$ is the angular carrier frequency; $\eta_0 \cong 120\pi\,\Omega$ is the vacuum wave impedance; c is the speed of light in vacuum; z_i is the pulse's initial position; ψ_0 is the carrier phase constant; ξ_0 is a parameter related to the pulse duration; P is the peak power of the pulse:

$$P = \frac{1}{2\mu_0}\int_0^\infty dr 2\pi r \,\mathrm{Re}\left\{\tilde{E}(r,0)\times\tilde{B}^*(r,0)\cdot\hat{z}\right\} \tag{3.9}$$

where μ_0 is the permeability of free space. Note that peak power is defined here as the average CW power at the peak of the pulse, which differs from the definition used in Appendix C by a factor of 2 (this difference is just a matter of convenience). By choosing values of ξ_0 such that the time variation of the sech pulse envelope is large compared to the time variation of the carrier and using Eq. (3), we may compute the pulse energy E_{pulse} as

$$E_{pulse} = \frac{1}{\mu_0}\int_{-\infty}^{\infty} dt\int_0^\infty dr 2\pi r\tilde{E}(r,0,t)\times\tilde{B}(r,0,t)\cdot\hat{z} \approx P\int_{-\infty}^{\infty} dt \mathrm{sech}^2\left(\frac{\omega t + kz_i}{\xi_0}\right) = P\frac{2\xi_0}{\omega} \tag{3.10}$$

We have chosen to model our pulse with a sech envelope because this allows Eq. (3.7) to satisfy the Maxwell equations in the paraxial wave approximation for $\xi_0 >> 1$. As shown in [Mac00], which discussion we rehash in Appendix D, the same cannot be said for other choices of pulse shapes. In particular, using a Gaussian pulse $\exp\left(-(\xi + kz_i)^2/\xi_0^{\,2}\right)$, instead of $\mathrm{sech}((\xi + kz_i)/\xi_0)$, would cause Eq. (1) to violate the Maxwell equations at large values of $(\xi + kz_i)$ (i.e. at the tails of the pulse). However, as will be seen in the next section, we are able to reproduce the results of [FPV10] – which used a Gaussian pulse – with our model, showing that the former approach does not suffer much in accuracy in the parameter space of [FPV10]. This is because the electrodynamics for most cases in [FPV10] is primarily influenced by fields close to the pulse peak, where both Gaussian and sech representations are accurate.

Following the convention of [FPV10], we define the pulse duration τ to be the single-sided $\exp(-1)$ duration of the pulse:

$$\tau = \frac{\xi_0}{\omega}\mathrm{sech}^{-1}(\exp(-1)). \tag{3.11}$$

Eq. (3.7) thus uniquely defines a pulsed radially-polarized laser beam after we specify six parameters: carrier wavelength λ, carrier phase constant ψ_0, beam waist radius w_0, initial pulse

position z_i, peak power P and pulse duration τ. The pulse energy E_{pulse} and parameter ξ_0 are then fixed by equations (3.10) and (3.11) respectively.

The electrodynamics of an electron in an electromagnetic field, ignoring radiative reaction, is described by the Newton-Lorentz equation of motion

$$\frac{d\vec{p}}{dt} = \frac{d(\gamma m\vec{v})}{dt} = -e\left(\vec{E} + \vec{v} \times \vec{B}\right), \tag{3.12}$$

where r, ϕ, z in the variables of Eq. (3.12) now denote the coordinates of the electron's position, m is the rest mass of the electron, e the absolute value of its charge, $\vec{p}$ its momentum, $\vec{v}$ its velocity and $\gamma \equiv 1/\sqrt{1-\beta^2}$ is the Lorentz factor, with $\beta \equiv |\vec{\beta}|$ and $\vec{\beta} \equiv \vec{v}/c$. The total energy and kinetic energy of the electron are given by $E_t = \gamma mc^2$ and $E_K = (\gamma - 1)mc^2$ respectively.

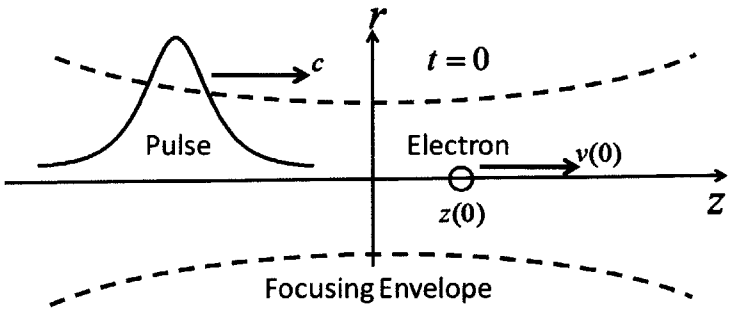

Fig. 3-3. Schematic of simulations at initial time. The electron begins in field-free vacuum.

We consider an electron initially ($t = 0$) on the beam axis ($r = 0$) of the laser at $z = z(0)$ (Fig. 3-3), moving in the longitudinal direction with velocity $\vec{v}(0) = v(0)\hat{z}$. The electron may be initially at rest ($v(0) = 0$) or moving ($v(0) > 0$; we do not consider $v(0) < 0$). In all cases, we are interested in the net energy the electron extracts from the laser field as the pulse propagates from a position (effectively) infinitely far behind the electron to a position (effectively) infinitely far in front of the electron. We do not limit the interaction distance by use of any additional optics. We also confine our attention to forward scattering cases (i.e. the electron's final velocity is in the direction of pulse propagation + z).

Setting $r = 0$ in Eq. (1), we have $\vec{E} = E_z\hat{z}$ and $\vec{B} = 0$, where

$$E_z = \left[\frac{1/z_0}{1+(z/z_0)^2}\sqrt{\frac{8\eta_0 P}{\pi}}\right]\sin\left(\omega t - kz + 2\tan^{-1}\left(\frac{z}{z_0}\right) + \psi_0\right)\operatorname{sech}\left(\frac{\omega t - k(z-z_i)}{\xi_0}\right) \quad (3.13)$$

Eq. (3.13) may be seen as the product of three parts: the *field amplitude*, given by the square bracketed factor, which is a Lorentzian in z; the *continuous wave (CW) carrier*, given by the $\sin(\cdot)$ factor; and the *pulse envelope*, given by the $\operatorname{sech}(\cdot)$ factor. The sign of E_z is determined exclusively by that of the CW carrier. If the CW carrier is positive, meaning its argument is between 0 and π radians, an electron traveling in the $+z$ direction is in a *decelerating cycle* and loses energy to the field. If the CW carrier is negative, meaning its argument is between π and 2π radians, an electron traveling in the $+z$ direction is in an *accelerating cycle* and gains energy from the field. An on-axis electron with no initial transverse velocity component is confined to move along the beam axis (so $\vec{v}(t) = v(t)\hat{z}\ \forall t$, $r(t) = 0\ \forall t$). Simplifying (3.12), we obtain the equations

$$\frac{d\beta}{dt} = -\frac{eE_z}{\gamma^3 mc}, \quad \frac{dz}{dt} = v = c\beta. \quad (3.14)$$

Eq. (3.14) may be solved numerically for the electron's speed, and hence its energy, at any time. To do so, however, we must first specify the laser field (by specifying λ, ψ_0, w_0, z_i, P and τ) as well as the electron's initial position $z(0)$ and speed $v(0)$. As mentioned, we always set z_i such that the pulse effectively begins infinitely far behind the electron. In addition, we fix $\lambda = 0.8\mu m$ throughout the text, leaving us with a total of six dimensions over which to study or optimize the problem. Although we fix λ, our results may be readily scaled to obtain the results for any λ by nature of Eqs. (3.13) and (3.14). If we let $\mathrm{T} \equiv \omega t$, $\varsigma \equiv z/z_0$ (with $\varsigma_i \equiv z_i/z_0$) and $\kappa \equiv kz_0 = 2(\pi w_0/\lambda)^2$, and apply Eq. (3.13), Eq. (3.14) may be cast in the form

$$\frac{d\beta}{d\mathrm{T}} = -\frac{e}{\gamma^3 mc^2}\left[\frac{1/\kappa}{1+\varsigma^2}\sqrt{\frac{8\eta_0 P}{\pi}}\right]\sin\left(\mathrm{T}-\kappa\varsigma+2\tan^{-1}(\varsigma)+\psi_0\right)\mathrm{sech}\left(\frac{\mathrm{T}-\kappa(\varsigma-\varsigma_i)}{\xi_0}\right)$$
$$\frac{d\varsigma}{d\mathrm{T}} = \frac{\beta}{\kappa} \qquad (3.15)$$

For given values of κ and ξ_0, Eq. (3.15) is completely independent of central wavelength λ. The results for any λ may thus be obtained from the results for $\lambda = 0.8\mu m$ by an appropriate scaling of beam waist w_0 and pulse duration τ. Note that κ determines the ratio w_0/λ and ξ_0 determines the number of cycles in the pulse envelope, regardless of λ. The scaling in t and z does not affect the maximum energy gain, only the optimal z_i.

By substituting Eqs. (3.7) and (3.8) into Eq. (3.12) and applying $\rho \equiv r/w_0$ along with the previous normalizations, it is straightforward to generalize our conclusion and see that for given values of κ and ξ_0, the electrodynamic equations are independent of λ even for the most general case where the electron is not necessarily on the beam axis. The acceleration of an (on-axis or otherwise) electron in infinite vacuum by a pulsed radially-polarized laser beam thus depends on λ only through κ and ξ_0. An important consequence of this is that for a given peak power P, a larger pulse energy is required for exactly the same maximum acceleration at a larger λ if focusing (w_0/λ) remains constant, because the number of carrier cycles in the pulse envelope must also remain constant, leading to a longer pulse.

The Gouy phase shift term $2\tan^{-1}(z/z_0)$ in the argument of the CW carrier in Eq. (3.13) prevents any particle from remaining in a single cycle indefinitely. As a result, the energy that an electron can gain from a pulsed radially-polarized laser beam has a theoretical limit ΔE_{lim} that may be computed by considering an electron that (unrealistically) remains at the pulse peak and in one accelerating cycle from the focus to infinity (or from $-z_0$ to z_0, which gives the same result, just with a different ψ_0), as was done in [FPV10]:

$$\Delta E_{\mathrm{lim}} = \int_0^\infty dz\left[\frac{e/z_0}{1+(z/z_0)^2}\sqrt{\frac{8\eta_0 P}{\pi}}\right]\sin\left(2\tan^{-1}(z/z_0)\right) = e\sqrt{\frac{8\eta_0 P}{\pi}} \cong \sqrt{\frac{P}{[PW]}}[GeV] \qquad (3.16)$$

where $P/[PW]$ refers to the laser peak power in petawatts. We will find it convenient to normalize our energy gain results by $\Delta E_{\lim}$ afterwards.

We solve Eq. (3.14) numerically via the Adams-Bashforth-Moulton method (*ode113* of *Matlab*). In every case, we ensure that the pulse begins so far behind the electron that the latter is initially not affected by the laser field. By this we mean that any fluctuation in the electron's energy is at first (for at least a few tens of picoseconds) below an arbitrarily small value. We also terminate our simulations only after the electron's energy has reached a steady state (equivalently, after electron position z has become so large that the Lorentzian field amplitude of Eq. (3.13) is negligibly small).

As discussed, Eq. (3.7) satisfies the Maxwell equations only for sufficiently large beam waists and pulse widths. To ensure the validity of our simulations, the smallest waist and pulse duration we consider are respectively $w_0 = 2\mu m$ and $\tau = 7.5 fs$, after the fashion of Fortin et. al. [FPV10] and based on findings by Varin et. al. [VPP05] that corrections to the paraxial radially-polarized laser beam are small or negligible for beam waists no smaller than $w_0 = 2\mu m$. For $\tau \geq 7.5 fs$, $\xi_0 > 10$, which at least approximately satisfies the requirement that $\xi_0 >> 1$.

3.3 Direct acceleration of an initially stationary electron: Benchmarking and simulation results

In [FPV10], Fortin et. al. studied the case of a pulsed radially-polarized laser beam incident on an electron that was initially stationary at the laser focus. The authors concluded that, for the range of laser peak powers and pulse durations studied, the optimal laser focusing is in general not the tightest. This conclusion, however, is true only for electrons required to start at the laser focus (i.e. $z(0) = 0$). Given P, τ and w_0 in general, $z(0) = 0$ (or even slightly less than 0, as the authors suggest) is not the optimal initial position. We find after optimizing over ψ_0 - w_0 - $z(0)$ space that the optimal focusing is in fact the tightest.

In Fig. 3-4, we plot the maximum energy gain and optimal beam waist computed by optimizing over ψ_0 - w_0 space for $z(0) = 0$ (as in [FPV10]). In Fig. 3-4(a), we also plot the maximum energy gain computed by optimizing over ψ_0 - w_0 - $z(0)$ space for $w_0 \geq 2$ μm (giving optimal $w_0 = 2$ μm). Our results for $z(0) = 0$ are clearly in good agreement with those in [FPV10] (slight differences may be

attributed to our use of a different pulse shape). We see that a substantial increase in maximum energy gain occurs after including the $z(0)$ dimension in the optimization space. In fact, 15 fs and 20 fs pulses can approximately give us the energy gain that for $z(0) = 0$ is achievable only with 7.5 fs and 10 fs pulses respectively.

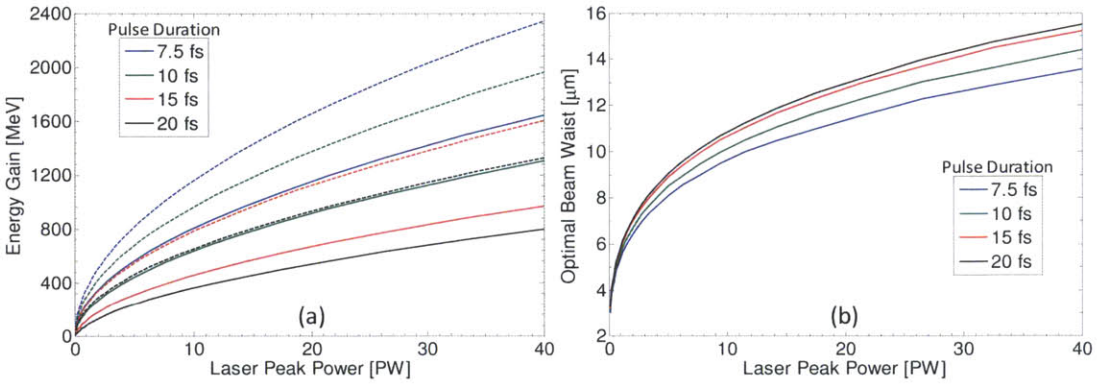

Fig. 3-4 (a) Maximum energy gain and (b) corresponding optimal beam waist vs. power P from 0.1 to 40 PW for various τ. All solid lines correspond to $z(0) = 0$. Dashed lines correspond to optimal $z(0)$ for $w_0 = 2$ μm (optimal waist). All cases shown correspond to forward scattering of the electron.

To illustrate how $z(0) = 0$ is not optimal in general, the energy gain (maximized over ψ_0 space) as a function of $z(0)$ normalized by z_0 for a 1 PW, 10 fs pulse is plotted for various waists in Fig. 3-5. As can be seen, the optimal $z(0)$ approaches the focus as w_0 increases for given P and τ, but in general may be quite a distance behind the focus.

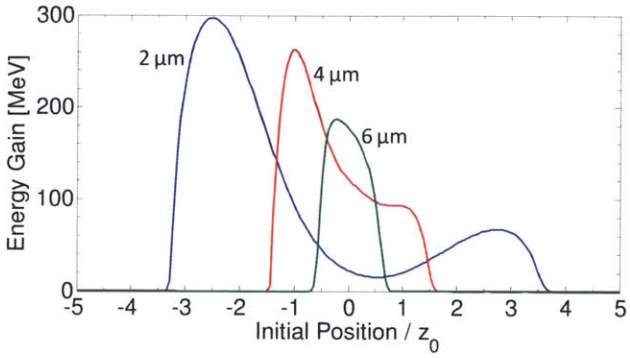

Fig. 3-5 Maximum energy gain vs. normalized $z(0)$ for $P = 1$ PW, $\tau = 10$ fs and various w_0. All cases shown correspond to forward scattering of the electron.

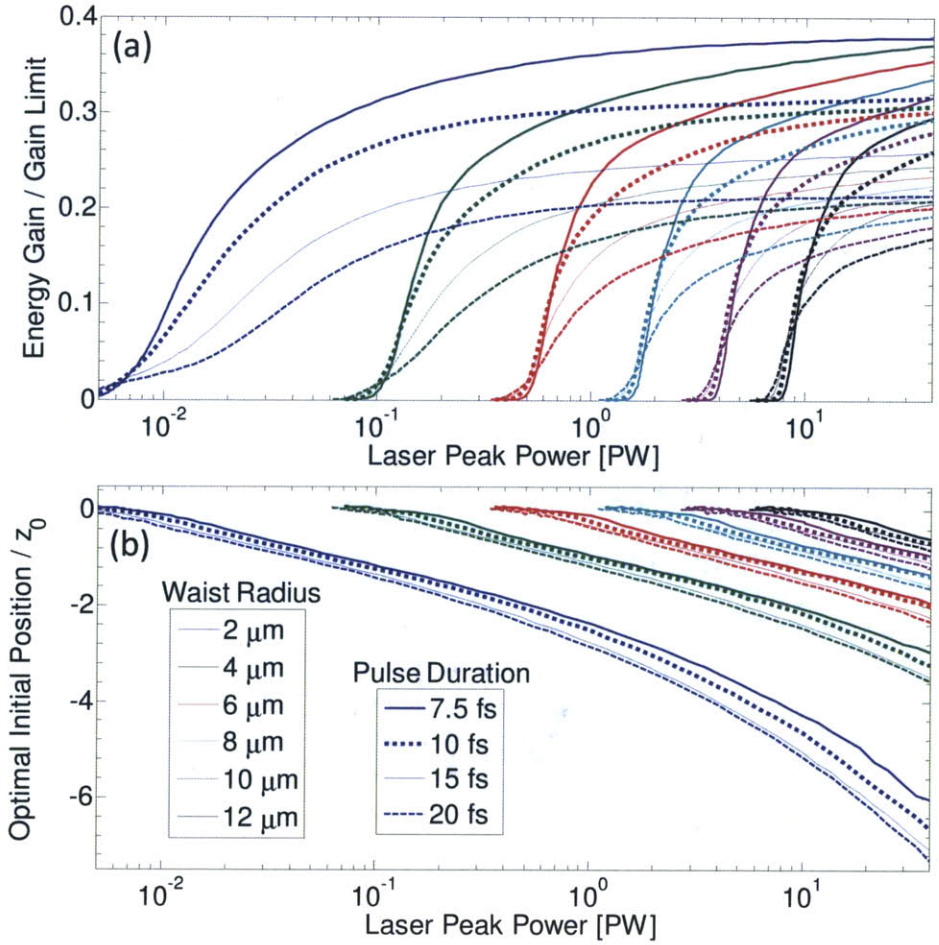

Fig. 3-6 (a) Normalized maximum energy gain and (b) corresponding normalized optimal initial position vs. P from 5 TW to 40 PW for various w_0 and τ. All cases shown correspond to forward

scattering of the electron. Cases of very non-relativistic final kinetic energy are not plotted to reduce clutter.

We would like to evaluate the power scaling characteristics for various τ and w_0, extending our region of study to include laser peak powers as low as 5 TW. The results of optimization over ψ_0-$z(0)$ space are shown in Fig. 3-6. To improve readability, we have normalized the electron's maximum energy gain at each P by the gain limit $\Delta E_{\lim}$ (Eq. (10)), and the electron's optimal initial position by the Rayleigh range z_0. Note that the $w_0 = 2$ μm plots in Fig. 3-6(a) are just normalized versions of the dashed lines in Fig. 3-4(a). From Fig. 3-6, we observe the following trends:

a) Given τ and w_0, a threshold power P_{th} exists such that negligible energy gain is obtained for $P < P_{th}$. P_{th} is approximately independent of τ and is approximated by the condition used in [FPV10] to find the threshold w_0 for given P with $z(0) = 0$:

$$a_0 \equiv \frac{e}{mc\omega z_0}\sqrt{\frac{8\eta_0 P_{th}}{\pi}} \approx 1 \tag{3.17}$$

where a_0 is simply the normalized field amplitude of E_z at the focus. As discussed in [FPV10], Eq. (3.17) is motivated by the observation made in ponderomotive acceleration studies (e.g. [FPV10]) that $a_0 \geq 1$ is required to access the relativistic regime of laser-electron interaction (except that for ponderomotive acceleration, a_0 is computed with the transverse rather than longitudinal field amplitude). For $w_0 = 2, 4, 6, 8, 10, 12$ μm, Eq. (3.17) gives $P_{th} \approx 4.163\times 10^{-3}$, 6.661×10^{-2}, 3.372×10^{-1}, 1.066, 2.602, 5.396 PW (4 sig. fig.) respectively, which by Fig. 3-6(a) are estimates accurate to well within an order of magnitude.

b) Given τ and w_0, energy gain (whether in MeV or normalized by $\Delta E_{\lim}$) increases with increasing P. That the normalized gain asymptotically approaches a constant value tells us that at $P >> P_{th}$, the energy gain in MeV is approximately proportional to $\sqrt{P}$, a behavior that has been noted for the $z(0) = 0$ case studied in [FPV10].

c) Given w_0 and P, energy gain increases with increasing τ up to an optimal τ and decreases as τ increases further. As the given P decreases toward P_{th}, this optimal τ increases, showing that

longer pulses are favored at lower powers. A close-up of Fig. 3-6(a) with energy gain in MeV is shown in Fig. 3-7 to illustrate this. The conclusion of [FPV10] that a shorter pulse leads to greater net acceleration is thus not generally true.

d) Given τ and P, energy gain decreases with increasing w_0. As far as we can determine in the paraxial wave approximation, the optimal focusing for direct electron acceleration is the tightest.

e) Given τ and w_0, the optimal initial position becomes more negative with increasing P for the vast majority of cases, especially where $P >> P_{th}$, in Fig. 3-6(b). At $P \approx P_{th}$, the optimal initial position is close to the focus and may even be slightly positive. For $P >> P_{th}$, the optimal initial position is negative and approximately proportional to $\sqrt[4]{P}$, as we have ascertained by curve-fitting.

f) Given w_0 and P, the optimal initial position becomes more negative with increasing τ for the vast majority of cases, especially where $P >> P_{th}$, in Fig. 3-6(b).

g) Given τ and P, the optimal initial position normalized by z_0 becomes more negative with decreasing w_0.

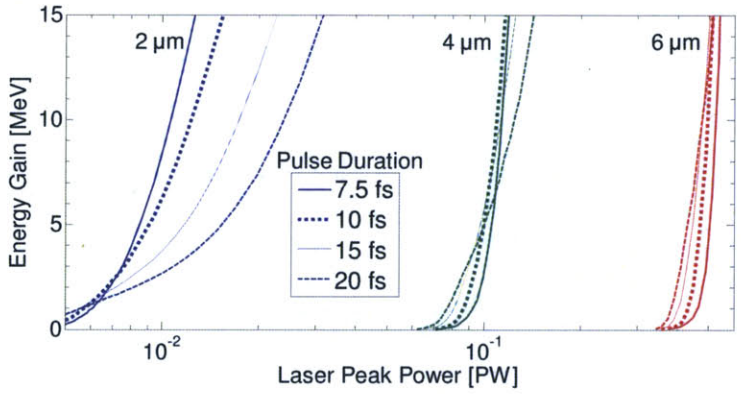

Fig. 3-7 Close-up of plot of maximum energy gain vs. P for various w_0 and τ.

One may intuitively expect $z(0) = 0$ to be the optimal initial position in general since, after all, the theoretical gain limit ΔE_{lim} was computed in Eq. (3.16) by assuming an electron that enters an accelerating cycle at the laser focus and staying in that cycle forever. However, an electron that starts at rest is bound to slip through a succession of accelerating and decelerating cycles before entering what is

effectively its final accelerating cycle (that is, the final accelerating cycle that has any significant impact on its energy) with a velocity that is in general quite different from its initial velocity, so the relationship between $z(0)$ and the electron's final energy gain is complicated. We also note that although including the $z(0)$ dimension in the optimization space significantly increases the electron's energy gain over the $z(0) = 0$ case, the electron still extracts at best less than $\Delta E_{\text{lim}}/2$ of energy from the pulse. In [FPV10], it is argued that sub-cycle direct acceleration can only take place from $z > z_0$ to ∞, so the energy gain will always be less than $\Delta E_{\text{lim}}/2$ for initially stationary electrons. We show in the next section that by using a pre-accelerated electron, we can make the electron enter its final accelerating cycle at a position $z < z_0$ and extract more than $\Delta E_{\text{lim}}/2$ of energy from the pulse.

3.4 Direct acceleration of a pre-accelerated electron

For convenience we introduce an artificial parameter D that we call the "protracted collision position" and define as the position where the electron would coincide with the pulse peak if the electron were to always travel at its initial speed $v(0)$:

$$\frac{v(0)}{D - z(0)} \equiv \frac{c}{D - z_i} \Rightarrow D \equiv \frac{z(0) - \beta(0) z_i}{1 - \beta(0)} \tag{3.18}$$

For the initially stationary electron studied in the previous section, $\beta(0) = 0$ so $D = z(0)$ as expected. For values of D far enough from the laser focus such that the electron always experiences a negligibly small electric field (resulting in little change in the electron's velocity from its initial value), D approximates the actual position where electron and pulse peak coincide, hence our name for it. In general, however, the position where electron and pulse peak coincide may be very different from D. Although D may not have much physical significance, it is useful as it allows us to control two variables, $z(0)$ and z_i, simultaneously: After specifying D for a particular simulation, we use Eq. (3.18) and our knowledge of the electric field profile to determine the set of values $z(0)$ and z_i closest to the focus but such that the effect of the electric field on the electron is initially below an arbitrarily small amount (i.e. the pulse effectively begins infinitely behind the electron, so the electron effectively begins in field-free

vacuum). Simply setting z_i to be an arbitrarily large negative number will of course also produce an accurate simulation, but the simulation time will be unnecessarily long.

In Figs. 3-8 and 3-9, we plot the maximum energy gain (normalized by $\Delta E_{\lim}$) and the corresponding optimal D (normalized by z_0) vs. P with w_0 and the electron's initial kinetic energy $E_K(0)$ as parameters. Fig. 3-8 and Fig. 3-9 correspond to the case of $\tau = 7.5$ fs and $\tau = 15$ fs respectively. In Fig. 3-10, we plot the normalized maximum energy gain vs. $E_K(0)$ with P and w_0 as parameters for $\tau = 10$ fs. The plots in Figs. 3-8 and 3-9 are obtained by optimizing over ψ_0-D space. From these figures, we observe the following trends:

a) Given τ and w_0, P_{th} decreases with increasing $E_K(0)$. Given τ and $E_K(0)$, P_{th} increases with increasing w_0. P_{th} is approximately independent of τ, as in the $v(0) = 0$ case.

b) Given τ, w_0 and P, there exists an initial kinetic energy threshold E_{Kth} such that negligible energy gain is obtained for $E_K(0) < E_{Kth}$. Given τ and w_0, E_{Kth} decreases with increasing P. Given τ and P, E_{Kth} increases with increasing w_0. E_{Kth} is approximately independent of τ. Although some of these trends are evident from Fig. 3-10, they may all be directly inferred from (a), which tells us that P_{th} is a strictly decreasing function of $E_K(0)$ (given τ and w_0 within the parameter space studied). Note also that if P_{th} is a strictly decreasing function of $E_K(0)$, $P = P_{th}$ if and only if $E_K(0) = E_{Kth}$.

c) Given τ, w_0 and P, energy gain increases with increasing $E_K(0)$ at least up to a certain $E_K(0)$. As can be seen from the $w_0 = 2$ μm plot in Fig. 3-10(a), the energy gain starts to fall after a certain $E_K(0)$.

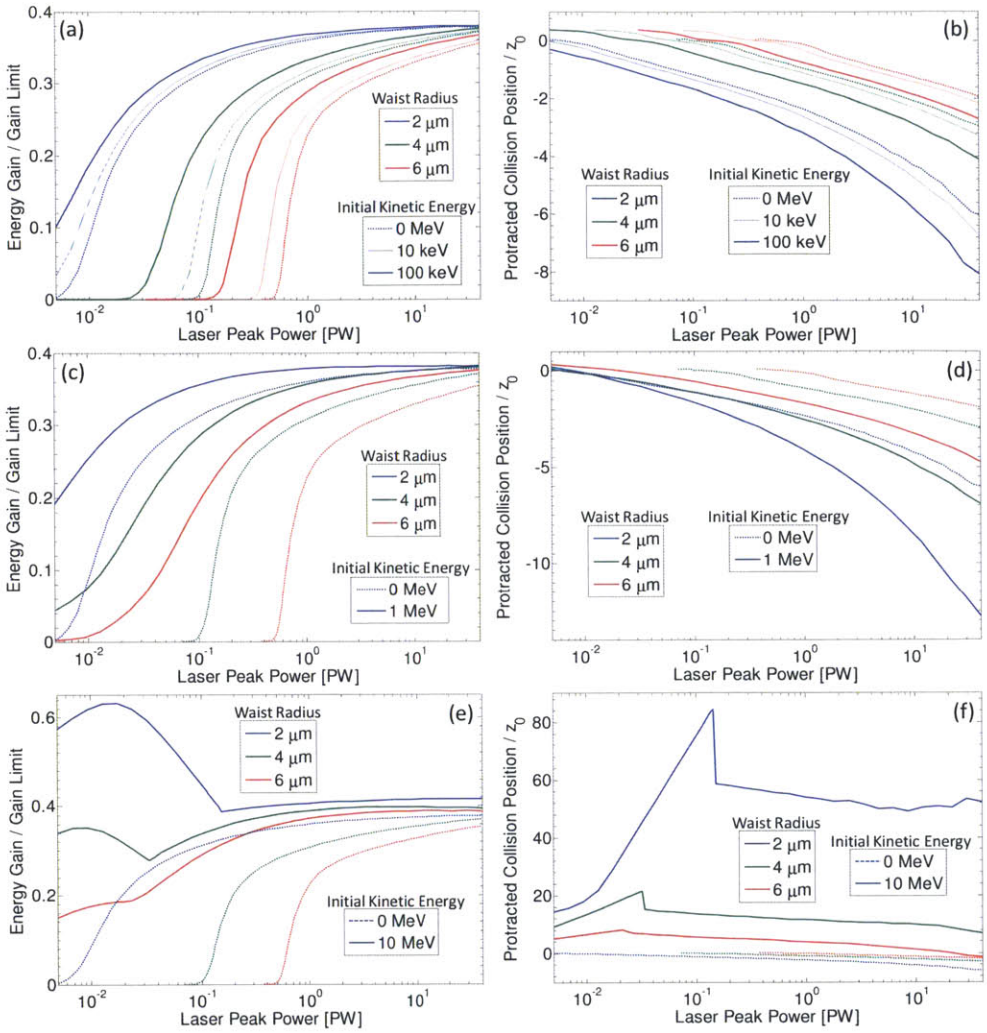

Fig. 3-8 Normalized maximum energy gain and corresponding normalized optimal D vs. P from 5 TW to 40 PW for various w_0 and $E_K(0)$: (a), (b) non-relativistic $E_K(0)$; (c), (d) marginally-relativistic $E_K(0)$; and (e), (f) relativistic $E_K(0)$. $\tau = 7.5$ fs. All cases shown correspond to forward scattering of the electron. Cases of very non-relativistic final kinetic energy are not plotted to reduce clutter.

d) Given $E_K(0)$, w_0 and P, energy gain increases with increasing τ up to an optimal τ and decreases as τ increases further. As the given P ($E_K(0)$) decreases toward P_{th} (E_{Kth}), this optimal τ increases, showing that longer pulses are favored at lower powers.

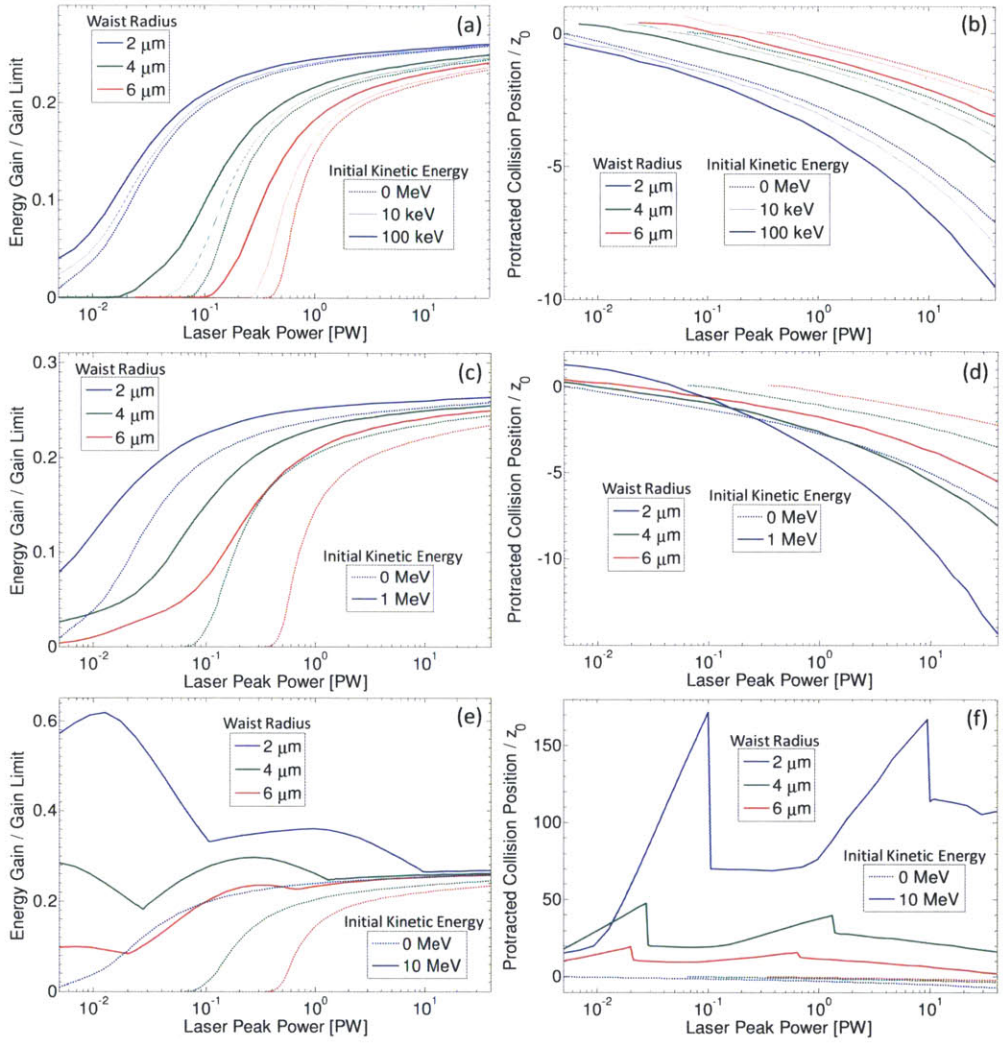

Fig. 3-9 Normalized maximum energy gain and corresponding normalized optimal D vs. P from 5 TW to 40 PW for various w_0 and $E_K(0)$: (a), (b) non-relativistic $E_K(0)$; (c), (d) marginally-relativistic $E_K(0)$; and (e), (f) very relativistic $E_K(0)$. $\tau = 15$ fs. All cases shown correspond to forward scattering of the electron. Cases of very non-relativistic final kinetic energy are not plotted to reduce clutter.

e) Given $E_K(0)$, τ and P, energy gain decreases with increasing w_0. Once again, the optimal focusing for direct electron acceleration is the tightest as far as we can determine in the paraxial wave approximation.

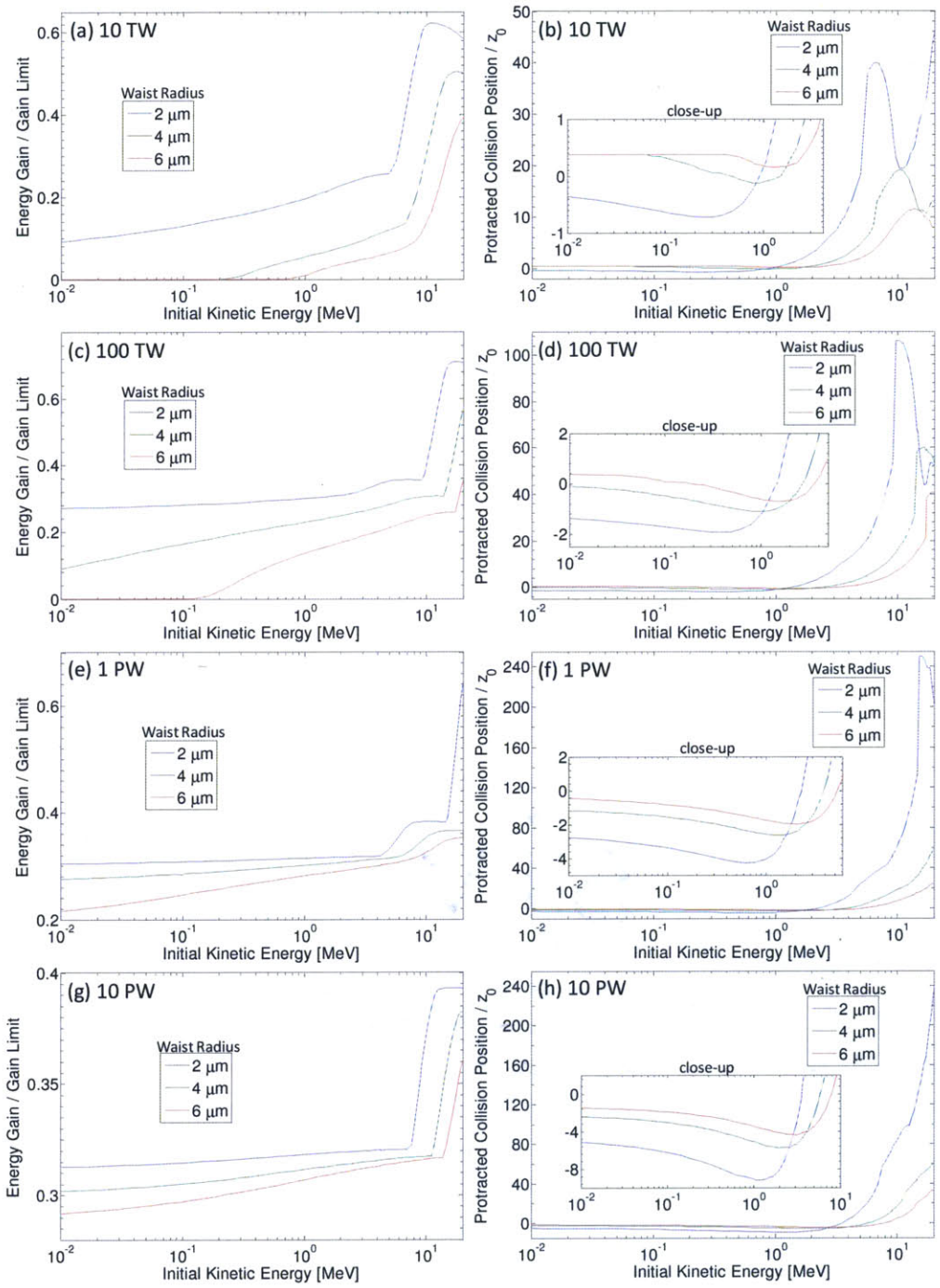

Fig. 3-10 Normalized maximum energy gain and corresponding normalized optimal D vs. $E_K(0)$ from 0.01 to 20 MeV for various w_0 and P: (a), (b) P =10 TW; (c), (d) $P = 100$ TW; (e), (f) $P = 1$ PW; and (g), (h) $P = 10$ PW. $\tau = 10$ fs. All cases shown correspond to forward scattering of the electron.

f) Given $E_K(0)$, τ and w_0, the energy gain in MeV increases with increasing P. The energy gain normalized by ΔE_{lim} also increases with increasing P at non-relativistic $E_K(0)$, but this is not true in general at relativistic $E_K(0)$, as is evident from Figs. 3-8(e) and 3-9(e). Fig. 3-10 corroborates our conclusion by showing that the normalized energy gain increases with increasing P for values of $E_K(0)$ up to a few MeV, but ceases to always do so beyond this range. Hence, although greater energy gain in MeV can always be achieved (for given $E_K(0)$, τ and w_0) by increasing P and optimizing parameters, the fraction of the theoretical energy gain limit extracted may in fact become smaller if $E_K(0)$ is relativistic.

g) At non-relativistic $E_K(0)$, D decreases from its value for the $v(0)=0$ case with increasing $E_K(0)$. That this decrease is small accords with physical intuition because relative to the speed of the pulse (c), an electron with non-relativistic $E_K(0)$ is practically stationary so one would expect the optimal D to be very close to that for the $v(0)=0$ case. This reasoning, of course, no longer applies at relativistic $E_K(0)$. It is evident from the plots of D in Fig. 3-10 that beyond a certain $E_K(0)$ (around 1 MeV) for each plot, the slope of D with respect to $E_K(0)$ is no longer always negative, and D itself may be located up to hundreds of times the Rayleigh range beyond the laser focus.

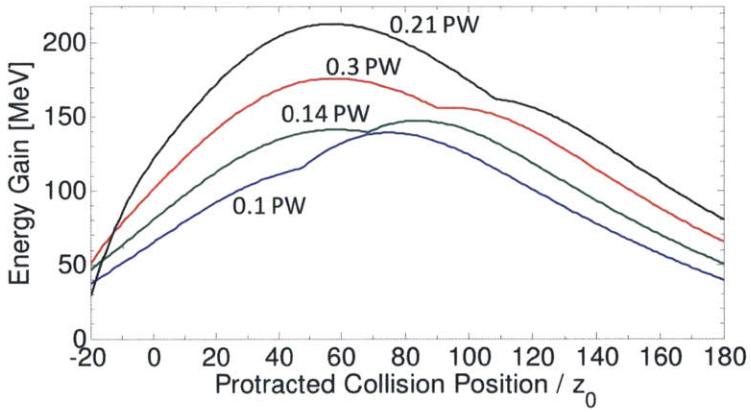

Fig. 3-11 Maximum energy gain vs. normalized D for $\tau = 7.5$ fs, $w_0 = 2$ μm and $E_K(0) = 10$ MeV for various P. All cases shown correspond to forward scattering of the electron.

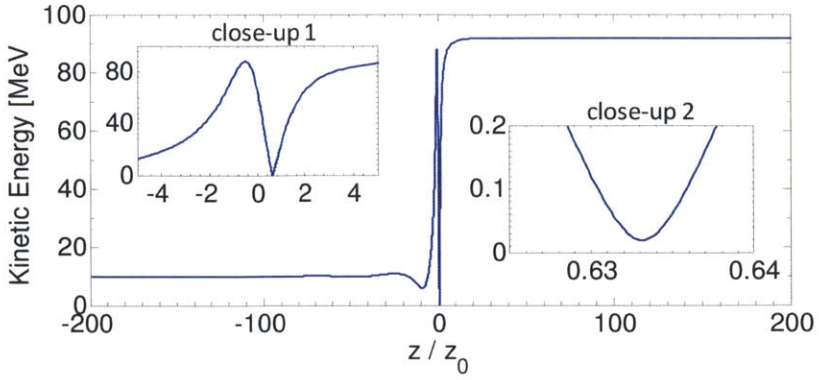

Fig. 3-12 Electron kinetic energy vs. normalized position for $P = 17.3$ TW, $w_0 = 2$ μm, $\tau = 7.5$ fs, $E_K(0) = 10$ MeV, and optimal ψ_0 and D. Inset "close-up 2" zooms into the point at which the electron enters its effectively final accelerating cycle.

The discontinuities in Figs. 3-8(f) and 3-9(f) are due to the existence of multiple energy gain local maxima in D for certain combinations of $E_K(0)$, τ, P and w_0. The cause of the discontinuity around $P = 0.15$ PW for the $w_0 = 2$ μm case of Fig. 3-8(f) is illustrated in Fig. 3-11, which plots energy gain, maximized over ψ_0 space, as a function of D. Although each local maxima varies continuously as P increases from 0.14 PW to 0.3 PW, the global maximum jumps at some point from one of the local maxima to the other, resulting in the discontinuity in Fig. 3-8(f). Similar situations are responsible for the discontinuities in Fig. 3-9(f).

As we have noted, a pre-accelerated electron can gain more than half the theoretical energy gain limit. It does so by entering its effectively final accelerating cycle within a Rayleigh range after passing the laser focus. Fig. 3-12 shows a plot of kinetic energy vs. displacement for one of the cases picked from the $w_0 = 2$ μm, $E_K(0) = 10$ MeV curve in Fig. 3-8. As we can see, the electron coming in from the left enters its effectively final accelerating cycle with a kinetic energy of a few tens of keV at a displacement of about $z = 0.633\, z_0 < z_0$, and leaves the interaction region with a final kinetic energy of over 90 MeV. The energy gain of over 80 MeV is clearly more than half the theoretical gain limit, which in this case ($P = 17.3$ TW) is about 129 MeV by Eq. (3.16).

To give an example of how relatively low-power lasers may be used in a direct acceleration scheme, we see that for either $\tau = 7.5$ fs (Fig. 3-8(e)) or $\tau = 15$ fs (Fig. 3-9(e)), a pulsed radially-polarized laser beam of $w_0 = 2$ μm and $P = 5$ TW can accelerate an electron from an initial kinetic energy of 10 MeV to

a final kinetic energy of about 50 MeV. Eqs. (3.10) and (3.11) give us pulse energies of about 45 mJ and 90 mJ for the 7.5 fs and 15 fs pulse respectively. This shows that lasers can already be very useful for electron acceleration at relatively low powers, just that the electrons must be pre-accelerated (preferably to relativistic speeds) to extract substantial energy from the laser pulse. Although it appears from our results that a smaller improvement in normalized energy gain is obtained with a pre-accelerated electron at higher laser powers, this does not discount the possibility of substantial improvements at these higher powers if we increase $E_K(0)$ to values beyond the range studied.

As another example, we note from Figs. 3-7 and 3-10 that a two-stage laser accelerator employing a pulsed radially-polarized laser beam of $w_0 = 2$ μm, $\tau = 10$ fs and $P = 10$ TW (giving a pulse energy of about 120 mJ) in each stage can accelerate an initially stationary electron to a kinetic energy of about 6.3 MeV in the first stage, and thence to a kinetic energy of about 36 MeV in the second stage. Note that the same pulse may be used in both stages, since the pulse transfers a negligible fraction of its energy to the electron in the first stage. Clearly, direct acceleration of electrons to substantial energies in infinite vacuum can in principle be realized without the use of petawatt peak-power laser technology. Lasers with peak powers of a few terawatts are already capable of accelerating electrons to energies of tens of MeV, high enough for applications like the production of hard X-rays via inverse Compton scattering [GBK+09]. In addition, recall that we have limited our studies to $w_0 \geq 2$ μm. If energy gain continues to increase with tighter focusing for waist radii below 2 μm, it is likely that much more impressive results (at least in terms of energy gain) may be obtained with lasers focused down to an order of a wavelength.

Because the electron in Fig. 3-12 moves at a relativistic speed for most of its trajectory, one may mistakenly expect its energy gain to be approximately 0. This is supported by the egregious approximation that $v(t) \approx c \ \forall t$, which enables an analytic computation of energy gain as (allowing α to be some constant determined by the particle's location relative to the center of the pulse envelope)

$$\Delta E_{v=c} = \int_{-\infty}^{\infty} dz(eE_z) \approx \int_{-\infty}^{\infty} dz\alpha \left[\frac{e/z_0}{1+(z/z_0)^2} \sqrt{\frac{8\eta_0 P}{\pi}} \right] \sin\left(2\tan^{-1}(z/z_0) + \psi_0\right) = 0 \qquad (3.19)$$

Our exact numerical simulations reveal that this is not the case. Although the electron is relativistic for most of its trajectory, the few places at which it becomes non-relativistic are sufficient to produce an asymmetry that prevents the actual integral of force over distance from vanishing.

This observation also encourages the hypothesis that the highest $E_K(0)$ with which an electron may be substantially accelerated by a pulsed radially-polarized laser beam is on the order of the theoretical gain limit $\Delta E_{\lim}$, because $\Delta E_{\lim}$ also represents the maximum *deceleration* of a pre-accelerated electron. If $E_K(0)$ is relativistic and $E_K(0) >> \Delta E_{\lim}$, the laser field can never at any point decelerate the electron to non-relativistic speeds so $v(t) \approx c \; \forall t$ would be true and Eq. (3.19) would hold. This hypothesis may be extended to any other direct acceleration scheme if a corresponding $\Delta E_{\lim}$ expression may be found for it. The electron's energy gain for a given laser should thus decrease after some point as $E_K(0)$ continues to increase, and become negligible for $E_K(0) >> \Delta E_{\lim}$. This implies that there exists a second set of power and initial kinetic energy threshold values (i.e.: different from the P_{th} and E_{Kth} predicted by (3.17)) observable only at values of $E_K(0)$ beyond the range studied given our range of P. This "second threshold" places an upper bound on $E_K(0)$ given P (and continues to place a lower bound on P given $E_K(0)$) for non-negligible acceleration. In the next chapter, we see that our hypothesis is correct and that an analytical formula can be derived to approximate the threshold for net acceleration of an on-axis electron in infinite vacuum by a radially-polarized beam for any initial electron velocity.

3.5 Two-color laser-driven direct acceleration of an electron in infinite vacuum

In this section, we show that a two-color pulsed beam can accelerate an electron by over 90% of the one-color beam's theoretical gain limit, for a given total energy and pulse duration. The scheme exploits how the Gouy phase shift will vary the interference pattern of the on-axis electric field with position along the beam axis. For most cases well above the threshold power for electron acceleration, maximum acceleration is obtained with an acceleration-favoring interference of fields only as the electron enters its effectively final accelerating cycle.

The two-color pulsed beam is the sum of two co-propagating pulsed radially-polarized laser beams, with central angular frequencies ω and 2ω, of equal pulse duration, peak power and Rayleigh range. The electron begins at rest on the beam axis in field-free vacuum (the pulse begins infinitely far away) and ends moving in field-free vacuum after the pulse has completely

overtaken it (the setup is identical to that in the previous sections, with the one-color beam replaced by a two-color beam). On the beam axis all transverse fields vanish, leaving the longitudinal electric field E_z, which is obtained by summing the E_z components of two one-color beams:

$$E_z = \left[\frac{1/z_0}{1+(z/z_0)^2}\sqrt{\frac{4\eta_0 P}{\pi}}\right]\left[\sin\left((\xi+\psi_a)+\psi_g+\psi_b\right)+\sin\left(2(\xi+\psi_a)+\psi_g+\psi_b\right)\right]\mathrm{sech}\left(\frac{\xi+kz_i}{\xi_0}\right) \tag{3.20}$$

where $\xi \equiv \omega t - kz$; $z_0 \equiv \pi w_0^{\,2}/\lambda$ is the Rayleigh range; $k \equiv 2\pi/\lambda = \omega/c$; w_0 is the waist radius of the fundamental harmonic beam; $\psi_g \equiv 2\tan^{-1}(z/z_0)$ is the Gouy phase shift; $\eta_0 \cong 120\pi\,\Omega$ is the vacuum wave impedance; z_i is the pulse's initial position (effectively $-\infty$); c is the speed of light in vacuum; $\xi_0 \equiv \omega\tau/\mathrm{sech}^{-1}(\exp(-1))$, where τ is the pulse duration; ψ_a and ψ_b are phase constants; $P/2$ is the peak power of each pulse; $z(0)$ is the initial electron position.

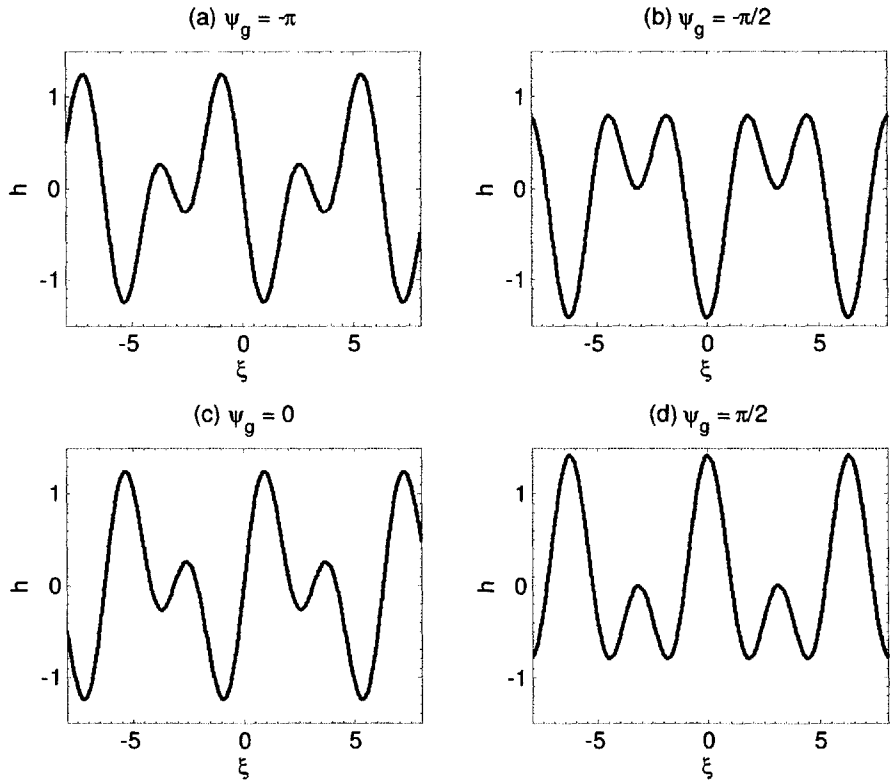

Fig. 3-13. Plots of $h \equiv \sqrt{0.5}\left[\sin\left(\xi + \psi_g\right) + \sin\left(2\xi + \psi_g\right)\right]$ for various ψ_g.

Our results should closely approximate those for the more general case of a slightly off-axis, non-relativistic electron, due to the electron confinement property of the transverse fields [Sal06, Sal07] and the fact that the laser pulse and phase move at or beyond the speed of light.

Consider the function $h \equiv \sqrt{0.5}\left[\sin\left(\xi + \psi_g\right) + \sin\left(2\xi + \psi_g\right)\right]$, to which Eq. (3.20) is proportional except for a translation in ξ and ψ_g, plotted in Fig. 3-13. The phase ψ_b in Eq. (3.20) controls the field pattern produced by interference at each position along the beam axis. For instance, setting $\psi_b = \pi$ would cause the field pattern to evolve, due to the Gouy phase shift, in the order (c)-(d)-(a)-(b)-(c) as the laser pulse propagates from $z = -\infty$ to $-z_0$, 0, z_0 and ∞ respectively. We also note that of all possible patterns, the one in Fig. 3-13(b) seems to favor electron acceleration most, since its ratio of most negative to most positive value is largest in magnitude. The position where the Fig. 3-13(b) wave pattern occurs is given by $z_b = -z_0 \tan\left(\pi/4 + \psi_b/2\right)$.

We numerically solve the Newton-Lorentz equations of motion using the Adams-Bashforth-Moulton method (*ode113* of *Matlab*). Although we set $\lambda = 0.8$ μm here, our results are readily scalable to any λ since the electrodynamic equations are independent of λ under the normalizations $\mathrm{T} \equiv \omega t$, $\varsigma \equiv z/z_0$ (with $\varsigma_i \equiv z_i/z_0$) and $\kappa \equiv kz_0 = 2\left(\pi w_0/\lambda\right)^2$ (as was explicitly shown for the one-color beam in the previous sections). We sweep over P - τ - w_0 space and optimize over ψ_a - ψ_b - $z(0)$ space for electron energy gain normalized by the one-color theoretical energy gain limit ΔE_{lim} given by (4.2.10). As Fig. 3-14(a) shows, the two-color beam with peak power $P/2$ in each beam, and therefore the same total power as the one-color beam ($\lambda = 0.8$) with peak power P, can accelerate an electron by more than 90% of the one-color beam's theoretical gain limit, whereas the one-color beam can manage less than 40% in the parameter space studied.

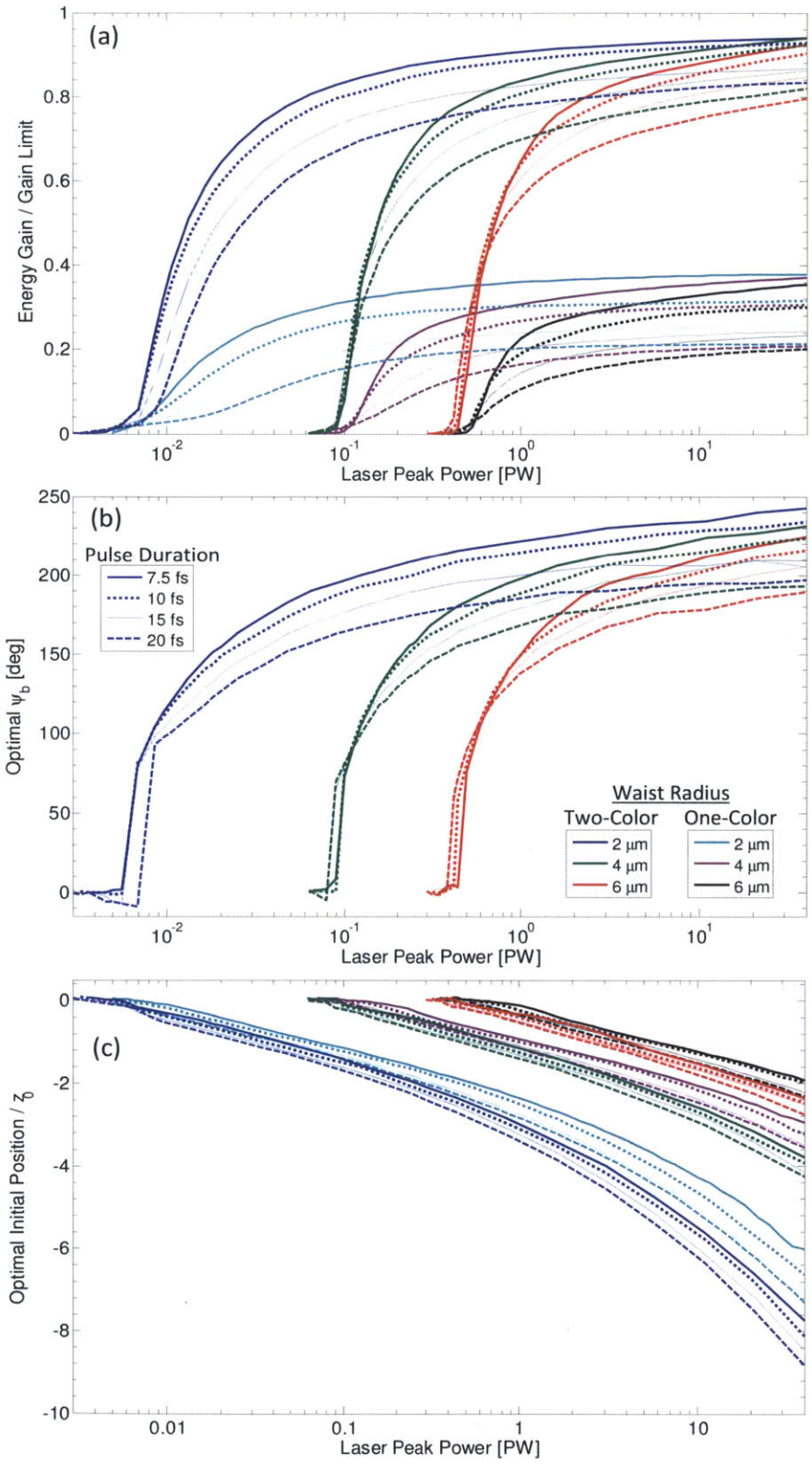

Fig. 3-14. Plots of (a) maximum normalized energy gain (b) corresponding optimal ψ_b (for two-color case) and (c) corresponding optimal normalized $z(0)$ vs. peak power.

Fig. 3-14(b) shows that well above the threshold power, the optimal ψ_b lies between $\pi/2$ and $3\pi/2$, i.e. the Fig 3-13(b) wave pattern occurs between $z=0$ and $z=\infty$, with a tendency to be around π (the Fig. 3-13(b) wave pattern occurs around $z=z_0$). This accords with physical intuition because a) due to the Gouy phase shift the electron can enter its effectively final accelerating cycle only after $z=0$ and b) when determining the best position for the Fig. 3-13(b) pattern, one must strike a compromise between the Lorentzian decay (due to beam divergence) in Eq. (3.20) and the fact that the acceleration-favoring Fig. 3-13(b) pattern will be maintained over a greater distance the further from the focus it occurs, due to the smaller rate of change with distance of the Gouy phase shift. Fig. 3-14(c) shows that the optimal initial position of the initially-stationary electron for the two-color beam tends to be slightly more negative than that for the one-color beam with the same peak power P, pulse duration τ and waist radius w_0.

We have omitted plots of optimal ψ_a vs. P because they consist of points erratically scattered between 0 and 2π radians, with no discernible pattern as a function of P. This apparently erratic behavior arises from the fact that the optimal ψ_a varies rapidly over a small interval in P, and this rapidly-varying pattern can be captured only with simulations of a very high density that are too expensive in terms of simulation time for the method we use here. In practice, one will have to seek the optimal ψ_a manually during an experiment or run a simulation specially for that case, given all other optimal conditions from our analysis.

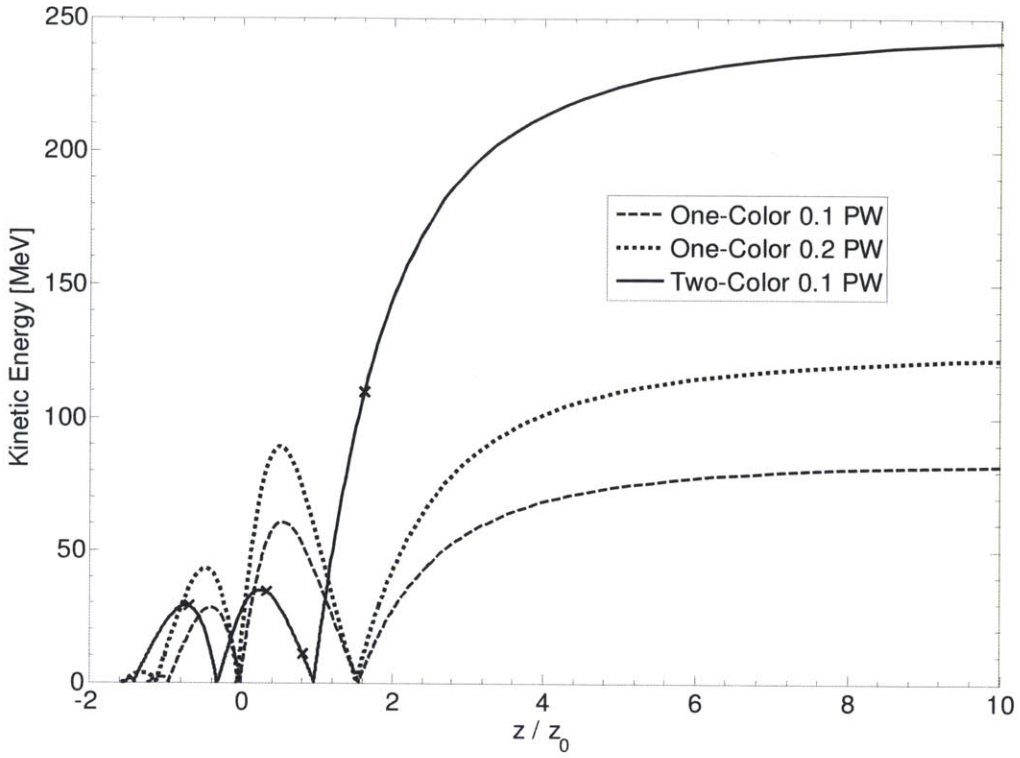

Fig. 3-15. Variation of kinetic energy with electron displacement of an electron hit by a pulse. In each case, $w_0 = 2$ μm and $\tau = 10$ fs, with all other parameters optimized. Crosses on the solid curve indicate the positions where the Fig. 3-16 plots are generated.

Applying the same method by which ΔE_{lim} was formulated for the one-color beam gives us a theoretical gain limit for the two-color beam: $\Delta E_{\text{lim},TC} = 2^{1/2} \Delta E_{\text{lim}}$ (given P). This may lead one to expect a two-color beam of total power P and a one-color beam of power $2P$ to be comparable in electron acceleration capability. However, the former in fact significantly outperforms the latter for P well above the electron acceleration threshold. As Fig. 3-15 shows, an electron in a 0.1 PW one-color beam slips through several accelerating and decelerating cycles, gaining and losing substantial amounts of energy, before finally entering its effectively final accelerating cycle. When the one-color beam is intensified to 0.2 PW (and optimum conditions re-computed), the final electron energy increases, but so have the heights of the intermediate energy peaks, which reduce net acceleration in this case by pushing back the position where the electron enters its final accelerating cycle. The two-color beam scheme achieves smaller intermediate peaks by varying the laser's interference pattern to increasingly

favor acceleration as the electron moves forward past the focus (Fig. 3-16), adopting the acceleration-favoring Fig. 3-13(b) pattern only as the electron enters its effectively final accelerating cycle, instead of maintaining the same peak accelerating field at every position as the one-color beam does.

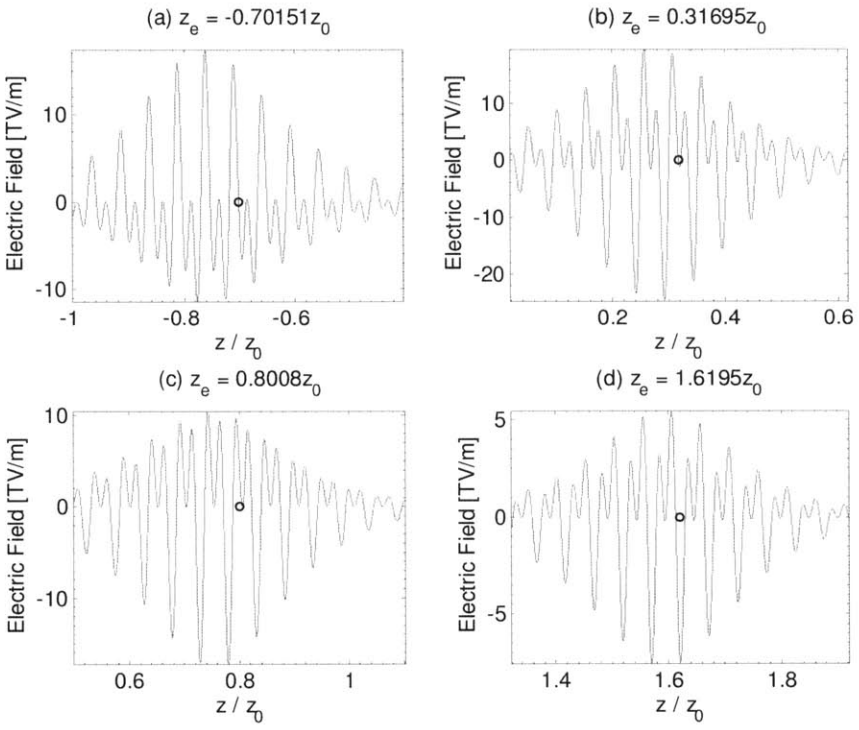

Fig. 3-16. E_z profile of laser pulse at selected positions of the electron's trajectory for the two-color $P = 0.1$ PW case in Fig. 3-15. Circles at $z = z_e$ indicate the electron's position. (a), (b), (c) and (d) correspond respectively to the crosses in Fig. 3-15 from left to right.

Note that our scheme is fundamentally different from vacuum beat wave acceleration [Hor88, ESK95], which also uses a superposition of co-propagating laser beams, but which accelerates electrons by the beat wave arising from the $-e\vec{v} \times \vec{B}$ (ponderomotive force) term in the Lorentz force equation $\vec{F} = -e\left(\vec{E} + \vec{v} \times \vec{B}\right)$, whereas our scheme accelerates electrons by the $-e\vec{E}$ term, using the Gouy phase shift to vary the overall interference pattern with position along the axis.

3.6 Summary and future work

In this chapter, we studied the direct acceleration of a free electron in infinite vacuum along the axis of a pulsed radially-polarized laser beam. By introducing appropriate normalizations to the electrodynamic equations, we have shown that our results for $\lambda = 0.8\mu m$ may be readily scaled to obtain the results for any λ. An important consequence of this is that for a given peak power, a larger pulse energy is required for exactly the same maximum acceleration at a larger λ if focusing (w_0/λ) remains constant, because the number of carrier cycles in the pulse envelope must also remain constant, leading to a longer pulse.

In all cases studied (regardless of power, pulse duration and electron initial speed), the greatest acceleration is achieved with the most tightly-focused laser. Also, the optimal pulse duration is a function of power, with shorter pulses favored at higher powers and longer pulses favored closer to the threshold. In all cases studied, energy gain in MeV increases with increasing peak power, but the energy gain normalized by the theoretical energy gain limit does not always do so. Greater acceleration may be achieved with pre-accelerated electrons. The net energy gained by an initially relativistic electron may even exceed more than half the theoretical energy gain limit, which is not possible with an initially stationary electron in the parameter space studied. We have also given some examples of how electron acceleration by tens of MeV is in principle demonstrable with laser powers as low as a few terawatts.

Finally, we proposed and studied the direct acceleration of an electron in infinite vacuum by a two-color pulsed radially-polarized laser beam. This scheme exploits the presence of the Gouy phase shift to accelerate a stationary electron by over 90% of the one-color theoretical energy gain limit, more than twice of what is possible with a one-color beam of equal total energy and pulse duration.

Future work includes the study of multi-color acceleration schemes (e.g.: three-color, four-color) that can possibly lead to energy gains beyond the one-color gain limit. A comprehensive treatment of the effect on electron bunch properties like energy spread and emittance of single-color and multi-color linear acceleration schemes in vacuum is also pending.

Chapter 4

A general threshold for net linear acceleration in unbounded vacuum

In the previous chapter, we explored the scaling laws associated with the linear acceleration of charged particles with pulsed radially-polarized beams in unbounded vacuum. Here, we broach the fundamental question of how net linear acceleration (linear acceleration referring, once again, to the fact that the force experienced by the particle is linearly proportional to the electric field) is possible in unbounded vacuum, and derive a general formula that may be applied to approximate the acceleration threshold of a given laser beam configuration (not just radially-polarized laser beams).

Proposals to achieve net linear acceleration in vacuum often introduce material boundaries to limit the region of laser-electron interaction [ESL09, HZT+96, ESK95, SK92, PBS05, PBC+05, SZ91]. The prospect of material damage places limits on the intensity of the laser light that can be used and hence the peak acceleration gradient. Proposals to accelerate electrons in unbounded vacuum have sometimes been met with controversy (e.g.: [Haa95, SEK+96, Haa96]) revolving around the Lawson-Woodward theorem, a theorem that describes conditions under which net acceleration of a charged particle by an electromagnetic wave is impossible. The objective of this chapter is two-fold: firstly, to show that the Lawson-Woodward theorem does not preclude the possibility of net linear acceleration of charged particles (including initially-relativistic particles)

in unbounded vacuum; secondly, to test our hypothesis that a charged particle in unbounded vacuum can be substantially linearly accelerated only if the accelerating field is capable of bringing the particle to a relativistic energy in its initial rest frame during the interaction. We verify the accuracy of this hypothesis by deriving an approximate formula for the threshold of net linear acceleration in unbounded vacuum, and showing the close correspondence between our formula and the results of numerical simulations using the exact equations.

4.1 The Lawson-Woodward theorem

The Lawson-Woodward theorem [ESK95] states that, under certain conditions, the net energy gain of a relativistic electron interacting with an electromagnetic field in vacuum is zero. These conditions are:

(i) The laser field is in vacuum with no walls or boundaries present,

(ii) The electron is highly relativistic (v~c) along the acceleration path,

(iii) No static electric or magnetic fields are present,

(iv) The region of interaction is infinite, and

(v) Ponderomotive effects (nonlinear forces) are neglected.

In order to achieve net energy gain, one or more of the above conditions must be violated. The proof of the Lawson Woodward theorem is as follows [ESK95]:

Suppose an electron of charge q in vacuum travels along the z-axis (x = 0, y = 0) and interacts linearly with the E_z component of a propagating electromagnetic field. Its net energy gain is then

$$\Delta U = q\int_{-\infty}^{\infty} dz E_z \,. \tag{4.1}$$

The z-directed electric field component of an electromagnetic wave in vacuum may be generally formulated as:

$$\begin{aligned} E_z &= (2\pi)^{-1}\int dk_x \int dk_y \tilde{E}_z(k_x,k_y)\exp\left[i\left(k_x x + k_y y + k_z z - \omega t\right)\right] \\ &= (2\pi)^{-1}\int dk_x \int dk_y \tilde{E}_z(k_x,k_y)\exp\left[i\left(k_z z - \omega t\right)\right] \end{aligned}, \tag{4.2}$$

where $k_z \equiv \sqrt{\omega^2/c^2 - k_x{}^2 - k_y{}^2}$. From Gauss' law we also have that

$$\nabla \cdot \vec{E} = 0 \Rightarrow E_z = -\frac{\vec{k}_\perp \cdot \vec{\tilde{E}}(k_x, k_y)}{k_z}. \tag{4.3}$$

Substituting (4.2) and (4.3) into (4.1) gives

$$q\int_{-\infty}^{\infty} dz E_z = \frac{q}{2\pi}\int_{-\infty}^{\infty} dz \left\{ \int dk_x \int dk_y \frac{-\vec{k}_\perp \cdot \vec{\tilde{E}}(k_x, k_y)}{k_z} \exp[i(k_z z - \omega t)] \right\}. \tag{4.4}$$

For the proof to proceed, it is necessary to set $t = z/c$, which is to say, assume that the particle always travels at approximately the speed of light c (condition (ii) of the Lawson-Woodward theorem). Doing so, we get

$$\begin{aligned} q\int_{-\infty}^{\infty} dz E_z &= \frac{q}{2\pi}\int_{-\infty}^{\infty} dz \left\{ \int dk_x \int dk_y \frac{-\vec{k}_\perp \cdot \vec{\tilde{E}}(k_x, k_y)}{k_z} \exp\left[i\left(k_z - \frac{\omega}{c} \right) z \right] \right\} \\ &= q\int dk_x \int dk_y \frac{-\vec{k}_\perp \cdot \vec{\tilde{E}}(k_x, k_y)}{k_z} \delta(k_z - \omega/c) \end{aligned}. \tag{4.5}$$

Next, transform into the polar coordinates (where $k_\perp = \sqrt{k_x{}^2 + k_y{}^2}$ and $\phi = \arctan(k_y/k_x)$) to get

$$q\int_{-\infty}^{\infty} dz E_z = q\int dk_\perp k_\perp \int d\phi \frac{-\vec{k}_\perp \cdot \vec{\tilde{E}}(k_x, k_y)}{k_z} \delta(k_z - \omega/c). \tag{4.6}$$

Now note that

$$\delta\left(k_z-\frac{\omega}{c}\right)=\frac{\delta(k_\perp)}{\left|\frac{\partial}{\partial k_\perp}\left(\sqrt{\frac{\omega^2}{c^2}-k_\perp{}^2}-\frac{\omega}{c}\right)\right|_{k_\perp=0}}. \qquad (4.7)$$
$$=\delta(k_\perp)\left|\left(\frac{k_z}{k_\perp}\right)\right|_{k_\perp=0}$$

Putting (4.7) into (4.6) gives us

$$q\int_{-\infty}^{\infty}dzE_z=q\int d\phi\int dk_\perp\left(\frac{-k_\perp}{k_z}\right)\left|\left(\frac{k_z}{k_\perp}\right)\right|_{k_\perp=0}\left|\vec{k}_\perp\cdot\vec{\tilde{E}}(k_x,k_y)\delta(k_\perp)\right| \qquad (4.8)$$
$$=0\Leftrightarrow\left[k_\perp\to 0\Rightarrow\vec{k}_\perp\cdot\vec{\tilde{E}}(k_x,k_y)\to 0\right]$$

where we obtain a net energy gain of 0 if the condition in the second line applies, which it should for most laser beams of practical interest. This concludes the proof of the Lawson-Woodward theorem.

To appreciate the possibility of linear acceleration in vacuum, it is important to note that the proof of the Lawson-Woodward theorem is contingent upon the assumption that $t = z/c$, i.e. that the particle is very relativistic throughout the interaction with the laser beam. However, we see from the simulation in Fig. 3-12 that an initially-relativistic particle interacting with the purely-linear force of a propagating electromagnetic wave in vacuum may be decelerated to non-relativistic speeds at some point, breaking condition (ii) (even as (i), (iii), (iv) and (v) continue to hold) and preventing progress from (4.4) to (4.5) in the above proof. Thus, net acceleration by a propagating electromagnetic wave in unbounded vacuum is permitted by the Lawson-Woodward theorem.

4.2 A threshold for net linear acceleration by a propagating field in unbounded vacuum

What exactly are the laser and particle parameters such that the Lawson-Woodward theorem would permit net linear acceleration in unbounded vacuum? Based on the fact that the proof of the Lawson-Woodward theorem is contingent upon the assumption that $t = z/c$, one would hypothesize that a charged particle (regardless of initial energy) in unbounded vacuum can be substantially accelerated by a force linear in the electric field of a propagating electromagnetic wave only if the accelerating field is capable of bringing the particle to a relativistic energy in its initial rest frame during the interaction. By "substantial acceleration" we mean the ratio of final to initial particle energy $\gamma_f/\gamma_0 >> 1$. Based on this hypothesis, we derive a formula for the threshold power and compare the formula with the results of exact numerical simulations over a broad range of parameters for different kinds of pulsed laser beams. The accuracy with which the formula matches our numerical simulations lends credence to our hypothesis and sheds light on the physical mechanism that enables net linear acceleration in unbounded vacuum: namely, that the ability of the accelerating field to bring the particle to a relativistic energy in its initial rest frame is critical to substantial net linear acceleration.

We will always assume that the pulse starts far enough behind the particle that the particle is initially in field-free vacuum, and that the particle's final energy is evaluated when the particle is once again in field-free vacuum (long after interaction with the pulse). In the rest frame of the on-axis particle (of charge q and mass m) traveling at its initial ($t = 0$) z-directed velocity v_0 in the lab frame, the Lorentz force accelerates the particle as

$$\frac{d(\gamma'\beta')}{dt'} = \frac{q}{mc} E_z(0,0,z,t) = A(z,t)\sin(\omega t - \mathrm{B(z)}), \tag{4.9}$$

where the last equality makes an assumption about the on-axis form of the electric field $E_z(x, y, z, t)$, the longitudinal component of the electric field in the laboratory frame. $v = \beta c$ is the particle velocity and $\gamma \equiv 1/\sqrt{1-\beta^2}$, where c is the speed of light in vacuum. Primes indicate variables in the initial particle's rest frame, so the Lorentz transform gives $z = \gamma_0(z' + v_0 t')$ and $t = \gamma_0(t' + (v_0/c^2)z')$, γ_0 being the initial γ. Let a particle be considered relativistic if $|\gamma\beta| > g_b$, where g_b is some reasonable value on the order of 1. The mathematical statement of our hypothesis is

$$\overline{M}\left(\gamma_f/\gamma_0\right)>>1 \rightarrow \overline{M}\left(M\left(\left|\gamma'(t')\beta'(t')\right|,t'\right)\right)>> g_b, \tag{4.10}$$

where $M(f(x),x)$ is the maximum of f over x, $\overline{M}(\cdot)\equiv M\left(M(\cdot,\psi_0),z(0)\right)$. $\psi_0\in[0,2\pi)$ is the carrier-envelope phase and $z(0)\in(-\infty,\infty)$ the initial particle position. Among the most commonly-studied fields are the radially-polarized laser beam [ESK95, SK92, WK10, VPP05 Sal07 KP07 WK11, SHK08, FPV10], for which $E_z(0,0,z,t)=L_r\sin(\psi_r)\mathrm{sech}(\xi_r/\xi_0)$, and the configuration of crossed Gaussian beams [[ESK95, Haa96, PBS05, SMK03], for which $E_z(0,0,z,t)=L_c X_c\sin(\psi_c)\mathrm{sech}(\xi_c/\xi_0)$. $L_r\equiv\sqrt{8\eta_0 P/\pi}/\left(z_0\left(1+\zeta^2\right)\right)$, $\psi_r\equiv\omega t-kz+2\tan^{-1}\zeta+\psi_0$, $\xi_r\equiv\omega t-k(z-z_i)$, $L_c\equiv\sin\theta\sqrt{8\eta_0 P/\pi}/\left(w_0\left(1+Z^2\right)\right)$, $X_c\equiv\exp(-b^2)$, $b^2\equiv Z^2\tan^2\theta/\left(\varepsilon^2\left(1+Z^2\right)\right)$, $\psi_c\equiv\omega t-kz\cos\theta-Zb^2+2\tan^{-1}Z+\psi_0$, $\xi_c\equiv\omega t-k\left(z\cos\theta-z_i\right)$; θ is the angle each beam makes with the axis in the crossed-beams scheme; λ is the carrier wavelength; $z_0\equiv\pi w_0^{\,2}/\lambda$; $k\equiv 2\pi/\lambda=\omega/c$; w_0 is proportional to the beam radius; $\zeta\equiv z/z_0$; $Z\equiv\zeta\cos\theta$; $\varepsilon\equiv w_0/z_0$; η_0 is the vacuum wave impedance; z_i is the pulse's initial position (effectively $-\infty$); ξ_0 controls the pulse duration; P is the total peak pulse power ($P/2$ peak power for each pulse in the crossed-beam scheme). Note that in either case, the field is of the form assumed in Eq. (4.9). Since we seek the boundary of negligible acceleration, where the particle energy does not change substantially according to our hypothesis, the particle approximately remains at its initial speed throughout ($v\approx v_0\neq c\ \forall t$), so $z(t')\approx\gamma_0\left(\gamma_0 z(0)+v_0 t'\right)$, $t(t')\approx\gamma_0\left(t'+v_0\gamma_0 z(0)/c^2\right)$. Eq. (4.9) may be solved as

$$\begin{aligned}
\gamma'(t')\beta'(t') &\approx \int_{t'(0)}^{t'} ds' A(z(s'),t(s'))\sin(\omega t(s')-\mathrm{B}(z(s'))) \\
&\approx \int_{t'(0)}^{t'} ds' A(z(s'),t(s'))\sin\left(\omega\gamma_0 s'-\dot{B}(z(t'))\gamma_0 v_0 s'+const.\right) \quad , \\
&\approx \frac{-A(z(t'),t(t'))}{\omega\gamma_0\left(1-\dot{B}(z(t'))v_0/\omega\right)}\cos\left(\omega\gamma_0 t'-\dot{B}(z(t'))\gamma_0 v_0 t'+const.\right)
\end{aligned} \tag{4.11}$$

where $\dot{B} \equiv dB/dz$ and $t'(0) = -v_0\gamma_0 z(0)/c^2$. To arrive at the second line of Eq. (4.11), we Taylor-expanded B(z) and discarded higher order terms (assuming this is valid). We then integrated by parts and noted that $A(z,t) \equiv a(z)\mathrm{sech}(\xi/\xi_0)$, the product of the beam and pulse envelopes, varies slowly compared with the carrier sinusoid to arrive at the third line. We then insert Eq. (4.11) into Eq. (4.10) to get

$$\overline{M}\left(\frac{\gamma_f}{\gamma_0}\right) >> 1 \rightarrow M\left(\left|\frac{a(z)}{\omega\gamma_0\left(1-\dot{B}(z)v_0/\omega\right)}\right|, z\right) >> g_b, \tag{4.12}$$

where the optimizations over ψ_0 and z(0) allowed us to set the sinusoid and the pulse envelope respectively in Eq. (4.11) to their maximum value of 1. It is straightforward to verify, by taking first and second derivatives, that M 's first argument in Eq. (4.12) is maximized at $z = 0$ (ignoring singularities) for both the radially-polarized laser beam and the crossed-beams cases. For the radially-polarized laser beam, Eq. (4.12) becomes

$$\overline{M}\left(\frac{\gamma_f}{\gamma_0}\right) >> 1 \rightarrow P >> \gamma_0^2\left(1-\beta_0\left(1-\varepsilon^2\right)\right)^2\left(\frac{g_b mc^2}{q\varepsilon^2}\right)^2 \frac{\pi}{2\eta_0}. \tag{4.13}$$

Setting $\beta_0 = 0$ in Eq. (4.13) gives the threshold power for an initially stationary electron obtained by a different procedure in [WK10]. For the crossed-beams configuration, we have

$$\overline{M}\left(\frac{\gamma_f}{\gamma_0}\right) >> 1 \rightarrow P >> \gamma_0^2\left(1-\beta_0\cos\theta\left(1-\varepsilon^2\right)\right)^2\left(\frac{g_b mc^2}{q\varepsilon\sin\theta}\right)^2 \frac{\pi}{2\eta_0}. \tag{4.14}$$

Eqs. (4.13) and (4.14) (and (4.12), of which they are special cases) are useful analytical approximations of Eq. (4.10), but only when the assumptions we have made in obtaining them are valid. For instance, when $\gamma_0 >> 1$ in the case of Eq. (4.13), or $\gamma_0 >> 1$ and $\cos\theta \approx 1$ in the case of Eq. (4.14), the width of $a(z(t'))$ in t' may be comparable to the period of the sinusoidal carrier in t', contrary to our assumption in Eq. (4.11) that A varies slowly with respect to the

sinusoidal carrier in the particle's frame. In such cases, one would expect Eq. (4.12) to be a relatively poor estimate of Eq. (4.10). To compare our theory with the results of exact numerical simulations, we solve Eq. (4.9) and $dz/dt = v$ using a fourth-order Runge-Kutta algorithm, optimizing for energy gain over ψ_0 - $z(0)$ space in various two-dimensional parameter sweeps. These are plotted in Figs. 1 and 2, where the corresponding acceleration threshold (setting $g_b = 1$) hypothesized in Eq. (4.10) as well as the analytical approximations obtained from Eq. (4.12) are also displayed. In all plots, Eq. (4.10) approximates the threshold of substantial acceleration with high accuracy, and Eq. (4.12) is a fair approximation of Eq. (4.10) most of the time.

Fig. 4-1 shows several parameter sweeps for electron acceleration by a pulsed radially-polarized beam. For many plots, we have chosen $\xi_0 = 13.37$ because it corresponds to a FWHM pulse duration of 10 fs for $\lambda = 0.8\mu$m. Fig. 4-2 shows parameter sweeps for the crossed-beams configuration. We note from Figs. 1(a)-(b) and 2(a)-(b) that the threshold power does not decrease indefinitely with increasing $K(0)$, but scales as γ_0^2 when $\beta_0 \to 1$ (one intuitively expects this behavior from the fact that the theoretical energy gain limit scales as $P^{1/2}$ [WK10, FPV10]). This implies that, unlike conventional accelerators, effectively-unbounded linear particle accelerators cannot be cascaded indefinitely for greater gain: the energy of an output particle is ultimately limited by the peak power of the strongest laser in the cascade.

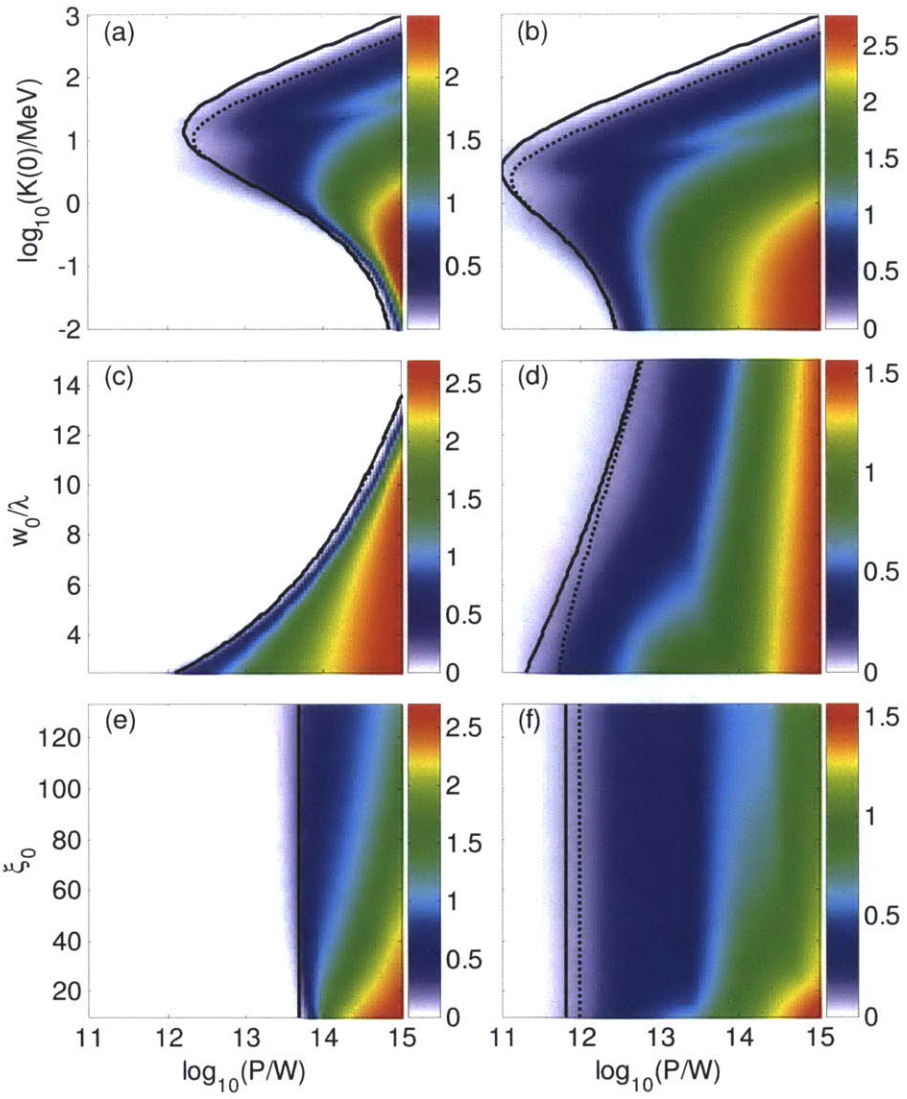

Fig. 4-1: Color maps of $\log_{10}(\gamma_f/\gamma_0)$ (γ_f/γ_0 being ratio of final to initial particle energy) for linear electron acceleration by a pulsed radially-polarized laser beam as a function of various parameters: initial kinetic energy $K(0)$ and peak pulse power P for normalized pulse duration $\xi_0 = 13.37$ and (a) normalized beam radius $w_0/\lambda = 10$, (b) $w_0/\lambda = 2.5$; w_0/λ and P for $\xi_0 = 13.37$ and (c) $K(0) = 0.1\,\mathrm{MeV}$, (d) $K(0) = 10\,\mathrm{MeV}$; ξ_0 and P for $w_0/\lambda = 6.25$ and (e) $K(0) = 0.1\,\mathrm{MeV}$, (f) $K(0) = 10\,\mathrm{MeV}$. Solid black lines demarcate the acceleration threshold predicted by our hypothesis. Dotted black lines correspond to the analytical approximation of this boundary.

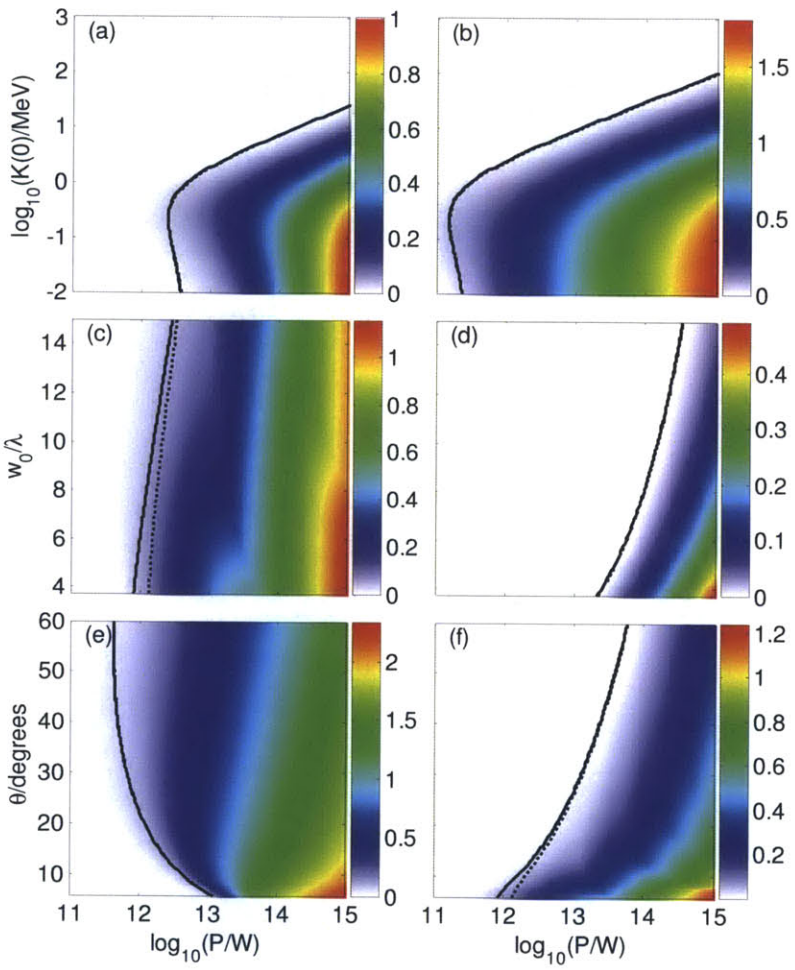

Fig. 4-2: Color maps of $\log_{10}(\gamma_f/\gamma_0)$ (γ_f/γ_0 being ratio of final to initial particle energy) for linear electron acceleration by the crossed-beams configuration as a function of various parameters: initial kinetic energy $K(0)$ and total peak pulse power P for normalized pulse duration $\xi_0 = 13.37$, (a) normalized beam radii $w_0/\lambda = 15$ and crossing angle $\theta = 45^0$, (b) $w_0/\lambda = 3.75$ and $\theta = 45^0$; w_0/λ and P for $\xi_0 = 13.37$, (c) $K(0) = 10\,\text{MeV}$ and $\theta = 2.5\lambda/\pi w_0$, (d) $K(0) = 10\,\text{MeV}$ and $\theta = 60^0$; θ and P for $\xi_0 = 13.37$, (e) $w_0/\lambda = 6.25$ and $K(0) = 0.1\,\text{MeV}$, (f) $w_0/\lambda = 6.25$ and $K(0) = 10\,\text{MeV}$. Solid black lines demarcate the acceleration threshold predicted by our hypothesis. Dotted black lines correspond to the analytical approximation of this boundary.

4.3 Summary and future work

We present a full derivation of the Lawson-Woodward theorem, a theorem which forbids electron acceleration in vacuum under a certain set of conditions. We point out that one of these conditions is broken when a particle is not always relativistic throughout its trajectory in unbounded vacuum. This permits an initially relativistic particle, interacting with the linear forces of a focused laser beam, to gain (or lose) net energy even in unbounded vacuum.

Our simulations support our hypothesis that substantial net linear acceleration is contingent on the accelerating field's ability to bring the particle to a relativistic energy in its initial rest frame during the interaction, at least for the types of beams and range of parameters considered in this chapter. In the process, we have derived a general formula for the acceleration threshold, which is useful as a practical guide to the laser intensities that linear acceleration in unbounded vacuum requires. The fact that a relativistic particle can be further accelerated by linear acceleration in unbounded vacuum is important because this enables the injection of a relativistic particle beam, which is more resistant to space-charge effects than a non-relativistic beam is. Although we have illustrated our theory with electron acceleration by a radially-polarized laser beam and the crossed-beams configuration, our theory may be readily extended to any other unbounded linear acceleration scheme that can be described by an equation of the general form in Eq. (4.9).

Future work includes the derivation of an analytical approximation to the energy gained by a relativistic electron interacting with the linear forces of an electromagnetic pulse.

Chapter 5

Electron acceleration and bunch compression by coherent terahertz pulses in waveguides

Following our work on the electrodynamics of single particles in laser fields at optical frequencies, preliminary simulations have shown that radially-polarized pulsed laser beams focused to a spot size on the order of a few wavelengths are capable of accelerating only something on the order of 10 fC of electrons, which is useful only for niche applications where few coherent x-rays are needed. Research into the use of optical photonic crystals for electron acceleration -- where the intensity of the unbounded vacuum schemes we have been studying is traded off for the longer interaction length provided by a guiding structure -- have also predicted accelerated electron bunches of similar sizes (see [CCE+10] and references therein). To accelerate electron bunches on the order of 1 pC or greater, it appears that a shift to longer wavelengths is necessary. The terahertz spectrum, which lies between the optical spectrum and the RF spectrum of conventional accelerators, suggests itself naturally.

In this chapter, we demonstrate the capabilities of waveguides optimized for acceleration and/or compression of relativistic electron bunches by coherent THz pulses. The relativistic few-femtosecond pico-Coulomb electron bunch achieved in the bunch compression scheme has applications in single-shot few-femtosecond electron diffraction [SM11]. We choose to study dielectric-loaded cylindrical metallic waveguides for their ease of manufacturing and theoretical

evaluation. The THz frequency range is chosen as the operation range because it appears to strike a compromise between the large wavelength and low acceleration gradient (due to breakdown limitations) of RF radiation and the small wavelength but high acceleration gradient of optical radiation. Note that a higher acceleration gradient is more favorable for bunch compression and acceleration, but space-charge effects make it difficult to confine a bunch of substantial charge well within a half-cycle if the wavelength is too small. The absence of plasma in a vacuum-core waveguide scheme precludes problems associated with the inherent instability of laser-plasma interactions. Although using a guiding structure leads to intensity limitations, it also increases acceleration efficiency due to a smaller driving energy required and a larger interaction distance.

The high thermal conductivity and breakdown properties of chemical-vapor-deposited diamond at THz frequencies are well-recognized, and has led to its use in waveguides for wakefield acceleration [AJK+12] and other applications involving intense terahertz radiation [YTU+01]. For this reason, we use diamond for the dielectric throughout this study and assume a relative dielectric constant of $\varepsilon_r = 5.5$ [Kub09]. We employ the fundamental transverse-magnetic waveguide mode (TM_{01} mode) because every field component in this mode vanishes on axis except for the z-directed electric field, so an electron bunch close to the axis will be accelerated mainly in the forward direction.

Fig. 5-1 illustrates an example of concurrent compression and acceleration of an electron bunch in our scheme. We present this example before any technical discussion to give some preliminary intuition of the electrodynamics that ensues when a 1 MeV electron bunch (obtained, for instance, from an RF gun) is injected into a coherent THz pulse propagating in a dielectric-loaded cylindrical metal waveguide.

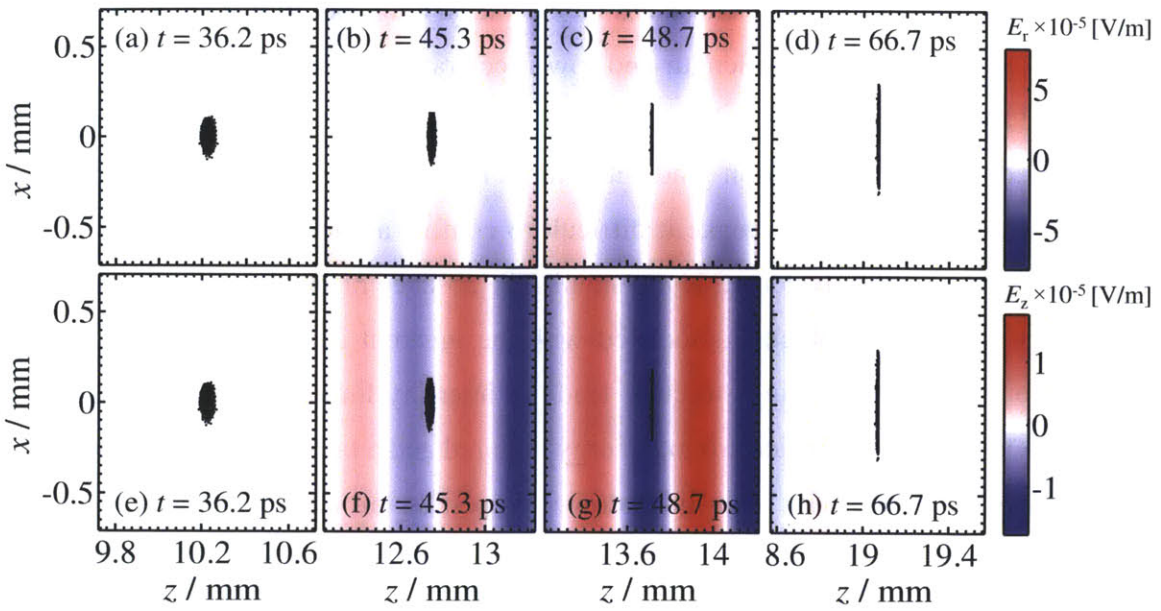

Fig. 5-1. Illustration of electron bunch acceleration and compression by a TM_{01} coherent THz pulse in a dielectric-loaded (diamond) cylindrical metal waveguide: The 8-cycle pulse is centered at 0.6 THz, with group velocity 0.399c and phase velocity c. The 1.6 pC-bunch has an initial mean kinetic energy of 1 MeV. Steps of the bunch evolution include: (a) arriving at the rear of the pulse, (b) slipping through an accelerating and compressing quarter-cycle, (c) maximum longitudinal compression and (d) transverse and longitudinal expansion as the electron bunch emerges from the head of the pulse. Each black dot indicates a macro-particle, with 1000 macro-particles used in the simulation. The color maps in (a)-(d) show the value of E_r in the y = 0 plane. (e)-(h) is identical to (a)-(d) respectively, except that the color maps show E_z instead of E_r.

Note that the work pursued here differs from the study presented in [YR05], which discusses the design of a uniformly-accelerating 100 MeV/m coherent THz pulse-driven waveguide accelerator. Here, we study the acceleration as well as bunch compression capabilities of a coherent THz pulse of finite duration. Moreover, the presented simulation results for coherent THz pulse-driven acceleration and compression cannot be taken for granted or inferred by scaling the results from studies at optical or RF frequencies, because of the non-negligible impact of space-charge.

In Sec. 5.1 and 5.2, we furnish a technical discussion of the equations upon which our model rests. In Sec. 5.3, we demonstrate the acceleration of a 1.6 pC electron bunch from a kinetic

energy of 1 MeV to about 10 MeV over an interaction distance of about 20mm, using a 20mJ pulse centered at 0.6 THz in a dielectric-loaded metallic waveguide. The implications of using an arbitrarily distant injection point, as well as the prospects of dielectric breakdown and thermal damage for our optimized design are also analyzed. In Sec. 5.4, we investigate the acceleration of 16 pC and 160 pC 1 MeV electron bunches. In Sec. 5.5, we optimize the dielectric-loaded metal waveguide design for simultaneous acceleration and bunch compression, achieving a 50 times (100 fs 1.6 pC electron bunch compressed to 2 fs over an interaction distance of about 18 mm) and 62 times (100 fs to 1.61 fs over an interaction distance of 42 cm) compression for 1 MeV and 10 MeV electron bunches, respectively.

5.1 Relativistic electrodynamics in a waveguide and simulation algorithms

This section introduces the equations governing the behavior of an electron bunch in the vacuum-filled core of a waveguide, and discusses our approach in modeling this behavior. The electron bunch is made up of N interacting electrons that may be modeled classically as N point charges propagating according to Newton's second law:

$$\frac{d\vec{p}_i(t)}{dt} = \vec{F}_i^{\,d}(t) + \sum_{\substack{j=1,\\ j\neq i}}^{N} \vec{F}_{i,j}^{\,pp}(t) + \vec{F}_i^{\,wf}(t) + \vec{F}_i^{\,rr}(t), \text{ with } i = 1,...,N, \tag{5.1}$$

where $\vec{p}_i(t) \equiv \gamma_i(t) m \vec{v}_i(t)$ is the momentum of electron i at time t, with m, $\vec{v}_i$, and $\gamma_i \equiv 1/\sqrt{1-\beta_i^2}$ being its rest mass, velocity and Lorentz factor, respectively. $\beta_i \equiv |\vec{\beta}_i|$, $\vec{\beta}_i \equiv \vec{v}_i / c$ and c is the speed of light in vacuum.

According to (5.1), each electron i is subject to four kinds of forces: the force $\vec{F}_i^{\,d}$ exerted by the driving electromagnetic field, the sum of forces $\vec{F}_{i,j}^{\,pp}$ exerted directly by other electrons j, the force $\vec{F}_i^{\,wf}$ exerted by wakefields that result from electromagnetic fields of other electrons reflecting off the waveguide walls, and finally the radiation reaction force $\vec{F}_i^{\,rr}$ that the electron

experiences as a result of its own radiation. In this study, we neglect $\vec{F}_i^{\mathrm{wf}}$ because the relatively short propagation distances and bunch lengths make the effect of wakefields negligible. For acceleration studies involving long propagation distances, or multiple bunches of substantial charge, wakefields should be taken into consideration by implementing formulas derived in previous studies [KHY+10]. We also neglect the radiation reaction force since the employed scheme accelerates the electrons primarily via the longitudinal component of the electric field, with minimal transverse wiggling. Consequently, radiation losses are negligible. Electrodynamic studies in which the radiation reaction force plays a significant role have commonly employed the Landau-Lifshitz formula [LL87] for the force.

The force $\vec{F}_i^{\,d}$ exerted by the driving field on electron i is given by the Lorentz force equation:

$$\vec{F}_i^{\,d}(t) = q\left[\vec{E}_{\mathrm{d}}(t,\vec{r}_i(t)) + \vec{v}_i(t)\times\vec{B}_{\mathrm{d}}(t,\vec{r}_i(t))\right], \tag{5.2}$$

where q is the electron's charge and $\vec{r}_i$ its position. $\vec{E}_d(t,\vec{r})$ and $\vec{B}_d(t,\vec{r})$ are respectively the electric field and magnetic flux density of the driving field. Similarly, we write the force $\vec{F}_{i,j}^{\mathrm{pp}}$ that electron j exerts on electron i as

$$\vec{F}_{\mathrm{pp};i,j}(t) = q\left[\vec{E}_j(t,\vec{r}_i(t)) + \vec{v}_i(t)\times\vec{B}_j(t,\vec{r}_i(t))\right], \tag{5.3}$$

where $\vec{E}_j(t,\vec{r})$ and $\vec{B}_j(t,\vec{r})$ are respectively the electric field and magnetic flux density due to electron j. These fields are derived by solving Maxwell's equations for a moving point charge in vacuum via the Liénerd-Wiechert potentials and the resulting electromagnetic fields are [Jac75]

$$\begin{aligned}
\vec{E}_i(t,\vec{r}) &= \frac{q}{4\pi\varepsilon_0}\frac{1}{\eta_{i,\tilde{t}_i}^3(\vec{r})R_{i,\tilde{t}_i}(\vec{r})}\left\{\frac{\vec{u}_{i,\tilde{t}_i}(\vec{r})}{\gamma_i^2(\tilde{t}_i)R_{i,\tilde{t}_i}(\vec{r})}+\frac{1}{\mathrm{c}}\left[\hat{i}_{i,\tilde{t}_i}(\vec{r})\times\left(\vec{u}_{i,\tilde{t}_i}(\vec{r})\times\frac{\dot{\vec{v}}_i(\tilde{t}_i)}{\mathrm{c}}\right)\right]\right\}, \\
\vec{B}_i(t,\vec{r}) &= \frac{1}{\mathrm{c}}\left(\hat{i}_{i,\tilde{t}_i}(\vec{r})\times\vec{E}_i(t,\vec{r})\right)
\end{aligned} \tag{5.4}$$

where ε_0 is the permittivity of free space, $\dot{\vec{v}}_i$ the acceleration of particle i, $R_{i,t}(\vec{r}) \equiv |\vec{r} - \vec{r}_i(t)|$, $\vec{u}_{i,\tilde{t}_i}(\vec{r}) \equiv \hat{i}_{i,\tilde{t}_i}(\vec{r}) - \vec{v}_i(\tilde{t}_i)/\mathrm{c}$ and $\eta_{i,\tilde{t}_i}(\vec{r}) \equiv \mathrm{d}t/\mathrm{d}\tilde{t}_i = 1 - \hat{i}_{i,\tilde{t}_i}(\vec{r}) \cdot \vec{v}_i(\tilde{t}_i)/\mathrm{c}$. $\tilde{t}_i = \tilde{t}_i(t, \vec{r})$ is the retarded time along particle i's trajectory corresponding to time t and observation point $\vec{r}$. Given t and $\vec{r}$, the retarded time $\tilde{t}_i$ solves the implicit equation

$$\tilde{t}_i = t - \frac{R_{i,\tilde{t}_i}(\vec{r})}{c} . \tag{5.5}$$

If $\vec{F}_i^d$ is the only non-zero term on the right-hand side of (5.1), the equation is simply an ordinary differential equation. With inter-particle interaction described by (5.3) and (5.4), the right-hand side of (5.1) becomes a function of $\tilde{t}_i$ as well as t, and the equation is no longer an ordinary differential equation. Note that (5.4) considers both the velocity field (near-field) and the radiation field (far-field), which are given by the first and second term respectively. If the effect of the radiation field is insignificant and we assume that each particle always travels at its current velocity during each time step, (5.4) can be simplified to a function of only t, making (5.1) an ordinary differential equation and reducing the computation of inter-particle forces considerably. The formulas that should replace (5.4) are then the space-charge formulas obtained by Lorentz-boosting the Coulomb field of each electron from the electron's rest frame to the lab frame. These formulas are used in particle tracer programs like the General Particle Tracer (GPT) [GPT]. A more detailed discussion of (5.4), (5.5) and the GPT space-charge formulation is given in Appendix F.

We chose not to use externally-provided software packages in part to ascertain, by implementing (5.4), the significance of non-uniform motion and electron radiation in inter-particle interaction. It turns out that for the regime investigated in this chapter, the use of the exact formulas in (5.4) affects overall acceleration and bunch compression results negligibly, and for computational efficiency one may simply revert to the Lorentz-boosted Coulomb fields in modeling inter-particle interaction.

We solve (5.1) using a fifth-order Runge-Kutta algorithm with adaptive step-size [PTV+92]. If the exact inter-particle fields (5.4) are used, we adapt the Runge-Kutta algorithm to the problem by maintaining a history of $\vec{r}_i$ and $\vec{p}_i$, i=1,...,N, in a ring buffer. At each time t, cubic spline

interpolation is applied to compute the retarded time (5.5) needed in (5.4). Gaussian-distributions of electrons in 6-dimensional phase space are generated by applying the Box-Muller transformation to the normalized output of the *rand*() function in C, and computations of variance and covariance (required for emittance calculations) are performed using the corrected two-pass algorithm [CGL83]. Multi-core processing capabilities are implemented using OpenMP.

In this study, we are interested in simulating bunches on the order of pCs and tens of pCs, implying that we deal with 10^7 – 10^8 electrons. To speed up the computational process, each particle $i = 1,\ldots,N$ is treated as a macro-particle – with the charge and mass of a large number of electrons – instead of a single electron. We can verify that this approach is a good approximation if the solution converges as the number of macro-particles increases while the total number of electrons is kept constant. We have verified this for all results presented in this chapter.

5.2 The pulsed TM_{01} mode in a dielectric-loaded metallic waveguide

For a general multilayer cylindrical waveguide, we obtain continuous-wave (CW) solutions by solving the Helmholtz equation in cylindrical coordinates:

$$\left(\nabla^2 + k^2\right)\begin{Bmatrix} E_z^{CW} \\ H_z^{CW} \end{Bmatrix} = 0 \quad \Rightarrow \quad \frac{1}{r}\frac{\partial}{\partial r}\left(r\frac{\partial}{\partial r}\begin{Bmatrix} \psi_e \\ \psi_h \end{Bmatrix}\right) + \left(k^2 - \kappa^2 - \frac{l^2}{r^2}\right)\begin{Bmatrix} \psi_e \\ \psi_h \end{Bmatrix} = 0, \tag{5.6}$$

where $k \equiv \omega/c = 2\pi/\lambda$, ω being angular frequency, c the speed of light in vacuum and λ the vacuum wavelength. $E_z^{CW} \equiv \psi_e(r)\cdot\exp(i(\omega t - \kappa z \pm l\phi))$ and $H_z^{CW} \equiv \psi_h(r)\cdot\exp(i(\omega t - \kappa z \pm l\phi))$ are the complex CW longitudinal electric and magnetic fields respectively, κ is the propagation constant, r the radial coordinate, ϕ the azimuthal coordinate, z the direction of propagation along the waveguide, and l a non-negative integer that determines the order of azimuthal variation. According to (5.6), a general solution for ψ_e in layer i of an n-layer cylindrical waveguide (the core counts as layer 1) is

$$\psi_{e,i}(r) = A_{e,i}J_l(h_i r) + B_{e,i}Y_l(h_i r),\ r_{i-1} \le r < r_i,\ i = 1,\ldots,n, \tag{5.7}$$

where $r_0 \equiv 0$, $r_n \equiv \infty$, and r_i for $0 < i < n$ is the radial position of the boundary between layers i and i+1. J_l and Y_l are Bessel functions of the first and second kind respectively, $A_{e;i}$ and $B_{e;i}$ are constant complex coefficients within each layer and $h_i \equiv (\varepsilon_{r;i}(\lambda)\mu_{r;i}(\lambda)k^2 - \kappa^2)^{1/2}$, $\varepsilon_{r;i}$ and $\mu_{r;i}$ being the dispersive relative permittivity and permeability respectively of the dielectric in layer i. The general solution for $\psi_{h;i}$ is identical in form to (5.7) except that "e" should be replaced by "h" in all subscripts. In the core, it is usually expedient to express (5.7) using the modified Bessel function of the first kind I_l, whereas in the final layer (which extends to infinity), it is usually expedient to express (5.7) using either the modified Bessel function of the second kind K_l for confined modes or the Hankel function of the second kind $H_l^{(2)}$ for leaky modes. These functions are all exactly represented by (5.7) if we allow the coefficients and arguments of J_l and K_l to take on complex values.

The transverse electromagnetic fields are obtained from the expressions for E_z and H_z via Ampere's law and Faraday's law. By matching boundary conditions among adjacent dielectric layers (continuity of E_z, H_z, E_ϕ, H_ϕ), as mathematically described in [YYM78] for the Bragg fiber, we obtain a characteristic matrix which has a non-trivial nullspace (zero determinant) if and only if a solution to (5.6) exists. Given l, along with the dimensions and dielectric properties of the waveguide layers, we determine numerically the set of values $\{k, \kappa\}$ for which the characteristic matrix has a zero determinant. This set of values $\{k, \kappa\}$ constitute the dispersion curves of the waveguide for a mode of azimuthal order l, and the $4n$ coefficients $A_{e;i}$, $B_{e;i}$, $A_{h;i}$ and $B_{h;i}$, i=1,...,n, are the components of a $4n$-long vector in the corresponding nullspace. The real-valued z-directed electric field $E_{z;i}$ of a pulse in any layer i is constructed by an inverse Fourier transform:

$$E_{z;i}(l,t,r,z,\phi) = \mathrm{Re}\left\{\int_{-\infty}^{\infty} F(\omega)E_{z;i}^{\mathrm{CW}}(l,\omega,t,r,z,\phi)\mathrm{d}\omega\right\} \quad r_{i-1} \le r < r_i, \; i = 1,\ldots,n, \tag{5.8}$$

where $F(\omega)$ is the complex envelope in the frequency domain. The same inverse Fourier transform is also applied to the other field components to obtain their real-valued pulsed versions.

The structure we consider in this chapter is a vacuum core with a single layer of dielectric of relative permittivity ε_r = 5.5 (a candidate for such a dielectric is diamond [Kub09]) with an external copper coating. The spatial mode of interest is the TM_{01} mode (i.e. l = 0 and radial

variation is of the lowest order), for which only the E_z, E_r and H_ϕ field components exist. The E_z field peaks on axis whereas the transverse fields vanish, so an electron bunch concentrated at the waveguide axis will experience forces mainly along the direction of propagation. This facilitates longitudinal compression and acceleration of the bunch without significant transversal wiggling, which is undesirable since it tends to increase radiative losses.

To excite the TM01 mode of the cylindrical waveguide, it would be necessary to apply a radially-polarized (preferably TM01) beam to the waveguide. Studies on coupling linearly-polarized THz pulses into cylindrical metal waveguides show that the dominant modes excited are the TE11, TE12 and TM11 modes [GJM+00], so a linearly-polarized incoming beam is unlikely to serve our purpose. Although THz pulses generated by optical rectification are typically linearly-polarized, the direct generation of radially-polarized THz pulses has been demonstrated [CDL+07, WZP+09]. Alternatively, a scheme to convert linearly-polarized THz pulses into radially-polarized pulses may be adopted [GBA+08].

Equation (5.8) provides a rigorous way to compute the electromagnetic field at any point in space and time required for an electrodynamic simulation. However, performing a summation over a large number of frequency components at every time step for every macro-particle is computationally expensive. To obtain an analytical approximation for more efficient numerical simulation, notice that in the vacuum-filled core, the CW TM_{01} mode is of the form:

$$\begin{aligned} E_{z,1}^{CW} &= A_{e;1} \mathrm{I}_0(q_1 r) \mathrm{e}^{\mathrm{i}(\omega t - \kappa z)} \\ E_{r,1}^{CW} &= A_{e;1} \frac{\mathrm{i}\kappa}{q_1} \mathrm{I}_1(q_1 r) \mathrm{e}^{\mathrm{i}(\omega t - \kappa z)} \\ H_{\varphi,1}^{CW} &= \frac{k}{\eta_0 \kappa} E_{r,1}^{CW}, \end{aligned} \tag{5.9}$$

where $q_i \equiv (\kappa^2 - \varepsilon_{r;i}(\lambda)\mu_{r;i}(\lambda)k^2)^{1/2}$ is the radial wavevector and η_0 is the vacuum impedance. We need to make three more assumptions in the remainder of the formulation: Firstly, variations in propagation constant κ across the spectrum are small enough that their effects on magnitude can be ignored. Secondly, variations in κ are negligible above the second order. Thirdly, the imaginary part of $\kappa(\omega)$ is negligible beyond its 0^{th} order term, and the quadrature term produced by this imaginary part in E_r does not contribute significantly to the field. Hence, Taylor-

expanding $\kappa(\omega)$ about central angular frequency ω_0 we have $\kappa(\omega_0 + \Delta\omega) \approx \kappa_0 - i\alpha + \kappa_1\Delta\omega + \kappa_2(\Delta\omega)^2/2$, where κ_i denotes the real part of the i^{th} derivative of $\kappa(\omega)$ with respect to ω at $\omega = \omega_0$. $\alpha > 0$ to be physically valid and represents field attenuation per unit distance.

To obtain the approximate analytical field solution, the rightmost expressions of (5.9) should be inserted into (5.8). Assuming a transform-limited Gaussian pulse at $z = 0$, we have $E_z(z = 0, t) \sim \exp(-(t/T_0)^2/2)\exp(i\omega_0 t)$, where $\omega_0 \equiv k_0 c$ is the central frequency and T_0 is the half-width at 1/e intensity, related to the full-width-at-half-maximum (FWHM) intensity T_{FWHM} as $T_{FWHM} = 2(\ln 2)^{1/2} T_0 \approx 1.665\, T_0$. This is related to the spectral FWHM intensity width $\Delta\omega_{FWHM}$ as $\Delta\omega_{FWHM} = 4\ln 2/T_{FWHM}$. Finally, we have

$$\begin{aligned} E_{z;1}(t,z) &\approx \mathrm{Re}\left\{ I_0(q_{1,0}r) e^{i(\omega_0 t - \kappa_0 z)} \int_{-\infty}^{\infty} A_0 e^{-\frac{(\Delta\omega T_0)^2}{2}} e^{-i\left(\kappa_1\Delta\omega + \frac{\kappa_2}{2}(\Delta\omega)^2\right)z} e^{i\Delta\omega t} d\Delta\omega \right\} \\ &= \frac{|E_{z0}| I_0(q_{1,0}r)}{\left[1 + \left(\kappa_2 z / T_0^{\,2}\right)^2\right]^{1/4}} e^{-\frac{(t-\kappa_1(z-z_i))^2}{2T_0^{\,2}\left[1+\left(\kappa_2 z/T_0^{\,2}\right)^2\right]}} e^{-\alpha(z-z_s)} \cos(\psi_T), \quad z \geq z_s \end{aligned} \tag{5.10}$$

where A_0 is an arbitrary complex constant which role is replaced in the second line of (5.10) by $|E_{z0}|$, which represents the amplitude of the longitudinal field at $t = 0$ and $z = z_i = z_s$, with z_i being the initial position of the pulse peak. $q_{1,0}$ is q_1 evaluated at ω_0. z_s is the position of the start of the waveguide, where pulse attenuation begins, and before which (5.10) does not apply. Note that setting $z_s \neq 0$ implies that some special pulse, not transform-limited, is being coupled into the waveguide. We set $z_s = 0$ for all simulations in this chapter. The carrier phase ψ_T is given by

$$\psi_T = \omega_0 t - \kappa_0 z + \frac{(t - \kappa_1(z - z_i))^2 \kappa_2 z / T_0^{\,2}}{2T_0^{\,2}\left[1 + \left(\kappa_2 z / T_0^{\,2}\right)^2\right]} - \mathrm{atan}\left(\frac{\kappa_2 z}{T_0^{\,2}}\right) + \psi_0, \tag{5.11}$$

where ψ_0 is a real phase constant. The corresponding E_z, E_r and H_ϕ fields are approximated as

$$E_{r;1}(t,r,z) \approx -\frac{\kappa_0}{q_{1,0}} \frac{I_1(q_{1,0}r)}{I_0(q_{1,0}r)} E_{z;1}(t,z) \tan(\psi_T), \quad H_{\varphi;1}(t,r,z) \approx \frac{k_0 E_{r;1}(t,r,z)}{\kappa_0 \eta_0}. \tag{5.12}$$

where $k_0 \equiv \omega_0/c$. Essentially, (5.10) and (5.12) furnish an approximate analytical description of a TM_{01} pulse moving with an approximate phase velocity and group velocity of $v_{ph} = \omega_0/\kappa_0$ and $v_g = 1/\kappa_1$ respectively in the vacuum core of a cylindrical waveguide. If $z_s = 0$, the pulse at the start of the waveguide ($z = z_s = 0$) is a transform-limited pulse with a peak longitudinal electrical amplitude of $|E_{z0}|$. The primary reason for introducing z_i in our formulas is to control when the pulse arrives at the start of the waveguide without having to compromise the intuitive convention of having t = 0 as the initial time (when the simulation begins and the initial electron bunch starts evolving according to (5.1)).

5.3 Acceleration of 1.6 pC electron bunches

5.3.1 Optimization procedure and acceleration results

In this section, we optimize the dielectric-loaded metal waveguide for electron bunch acceleration and perform a rudimentary thermal damage and dielectric breakdown analysis to verify the realism of the scheme. We numerically demonstrate the acceleration of a 1.6 pC electron bunch from a kinetic energy of 1 MeV to one of 10 MeV, using a 20mJ 10-cycle pulse centered at 0.6 THz. Note that for a 10-cycle pulse, $\Delta\omega_{FWHM}/\omega_0 = 4\ln 2/(\omega_0 T_{FWHM}) = 4\ln 2/(2\pi 10) = 4.41\%$. As will be seen in the results, some longitudinal compression is also inadvertently achieved in the process.

Optimizing the dielectric-loaded metallic waveguide for bunch acceleration involves adjusting a large number of parameters, including operating frequency, choice of waveguide mode, waveguide dimensions, laser pulse energy and pulse duration, the type of dielectric, the type of external conductor and initial electron bunch properties. To make this optimization tractable, we fix all parameters in advance based on the available technology except for three degrees of freedom: *i*) the carrier-envelope phase ψ_0, *ii*) the initial position of the pulse z_i (with initial position of electron fixed at $z = 0$), and *iii*) the radius of the vacuum core r_1. In particular, we fix the phase velocity at $v_{ph} = c$ and the center frequency at $f_0 = 0.6$ THz, which limits the dielectric thickness d to specific values depending on r_1. However, because acceleration results can be very

sensitive to small variations in the value of v_{ph}, we take the liberty of treating v_{ph} as an optimization parameter (but ensuring that $v_{ph} \approx c$) *after* using $v_{ph} = c$ to determine properties of the TM_{01} waveguide mode. Therefore, four degrees of freedom are ultimately considered. In practice, after the waveguide has been fabricated according to the optimal specifications, the operating frequency should be perturbed to vary the phase velocity until maximum electron acceleration is achieved. As long as the perturbation is small, the waveguide properties should be very close to those determined for $v_{ph} = c$ and $f_0 = 0.6$ THz. The electron acceleration process is much more sensitive to small variations in v_{ph} than to small variations in any other parameter caused by perturbing the operating frequency alone.

Fig. 5-2(a) shows a color map of the operation frequency as a function of r_1 and d. As noted before, we define the operation frequency as the frequency of the TM_{01} mode in the waveguide corresponding to $v_{ph} = c$. Fig. 5-2(b) shows a color map of the final electron kinetic energy of a single electron of initial kinetic energy 1 MeV, optimized over ψ_0, z_i and v_{ph} (ensuring that $v_{ph} \approx c$), as a function of r_1 and d. We see that greater electron acceleration is generally achieved at higher operation frequencies. However, choosing a very small wavelength makes it challenging to accelerate a large number of electrons due to smaller waveguide dimensions. As pointed out previously, the emergence of promising techniques to generate radiation in the vicinity of 0.6 THz [FPA+10] encourages us to make that choice of frequency, which has been marked out by the black contour line in Fig. 5-2(a). The same line is drawn in Fig. 5-2(b), and the optimized final kinetic energy, read along that line, is reproduced in Fig. 5-2(c), where an optimal choice of $d = 32$ μm, corresponding to a vacuum core radius of $r_1 = 380$μm, is evident. In Fig. 5-2(d), we plot the dispersion curves corresponding to the waveguide with $d = 32$ μm, $r_1 = 380$ μm, to show that at the operating frequency, the TM_{01} dispersion curve of our waveguide design is sufficiently linear within the 4.41% intensity FWHM spectral bandwidth. Hence, the electromagnetic fields are well approximated using (5.10) and (5.12).

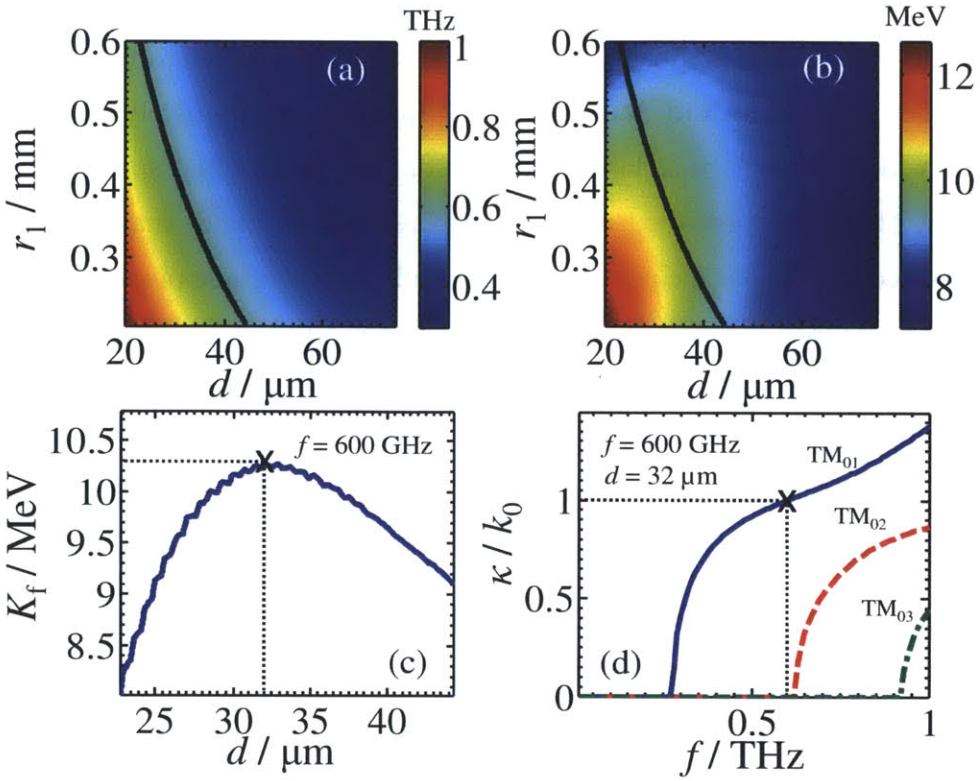

Fig. 5-2: Determination of the optimal waveguide for electron acceleration: (a) Color map of operation frequency as a function of core radius r_1 and dielectric thickness d, (b) Color map of final kinetic energy of a single electron of initial kinetic energy 1 MeV, optimized over ψ_0 and z_i, as a function of r_1 and d. The black line in (a) and (b) correspond to an operation frequency of 0.6 THz. The value of the color map in (b) along the 0.6 THz operation line is plotted in (c), where the optimum value of d is identified as d = 32 μm. (d) The dispersion curves corresponding to the final waveguide design.

The parameters of the final waveguide design are d = 32 μm, r_1 = 380 μm, v_{ph} = 0.99c, v_g = 0.7c, α = 5.21 m^{-1}, T_{FWHM} = 16.7ps, $\kappa_2 = 4.54\times10^{-22}$ s^2/m. The 20 mJ pulse yields a $|E_{z0}|$ of about 0.9GV/m. The initial parameters of the 1.6 pC, 1 MeV electron bunch with which we will demonstrate the acceleration are $\sigma_x = \sigma_y = \sigma_z$ = 30μm (a 100fs bunch) , $\sigma_{\gamma\beta x} = \sigma_{\gamma\beta y} = \sigma_{\gamma\beta z}$ = 0.006, where $\sigma_{\gamma\beta x}$, for instance, denotes the standard deviation of $\gamma\beta_x$. 10000 macro-particles, Gaussian-distributed in every dimension of phase space, were employed in the simulation.

Fig. 5-3 shows the evolution of bunch parameters as a function of mean particle position. We see from Fig. 5-3(a) that the 1.6 pC-bunch is accelerated from 1 MeV to 10 MeV of kinetic

energy in about 20mm, without any of its other properties deteriorating prohibitively. The corresponding average acceleration gradient is about 450 MeV/m. Note from Fig. 5-3(b)-(d) that, depending on the extraction point, the final bunch can possess a smaller transverse and longitudinal spread compared to the initial distribution, but the final energy spread is degraded from the initial spread.

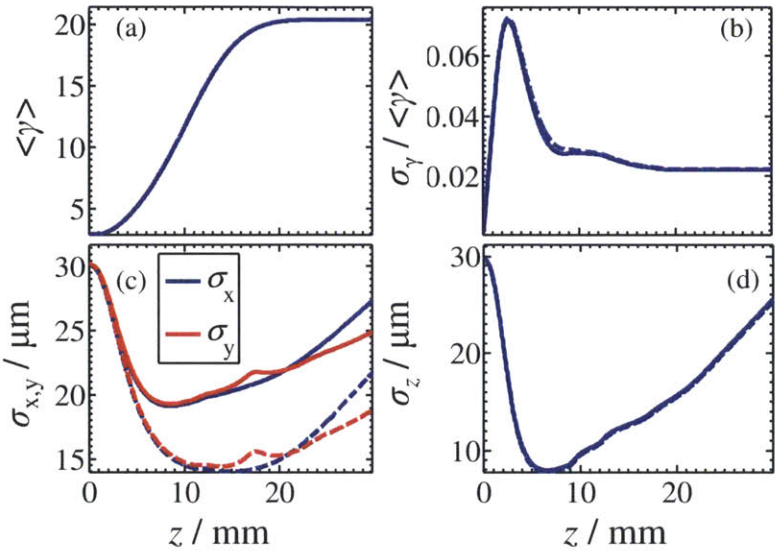

Fig. 5-3: Evolution of bunch parameters with mean bunch position for acceleration of a 1.6 pC electron bunch from 1 MeV to 10 MeV (kinetic energy) in about 20mm: (a) normalized mean energy, (b) relative energy spread, (c) transverse spread and (d) longitudinal spread. The symbol σ stands for the standard deviation of the variable in the subscript. Solid and dashed lines correspond to simulations with and without space charge respectively. 10000 macro-particles are used for the simulations. $\psi_0 = 1.34\pi$ and $k_0 z_i = 10.96\pi$. A 20 mJ, 10-cycle (16.7 ps), 0.6 THz-centered pulse is considered.

5.3.2 Injection point considerations

In our analysis, we have assumed the freedom to inject the electron bunch into any point of the electromagnetic field. According to our computations, the optimum injection point for the electron bunch is a point within the pulse (albeit in its tail). This may be challenging to realize if both the electron bunch and the electromagnetic pulse enter the waveguide from vacuum. The

objective of this section is to consider injection of the electron bunch at a point with negligible electric field values and assess the amount by which our predictions would change. The optimum THz waveguide for this case is a waveguide with r_1 = 338 μm and d = 33 μm. In addition, v_{ph} = 0.981c, $\psi_0 = 1.49\pi$, k_{0z_i} = 137.73. We ensure that the electric field's amplitude at the injection point is negligible by making the amplitude $7.4\times10^{-15}|E_{z0}|$. The evolution of the electron bunch is shown in Fig. 5-4, where we observe a final kinetic energy of 8.4 MeV (instead of the 9MeV observed before). The smaller energy gain in this case is partly due to the dispersion and attenuation that the pulse suffers from before the injected bunch begins interacting with the pulse. A final energy close to what is predicted in the previous section should therefore be achievable if the electron bunch and THz pulse can interact before the pulse has travelled too far along the waveguide.

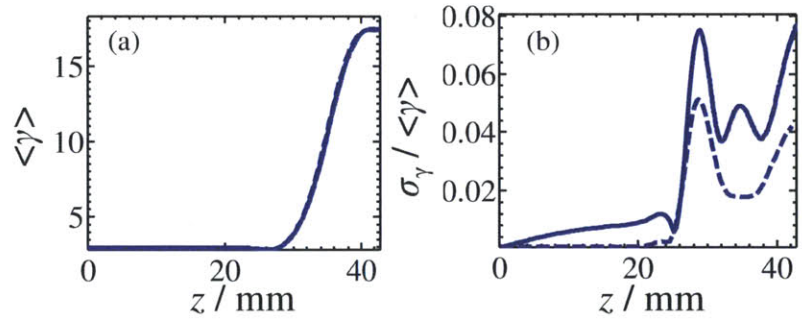

Fig. 5-4: Evolution of bunch parameters with mean bunch position for acceleration of a 1.6 pC electron injected at a distant point from the THz pulse peak: (a) normalized mean energy, (b) relative energy spread. Solid and dashed lines correspond to simulations with and without space charge respectively. 10000 macro-particles were used for the simulations.

5.3.3 Thermal damage and dielectric breakdown considerations

In this section, we assess the feasibility of the scheme from Section 4.1 in terms of its thermal damage and dielectric breakdown prospects. One concern is that the high energy injected into the waveguide and consequent energy dissipation would raise temperature of the copper coating beyond its melting point. Another concern is dielectric breakdown due to the high electric field values in the dielectric.

The energy dG transferred to a differential segment of copper at position z ($z = 0$ being the start of the waveguide) is related to the associated temperature rise $\Delta\theta = \theta - \theta_0$ as

$$\mathrm{d}G = \mathrm{d}m_{\mathrm{Cu}} C \Delta\theta . \tag{5.13}$$

The differential mass $\mathrm{d}m_{\mathrm{Cu}} = \rho_{\mathrm{Cu}}(2\pi r_2 \delta_{\mathrm{s}})\mathrm{d}z$, where ρ_{Cu} is the density of copper and δ_{s} is the skin depth. θ_0 is the original temperature of the copper and C its specific heat capacity. Ignoring dispersion for simplicity (and because it is negligibly small here), we write the power propagating down the waveguide, averaged over the rapid carrier fluctuations, as

$$P(t,z) \approx P_0 \mathrm{e}^{-\frac{(t-\kappa_1(z-z_i))^2}{T_0^2}} \mathrm{e}^{-2\alpha z}, \quad z \geq 0, \tag{5.14}$$

where P_0 is the average power that flows into the start of the waveguide when the pulse peak arrives there. Noting that $P = -\mathrm{d}G/\mathrm{d}t$ and that partial derivatives are relevant here because z and t are independent coordinates, (5.13) can be written as

$$-\frac{\partial P(t,z)}{\partial z} \approx \rho_{\mathrm{Cu}} 2\pi r_2 \delta_{\mathrm{s}} C \frac{\partial \theta(t,z)}{\partial t}. \tag{5.15}$$

Solving (5.15) for θ gives us

$$\theta(t,z) \approx \theta_0 - \frac{P_0 e^{-2\alpha z}}{\rho_{\mathrm{Cu}} \pi r_2 \delta_{\mathrm{s}} C} \int_{-\infty}^{t} \left(\frac{\kappa_1 t}{T_0^2} - \alpha \right) e^{-\left(\frac{t}{T_0}\right)^2} dt. \tag{5.16}$$

$\theta(\infty,z) - \theta_0$ gives the net temperature rise after the pulse has passed entirely through point z:

$$\theta(\infty,z) - \theta_0 \approx \frac{P_0 \alpha T_0}{\rho_{\mathrm{Cu}} \sqrt{\pi} r_2 \delta_{\mathrm{s}} C} e^{-2\alpha z}. \tag{5.17}$$

$\theta(\infty,z)$ is plotted in Fig. 5-5(a) for $\theta_0 = 27\ ^0$C. The relevant parameters for copper at 0.6 THz are $\rho_{Cu} = 8940$ kg/m^3, C = 385 J/kg/^{0}C and $\delta_s = 0.084$ μm.

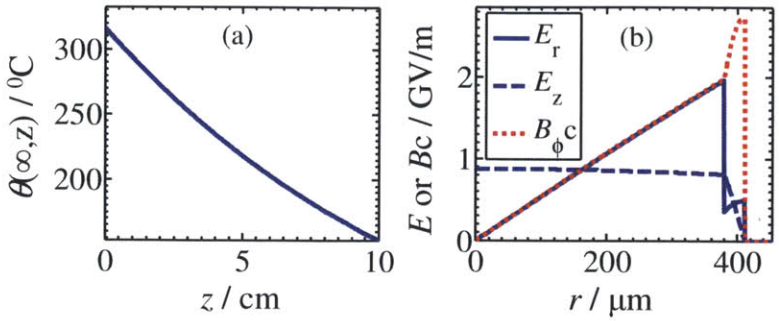

Fig. 5-5: Plots used to assess thermal damage and dielectric breakdown prospects for the scheme in Section 4.1. (a) Final temperature of copper cladding assuming initial temperature of 27 ^{0}C (z = 0 is the start of the waveguide), and (b) Field profile of the TM_{01} mode in the transverse direction of the cylindrical waveguide under study. Discontinuities occur at material boundaries (once at the vacuum-diamond interface and again at the diamond-copper interface).

From the values in Fig. 5-5(a), the fact that the melting point of copper is 1084 ^{0}C and also that we have even neglected the conductivity of copper, we can conclude that the metal coating in the designed waveguide withstands the passage of the pulse without melting.

Fig. 5-5(b) shows a typical profile of the electromagnetic amplitude of a mode in the transverse direction of the waveguide. The breakdown electric field for diamond has been reported as 10-20 MV/cm, depending on impurities. Reading off the plot we note that the maximum value of the electric field in the dielectric region is about 8 MV/cm. This is close to the breakdown limit though still under it, showing that it would not be feasible to enhance the performance of our design by increasing the peak power of the accelerating pulse. Since we are relatively far from the melting point, an increase in available pulse energy should be used to increase pulse duration instead of peak power.

5.4 Acceleration of 16 pC and 160 pC electron bunches

In this section, we explore the acceleration of electron bunches of greater charge. We see that it is feasible to use the dielectric-loaded metallic waveguide to accelerate electron bunches as large as 16 pC, but that this is not possible when the charge increases to 160 pC. All other bunch properties (including an initial kinetic energy of 1 MeV) remain the same from Section 4.1. We use a 20 mJ, 10-cycle, 0.6 THz-centered pulse, and the same optimized waveguide and injection conditions as in Section 4.1. Fig. 5-6 shows the evolution of the electron bunch for 1.6 pC, 16 pC and 160 pC-bunches. The effects of space charge are included in all computations.

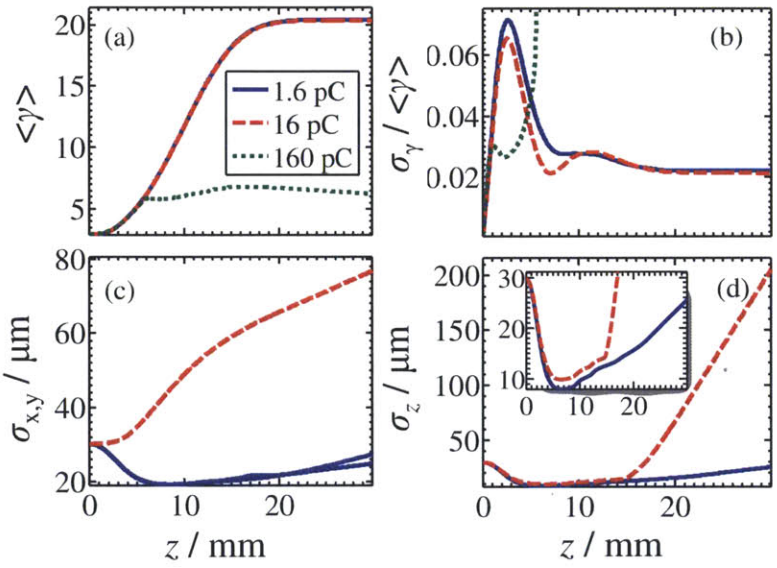

Fig. 5-6: Evolution of bunch parameters with mean bunch position for optimized acceleration of 1.6 pC, 16 pC and 160 pC electron bunches: (a) normalized mean energy, (b) relative energy spread, (c) transverse spread and (d) longitudinal spread. Using a 160 pC is not feasible and is shown only in (a) and (b). All results include space charge. 10000 macro-particles are used for all simulations. $\psi_0 = 1.34\pi$ and $k_0 z_i = 10.96\pi$. A 20 mJ, 10-cycle (16.7 ps), 0.6 THz-centered pulse is used in all cases.

From Fig. 5-6(a) and (b), we observe that there is little difference in the mean kinetic energy and energy spread evolution of a 16 pC-bunch and a 1.6 pC-bunch. The energy spread of a

160pC-bunch, however, deteriorates prohibitively and the bunch is not significantly accelerated. Since this rules out the feasibility of accelerating a 160 pC-bunch, we have omitted its plots from Fig. 5-6(c) and (d). The inability of the waveguide to accelerate a 160 pC-bunch is due to the overriding strength of the Coulomb repulsion, driving the electrons into the walls of the waveguide before significant acceleration takes place. Fig. 5-6(c) explains how the 1.6 pC and 16 pC-bunches are able to have such similar energy and energy spread profiles during the acceleration: the greater Coulomb repulsion in the 16 pC Coulomb is counter-balanced by larger transverse inter-particle spacing. Fig. 5-6(d) shows that due to the larger amount of space charge, the 16 pC expands rather rapidly compared to the 1.6 pC-bunch after the pulse has slipped behind the bunch, so a 16 pC-bunch accelerated via this scheme is likely to be useful for a shorter duration after being fully accelerated.

5.5 Concurrent phase-limited compression and acceleration of 1.6pC bunches

In this section, we optimize our waveguide design for simultaneous acceleration and bunch compression. We demonstrate phase-limited (longitudinal) bunch compression of 50 and 62 times for electron bunches of initial kinetic energy 1 MeV and 10 MeV respectively. By "phase-limited" we mean that the maximum compression results do not change substantially when space charge is removed from the simulations.

As in previous sections, we use a 20 mJ, 0.6 THz-centered pulse. For each case (the 1 MeV case and the 10 MeV case), the waveguide and injection conditions are optimized exactly as described in Section 4.1, except that in addition to ψ_0, z_i, r_1, and v_{ph}, we also optimize over pulse duration T_{FWHM} (keeping total energy constant at 20 mJ), for a total of five optimization parameters. The initial conditions of the electron bunch, unless otherwise specified, are the same as those in Section 4.1.

To optimize for simultaneous acceleration and compression, the figure-of-merit found to be most useful is the ratio of energy to bunch-length of the electron bunch. Unlike in Section 4.1, where we optimized using a single particle, here we optimized using 100 macro-particles and

included the effects of space charge. The optimized results are then verified with simulations that use10000 macro-particles.

For the 1MeV case, our optimized parameters are $\psi_0 = 0.73\pi$, $k_0 z_i = 13.3\pi$, $r_l = 447$ μm, $T_{FWHM} = 13.1$ ps (7.86 cycles). The evolution of the electron bunch parameters under these optimal conditions are presented in Figs. 5.7(a)-(c), where we observe a small net acceleration and a phase-limited compression of the electron bunch from 100 fs (30 μm) to about 2 fs over an interaction distance of about 18 mm. Note that there is a limited time window during which the electron bunch remains maximally compressed. Conceptually, this is unavoidable due to the presence of space charge which causes the bunch to expand after the bunch has slipped from the laser pulse.

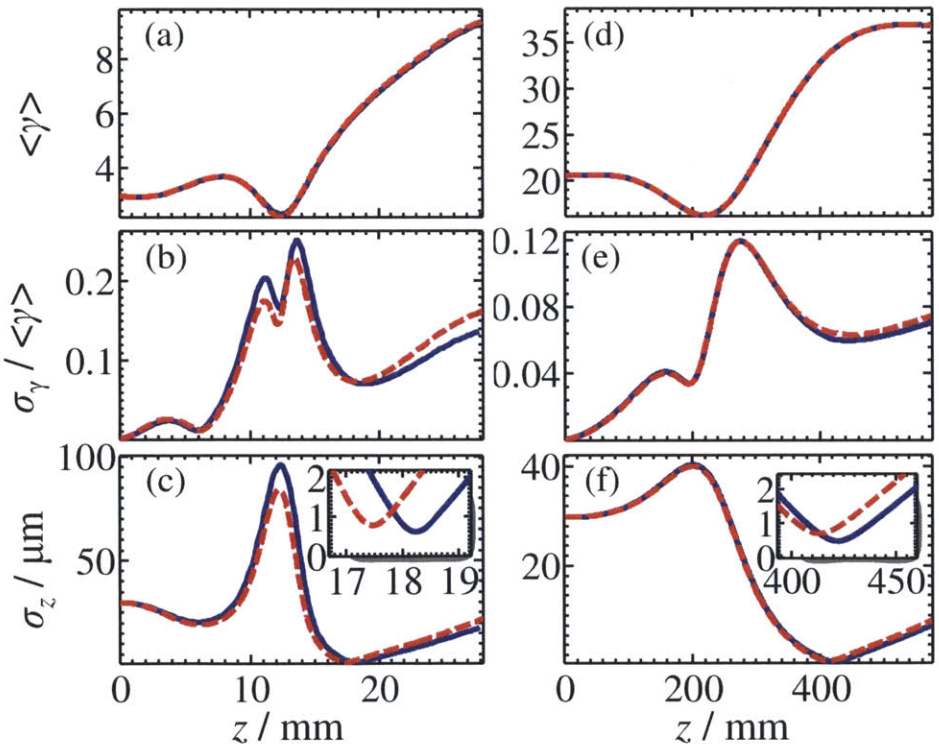

Fig. 5-7: Concurrent compression and acceleration of a 1.6 pC electron bunch under optimized conditions, with a compression factor of 50 and 62 achieved for initial kinetic energies of 1 MeV and 10 MeV respectively. The evolution of (a) normalized mean energy, (b) relative energy spread and (c) longitudinal spread are shown for a 1 MeV bunch subjected to a 20 mJ, 7.86-cycle (13.1ps), 0.6 THz-centered pulse ($\psi_0 = 0.73\pi$ and $k_0 z_i = 13.3\pi$). Similarly, the evolution of (e)

normalized mean energy, (f) relative energy spread and (g) longitudinal spread are shown for a 10MeV bunch subjected to a 20 mJ, 102.3-cycle (170.5 ps), 0.6 THz-centered pulse ($\psi_0 = 1.02\pi$ and $k_{0z_i} = 206\pi$). Blue solid curves and red dashed curves indicate simulations with and without space charge respectively. 10000 macro-particles were used for all simulations.

For the 10 MeV case, our optimized parameters are $\psi_0 = 1.02\pi$, $k_{0z_i} = 206\pi$, $r_i = 597$ μm, $T_{FWHM} = 170.5$ps (102.3-cycle). The evolution of the electron bunch parameters under these optimal conditions are presented in Figs. 7(d)-(f), where we observe a phase-limited compression of the electron bunch from 100 fs to 1.61fs over an interaction distance of 42 cm. Although the bunch is compressed by a slightly larger factor than in the 1 MeV case, the much larger interaction distance suggests that the superior strategy to obtain a high energy, compressed bunch is to compress it before acceleration.

5.6 Summary and future work

Achieving an efficient, practical compact accelerator for electron bunches of substantial charge will likely involve a tradeoff between the large wavelengths but low acceleration gradient of RF accelerators, and the high acceleration gradient but small wavelengths available at optical frequencies. The trade-off between acceleration gradient and wavelength, together with the emergence of efficient methods to generate coherent pulses at THz frequencies, make electron acceleration at THz frequencies a promising candidate for the substantial acceleration and compression of pico-Coulomb electron bunches. In this chapter, we numerically demonstrated the acceleration of a 1.6 pC electron bunch from a kinetic energy of 1 MeV to one of 10 MeV over an interaction distance of about 20 mm, using a 20 mJ pulse centered at 0.6 THz in a dielectric-loaded metallic waveguide. We have also analyzed the implications of using an arbitrarily distant injection point, as well as the prospects of dielectric breakdown and thermal damage for our optimized design.

In addition, we investigated the acceleration of 16 pC and 160 pC 1 MeV electron bunches, observing that performance does not change significantly for a 16 pC-bunch, but deteriorates prohibitively for a 160pC-bunch due to the overwhelming Coulomb repulsion. Finally, we optimized the dielectric-loaded metal waveguide design for simultaneous acceleration and bunch

compression, achieving a 50 times (100 fs 1.6 pC electron bunch compressed to 2 fs over an interaction distance of about 18mm) and 62 times (100 fs to 1.61 fs over an interaction distance of 42 cm) compression for a 1 MeV and 10 MeV electron bunch respectively. These results were achieved with a 20 mJ laser pulse centered at 0.6 THz, and encourage the exploration of THz-laser-driven electron acceleration as a path to compact electron acceleration and bunch compression schemes.

Future work includes research on ways to minimize the growth of the energy spread at the points of maximum compression in Fig. 5-7. Possible solutions include the use of chirped or ellipsoidal electron bunches [LVL+04]. The severity of the mismatch between the group velocity of the terahertz pulse and the speed of the electron also encourages the exploration of terahertz acceleration and bunch compression schemes in vacuum.

Chapter 6

Coherent nonlinear Thomson scattering of compressed electron bunches

In the previous chapters, we studied the acceleration and compression of electrons by coherent laser pulses. Since a major application of relativistic, compressed electron bunches is the generation of coherent x-rays, we now proceed to investigate the coherent nonlinear Thomson scattering (or low-energy inverse Compton scattering, as it is sometimes referred to in the literature) of electron bunches by a pulsed linearly-polarized optical laser beam in vacuum. Most numerical studies on the nonlinear Thomson scattering of multi-particle electron bunches have used a plane wave or a focused beam satisfying the paraxial wave equation to model the laser pulse. Here, we study both a plane wave model as well as one that exactly solves the Maxwell equations (see Appendix E). As pointed out in Section 3.1 and Appendix E, the paraxial Gaussian beam that is often used as a solution to the paraxial wave equation grossly violates the paraxial wave approximation at certain points in space regardless of beam waist width, making its validity in modeling off-axis particle electrodynamics questionable. Electrodynamic simulations comparing the results using the paraxial Gaussian beam to those using an exact solution of the Maxwell equations have also been performed, showing a large discrepancy in off-axis electrodynamics between the two cases even for a weakly-focused laser beam [MVP13].

In this chapter, we present the classical theory of nonlinear Thomson scattering, discuss an optimization scheme based on the approximate analytical formula for the on-axis intensity spectrum of nonlinear Thomson scattering, and study the results of scattering an optical laser pulse off an electron bunch under different degrees of laser focusing. The incident pulse we use is a 1 μm, 10-cycle pulse with a peak power of 0.55 TW. In each case, we compare the results obtained using the exact pulse solution with those obtained using an ideal pulsed plane wave of the same normalized vector potential a_0. Our purpose is threefold: Firstly, we want to investigate how the radiation spectrum changes and the on-axis brightness scales with increasing focusing; Secondly, we want to determine how the planar pulse and exact pulse results diverge as focusing increases; Thirdly, we are also interested in how the scattering pulse affects the electron bunch itself at different degrees of focusing. The effects of space charge is included in all our simulations. All numerical simulations are performed using code written in the C programming language, with multi-core processing capabilities enabled via OpenMP. Benchmarks for our code based on analytical theory are presented in Section 6.2.5.

6.1 Theory of multi-particle radiation

6.1.1 Radiation from a single particle

The electromagnetic fields in the time domain, namely (5.4), are useful for modeling particle-particle interaction in classical electrodynamic simulations. When the radiation of a particle bunch is important as an output of a system, it becomes relevant also to study the fields in the frequency domain. As the observation position becomes increasingly distant from the radiating particle, the near-fields (proportional to $1/R^2$) become increasingly insignificant relative to the far-fields (proportional to $1/R$). If our detector is sufficiently distant, we may ignore the near-fields in (5.4) and write the electromagnetic radiation of a single particle as

$$\begin{aligned} \vec{E} &= \frac{q}{4\pi\varepsilon_0 \mathrm{c}} \frac{1}{\eta'^3 R'} \left[\hat{i}' \times \left(\left(\hat{i}' - \frac{\vec{v}'}{c} \right) \times \frac{\dot{\vec{v}}'}{\mathrm{c}} \right) \right], \\ \vec{B} &= \frac{1}{\mathrm{c}} \hat{i}' \times \vec{E} \end{aligned} \tag{6.1}$$

where we have removed the functional dependencies to avoid clutter. A prime on a variable indicates that it is evaluated using physical quantities of the radiating particle at the retarded time. The magnetic field is always perpendicular to the electric field and power flows in the direction $\hat{i}'$, the unit vector pointing from the retarded position of the particle towards the observation point. Specifically, the radiated intensity has the form

$$\vec{S} = \vec{E} \times \frac{\vec{B}}{\mu_0} = \hat{i}' \frac{1}{\mu_0 c} \left| \vec{E} \right|^2 , \tag{6.2}$$

where μ_0 is the permeability of free space. The total radiated energy is

$$\begin{aligned} U &= \iint \left(\hat{i}' \cdot \vec{S} \right) R'^2 dt d\Omega \\ &= \frac{1}{\varepsilon_0 c} \left(\frac{q}{4\pi} \right)^2 \iint \frac{1}{\eta'^6} \hat{i}' \times \left(\left(\hat{i}' - \frac{\vec{v}'}{c} \right) \times \frac{\dot{\vec{v}}'}{c} \right) dt d\Omega \end{aligned} , \tag{6.3}$$

where the inner integral integrates over all present time, and the outer integral integrates over the entire solid angle. The correct variable of integration for the inner integral is t, not retarded time t', because $\vec{S}$ is the energy radiated per unit area per unit *present* (or observation) time. Note that the quantities in the inner integral are all evaluated at the retarded time even though the integral is over the present time. Since the sphere over which the integral takes place has radius R', this sphere is centered on the particle at its retarded time. To switch between retarded and present time, we differentiate (5.5) to find

$$\frac{dt}{dt'} = 1 - \hat{i}' \cdot \frac{\vec{v}'}{c} \equiv \eta' . \tag{6.4}$$

When the retarded particle is moving in the same direction as $\hat{i}'$ at a very relativistic speed ($\gamma' >> 1$), (6.4) becomes

$$\frac{\mathrm{d}t}{dt'} = 1 - \frac{|\vec{v}'|}{\mathrm{c}} \approx \frac{1}{2\gamma'^2} \Rightarrow \mathrm{d}t \approx \frac{\mathrm{d}t'}{2\gamma'^2} \ . \tag{6.5}$$

In other words, if the retarded particle is very relativistic, an event that occurs for a brief duration dt' at the retarded time is registered in a duration dt' that is much briefer – by something on the order of two Lorentz factors – at the observation point, at the present time. (6.5) lies at the heart of the principle of synchrotron radiation, in which a pulse released in a duration $\Delta t'$ at the retarded time is detected in a duration $\eta'\Delta t'$ by the observer in the present. The observed radiation spectrum is thus about a factor of $1/\eta'$ times broader than the radiation spectrum at the emission point, and radiation at very high frequencies can be generated in this way.

To calculate the radiation spectrum, we will find it useful to evaluate the Fourier transform of the electric field:

$$\begin{aligned} \vec{\tilde{E}}(\vec{r},\omega) &= \frac{1}{2\pi}\int \vec{E}(\vec{r},t)\mathrm{e}^{-\mathrm{i}\omega t}dt \\ &= \frac{1}{2\pi}\frac{q}{4\pi\varepsilon_0 \mathrm{c}}\int \frac{1}{\eta'^2 R'}\hat{i}'\times\left[\left(\hat{i}'-\frac{\vec{v}'}{c}\right)\times\frac{\dot{\vec{v}}'}{\mathrm{c}}\right]\mathrm{e}^{-\mathrm{i}\omega(t'+R'/c)}dt' \end{aligned} \ , \tag{6.6}$$

where we changed the variable of integration from the present time to the retarded time in the second equality. If we assume that R' is infinite (i.e. the observational sphere is infinitely far away) so that $\hat{i}'$ is not a function of t, we also have the identity

$$\frac{d}{dt'}\left[\frac{1}{\eta'}\hat{i}'\times\left(\hat{i}'\times\frac{\vec{v}'}{c}\right)\right] = \frac{1}{\eta'^2}\hat{i}'\times\left[\left(\hat{i}'-\frac{\vec{v}'}{c}\right)\times\frac{\dot{\vec{v}}'}{\mathrm{c}}\right] \ , \tag{6.7}$$

with which we may simplify (6.6) to give

$$\vec{\tilde{E}}(\vec{r},\omega) = \frac{1}{2\pi}\frac{q}{4\pi\varepsilon_0 \mathrm{c}}\frac{\mathrm{i}\omega}{R'}\mathrm{e}^{-\mathrm{i}\omega R'/c}\int \hat{i}'\times\left(\hat{i}'\times\frac{\vec{v}'}{\mathrm{c}}\right)\mathrm{e}^{-\mathrm{i}\omega\left(t'-\hat{i}'\cdot\vec{r}'/c\right)}dt' \ . \tag{6.8}$$

6.1.2 Radiation from multiple particles

Ultimately, we are interested in radiation from electron bunches and so it would be useful to extend the analysis of the previous sub-section to the case of multiple particles. While the collective electromagnetic fields is simply the sum of the contribution of each particle, owing to the linearity of Maxwell's equations, it is not so straightforward to compute the total resulting intensity. To do so, we make the simplifying assumption that the observation sphere is infinitely far away (the same assumption that took us from (6.6) to (6.8)), which implies that $\hat{i}' = \hat{i}_1' = \hat{i}_2' = \ldots$, where $\hat{i}_i'$ is the unit vector pointing from particle i to the desired point of observation. We then have

$$\vec{S} = \left(\sum_j \vec{E}_j\right) \times \frac{1}{\mu_0}\left(\sum_k \vec{B}_k\right) = \hat{i}' \frac{1}{\mu_0 c}\left|\sum_j \vec{E}_j\right|^2 . \tag{6.9}$$

The resulting total emitted energy is then given by

$$U = \iint \left(\hat{i}' \cdot \vec{S}\right) R'^2 dt d\Omega = \iint \frac{1}{\mu_0 c}\left|\sum_j \vec{E}_j\right|^2 R'^2 dt d\Omega . \tag{6.10}$$

By Parseval's theorem, we know that (6.10) may be written equivalently as

$$U = \iint \frac{2\pi}{\mu_0 c}\left|\sum_j \tilde{\vec{E}}_j\right|^2 R'^2 d\omega d\Omega . \tag{6.11}$$

The integrand in (6.11) is in units of J/(rad/s)/sr and we shall refer to it as the *intensity spectrum*. The integrand in (6.10) is in units of J/s/sr and we shall refer to it as the *angular intensity*. The intensity spectrum may be formulated from (6.8) as

$$
\begin{aligned}
\frac{\mathrm{d}^2 I}{\mathrm{d}\omega \mathrm{d}\Omega} &= \frac{2\pi}{\mu_0 c}\left|\sum_j \tilde{\tilde{E}}_j\right|^2 R'^2 \\
&= \frac{q^2\omega^2}{32\pi^3\varepsilon_0 \mathrm{c}}\left|\sum_j\left[\int \hat{i}'\times\left(\hat{i}'\times\frac{\vec{v}'}{\mathrm{c}}\right)\mathrm{e}^{-\mathrm{i}\omega\left(t'-\hat{i}'\cdot\vec{r}'/c\right)}dt'\right]_j\right|^2 \\
&= \frac{q^2\omega^2}{32\pi^3\varepsilon_0 \mathrm{c}}\left|\left(\hat{i}'\times\hat{i}'\times\right)\int\sum_j\left[\frac{\vec{v}'}{\mathrm{c}}\mathrm{e}^{\mathrm{i}\omega\left(\hat{i}'\cdot\vec{r}'/c\right)}\right]_j \mathrm{e}^{-\mathrm{i}\omega t'}dt'\right|^2 \\
&= \frac{q^2\omega^2}{32\pi^3\varepsilon_0 \mathrm{c}}\left|\left(\hat{i}'\times\hat{i}'\times\right)\int\sum_j\left[\frac{\vec{v}'}{\eta\mathrm{c}}\right]_j \mathrm{e}^{-\mathrm{i}\omega t_{adv}}dt_{adv}\right|^2
\end{aligned}
\quad , \tag{6.12}
$$

where the advanced time is defined as

$$
t_{adv} = t' - \frac{\hat{i}'\cdot\vec{r}'}{c} \quad . \tag{6.13}
$$

The physical interpretation of the advanced time is simply the observation time minus some arbitrary constant number.

Writing (6.12) as an integral over the advanced time reveals that (6.12) may be solved via a fast Fourier transform (FFT) algorithm if the integrand can be computed at regular intervals of the advanced time. Since the expression in square brackets (in (6.12)'s last line) is real, the resulting Fourier transform must be conjugate symmetric in frequency, and its squared-modulus must be symmetric in frequency. The (two-sided) intensity spectrum (6.12) is thus always symmetric about $f = 0$. The one-sided spectrum is obtained by doubling (6.12) and ignoring the negative-frequency portion of the spectrum.

6.1.3 Computational methods for the intensity spectrum

According to what the last line of (6.12) suggests, we may compute the intensity spectrum by accumulating the expression in square brackets, summed over all particles, at regular intervals of advanced time, and then apply the fast Fourier transform to the resulting data. This enables us to compute the intensity spectrum by the fast Fourier transform without the use of any interpolation

techniques. To accumulate the data at regular intervals of advanced time, it is convenient to solve the electrodynamic equation in advanced time t_{adv} instead of t. In other words, where we used to have

$$\begin{aligned} \frac{d\vec{p}_j}{dt} &= \frac{d\left(\gamma_j m_j \vec{v}_j\right)}{dt} = q_j\left(\vec{E}_j + \vec{v}_j \times \vec{B}_j\right) \\ \frac{d\vec{r}_j}{dt} &= \vec{v}_j \end{aligned}, \tag{6.14}$$

for each particle j, we now solve

$$\begin{aligned} \frac{d\vec{p}_j}{dt_{adv}} &= \frac{d\left(\gamma_j m_j \vec{v}_j\right)}{dt_{adv}} = \frac{q_j}{\eta_j}\left(\vec{E}_j + \vec{v}_j \times \vec{B}_j\right) \\ \frac{d\vec{r}_j}{dt_{adv}} &= \frac{\vec{v}_j}{\eta_j} \end{aligned} \tag{6.15}$$

instead.

With (6.15), we can easily control our ordinary differential equation solver to land on regular intervals of t_{adv}. This is not easy to do with (6.14) since t_{adv} is a function of both t and the particle's position. In addition, the integrand of the intensity spectrum expression can be directly computed and stored at each step (so storage of individual particle properties is unnecessary). A challenge associated with solving the electrodynamic equation in advanced time, however, lies in the initialization of particles, since it is more natural for the user to specify the particle bunch at an initial t instead of an initial t_{adv}, which then varies from particle to particle according to its displacement from the origin. In our algorithm, we deal with this problem by programming the solver to start at the smallest t_{adv} of all the particles, and assuming that every particle with a larger initial value of t_{adv} travels at its initial velocity until it arrives at the t_{adv} associated with the user-specified initial t and its user-specified initial position. We also ensure that the solver lands precisely on the initial t_{adv} of each particle, whereupon said particle arrives at its user-specified initial position with its user-specified initial velocity and begins interacting with the driving field and the fields from other particles.

Another challenge is the implementation of space charge. We can still implement the approach discussed in Appendix F.2 by assuming that each particle travels at a constant velocity between its retarded time and the retarded time of the particle it is acting upon (recall that since the particles are at the same advanced time at each time step, their retarded times must differ if their positions differ). This seems a reasonable approximation given that, in the first place, the space charge computation approach in Appendix F.2 is premised upon being able to make the approximation that each particle moves at a constant velocity for all time, at every time step.

One major drawback of solving the electrodynamic equation in advanced time is that the electrodynamic equation must be re-solved for each observation direction, which makes a sweep over the solid angles computationally expensive if many particles are involved. A faster method for the purposes of sweeping observation angle involves solving the electrodynamic equation in retarded time (i.e. (6.14)), interpolating the resulting data to obtain their values at constant intervals of advanced time, computing the integrand of the intensity spectrum expression from these values and then applying the fast Fourier transform to obtain the intensity spectrum. We have also implemented this alternative algorithm using cubic spline interpolation.

A third algorithm, which does not involve the storage of the history of each individual particle for purposes of cubic spline interpolation afterwards, involves directly interpolating for the observed fields for all solid angles of interest while solving the electrodynamic equation in retarded time. Compared with the second algorithm above, this approach has the advantage of being scalable to a very large number of particles ($>10^6$) because it avoids having to allocate memory to store the history of the mechanics of each individual particle. However, one cannot then apply a cubic spline interpolation to determine the properties of each particle at the desired advanced time and a linear interpolation must suffice, at least in a straightforward approach.

6.2 Analytical solutions and benchmarking of code

6.2.1 Synchrotron radiation of a single particle

Suppose a particle moves at speed v in a circle of radius ρ in the x-z plane (y=0). This is an idealized model of a betatron. The kinematic equations are

$$\begin{aligned}\frac{dx'}{dt'} &= v'\sin\left(\frac{v'}{\rho}t'\right)\\ \frac{dy'}{dt'} &= 0\\ \frac{dz'}{dt'} &= v'\cos\left(\frac{v'}{\rho}t'\right)\end{aligned}, \tag{6.16}$$

which we can solve (with appropriate initial conditions) as

$$\begin{aligned}x' &= -\rho\cos\left(\frac{v'}{\rho}t'\right)\\ y' &= 0\\ z' &= \rho\sin\left(\frac{v'}{\rho}t'\right)\end{aligned}. \tag{6.17}$$

The electron motion is illustrated in Fig. 6-1 below.

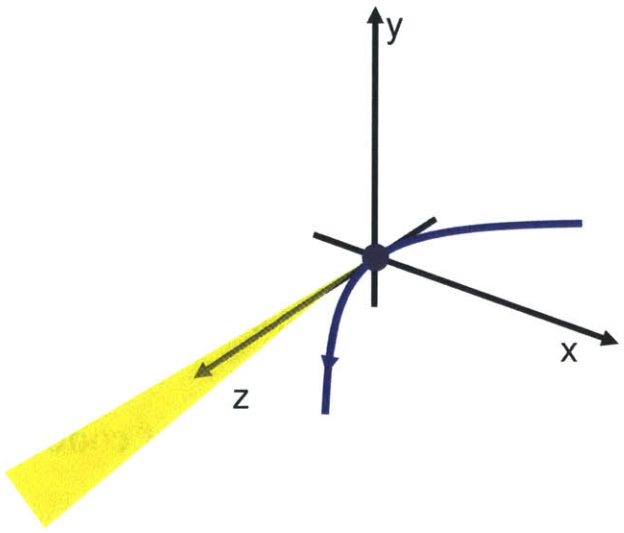

Fig. 6-1: Illustration of a single electron (purple circle) moving in a circular trajectory in the x-z plane, emitting radiation in the positive z-direction.

We are trying to solve for (6.12) given the kinematics in (6.17). Here, the second line of (6.12) is the form we will find most convenient, and we reproduce it again for easy reference:

$$\frac{\mathrm{d}^2 I}{\mathrm{d}\omega \mathrm{d}\Omega} = \frac{q^2\omega^2}{32\pi^3\varepsilon_0 \mathrm{c}}\left|\sum_j\left[\int \hat{\imath}'\times\left(\hat{\imath}'\times\frac{\vec{v}'}{\mathrm{c}}\right)\mathrm{e}^{-\mathrm{i}\omega\left(t'-\hat{\imath}'\cdot\vec{r}'/c\right)}dt'\right]_j\right|^2. \tag{6.18}$$

Setting $\hat{\imath}' = \hat{z}$ (i.e. the observation direction of interest lies in the positive direction along the z-axis), the cross product in the integrand of (6.18) may be written as

$$\hat{\imath}'\times\left(\hat{\imath}'\times\frac{\vec{v}'}{\mathrm{c}}\right) = -\hat{x}v\sin\left(\frac{v}{\rho}t'\right) \approx -\hat{x}\frac{v^2}{\rho}t'. \tag{6.19}$$

Similarly, we can simplify the advanced time argument of the exponential in the integrand as

$$\begin{aligned} t'-\frac{\hat{\imath}'\cdot\vec{r}'}{c} &= t'-\frac{\rho}{c}\sin\left(\frac{v}{\rho}t'\right) \\ &\approx t'-\frac{\rho}{c}\left(\frac{v}{\rho}t'-\frac{1}{3!}\left(\frac{v}{\rho}t'\right)^3\right), \\ &\approx \frac{t'}{2\gamma^2}+\frac{c^2}{6\rho^2}t'^3 \end{aligned} \tag{6.20}$$

where the second-last approximate equality involved a Taylor series expansion of the sine function and neglecting higher-order terms, and the last approximate equality involved assuming that the particle is highly relativistic ($\gamma >> 1$).

Substituting (6.20) and (6.19) into (6.18) gives the two-sided intensity spectrum:

$$\frac{\mathrm{d}^2 I}{\mathrm{d}\omega \mathrm{d}\Omega} \approx \frac{3q^2}{8\pi^3\varepsilon_0 \mathrm{c}}\gamma^2\left(\frac{\omega}{\omega_{cr}}\right)^2 K_{2/3}{}^2\left(\frac{\omega}{\omega_{cr}}\right), \tag{6.21}$$

which contains the critical frequency, given by

$$\omega_{cr} \equiv 3\gamma^3 \frac{c}{\rho}, \tag{6.22}$$

and the modified Bessel function of the second kind of fractional order:

$$\int_0^\infty \tau \sin\left[\frac{3}{2}x\left(\tau + \frac{1}{3}\tau^3\right)\right] d\tau = \frac{1}{\sqrt{3}} K_{2/3}(x). \tag{6.23}$$

In the case of a betatron with a static magnetic field given by

$$\vec{B} = B_0 \hat{y}, \tag{6.24}$$

the radius of curvature ρ is simply the radius of the circle the particle executes:

$$\rho = \frac{m\gamma v}{qB_0}. \tag{6.25}$$

For the cases of inverse Compton scattering (i.e. nonlinear Thomson scattering) or the free electron laser, the particle motion is approximately sinusoidal and the radius of curvature is not as straightforward to determine. We treat this in the following sub-section.

6.2.2 Radius of curvature

The general formula for the radius of curvature of the trajectory z(x) of a particle moving in the x-z plane is given as

$$\rho = \frac{\left[1 + (dz/dx)^2\right]^{3/2}}{d^2 z/dx^2}. \tag{6.26}$$

For the (approximately) sinusoidal motion of the electron in inverse Compton scattering and the free electron laser at low intensities, we may assume normalized velocities $\beta_z \sim 1$, $\beta_x << \beta_z$ and simplify (6.26) to

$$\rho \approx \frac{-1}{\beta_x \frac{d\beta_x}{dx}}. \tag{6.27}$$

Substituting in the appropriate expressions, we find that the radius of curvature for inverse Compton scattering is

$$\rho \approx \frac{\gamma mc}{2|q|E_0/c}, \tag{6.28}$$

where E_0 is the electric field amplitude of the incident electromagnetic field. The expression for radius of curvature in an undulator is very similar:

$$\rho \approx \frac{\gamma mc}{|q|B_0}, \tag{6.29}$$

where B_0 is the amplitude of the static magnetic field created by the undulator magnets. The extra factor of 2 in the denominator of (6.28) arises from the fact that the magnetic field of the plane wave also contributes to the transverse electron motion in the inverse Compton scattering case. Note that our model of the undulator really applies only close to the axis of the undulator. For a more comprehensive undulator model refer to [HK07].

Substituting (6.28) or (6.29) into (6.21) will give the intensity spectrum for a half-cycle of transverse electron motion in inverse Compton scattering or the free electron laser respectively. Of course, these processes typically consist of multiple cycles. We generalize (6.21) to the multicycle case in the following sub-section and obtain our final analytical expression for radiation from a transversely-oscillating relativistic electron.

6.2.3 Analytical intensity spectrum of a transversely-oscillating relativistic electron

A single electron passing through the alternating fields of a counterpropagating electromagnetic wave or an undulator may be approximated by a series of electrons executing circular motions. This is illustrated in Fig. 6-2. The backscattered radiation wavefront emitted in a certain phase of the electron's transverse oscillation travels at the speed of light, just slightly faster than the electron. When the electron, after a full cycle of motion, arrives at the corresponding phase in its new cycle, it emits another wavefront that lags behind the one previously emitted by a very small duration. The separation between these wavefronts is precisely the wavelength at which the scattered radiation constructively interferes. Note that this coherence mechanism is distinct from the frequency up-conversion mechanism of (6.5). Both mechanisms are involved in the free electron laser and inverse Compton scattering.

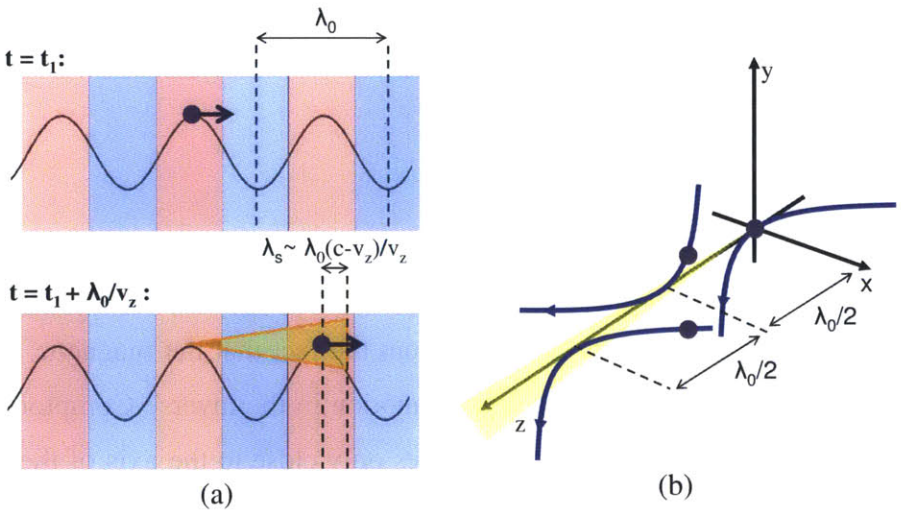

Fig. 6-2: (a) Illustration of the basic mechanism of the free electron laser, showing how each successive radiation wavefront lags behind the previous one by a duration of about $(1-\beta_z)\lambda_0/c$, where λ_0 is the period of the undulator, and v_z and $\beta_z=v_z/c$ are implicitly time-averaged values. This process may be analytically approximated as (b) a series of electrons executing properly-phased circular motions. The purple circles represent electrons. λ_s denotes the wavelength of the scattered light.

Fig. 6-2 also applies for inverse Compton scattering, except λ_0 then denotes half the wavelength (not the full wavelength) of the counterpropagating beam. Using the model in Fig. 6-2 (b), we suppose we have a string of particles (j = 0,1,2,...,2N-1), where N is the number of undulator or laser periods, spaced apart regularly in space and time:

$$\begin{aligned} \frac{dx}{dt} &= (-1)^j v \sin\left(\frac{v}{\rho}\left(t-\frac{j\lambda_0}{2v}\right)\right) \\ z &= \rho \sin\left(\frac{v}{\rho}\left(t-\frac{j\lambda_0}{2v}\right)\right)+\frac{j\lambda_0}{2} \end{aligned} \quad . \tag{6.30}$$

As before, we assume v~c. Allowing $\hat{i}' = \hat{z}$ for particle j, we can derive the multicycle versions of (6.19) and (6.20) respectively as

$$\hat{i}'\times\left(\hat{i}'\times\frac{\vec{v}'}{c}\right) = -(-1)^j \hat{x} v \sin\left(\frac{v}{\rho}\left(t'-\frac{j\lambda_0}{2v}\right)\right) \approx -(-1)^j \hat{x}\frac{v^2}{\rho}\left(t'-\frac{j\lambda_0}{2v}\right)', \tag{6.31}$$

and

$$\begin{aligned} t'-\frac{\hat{i}'\cdot\vec{r}'}{c} &= t'-\frac{\rho}{c}\sin\left(\frac{v}{\rho}\left(t'-\frac{j\lambda_0}{2v}\right)\right)-\frac{j\lambda_0}{2c} \\ &\approx t'-\frac{\rho}{c}\left(\frac{v}{\rho}\left(t'-\frac{j\lambda_0}{2v}\right)-\frac{1}{3!}\left(\frac{v}{\rho}\left(t'-\frac{j\lambda_0}{2v}\right)\right)^3\right)-\frac{j\lambda_0}{2c} \\ &\approx \frac{t'}{2\gamma^2}+\frac{c^2}{6\rho^2}\left(t'-\frac{j\lambda_0}{2v}\right)^3 \end{aligned} \quad . \tag{6.32}$$

Substituting (6.31) and (6.32) into (6.18), we get the two-sided intensity spectrum:

$$\frac{\mathrm{d}^2 I}{\mathrm{d}\omega \mathrm{d}\Omega} \approx \frac{3q^2}{8\pi^3 \varepsilon_0 \mathrm{c}} \gamma^2 \left(\frac{\omega}{\omega_{cr}}\right)^2 K_{2/3}{}^2\left(\frac{\omega}{\omega_{cr}}\right) \left|\sum_{j=0}^{2N-1} (-1)^j e^{-i\omega \frac{j\lambda_0}{2v}}\right|^2$$

$$= \frac{3q^2}{8\pi^3 \varepsilon_0 \mathrm{c}} \gamma^2 \left[\left(\frac{\omega}{\omega_{cr}}\right)^2 K_{2/3}{}^2\left(\frac{\omega}{\omega_{cr}}\right)\right] \frac{\sin^2\left(\frac{N\pi\omega}{\omega_s}\right)}{\cos^2\left(\frac{\pi\omega}{2\omega_s}\right)} \quad , \tag{6.33}$$

where $\omega_{cr} \equiv 3\gamma^3 c/\rho$ and $\omega_s \equiv 2\pi c/\lambda_s$, where

$$\lambda_s = \lambda_0\left(\frac{c}{\bar{v}_z} - \cos\theta\right) \approx \frac{\lambda_0}{1 - \frac{1}{2\gamma^2}\left(1 + \frac{a_0{}^2}{2}\right)} - \lambda_0 \cos\theta$$

$$\approx \frac{\lambda_0}{2\gamma^2}\left(1 + \frac{a_0{}^2}{2} + \gamma^2\theta^2\right) \quad . \tag{6.34}$$

In (6.34), the second-last approximate equality assumes $\gamma >> 1$ and the last approximate equality assumes $\theta << 1$, $\left(1 + a_0{}^2/2\right)/2\gamma^2 << 1$ where θ is the angle away from the z-axis. Since we deal only with the on-axis case here, $\theta = 0$ for the purposes of our formulation. For inverse Compton scattering $a_0 = -qE_0/mc\omega$, whereas for the free electron laser $a_0 = -qB_0/m\omega$.

Note that (6.33) is simply (6.21) with an extra interference factor, which is not a surprising result given our model in Fig. 6-2(b). To understand (6.33) better, it helps to see the expression as a product of three factors: the first factor that is proportional to γ^2, the second factor that is contained in the square parentheses, and the third factor that captures the interference. The first factor is constant for a given electron energy. The synchrotron radiation envelope represented by the second factor shifts its peak frequency, but does not change its height, as ω_{cr} changes. The third factor has peaks occurring at $\omega = \omega_s(2i+1)$, i an integer, with the height of each peak given by $4N^2$. These properties are illustrated in Fig. 6-3.

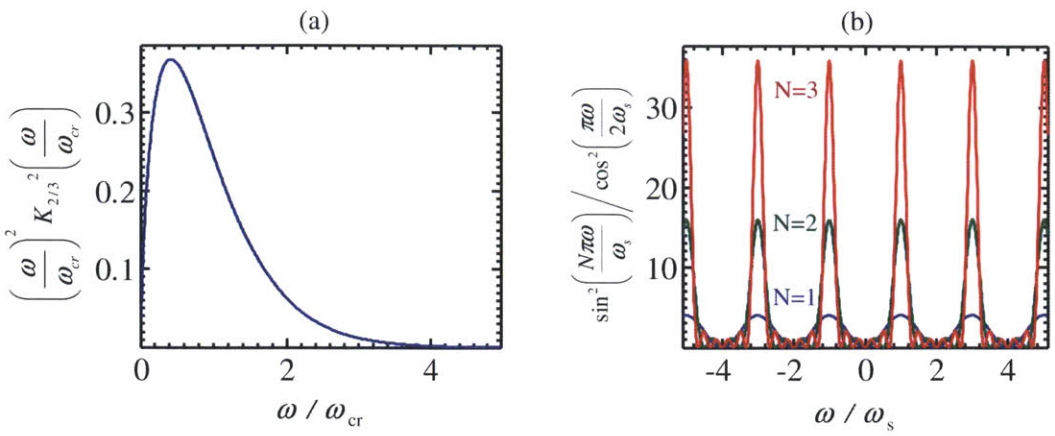

Fig. 6-3: Plots of (a) the synchrotron radiation envelope factor and (b) the coherent interference envelope factor in the analytic expression of inverse Compton scattering.

From Fig. 6-3(a), we note that the peak occurs around $0.4\omega_{cr}$. When $\omega_{cr} << \omega_s$, the first harmonic of the interference factor occurs far in the right tail of the synchrotron radiation envelope. As ω_s draws closer to ω_{cr}, assuming that N and the first factor in (6.34) do not vary in the process, the first harmonic's peak intensity increases as it approaches the envelope maximum near $0.4\omega_{cr}$. After arriving at this envelope maximum, the peak intensity of the first harmonic falls as ω_{cr}/ω_s is increased further, and the maximum spectral intensity is attained instead by higher harmonics. The expression ω_{cr}/ω_s is given for both inverse Compton scattering and the free electron laser as

$$\frac{\omega_{cr}}{\omega_s} = \frac{3}{2} a_0 \left(1 + \frac{a_0^{\,2}}{2} \right). \tag{6.35}$$

Note that our treatment applies only for the case of normal incidence. As we increase a_0, we thus expect the peak intensity of first harmonic to increase initially, reach its maximum around $a_0 = 1$, and then fall as a_0 is increased any further. As a_0 increases, the maximum intensity peak also shifts toward higher harmonics. This accurately reflects the observation in [SF96] that at sufficiently high intensities the low-order harmonics are suppressed while the higher-order harmonics are enhanced. The individual dependencies of ω_{cr} and ω_s are

$$\frac{\omega_{cr}}{\omega_0} = 3pa_0\gamma^2$$
$$\frac{\omega_s}{\omega_0} = \frac{2p\gamma^2}{1+a_0^2/2}, \tag{6.36}$$

where $p = 1$ for the free electron laser and $p = 2$ for inverse Compton scattering, and ω_0 is the frequency of the driving light. The location of the first harmonic relative to the synchrotron radiation envelope may thus be set via a_0, and the frequency of the first harmonic along with the maximum intensity of the entire spectrum then controlled by adjusting γ. ω_0 can also be adjusted in principle but is limited by the availability of coherent light sources at the desired frequency in practice. For this reason, most nonlinear Thomson scattering schemes that have been proposed limit themselves to light in the infrared regime.

6.2.4 Optimum radiation harmonic and scaling of optimum peak intensity with output wavelength

In this sub-section, we show that our model predicts that, for a given incident frequency ω_0, desired frequency ω_{out} and number of cycles N, with freedom only in the choices of a_0, γ and harmonic number m, the maximum on-axis spectral intensity is always achieved with the fundamental harmonic $m = 1$. We also show that when the incident frequency (but not the desired frequency) is varied, keeping interaction length and total charge constant, this maximum on-axis peak intensity is predicted to scale as ω_0.

We begin by making ω_{tr} our desired frequency, since the synchrotron radiation envelope peaks at ω_{tr}. Next, we note that the intensity spectrum scales as γ^2. Treating (6.35) as a cubic equation in a_0 and solving for its one real root as a function of $x = \omega_{tr}/\omega_s$, we find that (6.36) may be re-cast as (once again, $p = 1$ for the free electron laser and $p = 2$ for inverse Compton scattering)

$$\gamma^2 = \frac{\omega_{cr}/\omega_0}{2pa_0}$$

$$= \frac{\omega_{cr}/\omega_0}{2p\left\{\left[\frac{2}{3}\left(x+\sqrt{x^2+\frac{2}{3}}\right)\right]^{1/3} + \left[\frac{2}{3}\left(x-\sqrt{x^2+\frac{2}{3}}\right)\right]^{1/3}\right\}}. \quad (6.37)$$

As we see from Fig. 6-3(a), the peak of the synchrotron radiation envelope occurs at around $\omega = 0.4\omega_{cr}$. Positioning the peak of the m^{th} harmonic at this frequency involves setting $x = 2.5m$. Making this substitution in (6.37), we obtain γ^2 as a function of m and ω_{cr}/ω_0. For given incident frequency ω_0, peak emission frequency ω_{cr} and technology (p), γ^2 depends only on $1/a_0$, which we plot in Fig. 6-4. We see that the spectral intensity is maximized with a choice of $m = 1$.

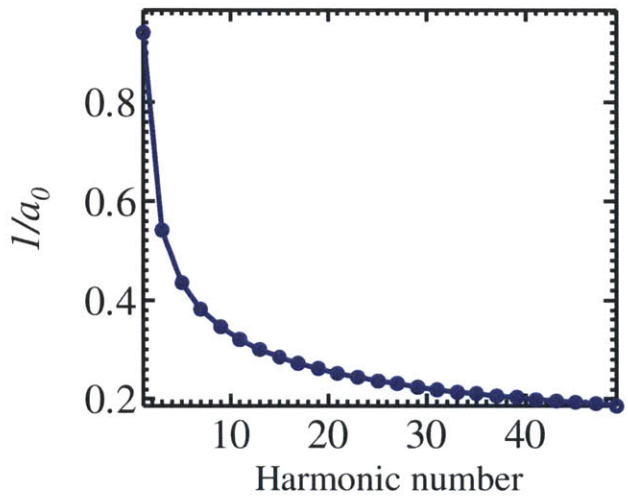

Fig. 6-4: Plot of $1/a_0$ as a function of the harmonic number. Note that only odd harmonics are considered because, as Fig. 6-3 shows, constructive interference occurs only at odd harmonics.

Of course, it is naive to assume that the maximum spectral intensity for a fixed output frequency is achieved when the desired harmonic coincides exactly with the synchrotron radiation envelope peak. A more rigorous way of obtaining the maximum spectral intensity for given ω_{out}/ω_0, charge q, and number of cycles N, is to repeat the optimization but without the constraint $\omega_{out} = 0.4\omega_{cr}$. To do so, let $y = \omega_{out}/\omega_{cr}$ and $\omega_{out} = m\omega_s$. (6.33) may then be written as

$$\frac{\mathrm{d}^2 I}{\mathrm{d}\omega \mathrm{d}\Omega} = I_0 \frac{y K_{2/3}{}^2(y)}{a_0}$$

$$a_0 = \left\{ \left[\frac{2}{3}\left(\frac{m}{y} + \sqrt{\left(\frac{m}{y}\right)^2 + \frac{2}{3}} \right) \right]^{1/3} + \left[\frac{2}{3}\left(\frac{m}{y} - \sqrt{\left(\frac{m}{y}\right)^2 + \frac{2}{3}} \right) \right]^{1/3} \right\}. \tag{6.38}$$

$$I_0 = \frac{3q^2 N^2}{4p\pi^3 \varepsilon_0 \mathrm{c}} \frac{\omega_{out}}{\omega_0}$$

Note for completeness that we also have

$$\gamma^2 = \frac{\omega_{out}}{\omega_0} \frac{1}{m} \frac{\left(1 + a_0{}^2/2\right)}{2p}. \tag{6.39}$$

We seek to maximize (6.38) by varying only m and y. Plots of (6.38) and (6.39) as a function of y for various m are shown in Fig. 6-5.

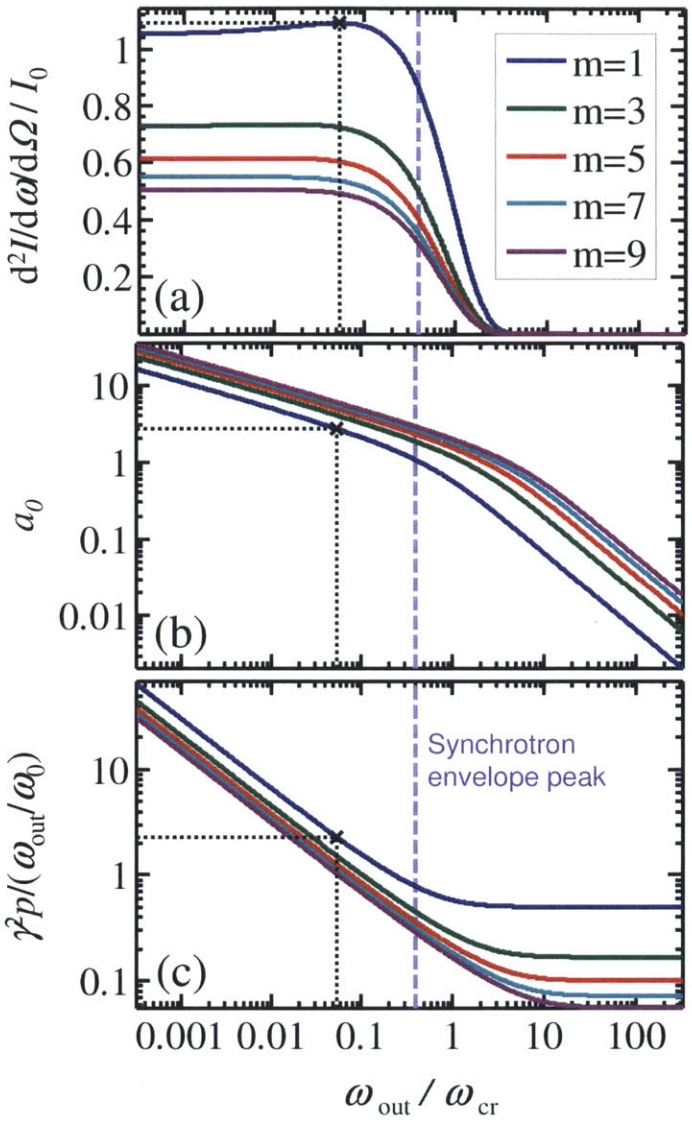

Fig. 6-5: Plots of (a) normalized spectral intensity peak, (b) corresponding a_0 and (c) corresponding normalized γ^2 as a function of parameter $y = \omega_{out}/\omega_{cr}$, for various harmonic numbers m. The black cross in each plot marks the point corresponding to optimum intensity in y-m space. The purple dashed vertical line marks the value of y corresponding to the result of the "naive" approach wherein $\omega_{out} = 0.4\omega_{cr}$ was assumed. Here, the optimal ω_{out} is determined as $0.054\omega_{cr}$.

From Fig. 6-5, we see that regardless of the choice of ω_{out}, the maximum intensity is always achieved with the first harmonic if no restrictions are placed on a_0 and γ. We also note that the value of the maximum intensity obtained by this optimization is not far off from the value

obtained by setting $\omega_{out} = 0.4\omega_{cr}$, namely, on the order of 1. We will later see that in exact electrodynamic simulations where the incident pulse has a smoothly-varying (e.g.: Gaussian) temporal envelope, the variation of a_0 and γ during the laser-electron interaction lead to spectral broadening and peak shifts that cause the optimum ω_{out} to fall roughly between $0.054\omega_{cr}$ and $0.4\omega_{cr}$ in practice. The observation that the maximum normalized on-axis spectral intensity is on the order of 1 allows us to write this maximum value as

$$\left.\frac{\mathrm{d}^2 I}{\mathrm{d}\omega \mathrm{d}\Omega}\right|_{\max} \sim \frac{3q^2 N^2}{4p\pi^3 \varepsilon_0 c}\frac{\omega_{out}}{\omega_0}. \tag{6.40}$$

The three factors in (6.40) with which the maximum spectral intensity may be most readily controlled are: (a) Amount of charge, with the intensity scaling as q^2, where q may be interpreted here as the total charge (this assumes every particle in the bunch radiates coherently on-axis); (b) interaction length, with the intensity scaling as N^2, where N is the number of cycles; and (c) the ratio ω_{out}/ω_0. If the amount of charge and the interaction length L is kept constant, then intensity scales as ω_0 since $N \sim \omega_0 L$. However, if the charge is allowed to vary, the ability of longer-wavelength schemes to accommodate a larger amount of charge may give longer-wavelength schemes an advantage over shorter-wavelength schemes where on-axis intensity is concerned in the end. Non-linearities that appear at large N, even for small a_0 [HAS+10, AAG+11], also make it difficult to increase peak spectral intensity indefinitely by only increasing N, and are another factor in favor of longer-wavelength schemes for a given interaction length.

6.2.5 Benchmarking the code

In this subsection, we compare results obtained from the analytical expressions for synchrotron radiation and inverse Compton scattering, which we derived in the previous sub-sections, with the results of the same scenarios simulated with our code. We find excellent agreement between the results of our code and those of our theory.

In the synchrotron radiation scenario, we assume a particle traveling in a constant magnetic field of 1 T at a kinetic energy of 10 MeV. The analytical formula of relevance is (6.21). Fig. 6-6

compares the numerical and analytical results. As can be seen, the curves practically lie directly on one another.

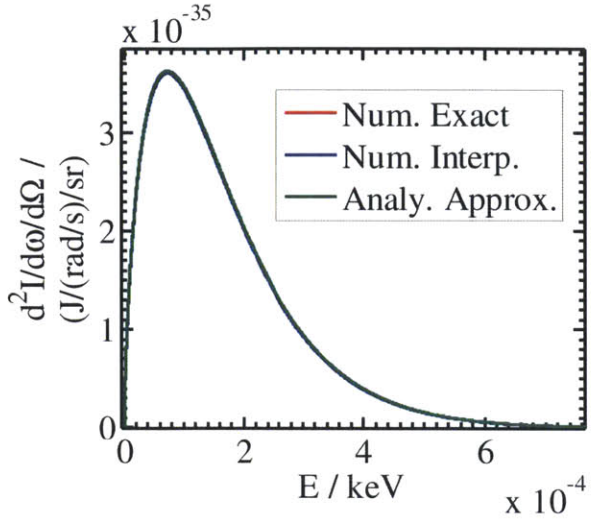

Fig. 6-6: On-axis one-sided intensity spectrums of a single electron in a betatron, computed using our code and the analytical formula. "Num. Exact" refers to the advanced-time version of the code, which does not involve interpolation; "Num Interp." refers to the retarded-time version of the code, which employs cubic spline interpolation to achieve uniform spacing in advanced time of particle properties for the fast Fourier transform algorithm.

In the inverse Compton scattering scenario, we study the intensity spectrum from a single electron traveling at a kinetic energy of 43.02 MeV into a counter-propagating electromagnetic plane wave of peak $a_0 = 0.7$ with a Gaussian temporal pulse profile. The intensity FWHM of the electromagnetic pulse contains 100 cycles, and we correspondingly set $N = 100$ in our analytical formula (6.33). Our results are plotted in Fig. 6-7.

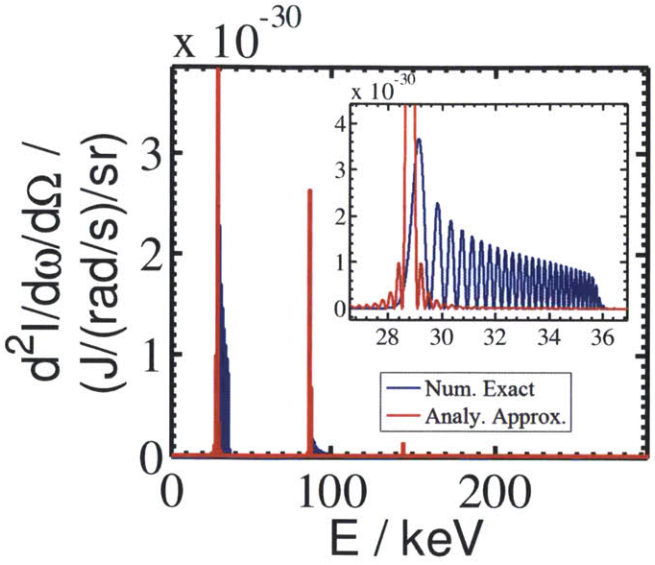

Fig. 6-7: On-axis one-sided intensity spectrums of a single electron in an inverse Compton scattering scheme, computed using our code and the analytical formula. "Num. Exact" refers to the advanced-time version of the code.

We see from Fig. 6-7 that the analytical formula predicts the peak frequencies in the simulation very well. However, the spectral peaks in the simulation are much broader and lower than those in theory. This is consistent with the fact that variations of a_0 and γ during the laser-electron interaction when the temporal pulse profile is smoothly-varying lead to spectral broadening and peak shifts, as has been observed previously in the literature [Kra04].

6.3 Nonlinear Thomson scattering with coherent electron bunches and relativistic electron sheets

In this section, we use our code to compute the radiation spectrum emitted by single electrons and relativistic electron sheets, which we idealize as two-dimensional sheets of electrons with a negligible spread in the z-direction (at least at the start of the simulation). Our study of backscattered radiation from these sheets is motivated by our interest in compressing electron bunches via interaction with a high intensity TM01 laser mode to sub-nm lengths for coherent inverse Compton scattering. Schemes to directly generate relativistic electron sheets by propagating an intense laser pulse through a plasma to form a breaking wake wave [BET03] or

by propagating an intense laser pulse through a thin nanofilm [KCH+07] have also been proposed. Experiments [PMK+07] have verified the principle of coherent backscattering off these relativistic electron sheets. In our multi-particle studies, we are interested in studying how the emitted spectrum of an electron sheet changes as a_0 changes (by varying the beam waist of the incident laser beam) for a given incident pulse energy and pulse duration. We model our linearly-polarized laser pulse with a plane wave as well as with a pulsed beam solution that exactly solves the Maxwell equations (c.f. Appendix E). Interest in the generation of attosecond x-ray pulses via nonlinear Thomson scattering with tightly-focused laser beams [LLC06, LLC+05, LXL+10] is additional motivation to examine the tight-focusing scenarios.

6.3.1 Nonlinear Thomson scattering spectrum of a coherent electron bunch

In this sub-section, we investigate the nonlinear Thomson scattering of a Gaussian-pulsed optical plane wave off an ideal coherent electron bunch, which we model with a single macro-particle. We show that there is fair agreement between the behavior of the computed on-axis intensity spectrum as a_0 is changed and the predictions of our approximate theory in Section 6.2. However, the overlap of higher harmonics at large values of a_0 [Kra04] makes our simple model's prediction that the maximum peak intensity is always achieved by the fundamental mode no longer true.

Consider a coherent 1.6fC electron bunch -- which we may effectively model as a single macro-particle of charge -1.6fC -- traveling with a kinetic energy of 30 MeV into a counterpropagating pulsed linearly-polarized (along the $\phi = 0$ direction) plane wave of wavelength 1 μm, $a_0 = 0.1$ and duration 100 cycles. The intensity profile and spectral intensity at various inclination angles θ for azimuthal angles $\phi = 0$ and $\phi = \pi/2$ is shown in Fig. 6-8.

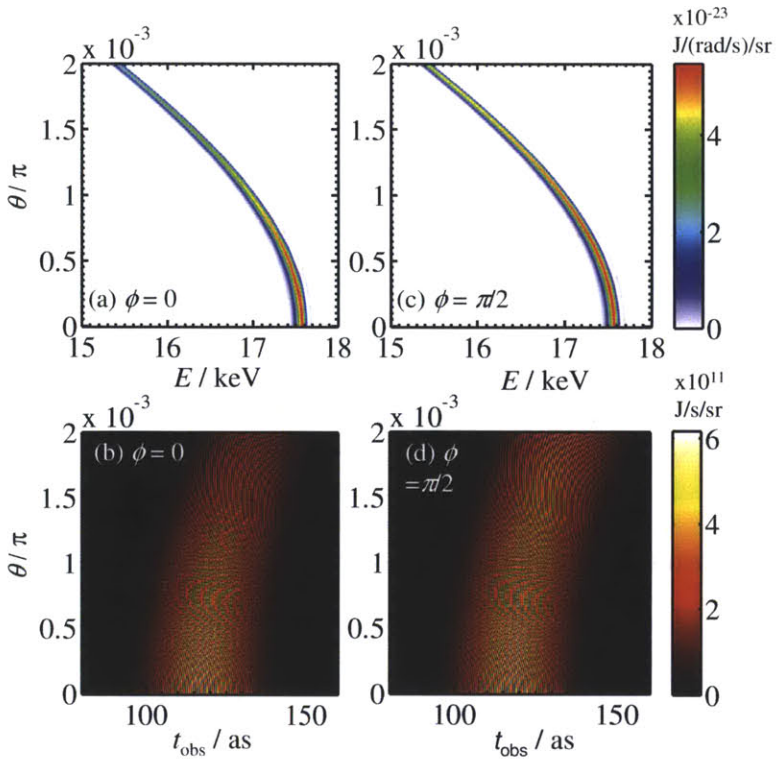

Fig. 6-8: Color maps of (a) intensity spectrum as a function of photon energy and inclination angle θ, and (b) intensity profile as a function of observation time and θ for azimuthal angle ϕ = 0. (c) and (d) are the same as (a) and (b) respectively except that $\phi = \pi/2$. Here, a 30 MeV, -1.6 fC macro-particle (which we use to model a 1.6 fC coherent electron bunch) collides with a counterpropagating infrared laser pulse of $a_0 = 0.1$ and duration 100 cycles.

In Fig. 6-8, we see that the pulse profile in both frequency and time domains appear to die out more quickly with increasing θ when $\phi = 0$ than when $\phi = \pi/2$. This makes intuitive sense because the transverse oscillations of the electron take place entirely along the $\phi = 0$ direction, and the larger range of displacements associated with the $\phi = 0$ direction is naturally associated with a smaller range of emission angles. The on-axis intensity spectrum and intensity profiles are plotted in Fig. 6-9(a) and (b) respectively. Integrating the intensity spectrum over the photon energies give the total emitted energy per unit solid angle (i.e. energy density), which we plot as a function of θ and ϕ in Fig. 6-9(c). Fig. 6-9(d) is like (c) except the integral over the photon energies has been restricted to a 0.1% bandwidth about the peak photon energy.

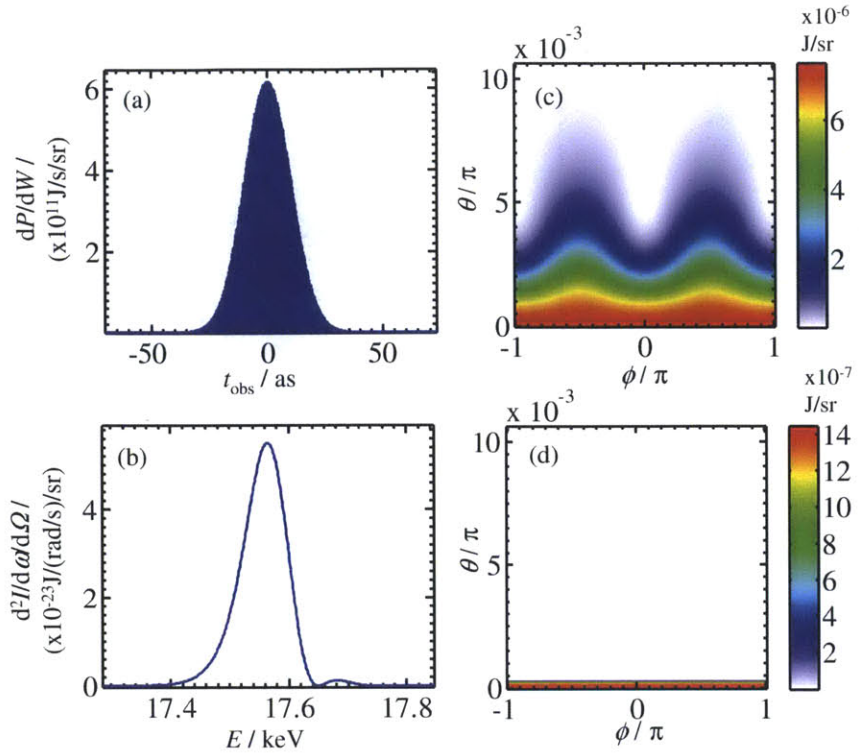

Fig. 6-9: Plots of (a) on-axis one-sided intensity spectrum and (b) on-axis intensity profile for the scenario in Fig. 6-8. Colormaps of energy density as a function of azimuthal and inclination angle are plotted in (c) for total energy and in (d) for the energy contained in 0.1% of the peak emission frequency.

The duration of the temporal pulse in Fig. 6-9(a) is about 23.7 as (the intensity FWHM duration of a Gaussian pulse fit). The on-axis 0.1% bandwidth (BW) flux density computed from Fig. 6-9(b) is about 1.451 μJ/sr/(0.1% BW). The total energy radiated is 2.18 nJ. The energy contained in the 0.1% bandwidth is 3.59 pJ, which corresponds to 1277 photons of energy 17.57 keV. This corresponds to an efficiency of 0.1277 monoenergetic 17.57 keV photons per electron.

We now repeat the same scenario except that we have a 10-cycle instead of a 100-cycle pulse. Our results are shown in Fig. 6-10 and 6-11.

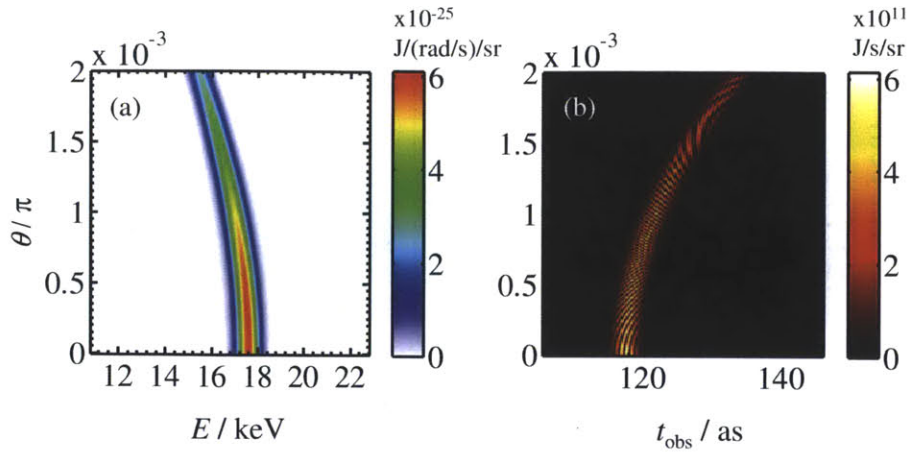

Fig. 6-10: Color maps of (a) intensity spectrum as a function of photon energy and inclination angle θ, and (b) intensity profile as a function of observation time and θ for azimuthal angle ϕ = 0. Same scenario as Fig. 6-8 except we use a 10-cycle pulse.

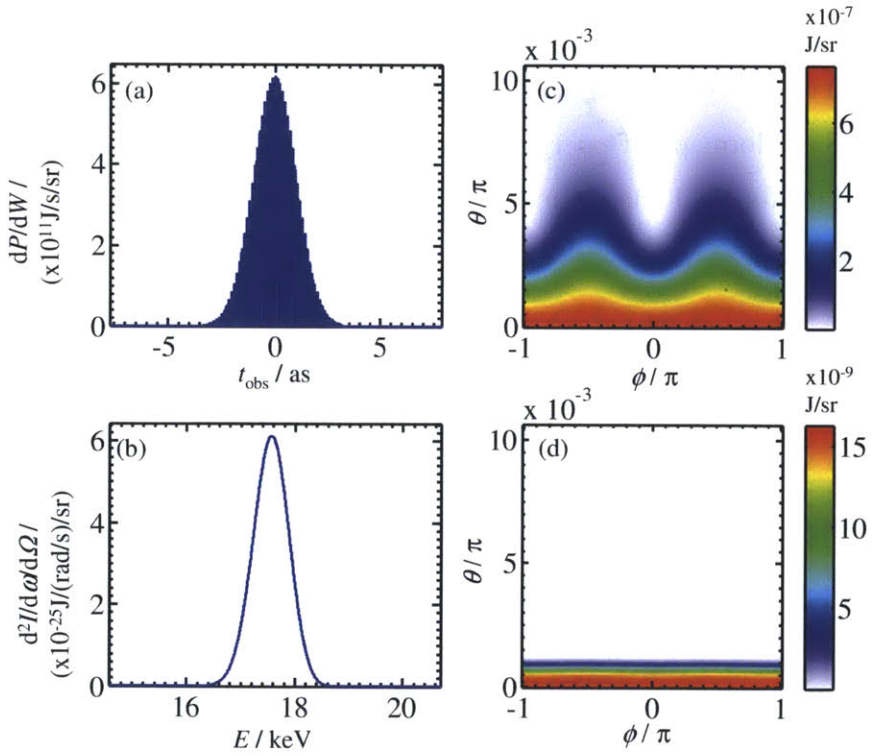

Fig. 6-11: Plots of (a) on-axis one-sided intensity spectrum and (b) on-axis intensity profile for the scenario in Fig. 6-10. Colormaps of energy density as a function of azimuthal and inclination angle are plotted in (c) for total energy and in (d) for the energy contained in 0.1% of the peak emission frequency.

In Figs. 6-10 and 6-11, the on-axis pulse duration (Gaussian-fitted FWHM) is 2.37 as. The on-axis 0.1% bandwidth (BW) flux density is about 16.3nJ/sr/(0.1% BW). The total energy radiated is 0.218 nJ. The energy contained in the 0.1% bandwidth is 0.325 pJ, which corresponds to 116 photons of energy 17.57 keV. This corresponds to an efficiency of 0.0116 monoenergetic 17.57 keV photons per electron.

Comparing the 100-cycle (Figs. 6-8 and 6-9) and 10-cycle (Fig 6-10 and 6-11) simulations, we observe that the peak on-axis spectral intensity scales as N^2, the spectral width scales as 1/N, the pulse duration scales as N, the pulse peak is independent of N, the total emitted energy scales as N and the range of inclination angles over which monoenergetic radiation is emitted scales as $N^{-1/2}$. All this accords with our theory in Section 6.2 as well as the findings of traditional free electron laser theory [Kim89]. From Figs. 6-8 and 6-10, it is also evident that the peak frequency of the intensity spectrum shifts more drastically as θ increases in the 100-cycle case compared to the 10-cycle case.

To study how the on-axis intensity spectrum varies with a_0, we plot in Fig, 6-12 the on-axis intensity spectrum for the case of a single macro-particle with -1.6 pC of charge traveling with a kinetic energy computed from (6.39) for a spectral peak in the vicinity of 18 keV (69 pm). The counterpropagating Gaussian-pulsed linearly-polarized plane wave has a central wavelength of 1 μm. Once again, we consider 10-cycle and 100-cycle pulses. More data corresponding to each curve in Fig. 6-12 is presented in Table 6.1.

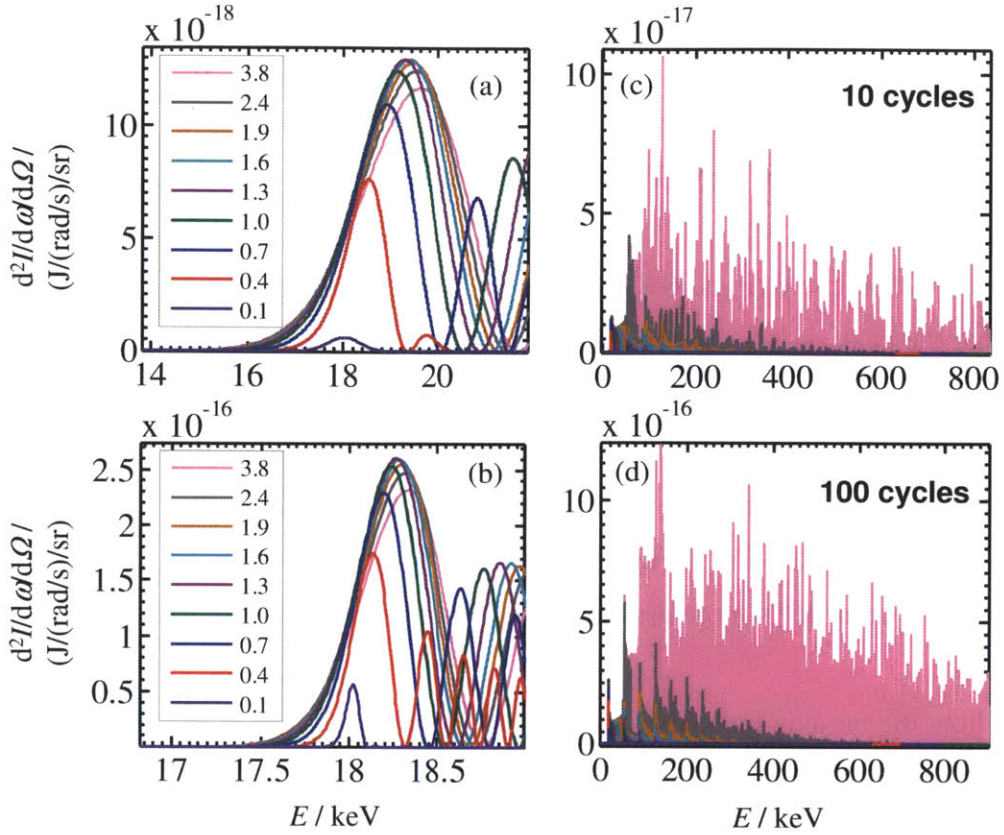

Fig. 6-11: Plots of on-axis one-sided intensity spectrum for nonlinear Thomson scattering off a single macro-particle of charge -1.6 pC of charge traveling with a kinetic energy computed from (6.39) for a spectral peak in the vicinity of 18 keV. The incident wave has a central wavelength of 1 μm, an a_0 given in the legend of the plots and a pulse duration of (a) 10 cycles and (b) 100 cycles. (c) and (d) are the zoomed-out versions of (a) and (b) respectively. Note that what appears to be dense fluctuations in (c) and (d) are really a multiplicity of peaks that resolve into smooth, continuous curves (such as we have in (a) and (b)) upon zooming in.

a_0	Theoretical ω_1/ω_{cr}	10-cycle 1st harmonic frequency [keV]	10-cycle 1st harmonic energy density [photons/s/sr /0.1%BW]	100-cycle 1st harmonic frequency [keV]	100-cycle 1st harmonic energy density [photons/s/sr /0.1%BW]
0.1	6.6335	18.022	$5.952\text{x}10^{12}$	18.0214	$5.298\text{x}10^{14}$
0.4	1.5432	18.522	$7.231\text{x}10^{13}$	18.1299	$1.652\text{x}10^{15}$
0.7	0.7650	18.9082	$1.037\text{x}10^{14}$	18.1895	$2.175\text{x}10^{15}$
1.0	0.4444	19.1228	$1.177\text{x}10^{14}$	18.2343	$2.404\text{x}10^{15}$
1.3	0.2780	19.2679	$1.226\text{x}10^{14}$	18.2618	$2.470\text{x}10^{15}$
1.6	0.1827	19.3588	$1.230\text{x}10^{14}$	18.2783	$2.460\text{x}10^{15}$
1.9	0.1251	19.4245	$1.215\text{x}10^{14}$	18.293	$2.420\text{x}10^{15}$
2.4	0.0716	19.5074	$1.180\text{x}10^{14}$	18.3162	$2.343\text{x}10^{15}$
3.8	0.0213	19.5754	$1.109\text{x}10^{14}$	18.3329	$2.2\text{x}10^{15}$

Table 6.1: Table of peak photon energy and energy density corresponding to the curves in Fig. 6-11. The energy densities were computed by integrating the intensity spectrum over the range of photon energies of interest.

In Fig. 6-11, we see that the intensity peak of the first harmonic increases as a_0 is increased, but more and more slowly as a_0 approaches a value around 1.0, and the intensity peak starts to decrease gradually after a certain point. That the first harmonic intensity does not rise indefinitely with increasing a_0 agrees with the predictions of our approximate theory illustrated in Fig. 6-5. However, the theory predicts the optimal a_0 only fairly well (prediction of optimal a_0 around 2.66, whereas in our simulations the value is highest at 1.6 in the 10-cycle case and highest at 1.3 in the 100-cycle case, which we can also see in Table 6.1; because 0.1% BW is so small, energy density approximately scales as intensity peak here). Nevertheless, the actual value of the intensity peak varies so slowly with a_0 around the optimum that the theory can still be relied upon to give an intensity peak very close to the maximum. The discrepancies between the results of the approximate theory and those of the simulation are due to two main reasons: Firstly, the broadening of the first harmonic as a_0 increases, as observed also in [Kra04], and secondly, the shift of the peak intensity that is also a result of the variation in the electron's kinetic energy

as it traverses the Gaussian pulse. This shift decreases as the pulse is broadened from 10 cycles to 100 cycles.

In Figs. 6-11(c) and (d), we also see the overlap of higher harmonics observed in [Kra04], as well as the observation in [SF96] that at high laser intensities, the lower harmonics are suppressed while the higher harmonics are enhanced. The increase in nonlinearities as one increases the number of interaction cycles [HAS+10] for the same a_0 is also evident as we go from the 10-cycle to the 100-cycle pulse.

According to the theory in Section 6.2, the maximum spectral intensity is always achieved with the fundamental mode for a given desired output photon energy, assuming a_0 and γ can be varied freely. However, the theory does not take into consideration the overlap of higher-order harmonics, which can potentially increase the intensity at higher harmonics. In Fig. 6-12, we use the 10-cycle $a_0 = 3.8$ case in Fig. 6-11(a) to illustrate this. Scaling the value of γ down (without changing a_0) so that the strongest harmonic coincides with the first harmonic of the original spectrum, we see the height of the strongest harmonic decrease proportionally with γ, as expected, but it still surpasses the original peak, making the use of higher harmonics to achieve greater peak spectral intensity a feasible measure in nonlinear Thomson scattering.

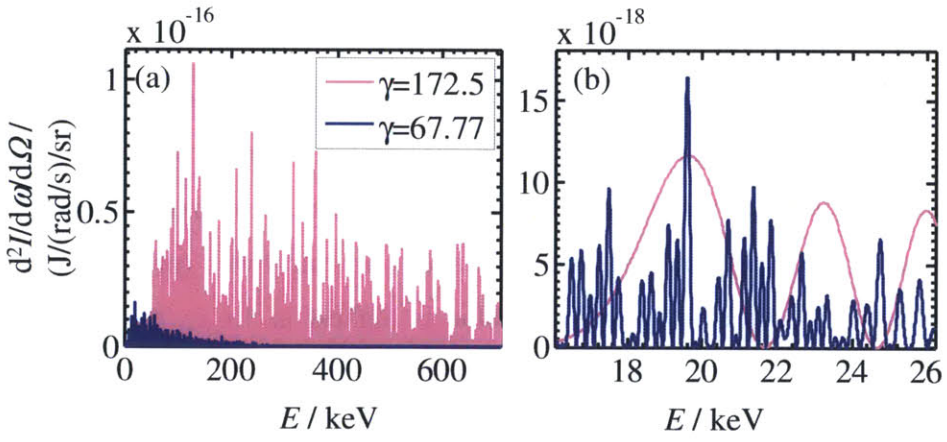

Fig. 6-12: An example illustrating how greater spectral intensity at a given output photon energy (19.6 keV here) may be achieved by using a higher harmonic. Conditions are as in the $a_0 = 3.8$, 10-cycle case in Fig.6-11. (b) is a zoomed-in version of (a).

6.3.2 Multiparticle simulations of nonlinear Thomson scattering off relativistic electron mirrors

In this sub-section, we study how the emitted spectrum of a relativistic electron sheet changes as a_0 changes (by varying the beam waist of the incident laser beam) for a given incident pulse energy and pulse duration. We model our linearly-polarized laser pulse with a plane wave as well as with a pulsed beam solution that exactly solves the Maxwell equations (c.f. Appendix E).

We model a 1.6 pC relativistic electron sheet using 400 macroparticles. For the purposes of this study, the initial sheet is highly idealized, with zero positional spread along the z axis, a Gaussian spread of standard deviation 1 μm in the x and y directions and zero momentum spread. Space charge is turned on. The incident laser pulse is a 10-cycle pulse of varying intensity (a_0 is the parameter varied in this study) and central wavelength 1μm. In the case of the exact pulsed beam solution, we fix the peak pulse power at 0.55 TW. The degree of focusing required to attain the various a_0 considered in this study is given in Table 6.2. We adjust the kinetic energy of the electron sheet via (6.39) in each case to target a photon energy of 17.6 keV. In all cases, the electron sheet encounters the pulse after about 1 ps of propagation in free space.

a_0	w_0/λ	ε_d
0.1	35.73	000891
0.4	8.916	0.0357
0.7	5.09	0.0625
1.0	3.58	0.0895
1.3	2.73	0.117
1.6	2.20	0.144
1.9	1.85	0.172

Table 6.2: Amount of focusing corresponding to various a_0 (computed on-axis at the pulse peak) for an exact pulsed beam solution of Maxwell's equations for a 10-cycle, 0.55 TW peak power and central wavelength 1μm pulse. w_0 is the beam waist radius and divergence angle $\varepsilon_d = 1/\pi/w_0$.

Fig. 6-13 shows the radiation spectrum corresponding to laser pulses of peak a_0 = 0.1, 0.4, 0.7 and 1.0. We see that the extent of the radiation spectrum in θ is smaller here in the single-particle scenarios studied in the previous subsection. This is not surprising since a larger source size is generally associated with a smaller range of emission angles. For a_0 = 0.1 and a_0 = 0.4, the plane wave and exact pulse results agree closely. When a_0 is as high as 0.7, the radiation spectrum in the exact pulse case has started to diverge significantly from that in the plane wave case. This is once again not surprising since from Table 6.2, the beam waist radius at a_0 = 0.7 is about 5 μm, which is within an order of magnitude of the size of the electron sheet. The nonlinear Thomson scattering spectrum thus deteriorates because different parts of the relativistic electron sheet experience substantially different effective a_0. At a_0 = 1.0, the spectrum has degraded so much that the peak photon energy has shifted significantly from the targeted photon energy of 17.6 keV. Fig. 6-14 show the spectra for $a_0 > 1.0$.

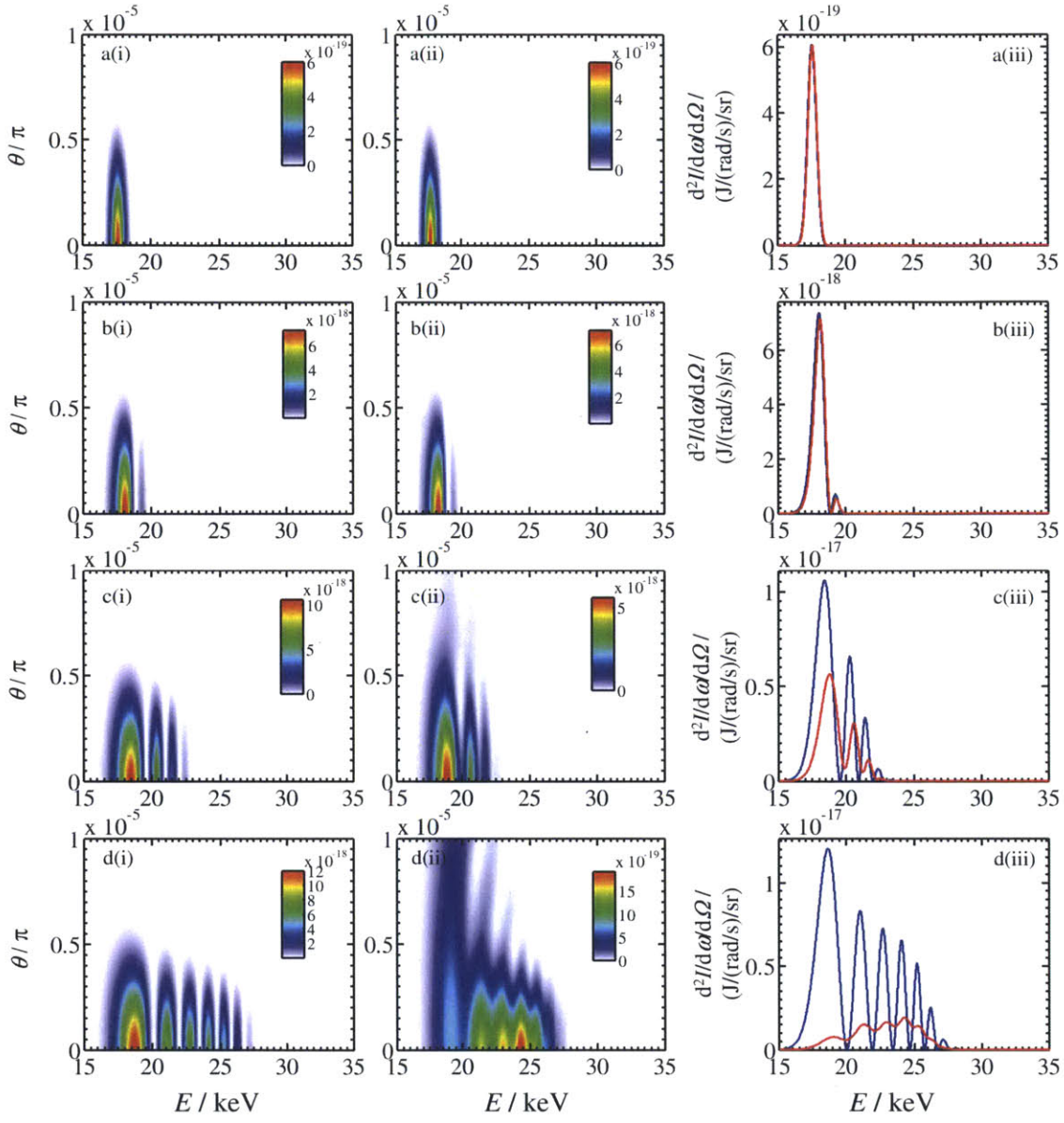

Fig. 6-13: Spectra of radiation from a relativistic electron sheet for a counterpropagating laser pulse of peak normalized potential (a) $a_0 = 0.1$, (b) $a_0 = 0.4$, (c) $a_0 = 0.7$ and (d) $a_0 = 1.0$. In each case we plot (i) the spectrum from an incident plane wave, (ii) spectra from an incident pulse that exactly satisfies Maxwell's equations (iii) on-axis spectra from the plane wave (blue) and exact pulse (red) cases. Results are obtained for $\phi = 0$ on the infinitely-distant observation sphere. Full details of the relativistic electron sheet and incident pulse are given in the text.

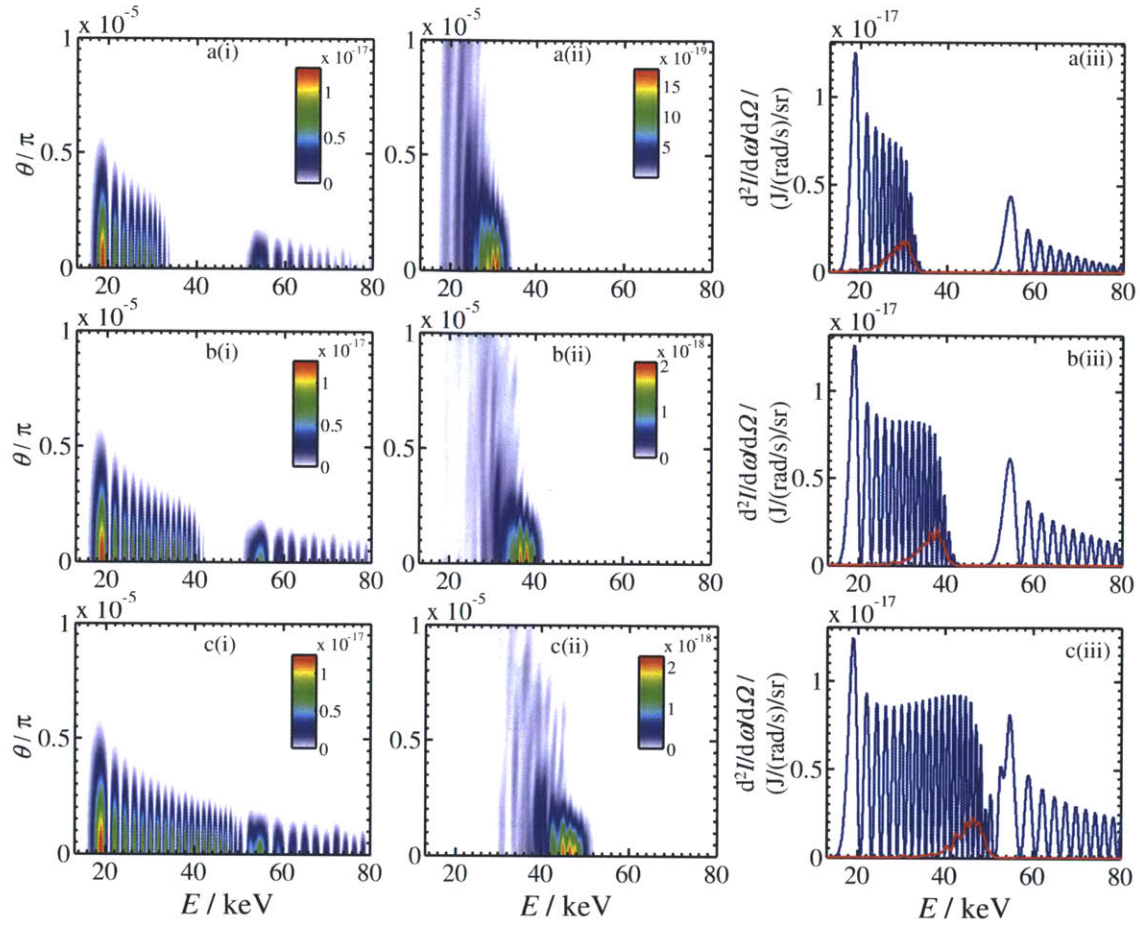

Fig. 6-14: Same as Fig. 6-13 except now we consider (a) $a_0 = 1.3$, (b) $a_0 = 1.6$, and (c) $a_0 = 1.9$.

In Figs. 6-13(d) and 6-14, we note that increasing a_0 shifts the peak to larger and larger photon energies. This is because the electrons seeing the intended a_0, which occurs on-axis, are relatively few compared to those seeing the a_0 away from the axis. One could adjust the energy of the electron sheet to shift the peak to the desired photon energy, as we illustrate in Fig. 6-12, but that would lead to an even lower spectral peak. We also notice that at lower photon energies, the radiation in the exact pulse case is emitted over a broader and broader range of θ as a_0 increases from $a_0 = 0.1$ to $a_0 = 1.0$. This indicates that a smaller and smaller (in transverse dimensions) group of electrons experience an a_0 close to the on-axis a_0. The smaller transverse size of this radiating group of particles naturally leads to a wider range of emission angles. We conclude that the beam width of a focused laser beam should exceed the width of the electron bunch by at least an order of magnitude in order for the plane wave approximation to hold. Relevant data computed for the cases in Figs. 6-13 and 6-14 is presented in Table 6.3.

a_0	Plane wave Gaussian pulse on-axis peak photon energy (keV)	Plane wave Gaussian pulse 0.1% bandwidth energy (photons/0.1% BW)	Plane wave Gaussian pulse total emitted energy (J)	Exact pulse on-axis peak photon energy (keV)	Exact pulse 0.1% bandwidth energy (photons/0.1% BW)	Exact pulse total emitted energy (J)
0.1	17.5662	1847.5877	$2.4423\text{x}10^{-10}$	17.5914	1837.8903	$2.4266\text{x}10^{-10}$
0.4	18.0518	21578.7774	$3.6791\text{x}10^{-9}$	18.1327	21224.3004	$3.5435\text{x}10^{-9}$
0.7	18.4391	30398.1963	$1.0061\text{x}10^{-8}$	18.8107	25996.0368	$8.7425\text{x}10^{-9}$
1.0	18.6523	34600.3002	$1.7848\text{x}10^{-8}$	24.2915	3721.8168	$8.4056\text{x}10^{-9}$
1.3	18.7939	36349.1639	$2.6019\text{x}10^{-8}$	29.8255	2781.5812	$7.0795\text{x}10^{-9}$
1.6	18.8988	36792.1725	$3.4153\text{x}10^{-8}$	37.978	1828.6882	$6.8489\text{x}10^{-9}$
1.9	18.966	36675.7091	$4.232\text{x}10^{-8}$	46.3794	1672.1966	$7.4308\text{x}10^{-9}$

Table 6.3: Peak photon energy, emitted energy in 0.1% bandwidth about the peak and total emitted energy for the cases shown in Figs. 6-13 and 6-14. The total emitted energy was computed by integrating over all ϕ and assuming the detector spans an emission angle $0 < \theta < \pi\text{x}10^{-5}$.

From Table 6.3, we see that the monochromatic (i.e. 0.1% bandwidth) emitted photon count in the plane wave case increases rapidly at low a_0 as a_0 increases, but the growth slows rapidly as we approach $a_0 \sim 1.0$. There is a point beyond which the energy reflected from a relativistic electron sheet cannot be increased substantially by simply increasing in the intensity of the incident laser pulse. Instead, the charge of the bunch or the number of cycles in the interaction length must be increased to achieve a greater count of monochromatic emitted photons.

Fig. 6-15 shows the evolution of the electron bunch statistics for the $a_0 = 0.1$ case in Fig. 6-13(a), for the plane wave and exact pulse models. We see that the statistical evolution is very similar in both cases, as the closeness in their radiation spectra already leads us to expect. Fig. 6-16 shows the instantaneous particle distribution at $t = 1.004$ ps, which is slightly after when the bunch coincides with the peak of the pulse. We see very similar particle distributions in both the plane wave and exact pulse cases. Fig. 6-16(b) shows that the longitudinal force (absent in the plane wave case) experienced by the particles in the exact pulse case are about 3 orders of magnitude less than the transverse force, and so the former have hardly any effect on the electrodynamics of the bunch.

The effects of the longitudinal force become very significant in the case of tight-focusing, however, as we see in Figs. 6-17 and 6-18, which are the same as Figs. 6-15 and 6-16 respectively but for the $a_0 = 1.6$ case in Fig. 6-14(b). During interaction with the pulse, the longitudinal spread and emittance of the bunch are worse by about 2 and 3 orders of magnitude respectively when the exact pulse model is used instead of the plane wave model. The increase of the longitudinal spread to 10^{-10} m alone is sufficient to affect results significantly since this spread is on the order of the desired emission wavelength, and will cause the temporal coherence of the x-ray output to deteriorate. Fig. 6-17(b) shows that the maximum mean transverse momentum achieved by the bunch is noticeably smaller in the exact pulse case than in the plane wave case, which explains the shift of the spectral peak to higher frequencies under the exact pulse model. In Fig. 6-18, we see that the longitudinal force of the exact pulse is now only about 30 times smaller than the transverse force during the laser-electron interaction. The particle distribution is spread out over a larger longitudinal space owing to the significant effect of the longitudinal force. It is interesting to note that switching from a plane wave to an exact pulse model, even in the tightly focused case, does not affect the energy spread of the bunch significantly: In Fig. 6-17(d), we do see the longitudinal momentum spread increase by an order of magnitude, but this has hardly any effect on the relative energy spread (shown in 6-17(f)) due to the high energy of the electrons.

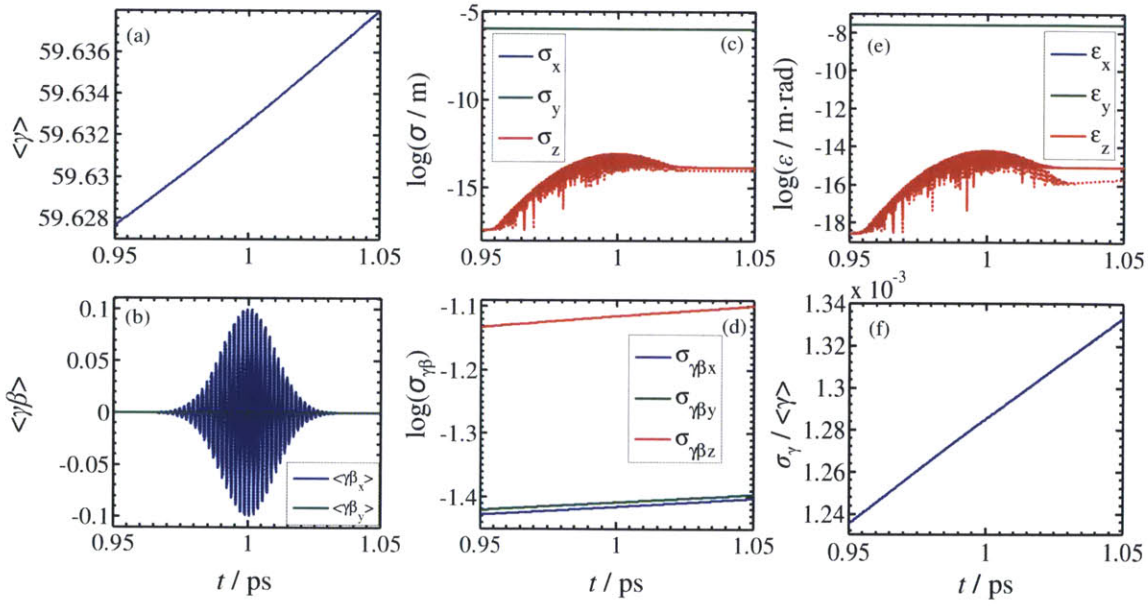

Fig. 6-15: Statistics of the electron bunch for the $a_0 = 0.1$ case in Fig. 6-13(a): (a) mean Lorentz factor (normalized energy), (b) mean normalized momentum, (c) spatial spread (d) normalized momentum spread, (e) emittance and (f) relative energy spread. Angular parentheses around a variable denote the mean of the variable. The symbol σ denotes the standard deviation of its subscript variable. Dotted lines correspond to the plane wave model, solid lines to the exact pulse model.

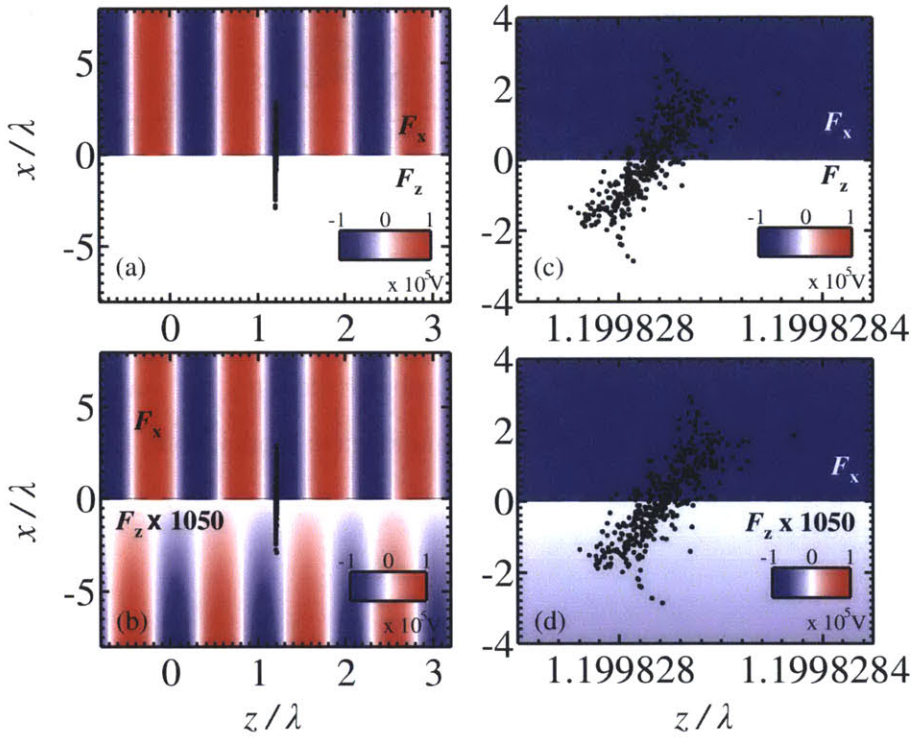

Fig. 6-16: Particle distribution in the y=0 plane at $t = 1.004$ ps in the $a_0 = 0.1$ case of Fig. 6-13(a) for (a) the plane wave model and (b) the exact pulse model. Color maps show the force in the y = 0 plane for a particle moving in the z direction at the speed of light. (c) and (d) are zoomed-in versions of (a) and (b) respectively. Forces are normalized by qk, where q is the particle charge and k is the wavevector.

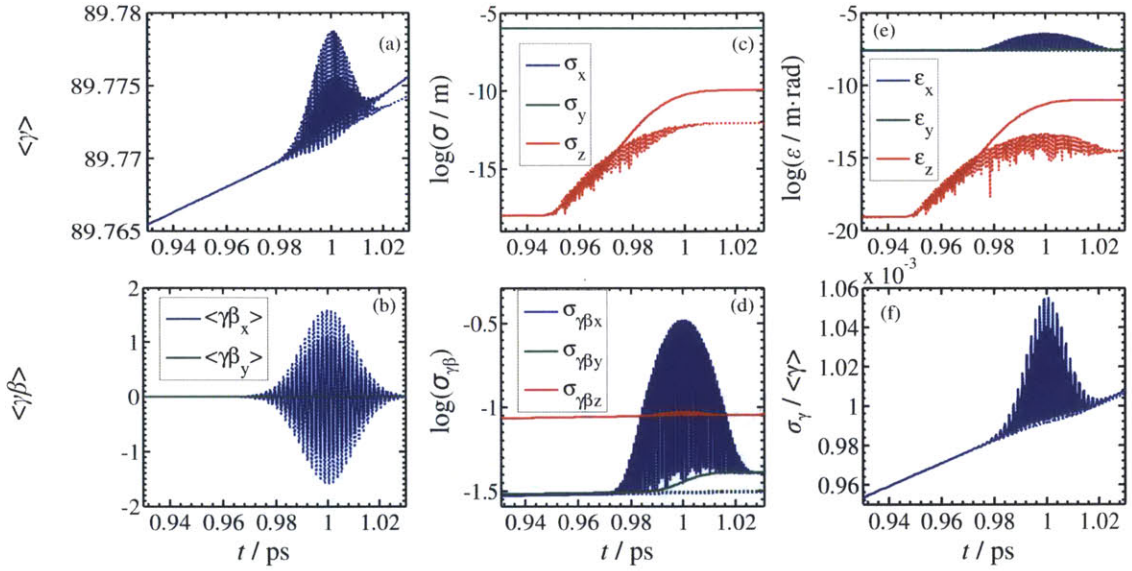

Fig. 6-17: Statistics of the electron bunch for the $a_0 = 1.6$ case in Fig. 6-14(b): (a) mean Lorentz factor (normalized energy), (b) mean normalized momentum, (c) spatial spread (d) normalized momentum spread, (e) emittance and (f) relative energy spread. Angular parentheses around a variable denote the mean of the variable. The symbol σ denotes the standard deviation of its subscript variable. Dotted lines correspond to the plane wave model, solid lines to the exact pulse model.

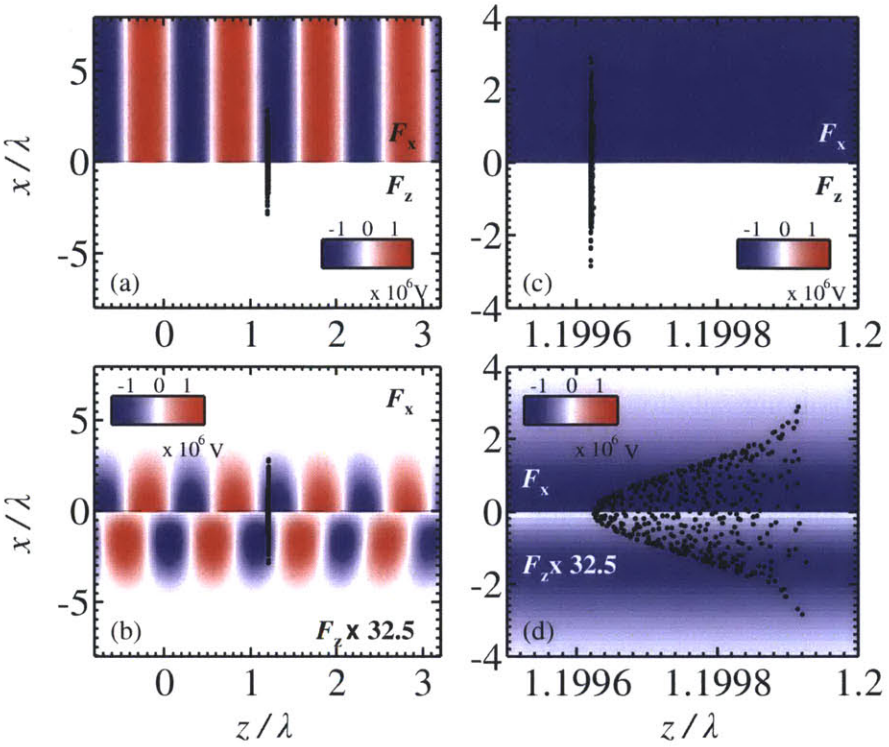

Fig. 6-18: Particle distribution in the y=0 plane at t = 1.004 ps in the a_0 = 1.6 case of Fig. 6-14(b) for (a) the plane wave model and (b) the exact pulse model. Color maps show the force in the y = 0 plane for a particle moving in the z direction at the speed of light. (c) and (d) are zoomed-in versions of (a) and (b) respectively. Forces are normalized by qk, where q is the particle charge and k is the wavevector.

6.4 Summary and future work

In this chapter, we have presented the classical theory of nonlinear Thomson scattering and derived an approximate analytical formula for the on-axis intensity spectrum of a single relativistic particle traveling into a counterpropagating linearly-polarized electromagnetic pulse. From this formula, we deduce that if we restrict ourselves to the first harmonic and are free to choose any combination of normalized vector potential a_0 and electron Lorentz factor γ we like, There is an optimal a_0 that gives the maximum spectral intensity peak for a given output and input frequency. Beyond a certain point, it is futile to obtain greater monochromatic (by which we mean 0.1% bandiwidth) output by increasing the intensity of the incident laser pulse. Instead, the amount of charge in the bunch or the number of cycles in the laser-electron interaction must

be increased. Our approximate theory also concluded that the maximum spectral intensity at a given output frequency is always obtained with the first harmonic. This is no longer true when nonlinearities are taken into account, as we show by computing the radiation spectrum of a particle interacting with a Gaussian-pulsed plane wave in Fig. 6-12: higher-harmonics may indeed be useful in achieving higher peak spectral intensities.

We used the analytical formulas we derived for synchrotron radiation and inverse Compton scattering to benchmark our radiation code. We also discussed the implementation of different algorithms: one involving solution of the electrodynamic equation in retarded time and linear interpolation, another solution of the electrodynamic equation in retarded time and cubic spline interpolation, yet another solution of the electrodynamic equation in advanced time and no interpolation required. Each approach has its advantages and disadvantages, which we also discussed.

Finally, we studied the scattering of an optical laser pulse off an electron bunch under different degrees of laser focusing. The incident pulse is a 1 μm, 10-cycle pulse with a peak power of 0.55 TW. In each case, we compare the results obtained using the exact pulse solution with those obtained using an ideal pulsed plane wave of the same normalized vector potential a_0. From our results, we conclude that for an actual laser pulse to approximate an ideal plane wave as far as the radiation spectrum of an electron bunch in nonlinear Thomson scattering is concerned, the beam waist width of the laser focus should be at least an order of magnitude greater than the transverse width of the electron bunch. Tight-focusing causes electrons at different transverse locations of the bunch to experience a substantially different a_0, leading to weak emission over a large range of inclination angles at photon energies associated with the on-axis a_0, due to the relatively small size of the part of the bunch that experiences an a_0 close to the on-axis a_0.

Future work includes a more comprehensive characterization of coherent x-ray generation via inverse Compton scattering with an exact pulse solution in vacuum under various focusing and pulse duration conditions. Since (6.38) tells us that the maximum spectral intensity is proportional to $q^2\omega_0$ for fixed interaction length (which scales as $N\omega_0$) and output frequency, where q is total charge and ω_0 the input frequency, it appears beneficial to consider lower input frequencies. This is because the increase in the amount of charge that can be accommodated at a lower frequency is likely to more than offset the intensity's proportionality to ω_0. This prompts

us to look more closely at nonlinear Thomson scattering schemes using incident Terahertz pulses, which has been proposed before [HFM+11]. As intense coherent electromagnetic sources become available at an increasing number of places in the electromagnetic spectrum, a study pertaining to the optimum input frequency for nonlinear Thomson scattering given a fixed amount of charge in an electron bunch will also be highly relevant.

Appendix A

The objective of this appendix is to derive and discuss the properties of (2.5) as an equation with $\gamma\beta$ as the unknown. For convenience we reproduce (2.5) here:

$$\gamma - \gamma\beta\beta_{ph} = G\,, \tag{A.1}$$

where $\gamma = (1 + (\gamma\beta)^2)^{1/2}$. G is in the most general case a function of given parameters a_0, ψ, ψ_s, β_{ph} and β_s, and will be treated as a constant parameter for our purposes here. Physics requires that γ, $\gamma\beta$, G, βph $\in\Re$, $\gamma \geq 1$ and $|\beta| < 1$. As the particle approaches the speed of light, $|\beta| \rightarrow 1 \Rightarrow \gamma \rightarrow \infty$. Recall we have assumed that $\beta_{ph} > 0$, without any loss of generality in the physical problem. We plot the expression $\gamma - \gamma\beta\beta_{ph}$ as a function of $\gamma\beta$ for various values of β_{ph} in Fig. A-1.

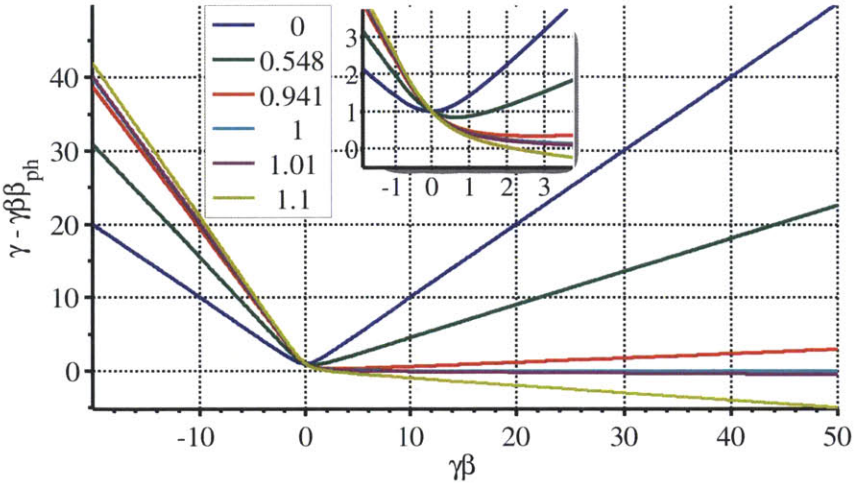

Fig. A-1: Plots of $\gamma - \gamma\beta\beta_{ph}$ as a function of $\gamma\beta$ for the various values of β_{ph} indicated in the legend. The inset zooms into the plot near the origin so that the minima of the curves corresponding to $\beta_{ph} < 1$ are more easily seen.

Several features are immediately evident from Fig. A-1:

1. Regardless of β_{ph}, the curves become asymptotically linear when $|\gamma\beta| >> 1$. This is obvious from (A.1) since $\gamma - \gamma\beta\beta_{ph} \approx \gamma\beta(1 - \beta_{ph})$, $\gamma\beta >> 1$ and $\gamma - \gamma\beta\beta_{ph} \approx -\gamma\beta(1 + \beta_{ph})$, $\gamma\beta << -1$.
2. A curve that corresponds to $\beta_{ph} < 1$ has a minimum which occurs at $\beta = \beta_{ph}$. $\gamma - \gamma\beta\beta_{ph} \geq (1 - \beta_{ph}^2)^{1/2}$. This is easily proven mathematically by taking derivatives of $\gamma - \gamma\beta\beta_{ph}$ with respect to $\gamma\beta$.
3. For $\beta_{ph} = 1$, $\gamma - \gamma\beta\beta_{ph} \rightarrow 0$ as $\beta \rightarrow 1$. Otherwise, $\gamma - \gamma\beta\beta_{ph} > 0$. $\gamma - \gamma\beta\beta_{ph}$ is a strictly decreasing function of $\gamma\beta$ for finite $\gamma\beta$.
4. For $\beta_{ph} > 1$, $\gamma - \gamma\beta\beta_{ph}$ spans the entire range of $\Re$, and is a strictly decreasing function of $\gamma\beta$.

It is straightforward to solve (A.1) as a quadratic equation. We get

$$\gamma\beta = \left(G\beta_{ph} \pm \sqrt{\beta_{ph}^2 + G^2 - 1}\right)\gamma_{ph}^2, \quad \beta_{ph} \neq 1, \tag{A.2}$$

The case for $\beta_{ph} = 1$ may be solved separately (we get exactly one solution for a given G) and is not complicated so we do not address it here. We need to verify that the results in (A.2) are solutions to (A.1) by inserting (A.2) into (A.1). Doing so gives

$$\gamma - \gamma\beta\beta_{ph} = \gamma_{ph}^{\,2}\left|\beta_{ph}\sqrt{\beta_{ph}^2 + G^2 - 1} \pm G\right| - \gamma_{ph}^{\,2}\beta_{ph}\left(G\beta_{ph} \pm \sqrt{\beta_{ph}^2 + G^2 - 1}\right), \qquad \text{(A.3)}$$

where the choice of sign corresponds to that in (A.2). The right side of (A.3) evaluates to G if the inserted $\gamma\beta$ is a solution of (A.1).

When $\beta_{ph} < 1$, $\beta_{ph}(\beta_{ph}^{\,2} + G^2 - 1)^{1/2} <$ G and we see that (A.3) yields G for either choice of sign. Hence, every physically valid choice of G yields two solutions for $\gamma\beta$, the solutions being identical if and only if $\beta_{ph}^{\,2} + G^2 - 1 = 0$. This agrees with the observation about Fig. A-1 made in Point 2 above. Since the minimum occurs at $\beta = \beta_{ph}$, we are guaranteed that $\beta = \beta_{ph}$ in the case of one distinct solution. In the case of two distinct solutions, we are guaranteed that $\beta < \beta_{ph}$ for the choice of "–" and $\beta > \beta_{ph}$ for the choice of '+' in (A.2). This fact has been used to determine the correct values of S in (2.20), which gives the final normalized momentum of a particle under maximum acceleration conditions, for the different scenarios.

When $\beta_{ph} > 1$, however, $\beta_{ph}(\beta_{ph}^{\,2} + G^2 - 1)^{1/2} >$ G and (A.3) evaluates to G only for the choice of "–". Also, $\beta_{ph}^{\,2} + G^2 - 1 > 0$, so a solution always exists. Hence, we have exactly one solution when $\beta_{ph} > 1$, which is reflected in Point 4 on Fig. A-1 above.

Appendix B

The objective of this appendix is to prove the following statements made about the separatrix minimum in Sections 2.2.3 and 2.3.2:

1. For constant β_{ph}, the separatrix minimum decreases as a_0 increases
2. For constant a_0, the separatrix minimum decreases as β_{ph} increases for $0 < \gamma_{ph}\beta_{ph} < a_0$, and increases as β_{ph} increases for $\gamma_{ph}\beta_{ph} > a_0$, so that for given a_0, the least separatrix minimum possible occurs when $\gamma_{ph}\beta_{ph} = a_0$.

Note that we assume without loss of generality that $\beta_{ph} > 0$, $a_0 > 0$. For given β_{ph} and a_0, the formula for the separatrix minimum is given in (2.13) as:

$$(\gamma\beta)_{\text{sep min}} = \gamma_{ph}\beta_{ph}\left(2\gamma_{ph}\beta_{ph}a_0 + 1\right) - \gamma_{ph}\sqrt{4\gamma_{ph}\beta_{ph}a_0}\sqrt{\gamma_{ph}\beta_{ph}a_0 + 1}. \tag{B.1}$$

Taking the partial derivative of (B.1) with respect to a_0, we have:

$$\begin{aligned}\frac{\partial}{\partial a_0}(\gamma\beta)_{\text{sep min}} &= 2\left(\gamma_{ph}\beta_{ph}\right)^2 - 2\gamma_{ph}\sqrt{\gamma_{ph}\beta_{ph}}\left(\frac{\gamma_{ph}\beta_{ph}a_0 + 1/2}{\sqrt{a_0}\sqrt{\gamma_{ph}\beta_{ph}a_0 + 1}}\right) \\ &= 2\left(\gamma_{ph}\beta_{ph}\right)^2 - 2{\gamma_{ph}}^2\beta_{ph}\left(\frac{\sqrt{\gamma_{ph}\beta_{ph}{a_0}^2 + a_0 + 1/4\gamma_{ph}\beta_{ph}}}{\sqrt{\gamma_{ph}\beta_{ph}{a_0}^2 + a_0}}\right) \\ &< 2{\gamma_{ph}}^2\beta_{ph}\left(\beta_{ph} - 1\right) < 0.\end{aligned} \tag{B.2}$$

This proves Point 1 above (that for constant β_{ph}, the separatrix minimum decreases as a_0 increases).

Next, we take the partial derivative of (B.1) with respect to $\gamma_{ph}\beta_{ph}$:

$$\frac{\partial}{\partial(\gamma\beta)_{\mathrm{ph}}}(\gamma\beta)_{\mathrm{sep\,min}} = 4a_0(\gamma\beta)_{\mathrm{ph}} + 1 - 2\beta_{\mathrm{ph}}\sqrt{(\gamma\beta)_{\mathrm{ph}}a_0}\sqrt{(\gamma\beta)_{\mathrm{ph}}a_0 + 1} - \frac{\gamma_{\mathrm{ph}}\sqrt{a_0}\sqrt{(\gamma\beta)_{\mathrm{ph}}a_0 + 1}}{\sqrt{(\gamma\beta)_{\mathrm{ph}}}} - \frac{\gamma_{\mathrm{ph}}a_0\sqrt{(\gamma\beta)_{\mathrm{ph}}a_0}}{\sqrt{(\gamma\beta)_{\mathrm{ph}}a_0 + 1}}. \tag{B.3}$$

The sign of this expression is plotted over a large range of a_0 and $\gamma_{\mathrm{ph}}\beta_{\mathrm{ph}}$ in Fig. B-1. From the plot, and the fact that (B.3) is continuous in a_0 and $\gamma_{\mathrm{ph}}\beta_{\mathrm{ph}}$, we infer that there is a zero-crossing at $\gamma_{\mathrm{ph}}\beta_{\mathrm{ph}} = a_0$. We can directly verify this by making the substitution in (B.3). From the sign on either side of the zero-crossing, we can also tell that this turning-point is a minimum in $\gamma_{\mathrm{ph}}\beta_{\mathrm{ph}}$ (note that a_0 is constant and $\gamma_{\mathrm{ph}}\beta_{\mathrm{ph}}$ is the variable in question here). These observations allow us to confidently infer Point 2 above, even though a rigorous mathematical proof is not given.

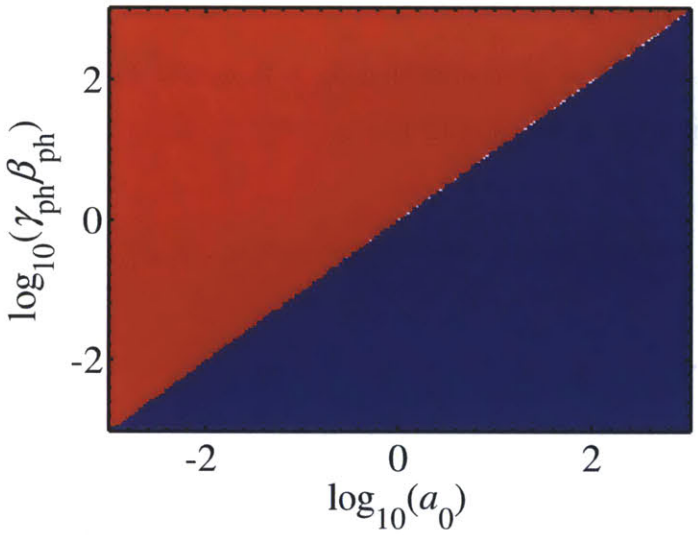

Fig. B-1: Color map of the sign of the expression (B.3) as a function of a_0 and $\gamma_{\mathrm{ph}}\beta_{\mathrm{ph}}$. Red denotes positive, blue negative and white (numerical) zero.

When $\gamma_{\mathrm{ph}}\beta_{\mathrm{ph}} = a_0$, the separatrix minimum is the least it can possibly be for fixed a_0. Its value is then

$$(\gamma\beta)_{\mathrm{sep\,min\,min}} = -a_0. \tag{B.4}$$

Appendix C

The objective of this appendix is to derive formulas for the paraxial electromagnetic fields of the radially-polarized Laguerre-Gauss (LG) vacuum modes without azimuthal variation, as well as formulas for properties like peak power and second irradiance moment of these beams. We will denote a LG beam with no azimuthal variation in vacuum using the symbol TM_{0p}, where p gives the order of its radial variation. A general LG beam in vacuum is denoted LG_{lp}, where l gives the order of its azimuthal variation (LG_{0p} is thus synonymous with TM_{0p}). We do not consider beams with azimuthal variations for particle acceleration since the lack of continuous rotational symmetry in the transverse plane (being the x-y plane in our choice of coordinate system) makes the beams unlikely candidates for effective acceleration of particle bunches along the beam axis. We thus treat only the TM_{0p} beams here. To benefit a more general audience, this exposition assumes a reader not familiar with solving Maxwell's equation in vacuum. The reader may also skip to Section C.4 for a summary of the formulas derived here.

According to Maxwell's equations, the electric field $\vec{E}$ and magnetic field $\vec{H}$ evolve in vacuum as

$$\begin{aligned} \nabla \cdot \varepsilon_0 \vec{E} &= 0 \\ \nabla \cdot \vec{H} &= 0 \\ \nabla \times \vec{E} &= -\frac{\partial \mu_0 \vec{H}}{\partial t} \cdot \\ \nabla \times \vec{H} &= \frac{\partial \varepsilon_0 \vec{E}}{\partial t} \end{aligned} \tag{C.1}$$

where ε_0 and μ_0 are the vacuum permittivity and permeability respectively. As described in any standard electromagnetics text (e.g. [Jac75]), the solutions for $\vec{E}$ and magnetic flux density $\vec{B} \equiv \mu_0 \vec{H}$ may be expressed in terms of vector potential $\vec{A}$ and scalar potential Φ as

$$\begin{aligned} \vec{E} &= -\frac{\partial \vec{A}}{\partial t} - \nabla \Phi \\ \vec{B} &= \nabla \times \vec{A} \end{aligned} \quad . \tag{C.2}$$

This is readily verified by substituting (C.2) into the second and third lines of (C.1), namely, Gauss's law for magnetism and Faraday's law respectively. Substituting (C.2) into the first and last lines of (C.1) – namely, Gauss's law and Ampere's law respectively – give partial differential equations that are used to solve for $\vec{A}$ and Φ. Before we proceed to obtain these equations, note that the same electromagnetic fields in (C.2) are obtained when we replace $\vec{A}$ and Φ by $\vec{A}'$ and Φ' respectively such that

$$\begin{aligned} \vec{A}' &= \vec{A} + \nabla V \\ \Phi' &= \Phi - \frac{\partial V}{\partial t} \end{aligned} \quad , \tag{C.3}$$

where V is an arbitrary function of space and time. We partially remove this degree of freedom by imposing an additional constraint on $\vec{A}$ and Φ known as the Lorentz gauge:

$$\frac{1}{c^2}\frac{\partial \Phi}{\partial t} = -\nabla \cdot \vec{A} \, , \tag{C.4}$$

where c is the vacuum speed of light: $c \equiv 1/\sqrt{\mu_0 \varepsilon_0}$. From the form of (C.4), one can see that the Lorentz gauge is Lorentz invariant, meaning that Lorentz-boosting into a different inertial frame of reference will transform $\vec{A}$ and Φ into a different pair functions that will nevertheless continue to satisfy an equation of the form (C.4). For a gauge that is not Lorentz invariant, such

as the Coulomb gauge ($\nabla \cdot \vec{A} = 0$), the gauge is fixed in one inertial frame of reference, but changes in form when one moves to a different frame. Under the Lorentz gauge, V in (C.3) must satisfy the additional constraint

$$\nabla^2 V - \frac{1}{c^2}\frac{\partial^2 V}{\partial t^2} = 0, \tag{C.5}$$

which results from substituting (C.3) into (C.4). To obtain the partial differential equations that can be solved for $\vec{A}$ and Φ, we substitute (C.2) into the first and last lines of (C.1) and simplify the result using (C.4) to get

$$\begin{aligned} \nabla^2 \vec{A} - \frac{1}{c^2}\frac{\partial^2 \vec{A}}{\partial t^2} &= 0 \\ \nabla^2 \Phi - \frac{1}{c^2}\frac{\partial^2 \Phi}{\partial t^2} &= 0 \end{aligned}, \tag{C.6}$$

A valid solution for $\vec{A}$ and Φ must satisfy both (C.4) and (C.6). Fourier transforming into the frequency domain, (C.4) and (C.6) become

$$\begin{aligned} \frac{jk}{c}\tilde{\Phi} &= -\nabla \cdot \tilde{\vec{A}} \\ \nabla^2 \tilde{\vec{A}} + k^2 \tilde{\vec{A}} &= 0, \\ \nabla^2 \tilde{\Phi} + k^2 \tilde{\Phi} &= 0 \end{aligned} \tag{C.7}$$

where $k \equiv \omega/c$ and the tilde (~) sign above any variable denotes the Fourier transform of that particular variable.

C.1 The paraxial wave equation

It is relatively complicated to obtain analytical solutions for a focused laser beam satisfying (C.7) (although we do undertake this in Appendix E, following the approach of [Apr10]). It pays

to see if we can simplify (C.7) into a differential equation for which analytical solutions are readily available. Let the vector potential $\vec{A}$ be polarized in one Cartesian direction, say, the z-direction:

$$\vec{A} = A\hat{z} = A_{0z}e^{i\eta}\hat{z}, \tag{C.8}$$

where $\eta \equiv \omega t - kz + \psi_0$, ψ_0 being a phase constant, and we have set $A = A_{0z}e^{i\eta}$ with the intention of treating A_{0z} as a time-independent envelope that varies slowly with z compared to the carrier factor $e^{i\eta}$. The time-independence of A_{0z} simply means that (C.8) is a CW solution. We will broach the matter of converting CW solutions of laser beams into pulsed solutions under the paraxial wave approximation in Appendix D. The assumption that A_{0z} varies slowly in z has been argued to lead to solutions that closely approximate the electromagnetic fields of a weakly-focused laser beam (see [Hau84] or any standard optics text).

Putting (C.8) into the second line of (C.7), we obtain

$$\left(\frac{\partial^2}{\partial x^2} + \frac{\partial^2}{\partial y^2} + \frac{\partial^2}{\partial z^2}\right)A_{0z} - 2ik\frac{\partial A_{0z}}{\partial z} = 0. \tag{C.9}$$

Since $\tilde{A}_{0z}$ is assumed to vary slowly in z, it is often assumed in what is known as the paraxial wave approximation that [Hau84]

$$\left|\frac{\partial^2 A_{0z}}{\partial z^2}\right| << \left|2k\frac{\partial A_{0z}}{\partial z}\right|, \tag{C.10}$$

which simplifies (C.9) to

$$\left(\frac{\partial^2}{\partial x^2} + \frac{\partial^2}{\partial y^2}\right)A_{0z} - 2ik\frac{\partial A_{0z}}{\partial z} = 0. \tag{C.11}$$

(C.11) is a very pleasing result because it is simply a two-dimensional Schrodinger equation in free space (with z in place of t), which has been studied to a great extent in nonrelativistic quantum physics. One of the most well-known solutions to (C.11) is the Gaussian beam. Although the Gaussian beam solution has enjoyed a lot of popularity as a model for the free-space propagation of weakly focused laser beams, it should be noted that the Gaussian beam in fact grossly violates (C.10) at certain points in space away from the beam axis, regardless of focusing, as we show in Section 3.1. Throughout this thesis, we have used the Gaussian beam solution only to model on-axis electrodynamics, and have moreover taken care to ensure that on-axis fields of paraxial beam agrees with those of the exact beam (derived in Appendix E) in our regime of interest (c.f. Section 3.1). The use of the Gaussian beam solution to model free-space electrodynamics away from the beam axis has been argued to be unreliable even for a weakly-focused beam [MVP13].

Once a solution to A_{0z} is obtained, we may derive the electromagnetic field of a radially-polarized laser beam via (C.2) as

$$\begin{aligned}\vec{E} &= -\frac{\mathrm{i}\omega}{k^2}\mathrm{e}^{\mathrm{i}\eta}\left[\hat{\mathrm{r}}\frac{\partial^2 A_{0z}}{\partial r\partial z}+\hat{z}\left(-2\mathrm{i}k\frac{\partial A_{0z}}{\partial z}-\frac{\partial^2 A_{0z}}{\partial z^2}\right)\right]\\ &\approx -\frac{\omega}{k}\mathrm{e}^{\mathrm{i}\eta}\left[\hat{\mathrm{r}}\frac{\partial A_{0z}}{\partial r}+\hat{\mathrm{z}}2\frac{\partial A_{0z}}{\partial z}\right]\\ \vec{B} &= -\hat{\phi}\mathrm{e}^{\mathrm{i}\eta}\frac{\partial A_{0z}}{\partial r}\end{aligned} \quad . \tag{C.12}$$

All that remains to obtain the real electromagnetic fields of a radially-polarized beam is to solve (C.11) for A_{0z} and then take the real part of (C.12).

C.2 Radially-polarized Laguerre-Gaussian modes in free space

A cylindrically-symmetric solution to (C.11) is the Laguerre-Gaussian beam:

$$
\begin{aligned}
A_{0z} &= A_0\left(fe^{-f\rho^2}\right)\left(\frac{f}{f^*}\right)^p L_p^l(2\rho^2 \mid f \mid^2)(f\rho)^l e^{\mathrm{i}l\phi} \\
&= A_0\left(fe^{-f\rho^2}\right)\left(\frac{f}{f^*}\right)^p L_p^0(2\rho^2 \mid f \mid^2), \quad l=0
\end{aligned}
\qquad (C.13)
$$

where $f \equiv \mathrm{i}/(\mathrm{i}+z/z_0)$, z_0 is the Rayleigh range of the fundamental mode (this physical interpretation of z_0 is justified by the result for the second irradiance moment computed in C.3) and $\rho \equiv r/w_0$, with w_0 related to z_0 by $z_0 \equiv kw_0{}^2/2$. $L_p^l(x)$ is the generalized Laguerre polynomial, which is given by the Rodrigues equation:

$$
L_p^l(x) = \sum_{m=0}^{p}(-1)^m \frac{(p+l)!}{(p-m)!(l+m)!m!}x^m . \qquad (C.14)
$$

The derivatives of (C.13) (for $l = 0$) relevant for evaluating (C.12) are

$$
\begin{aligned}
\frac{\partial A_{0z}}{\partial r} &= A_0\left(fe^{-f\rho^2}\right)\left(\frac{f}{f^*}\right)^p\left(\frac{2f\rho}{w_0}\right)\left(-L+2f^*L'\right) \\
\frac{\partial A_{0z}}{\partial z} &= A_0\left(fe^{-f\rho^2}\right)\left(\frac{f}{f^*}\right)^p \frac{f}{z_0}\left[\mathrm{i}L\left(1-f\rho^2+2pf^*\right)-L'4\rho^2 f^*\frac{z}{z_0}\mid f\mid^2\right]
\end{aligned}
\qquad (C.15)
$$

where $L \equiv L_p^0(2\rho^2 \mid f \mid^2)$, $L' \equiv \mathrm{d}L_p^0(x)/\mathrm{d}x\mid_{x=2\rho^2|f|^2} = -L_{p-1}^1(2\rho^2 \mid f \mid^2)$. A_0 is a scaling factor that may be taken as a real positive number without any loss of generality. We now proceed to derive formulas for the peak power and second irradiance moment of the beam.

C.3 Beam properties

Peak power P is given by

$$
\begin{aligned}
P &= \frac{2\pi}{\mu_0}\int \mathrm{Re}(E_r)\mathrm{Re}(B_\phi)\,r\,dr\Big|_{\eta=z=0} \\
&= \frac{2\pi c}{\mu_0}\int \mathrm{Re}\left(\frac{\partial A_{0z}}{\partial r}\Big|_{z=0}\right)^2 r\,dr \\
&= \frac{2\pi c}{\mu_0}\int \left[2\rho A_0 e^{-\rho^2}\left(-L_p^0(2\rho^2) - 2L_{p-1}^1(2\rho^2)\right)\right]^2 \rho\,d\rho \\
&= \frac{\pi c}{\mu_0}\int_0^\infty x A_0{}^2 e^{-x}\left[L_p^0{}^2(x) + 4L_p^0(x)L_{p-1}^1(x) + 4L_{p-1}^1{}^2(x)\right]dx
\end{aligned}
\qquad \text{(C.16)}
$$

To proceed, recall the three-point rule

$$
L_p^l(x) = L_p^{l+1}(x) - L_{p-1}^{l+1}(x), \qquad \text{(C.17)}
$$

and the Laguerre polynomial orthogonality relation (for integer l, m and n)

$$
\int_0^\infty x^l \mathrm{e}^{-x} L_n^l(x) L_m^l(x)\,dx = \frac{(n+l)!}{n!}\delta_{mn}. \qquad \text{(C.18)}
$$

We then have

$$
\begin{aligned}
P &= \frac{\pi c}{\mu_0}\int_0^\infty x A_0{}^2 e^{-x} L_p^0{}^2(x)\,dx \\
&= \frac{\pi c}{\mu_0} A_0{}^2 (2p+1)
\end{aligned}
\qquad \text{(C.19)}
$$

where the second equality is due again to application of (C.17) and (C.18). We may also write A_0 as a function of P:

$$
A_0 = \sqrt{\frac{\mu_0 P}{\pi c(2p+1)}}. \qquad \text{(C.20)}
$$

The second irradiance moment $\langle r^2 \rangle$ of a beam is often used to measure the tightness of its focusing:

$$\begin{aligned}\langle r^2 \rangle &\equiv \frac{\iint dA \langle S_z \rangle_t r^2}{\iint dA \langle S_z \rangle_t} \\ &= \frac{{w_0}^2}{2} \frac{\int_0^\infty x^2 e^{-x} \left(L_p^0(x) + 2L_{p-1}^1(x) \right)^2 dx}{\int_0^\infty x e^{-x} \left(L_p^0(x) + 2L_{p-1}^1(x) \right)^2 dx} \\ &= \frac{{w_0}^2}{2(2p+1)} \int_0^\infty x^2 e^{-x} \left(L_p^2(x) - L_{p-2}^2(x) \right)^2 dx \\ &= \frac{\left(p^2 + p + 1\right)}{(2p+1)} {w_0}^2\end{aligned} \quad , \tag{C.21}$$

where the angular brackets with subscript t refer to a time average, S_z is the Poynting vector $\vec{S} \equiv \vec{E} \times \vec{H}$ in the z-direction, and we have again used (C.17) and (C.18) in our derivation. For $p = 0$, the second irradiance moment is simply ${w_0}^2$, lending physical significance to w_0 as the waist radius of the beam.

C.4 Summary of formulas for radially-polarized Laguerre-Gaussian paraxial beams with no azimuthal variation

Here we give a summary of the salient formulas used or derived in this appendix. Consistent with the paraxial wave approximation (C.10), we found the electric field $\vec{E}$ and magnetic flux density $\vec{B}$ of a radially-polarized beam to be given by

$$\begin{aligned}\vec{E} &\approx -\frac{\omega}{k} e^{i\eta} \left[\hat{r} \frac{\partial A_{0z}}{\partial r} + \hat{z} 2 \frac{\partial A_{0z}}{\partial z} \right] \\ \vec{B} &= -\hat{\phi} e^{i\eta} \frac{\partial A_{0z}}{\partial r}\end{aligned} \quad . \tag{C.22}$$

where ω is the CW angular frequency, $k = \omega/c$ and $\eta = \omega t - kz + \psi_0$. The partial derivative expressions corresponding to a Laguerre-Gaussian beam with no azimuthal variation are given by

$$\begin{aligned} \frac{\partial A_{0z}}{\partial r} &= A_0\left(fe^{-f\rho^2}\right)\left(\frac{f}{f^*}\right)^p\left(\frac{2f\rho}{w_0}\right)\left(-L+2f^*L'\right) \\ \frac{\partial A_{0z}}{\partial z} &= A_0\left(fe^{-f\rho^2}\right)\left(\frac{f}{f^*}\right)^p\frac{f}{z_0}\left[\mathrm{i}L\left(1-f\rho^2+2pf^*\right)-L'4\rho^2f^*\frac{z}{z_0}|f|^2\right] \end{aligned}, \tag{C.23}$$

where $L \equiv L_p^0(2\rho^2|f|^2)$, $L' \equiv \mathrm{d}L_p^0(x)/\mathrm{d}x|_{x=2\rho^2|f|^2} = -L_{p-1}^1(2\rho^2|f|^2)$. $f \equiv \mathrm{i}/\left(\mathrm{i}+z/z_0\right)$, z_0 is the Rayleigh range of the fundamental mode and $\rho \equiv r/w_0$, with beam waist radius w_0 related to z_0 by $z_0 \equiv kw_0^{\,2}/2$. $L_p^l(x)$ is the generalized Laguerre polynomial, which is given by the Rodrigues equation:

$$L_p^l(x) = \sum_{m=0}^{p}(-1)^m\frac{(p+l)!}{(p-m)!(l+m)!m!}x^m. \tag{C.24}$$

The constant parameter A_0 is used to set the peak power P via the relation

$$A_0 = \sqrt{\frac{\mu_0 P}{\pi c(2p+1)}}. \tag{C.25}$$

Finally, the second irradiance moment, which may be used to compare the degree of focusing between beams of different orders, is given by

$$\left\langle r^2\right\rangle = \frac{\left(p^2+p+1\right)}{(2p+1)}w_0^{\,2}. \tag{C.26}$$

True CW operation is impossible in reality since a CW beam contains infinite energy (although of course a CW approximation can be very accurate when the actual pulse duration is very long). Appendix D discusses how to construct a pulsed solution from a paraxial CW beam solution without resorting to a complicated inverse Fourier transform.

Appendix D

The objective of this appendix is to show how to construct a pulsed solution from a paraxial CW beam solution, and to derive an approximate formula relating pulse energy to peak pulse power and pulse duration. The results of this appendix apply to any paraxial beam, not just the radially-polarized Laguerre-Gaussian beams.

Our first task is to determine a pulse envelope for a CW beam solution of the paraxial wave equation consistent with the paraxial wave approximation. Our derivation follows the procedure in [Mac00]. To begin, consider the pulsed scalar potential

$$A = A_{0z} e^{i\eta} g(\eta_1), \tag{D.1}$$

where $\eta \equiv \omega t - kz + \psi_0$, as before, and $\eta_1 \equiv \omega t - kz + \psi_1$, with ψ_1 being some constant that we can use, for instance, to control the initial pulse position z_i by setting $\psi_1 = kz_i$. $g(\eta_1)$ is the pulse envelope which form it is now our goal to determine and A_{0z} is some function of space (but not time) that satisfies the paraxial wave equation

$$\left(\frac{\partial^2}{\partial x^2} + \frac{\partial^2}{\partial y^2}\right) A_{0z} - 2ik\frac{\partial A_{0z}}{\partial z} = 0. \tag{D.2}$$

In other words, (D.1) is simply (C.8) multiplied by a pulse envelope. The original wave equation that A should approximately satisfy is

$$\nabla^2 A - \frac{1}{c^2}\frac{\partial^2 A}{\partial t^2} = 0, \tag{D.3}$$

Substituting (D.1) as an ansatz in (D.3), we obtain

$$e^{i\eta} g(\eta_1)\left(\frac{\partial^2}{\partial x^2} + \frac{\partial^2}{\partial y^2} + \frac{\partial^2}{\partial z^2}\right) A_{0z} + 2\frac{\partial\left[e^{i\eta} g(\eta_1)\right]}{\partial z}\frac{\partial A_{0z}}{\partial z} = 0. \tag{D.4}$$

Applying the paraxial wave approximation (C.10) to remove the second derivative with respect to z, we finally obtain

$$\left(\frac{\partial^2}{\partial x^2} + \frac{\partial^2}{\partial y^2}\right) A_{0z} - 2ik\frac{\partial A_{0z}}{\partial z}\left[1 - i\frac{g'(\eta_1)}{g(\eta_1)}\right] = 0, \tag{D.5}$$

where $g'(\eta_1) \equiv dg(\eta_1)/d\eta_1$. (D.5) reduces approximately to (D.2) – and so (D.4) is approximately solved – if the proposed form for $g(\eta_1)$ satisfies

$$\left|\frac{g'(\eta_1)}{g(\eta_1)}\right| << 1, \ \forall \eta_1 . \tag{D.6}$$

As pointed out in [Mac00], (D.6) is arbitrarily well satisfied by a sech pulse

$$\begin{aligned} g(\eta_1) &= \operatorname{sech}\left(\frac{\eta_1}{\xi_0}\right) \\ \left|\frac{g'(\eta_1)}{g(\eta_1)}\right| &= \left|\frac{1}{\xi_0}\tanh\left(\frac{\eta_1}{\xi_0}\right)\right| << 1, \ \forall \eta_1 \end{aligned} \tag{D.7}$$

for a large-enough value of the parameter ξ_0. This is not true for a Gaussian pulse:

$$g_{\text{gauss}}(\eta_1) = \exp\left(-\frac{\eta_1^2}{\xi_0}\right)$$
$$\left|\frac{g_{\text{gauss}}'(\eta_1)}{g_{\text{gauss}}(\eta_1)}\right| = \left|\frac{2\eta_1}{\xi_0}\right| . \tag{D.8}$$

The second line of (D.8) is violated for values of η_1 that are too large, which correspond to the region in the wings of the pulse. Because of this, we are motivated to use a sech pulse envelope to model our pulsed beam solution.

To convert the CW beam fields (C.22) to the fields of a pulsed beam, we simply multiply the fields with the pulse envelope $g(\eta_1)$. This is consistent with (D.6) because it assumes that, when (D.1) is substituted into (C.2), terms proportional to derivatives of $g(\eta_1)$ are negligible compared to those proportional to $g(\eta_1)$. To approximate the pulse energy in terms of peak pulse power P and the pulse duration parameter ξ_0, we write

$$\begin{aligned} U &\equiv \int \mathrm{d}t \iint \mathrm{d}A S_z \\ &\approx \left[\int \mathrm{d}t \,\mathrm{sech}^2\left(\frac{\eta}{\xi_0}\right)\right] \iint \mathrm{d}A \left\langle S_{z,\mathrm{CW}} \right\rangle_t , \\ &= \left[\frac{2\xi_0}{\omega}\right]\frac{P}{2} = \frac{P\xi_0}{\omega} \end{aligned} \tag{D.9}$$

which is consistent with our assumption that the carrier varies rapidly with respect to the pulse envelope. S_z is the Poynting vector in the z-direction and $S_{z,\mathrm{CW}}$ is likewise but computed from fields with the pulse envelope removed. The pulse duration parameter ξ_0 is related to the number of cycles n_{IFWHM} in the intensity full-width-half-maximum (FWHM) of the pulse as

$$\xi_0 = \frac{n_{\mathrm{IFWHM}}\pi}{\mathrm{arcsech}\left(1/\sqrt{2}\right)} \approx 3.5644 n_{\mathrm{IFWHM}} . \tag{D.10}$$

In many of our simulations, we control our pulse duration parameter via the number of cycles n_{HW} in the half-width-1/e-maximum of the *field* FWHM instead, after the convention of publications like [FPV10], so we have

$$\xi_0 = \frac{n_{HW} 2\pi}{\text{arcsech}(\exp(-1))} \approx 3.7909 n_{HW} . \tag{D.11}$$

Note that for a given ξ_0, n_{HW} and n_{IFWHM} are by definition very close to each other, which makes the choice of either convention for defining pulse duration a mere academic exercise for most purposes.

Appendix E

The objective of this appendix is to describe the procedure by which we compute the fields of an exact pulsed beam solution to Maxwell's equations in free space. In addition to what is outlined in [Apr10], we also describe issues related to the numerical implementation of the field solutions and how to overcome them.

We begin with the observation made in [Apr10] that an exact solution to the Helmholtz equation

$$\nabla^2\tilde{\Psi} + k^2\tilde{\Psi} = 0 \tag{E.1}$$

exists in form

$$\tilde{\Psi} = C_0 \exp(-ka)\frac{\sin(k\tilde{R})}{k\tilde{R}}, \tag{E.2}$$

where $\tilde{R} \equiv \sqrt{r^2 + (z + ia)^2}$, a is known as the confocal parameter, and C_0 is a (possibly complex) normalization constant used to determine the power of the beam. The factor $\exp(-ka)$, while not necessary in solving (E.1), is essential in preventing (E.2) from blowing up for even moderately large values of a.

E.1 Reduction to the paraxial beam scalar potential

Before going any further with (E.2), we would like to verify that it reduces to the paraxial beam scalar potential in the limit of large a. A rearrangement of the paraxial potential (C. 8) (with (C.13)) for the fundamental mode ($p = 0$) gives

$$\begin{aligned} A &= A_0 f e^{-f\rho^2} \exp(\mathrm{i}\eta) \\ &= A_0 \frac{iz_0}{z+iz_0} \exp\left(\frac{-\mathrm{i}kr^2}{2(z+iz_0)}\right)\exp(\mathrm{i}\eta)' \end{aligned} \tag{E.3}$$

In the limit of large a,

$$\begin{aligned} \tilde{R} &= \sqrt{r^2+(z+\mathrm{i}a)^2} \\ &= (z+\mathrm{i}a)\sqrt{1+\left(\frac{r}{z+\mathrm{i}a}\right)^2}, \\ &\approx z+\mathrm{i}a+\frac{r^2}{2(z+\mathrm{i}a)} \end{aligned} \tag{E.4}$$

where the last approximate equality involved a Taylor expansion of the square-root, assuming r is small enough for this to be valid. Substituting (E.4) into (E.2) gives the exact-solution counterpart to (E.3):

$$\begin{aligned} \tilde{\Psi}\exp(\mathrm{i}(\omega t+\psi_0)) &= C_0 \exp(\mathrm{i}(\omega t+\psi_0)-ka)\frac{\sin(k\tilde{R})}{k\tilde{R}} \\ &\approx C_0 \exp(\mathrm{i}(\omega t+\psi_0)-ka)\frac{\exp\left(\mathrm{ik}\left(z+\mathrm{i}a+\frac{r^2}{2(z+\mathrm{i}a)}\right)\right)-\exp\left(-\mathrm{ik}\left(z+\mathrm{i}a+\frac{r^2}{2(z+\mathrm{i}a)}\right)\right)}{2\mathrm{i}\left(z+\mathrm{i}a+\frac{r^2}{2(z+\mathrm{i}a)}\right)}, \\ &\approx C_0 \frac{\exp\left(\mathrm{ik}\left(2z+\frac{r^2}{2(z+\mathrm{i}a)}\right)\right)\exp(-2ka)-\exp\left(\frac{-\mathrm{ik}r^2}{2(z+\mathrm{i}a)}\right)}{2\mathrm{i}(z+\mathrm{i}a)}\exp(\mathrm{i}\eta) \\ &\approx \frac{C_0}{2}\frac{\mathrm{i}}{(z+\mathrm{i}a)}\exp\left(\frac{-\mathrm{ik}r^2}{2(z+\mathrm{i}a)}\right)\exp(\mathrm{i}\eta) \end{aligned} \tag{E.5}$$

where the approximate equality in the second line involves approximating $\tilde{R}$ as in (E.4), the approximate equality in the third line involves ignoring the r-dependence in the magnitude and the approximate equality in the last line involves dropping the backward-propagating term, which factor of $\exp(-2ka)$ makes it negligible compared to the forward propagating term for $ka \gg 1$, as is the case for a weakly-focused (i.e. paraxial) beam.

Except for a constant factor, the expression in the final line of (E.5) is equivalent to that in (E.3) when we set $z_0 = a$. We thus conclude that (E.2) reduces to the paraxial beam solution in the limit of large a.

E.2 From CW potential to time-domain pulsed potential

We would like to construct a pulsed scalar potential in the time-domain from the CW potential (E.2). We follow the recommendation of [Apr10] in performing an inverse Fourier transform with the Poisson spectrum. The inverse Fourier transform of the Poisson spectrum is

$$\int_{-\infty}^{\infty}\left[\left(\frac{s}{\omega_0}\right)^{s+1}\frac{\omega^s \exp(-s\omega/\omega_0)}{\Gamma(s+1)}\theta(\omega)\right]\exp(\mathrm{i}\omega t)\mathrm{d}\omega = \left(1-\frac{\mathrm{i}\omega_0 t}{s}\right)^{-s-1}, \tag{E.6}$$

where the expression in the square brackets is the Poisson spectrum. s is a parameter related to the pulse duration, ω_0 the peak angular frequency of the spectrum, $\Gamma(\cdot)$ the gamma function and $\theta(\cdot)$ the Heaviside step function. As noted in [Apr10],

$$\left(1-\frac{\mathrm{i}\omega_0 t}{s}\right)^{-s-1} \sim \exp\left(-\frac{t^2}{2s/\omega_0^{\,2}}+\mathrm{i}\omega_0 t\right), \quad s \gg 1, \tag{E.7}$$

which allows us to relate s to the number of cycles in the intensity FWHM of the pulse n_{IFWHM} as

$$s = \frac{(n_{\mathrm{IFWHM}}\pi)^2}{\ln 2} \approx 14.24 n_{\mathrm{IFWHM}}^{\,2} \approx (3.77 n_{\mathrm{IFWHM}})^2. \tag{E.8}$$

The time-domain scalar pulse which frequency domain spectrum is proportional to the product of the Poisson spectrum and the CW potential (E.2) is then

$$\Psi(t) = C_0 \frac{\exp(\mathrm{i}\psi_0)}{k_0 \tilde{R}} \left(f_+^{-s-1} - f_-^{-s-1} \right), \tag{E.9}$$

where $f_\pm = 1 - \frac{\mathrm{i}}{s}\left(\omega_0 t \pm k_0 \tilde{R} + \mathrm{i} k_0 a + \psi_1\right)$, ψ_0 is the phase constant associated with the carrier-envelope phase (much like in ψ_0 Appendix C) and ψ_1 is a constant that can be used to control the initial position of the pulse (much like in ψ_1 Appendix C). C_0 may be taken as a real normalization constant.

E.3 From scalar potential to vector electromagnetic fields

From (E.9), we would like to obtain vector electromagnetic fields of our mode of choice. Recall from Appendix C that in the Lorentz gauge,

$$\begin{aligned} \frac{1}{c^2}\frac{\partial \Phi}{\partial t} &= -\nabla \cdot \vec{A} \\ \nabla^2 \vec{A} - \frac{1}{c^2}\frac{\partial^2 \vec{A}}{\partial t^2} &= 0 \ , \\ \nabla^2 \Phi - \frac{1}{c^2}\frac{\partial^2 \Phi}{\partial t^2} &= 0 \end{aligned} \tag{E.10}$$

Since $\Psi(t)$ is a solution of the wave equation, we may determine $\vec{A}$ and Φ by, for instance, setting $\vec{A} = \Psi(t)\hat{\mathrm{i}}$ where $\hat{\mathrm{i}}$ is a unit vector in one of the Cartesian directions, and integrating for Φ via the first line of (E.10). An alternative approach that avoids integration involves using the Hertz potentials $\vec{\Pi}_\mathrm{e}$ and $\vec{\Pi}_\mathrm{m}$, related to $\vec{A}$ and Φ via the relation

$$\begin{aligned}\Phi &= -\nabla\cdot\vec{\Pi}_e \\ \vec{A} &= \frac{1}{c^2}\frac{\partial\vec{\Pi}_e}{\partial t}+\mu_0\nabla\times\vec{\Pi}_m\end{aligned}, \tag{E.11}$$

Substituting (E.11) into the first line of (E.10), one sees that the Lorentz gauge is automatically satisfied. Substituting (E.11) into the last two lines of (E.10) gives us wave equations for $\vec{\Pi}_e$ and $\vec{\Pi}_m$:

$$\begin{aligned}\nabla^2\vec{\Pi}_e-\frac{1}{c^2}\frac{\partial^2\vec{\Pi}_e}{\partial t^2}&=0 \\ \nabla^2\vec{\Pi}_m-\frac{1}{c^2}\frac{\partial^2\vec{\Pi}_m}{\partial t^2}&=0\end{aligned}. \tag{E.12}$$

Substituting (E.11) into (C.2) gives us the electromagnetic fields in terms of the Hertz potentials:

$$\begin{aligned}\vec{E} &= \nabla\times\nabla\times\vec{\Pi}_e-\mu_0\frac{\partial\vec{\Pi}_m}{\partial t} \\ \vec{H} &= \nabla\times\nabla\times\vec{\Pi}_m+\varepsilon_0\frac{\partial\vec{\Pi}_e}{\partial t}\end{aligned}, \tag{E.13}$$

To get the fields of a linearly-polarized pulsed beam, we set $\vec{\Pi}_e=\Psi(t)\hat{\mathrm{x}}$ and $\vec{\Pi}_m=0$ to obtain

$$\begin{aligned}\vec{E}_{\mathrm{LP}} &= \left[-\hat{\mathrm{x}}\left(\frac{\partial^2}{\partial y^2}+\frac{\partial^2}{\partial z^2}\right)+\hat{\mathrm{y}}\frac{\partial^2}{\partial x\partial y}+\hat{\mathrm{z}}\frac{\partial^2}{\partial x\partial z}\right]\Psi \\ \vec{H}_{\mathrm{LP}} &= \left[\hat{\mathrm{y}}\varepsilon_0\frac{\partial^2}{\partial z\partial t}-\hat{\mathrm{z}}\varepsilon_0\frac{\partial^2}{\partial y\partial t}\right]\Psi\end{aligned}, \tag{E.14}$$

To get the fields of a radially-polarized pulsed beam, we set $\vec{\Pi}_e = \Psi(t)\hat{z}$ and $\vec{\Pi}_m = 0$ to obtain

$$\begin{aligned} \vec{E}_{RP} &= \left[\hat{r}\frac{\partial^2}{\partial r \partial z} - \hat{z}\frac{1}{r}\frac{\partial}{\partial r}\left(r\frac{\partial}{\partial r}\right)\right]\Psi \\ \vec{H}_{RP} &= -\hat{\phi}\varepsilon_0\frac{\partial^2}{\partial r \partial t}\Psi \end{aligned}, \tag{E.15}$$

Note that higher-order generalizations of (E.2) would allow us to model higher-order vacuum modes. Some of these solutions have been explored in [Apr08].

E.4 Circumventing numerical singularities by Taylor series expansion

The presence of factors of $1/\tilde{R}$ in the analytical solution for the electromagnetic fields makes a straightforward numerical computation of the fields challenging where $\tilde{R}$ is close to 0 in magnitude. To avoid numerical errors, the formula for $\Psi(t)$ that we use when $\tilde{R}$ is close to 0 involves a Taylor series expansion of (E.2) about $\tilde{R} = 0$. Specifically,

$$\begin{aligned} &\Psi(t) \\ &= C_0\int_{-\infty}^{\infty}\left[\left(\frac{s}{\omega_0}\right)^{s+1}\frac{\omega^s \exp(-s\omega/\omega_0)}{\Gamma(s+1)}\theta(\omega)\right]\frac{2i}{k_0 e^{ka}}\sum_{n=0}^{\infty}\frac{k^{2n+1}\tilde{R}^{2n}(-1)^n}{(2n+1)!}\exp(i\omega t)d\omega \\ &= C_0\sum_{n=0}^{\infty}\frac{2}{k_0 c^{2n+1}}\frac{\tilde{R}^{2n}}{(2n+1)!}\left(\frac{\partial}{\partial t}\right)^{2n+1} f^{-s-1} \\ &= C_0\sum_{n=0}^{\infty}\frac{2i(k_0\tilde{R})^{2n}}{s^{2n+1}(2n+1)!}(-1)^n\left[\prod_{m=1}^{2n+1}(s+m)\right]f^{-s-2n-2} \end{aligned}, \tag{E.16}$$

where $f = 1 - \frac{i}{s}(\omega_0 t + ik_0 a + \psi_1)$. Note that we no longer have factors of $1/\tilde{R}$ to deal with. When asked to compute the value of a field at a certain point in space-time, our algorithm first

tests to see if $|\tilde{R}| < \varepsilon$, where ε is a value between 0 and 1 (a reasonable value is 0.5), and uses the field formulas computed from (E.16) if $|\tilde{R}| < \varepsilon$. Otherwise it uses the field formulas computed from (E.2).

Appendix F

The objective of this appendix is to give a more thorough discussion of the electromagnetic fields of a moving electron (5.4), as well as to present the space-charge formulas to which one may reduce (5.4) if one may assume that the velocity of each electron changes negligibly enough between the retarded time and the present time.

F.1 Electromagnetic fields of a moving electron

As in the main body of the text, let $\vec{E}_i(t,\vec{r})$ and $\vec{B}_i(t,\vec{r})$ be respectively the electric field and magnetic flux density observed at time t and position $\vec{r}$, due to particle i moving in vacuum. These fields may be obtained via the Liénard-Wiechert potentials, which solve Maxwell's equations for a point charge moving in vacuum [1]. The observed electromagnetic fields are:

$$\vec{E}_i(t,\vec{r}) = \frac{q}{4\pi\varepsilon_0}\frac{1}{\eta^3_{i,\tilde{t}_i}(\vec{r})R_{i,\tilde{t}_i}(\vec{r})}\left\{\frac{\vec{u}_{i,\tilde{t}_i}(\vec{r})}{\gamma^2_{i,\tilde{t}_i}R_{i,\tilde{t}_i}(\vec{r})}+\frac{1}{\mathrm{c}}\left[\hat{i}_{i,\tilde{t}_i}(\vec{r})\times\left(\vec{u}_{i,\tilde{t}_i}(\vec{r})\times\frac{\dot{\vec{v}}_{i,\tilde{t}_i}}{\mathrm{c}}\right)\right]\right\}, \qquad \text{(F.1)}$$

$$\vec{B}_i(t,\vec{r}) = \frac{1}{\mathrm{c}}\hat{i}_{i,\tilde{t}_i}(\vec{r})\times\vec{E}_i(t,\vec{r})$$

where ε_0 is the permittivity of free space, q the particle's charge and c the speed of light in vacuum. $\vec{r}_{i,s}$, $\vec{v}_{i,s}$, $\dot{\vec{v}}_{i,s}$ and $\gamma_{i,s}=\left(1-\left|\vec{v}_{i,s}\right|^2/c^2\right)^{-1/2}$ are respectively the position, velocity, acceleration and Lorentz factor of particle i at time s. $\vec{R}_{i,s}(\vec{r})\equiv\vec{r}-\vec{r}_{i,s}$, $R_{i,s}(\vec{r})\equiv\left|\vec{R}_{i,s}(\vec{r})\right|$,

$\vec{u}_{i,s}(\vec{r}) \equiv \hat{i}_{i,s}(\vec{r}) - \vec{v}_{i,s}/\mathrm{c}$, $\eta_{i,s}(\vec{r}) \equiv \mathrm{d}t/\mathrm{d}\tilde{t}_i|_{\tilde{t}_i=s} = 1 - \hat{i}_{i,s}(\vec{r}) \cdot \vec{v}_{i,s}/\mathrm{c} = \hat{i}_{i,s}(\vec{r}) \cdot \vec{u}_{i,s}(\vec{r})$ and

$\hat{i}_{i,s}(\vec{r}) = \vec{R}_{i,s}(\vec{r})/R_{i,s}(\vec{r})$ is the unit vector that points from particle *i*'s position at time *s* toward the observation position $\vec{r}$. The term in (F.1) that falls off as the inverse of the inter-particle distance $R_{i,\tilde{t}_i}$ is known as the radiation field (far-field), whereas the term falling off as the inverse of $R_{i,\tilde{t}_i}^2$ is known as the velocity field (near-field).

Although our notation appears complicated, we prefer it when introducing (F.1) because it makes the functional dependencies of every variable clear: $\eta_{i,s}(\vec{r})$, for instance, is simply read as "the variable η corresponding to particle *i* at time *s* and observation point $\vec{r}$". $\tilde{t}_i = \tilde{t}_i(t,\vec{r})$ is the retarded time along particle *i*'s trajectory corresponding to observation time *t* and observation point $\vec{r}$. Given observation coordinates *t* and $\vec{r}$, the retarded time $\tilde{t}_i$ solves the implicit equation

$$\tilde{t}_i = t - \frac{R_{i,\tilde{t}_i}(\vec{r})}{c} . \qquad \text{(F.2)}$$

In other words, the retarded time is defined so that the following is true: The difference between the observation time and the retarded time is exactly equal to the time taken by light in the medium to travel the shortest distance possible (i.e. in a straight line) between the particle's position at the retarded time and the observer's position. The reason the retarded time is not equal to the present time *t* is because light needs time to travel from one point to another. Fields (note that we write "fields" instead of "radiation" because we refer to both near-fields and far-fields, both of which need time to travel) arriving at $\vec{r}$ at time *t* must have been emitted at an earlier time by the particle. This earlier time is precisely the retarded time $\tilde{t}_i$ that we seek. Fig. F-1 illustrates the physical significance of several quantities in (F.1) and (F.2).

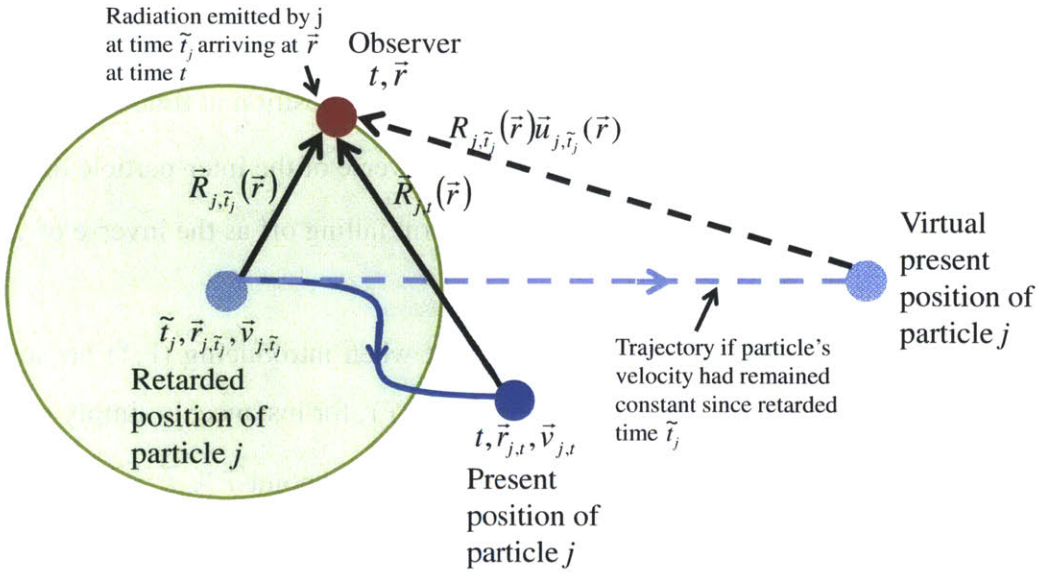

Fig. F-1: Diagram illustrating physical significance of quantities defined in the text. At time t, fields (including near-fields and far-fields) emitted by the particle (particle *j*) arrives at the observer's position $\vec{r}$. The time at which the particle emitted the field is known as the retarded time.

Fig. F-1 introduces a new term: the "virtual present position" of a particle. This is simply the position the particle would have occupied had it remained traveling at a constant velocity since the retarded time in question. $R_{i,\tilde{t}_i}(\vec{r})\vec{u}_{i,\tilde{t}_i}(\vec{r}) = R_{i,\tilde{t}_i}(\vec{r})\hat{i}_{i,\tilde{t}_i}(\vec{r}) - \vec{v}_{i,\tilde{t}_i}\left(R_{i,\tilde{t}_i}(\vec{r})/\mathrm{c}\right)$ then has the physical significance of being the displacement of the observer from the virtual present position of particle *i*. In the case where a particle really travels with a constant velocity, the present position precisely coincides with the virtual present position. Note that in any case, the electric near-field (the first term of the first line in (F.1)) points in the direction from the virtual present position toward the observation position.

Because (F.2) must be solved implicitly for $\tilde{t}_i$, it may not be obvious that there is at most one solution for $\tilde{t}_i$ given observation coordinates (*t*,*x*,*y*,*z*). To see this, consider the function

$$f(s) = (t-s) - \frac{R_{i,s}(\vec{r})}{c} = (t-s) - \frac{|\vec{r} - \vec{r}_i(s)|}{c} . \qquad \text{(F.3)}$$

When $f = 0$ in (F.3), (F.2) is recovered (with s set to $\tilde{t}_i$). Solving (F.2) is thus equivalent to finding the zero-crossing of f in (F.3). To prove that f has at most one zero-crossing – and hence that (F.2) has at most one value of $\tilde{t}_i$ corresponding to a given (t,x,y,z) – it is sufficient to show that the derivative of f with respect to s is never 0. This is done as

$$\frac{\partial f}{\partial s} = -1 + \hat{i}_{i,s}(\vec{r}) \cdot \vec{v}_i(s)/\mathrm{c} \neq 0 \ , \tag{F.4}$$

where we know the derivative is never 0 since that would require the particle to travel exactly at the speed of light in vacuum, which it never can due to its non-zero mass. From the way f is composed of physical quantities, it is reasonable to assume that f varies smoothly and continuously in s. If f is smooth and continuous and has no stationary point in s, f must be either strictly increasing or strictly decreasing in s. This allows for at most one zero crossing. Note that our proof did not use the fact that $\tilde{t}_i \leq t$, which causality requires.

The fact that $\tilde{t}_i$ has at most one solution for given (t,x,y,z) and given source particle i implies that if we choose (t,x,y,z) to lie along the world line of this particle i, $\tilde{t}_i = t$ is the only solution since $\tilde{t}_i = t$ is clearly one of the solutions. This has an important implication for computing space-charge using (F.1) in vacuum electrodynamic simulations: (F.1) cannot be used to compute the effect of electromagnetic fields emitted by a certain point particle on itself, since then $R_{i,\tilde{t}_i} = 0$ and (F.1) predicts infinite electromagnetic fields acting on the particle. This is akin to how it is nonsensical to use Coulomb's law to predict the electrostatic force of a certain stationary point charge on itself. The radiation reaction experienced by a particle when it radiates must be taken into account by other terms in the electrodynamic equations.

In our simulations, when the computed $R_{i,\tilde{t}_i}$ between two distinct particles is smaller than a certain value (for electrons, this value may be chosen to be the classical electron radius, of about 2.82×10^{-15}m), we assume that the affected particle experiences no forces from the source particle. In other words, we consider the two particles to be part of a larger macro-particle for the purposes of the computation.

The total electromagnetic field observed at time t and position $\vec{r}$ due to a particle bunch moving in vacuum is given by

$$\begin{aligned}\vec{E}(t,\vec{r}) &= \sum_i \vec{E}_i(t,\vec{r}) \\ \vec{B}(t,\vec{r}) &= \sum_i \vec{B}_i(t,\vec{r})\end{aligned} \tag{F.5}$$

As we have mentioned, (F.1) includes both the near-field and the far-field, which are given respectively by the first and second term in the first line. In simulating the inter-particle interactions of a localized particle bunch, the far-field – which is proportional to the inverse of the inter-particle distance R – is often insignificant compared to the near-field, which is proportional to the inverse of R^2. For greater computational speed, one may thus choose to drop the far-field component of the calculation.

If the effect of the radiation field is insignificant and we assume that each particle always travels at its present velocity during each time step, (F.1) can be simplified to a function of only t, making (2.1) an ordinary differential equation and reducing the computation of inter-particle forces considerably. The formulas that should replace (F.1) are then the space-charge formulas obtained by Lorentz-boosting the Coulomb field of each electron from the electron's rest frame to the lab frame. These formulas are used in particle tracer programs like the General Particle Tracer (GPT) [27].

F.2 Space-charge in the limit of a constantly-moving particle

It is possible to take inter-particle interaction into account while keeping the Lorentz force equation as an ordinary differential equation if we make the approximation that each particle has always been traveling at its present velocity at a given time step, and that the effect of the radiation field is insignificant. This is done in many particle tracking algorithms including the General Particle Tracer (GPT) [5].

In this case, to compute the force exerted on particle i by particle j, we transform into the rest frame of particle j, compute the static Coulomb force that j exerts on i in this frame, and transform this force back into the laboratory frame. This involves two Lorentz boosts: one into

the rest frame of j and one back into the laboratory frame, for each particle j. Let i be located at observation point $(t,\vec{r})$ in the laboratory frame. The electromagnetic fields that i experiences due to j are then

$$\begin{aligned}\vec{E}(t,\vec{r}) &= \sum_{j,j\neq i}\gamma_j\left[\vec{E}_{ij}{}' - \frac{\gamma_j{}^2}{\gamma_j+1}\left(\vec{\beta}_j\cdot\vec{E}_{ij}{}'\right)\vec{\beta}_j\right] \\ \vec{B}(t,\vec{r}) &= \sum_{j,j\neq i}\frac{\gamma_j\vec{\beta}_j\times\vec{E}_{ij}{}'}{\mathrm{c}}\end{aligned}, \tag{F.6}$$

where all non-primed variables are evaluated in the laboratory frame (at time t) and all primed variables are their Lorentz-transformed counterparts in the rest frame of particle j. $\vec{E}_{ij}{}'$ is the static Coulomb field that j exerts on i in the rest frame of j, $\vec{\beta}_j = \vec{v}_j/\mathrm{c}$ and $\gamma_j = \left(1-\left|\vec{\beta}_j\right|^2\right)^{-1/2}$. In the rest frame of j, we have

$$\begin{aligned}\vec{E}_{ij}{}' &= \frac{q\vec{r}_{ij}{}'}{4\pi\varepsilon_0\left|\vec{r}_{ij}{}'\right|^2} \\ \vec{r}_{ij}{}' &= \vec{r}_{ij} + \frac{\gamma_j{}^2}{\gamma_j+1}\left(\vec{r}_{ij}\cdot\vec{\beta}_j\right)\vec{\beta}_j\end{aligned}. \tag{F.7}$$

where $\vec{r}_{ij} = \vec{r} - \vec{r}_j(t) \equiv \vec{R}_{j,t}(\vec{r})$ is the displacement vector pointing from the position of j to that of i at time t. To see that (F.6) and (F.7) give precisely the electromagnetic fields in (F.1) and (F.5) when the particles are assumed to travel at velocities that are constant in time, we simplify (F.1) for the case of a single particle j traveling at $\vec{v}_j$ for all time and acting on a particle i located at observation point $(t,\vec{r})$:

$$\vec{E}(t,\vec{r}) = \frac{q}{4\pi\varepsilon_0}\frac{\vec{r}_{ij}}{|\vec{r}_{ij}|^3}\frac{1}{\gamma_j^2\left[1-\left(|\vec{v}_j|\sin\theta_t/\mathrm{c}\right)^2\right]^{3/2}}, \tag{F.8}$$

Note that all variables of particle j in (F.8) are computed at the observation time t. Fig. F-2 illustrates some of the relevant variables used in (F.7) and in deriving (F.8).

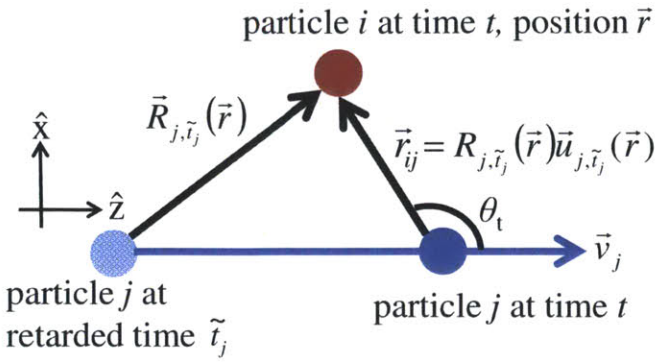

Fig. F-2: Schematic illustrating the physical significance of quantities used in (F.7) and (F.8). Particle j travels at constant velocity $\vec{v}_j$, and its fields act on particle i.

We can re-write $\vec{r}_{ij}'$ in terms of θ_t and $\vec{r}_{ij}$ as

$$\vec{r}_{ij}' = |\vec{r}_{ij}|\left(\hat{x}\sin\theta_t + \hat{z}\gamma_j\cos\theta_t\right), \tag{F.9}$$

where $\hat{z}$ and $\hat{x}$ are orthonormal basis vectors such that $\hat{z}$ points in the direction of particle j's travel and $\hat{x}$ lies in the plane of both particles, as defined in Fig. F-1. Substituting (F.9) into (F.6) and (F.7) for a single particle j acting on i gives us

$$\vec{E}(t,\vec{r}) = \gamma_j \frac{q\vec{r}_{ij}}{4\pi\varepsilon_0|\vec{r}_{ij}'|^3} = \gamma_j \frac{q}{4\pi\varepsilon_0}\frac{\vec{r}_{ij}}{\left[|\vec{r}_{ij}|\gamma_j\sqrt{1-\left(|\vec{v}_j|\sin\theta_t/c\right)^2}\right]^3}, \tag{F.10}$$

which is precisely (F.8). To see that the magnetic fields in (F.6) and (F.1) are also consistent, note that

$$\hat{i}_{j,\tilde{t}_j}(\vec{r}) = \frac{\vec{r}_{ij}}{|\vec{r}_{ij}'|} + \frac{\vec{v}_j}{c}. \tag{F.11}$$

The first term of (F.11) is parallel to $\vec{E}$ in (F.10), whereas the second term of (F.11) is parallel to the second term of $\vec{E}$ within the summation in (F.6). As a result, we have

$$\frac{1}{c}\hat{i}_{j,\tilde{t}_j}(\vec{r})\times\vec{E}(t,\vec{r})=\frac{1}{c}\frac{\vec{v}_j}{c}\times\left(\gamma_j\vec{E}_{ij}{}'\right)=\frac{\gamma_j\vec{\beta}_j\times\vec{E}_{ij}{}'}{c}\ . \qquad \text{(F.12)}$$

The left-hand side of (F.12) is the expression for $\vec{B}$ given in (F.1), whereas the rightmost side of (F.12) is the expression for $\vec{B}$ (associated with particle *j*) given in (F.6). Using (F.6) and (F.7) to approximate the inter-particle forces is thus equivalent to using the exact formulas (F.1) and (F.5) under the assumption at every instant in time that the particles have been travelling at their respective instantaneous velocities for all time.

List of Acronyms

RF	Radio-frequency
CW	Continuous-wave
THz	Terahertz
TM	Transverse-magnetic
TM_{0p}	Transverse-magnetic mode of azimuthal order 0 (i.e. no azimuthal variations) and radial order p
LG	Laguerre-Gauss/ Laguerre-Gaussian
LG_{lp}	Laguerre-Gauss mode of azimuthal order l and radial order p.
FWHM	Full-width-half-maximum
FFT	Fast Fourier transform
FEL	Free electron laser
ICS	Inverse Compton scattering

Partial List of Symbols

E_0	Electric field amplitude
ε_0	Permittivity of free space
ψ	Carrier's total phase
ψ_0	Carrier phase constant
q	Charge
m	Mass
ω	Angular carrier frequency
λ	Wavelength in vacuum
k	Magnitude of wavevector
c	Speed of light in vacuum
β	Particle speed normalized to c
γ	Relativistic Lorentz factor
β_{ph}	Phase velocity normalized to c
γ_{ph}	Relativistic Lorentz factor of a particle moving at normalized speed β_{ph}
K_{ph}	Kinetic energy of a particle moving at normalized speed β_{ph}
a_0	Field vector potential, $a_0 = qE_0/(mc\omega)$
$G(\psi)$	$a_0\beta_{\text{ph}}(\sin\psi - \sin\psi_s) + (\gamma - \gamma\beta\beta_{ph})_s$, where subscript s denotes initial conditions
H	Hamiltonian
P	Peak pulse power
w_0	Beam waist radius
z_0	Rayleigh range ($z_0 = \pi w_0^2/\lambda$)

η_0	Vacuum impedance
ξ_0	Pulse duration parameter (proportional to pulse duration)
E_K	Kinetic energy of particle
D	Protracted collision position
$\langle x \rangle$	Mean of variable x
σ_x	Standard deviation of variable x
N	Number of interaction cycles in nonlinear Thomson scattering
ω_{cr}	Critical frequency of synchrotron radiation
$\frac{d^2 I}{d\omega d\Omega}$	Spectral intensity of nonlinear Thomson scattering radiation in J/(rad/s)/sr

Bibliography

[Apr08] A. April, "Nonparaxial Elegant Laguerre-Gaussian Beams." Opt. Lett. 33, 1392–1394 (2008).

[Apr10] A. April, "Ultrashort, strongly focused laser pulses in free space," in *Coherence and Ultrashort Pulse Laser Emission*, edited by F. J. Duarte, InTech (2010).

[AAG+11] F. Albert, S. G. Anderson, D. J. Gibson, R. A. Marsh, C. W. Siders, C. P. J. Barty, and F. V. Hartemann, "Three-dimensional theory of weakly nonlinear Compton scattering." Phys. Plasmas 18 (2011).

[AJK+12] S. Antipov, C. Jing, A. Kanareykin, J. E. Butler, V. Yakimenko, M. Fedurin, K. Kusche, and W. Gai, "Experimental demonstration of wakefield effects in a THz planar diamond accelerating structure," Appl. Phys. Lett. 100 132910 (2012).

[ASB+12] G. Andonian, D. Stratakis, M. Babzien, S. Barber, M. Fedurin, E. Hemsing, K. Kusche, P. Muggli, B. O'Shea, X. Wei, O. Williams, V. Yakimenko, and J. B. Rosenzweig, "Dielectric wakefield acceleration of a relativistic electron beam in a slab-symmetric dielectric lined waveguide," Phys. Rev. Lett. 108, 244801 (2012).

[BET03] S. V. Bulanov, T. Esirkepov, and T. Tajima, "Light intensification towards the Schwinger limit." Phys. Rev. Lett. 91, 085001 (2003).

[BPP+04] S.-W. Bahk, P. Rousseau, T. A. Planchon, V. Chvykov, G. Kalintchenko, A. Maksimchuk, G. A. Mourou, and V. Yanovsky, "Generation and characterization of the highest laser intensities (1022W/cm2)", Opt. Lett. 29, 2837 (2004).

[BZ07] P. Baum and A. Zewail, "Attosecond electron pusles for 4D diffraction and microscopy," Proc. Natl. Acad. Sci. USA 102, 18409–18414 (2007).

[Cha71] Y. W. Chan, "Ultra-intense laser radiation as a possible energy booster for relativistic charged particle", Phys. Lett. 35A, 305 (1971).

[Cow03] B. M. Cowan, "Two-dimensional photonic crystal accelerator structures," Phys. Rev. STAB 6, 101301 (2003).

[Cow08] B. M. Cowan. "Three-dimensional dielectric photonic crystal structures for laser-driven acceleration," Phys. Rev. STAB 11, 011301 (2008).

[CCE+10] B. E. Carlsten, E. R. Colby, E. H. Esarey, M. Hogan, F. X. Kärtner, W. S. Graves, W. P. Leemans, T. Rao, J. B. Rosenzweig, C. B. Schroeder, D. Sutter, W. E. White, "New source technologies and their impact on future light sources", Nucl. Instrum. Meth. A 622, 657-668 (2010).

[CDL+07] G. Chang, C. J. Divin, C.-H. Liu, S. L. Williamson, A. Galvanauskas, and T. B. Norris. "Generation of radially polarized terahertz pulses via velocity-mismatched optical rectification." Opt. Lett. **32**, 433–435 (2007).

[CEL01] P. Catravas, E. Esarey, and W. P. Leemans, "Femtosecond x-rays from Thomson scattering using laser wakefield accelerators." Meas. Sci. Technol. 12, 1828 (2001).
[CFB+11] H. N. Chapman, P. Fromme, A. Barty, T. A. White, R. A. Kirian, A. Aquila, M. S. Hunter, et. al, "Femtosecond X-ray Protein Nanocrystallography," Nature 470 73–77 (2011).
[CGL83] T. F. Chan, G. H. Golub, and R. J. LeVeque, "Algorithms for computing the sample variance: Analysis and recommendations," The American Statistician 37, 242-247 (1983).
[CMD+93] C. E. Clayton, K. A. Marsh, A. Dyson, M. Everett, A. Lal, W. P. Leemans, R. Williams, and C. Joshi, "Ultrahigh-gradient acceleration of injected electrons by laser-excited relativistic electron plasma waves", Phys. Rev. Lett. 70, 37 (1993).
[CMU98] S. Chen, A. Maksimchuk and D. Umstadter, "Experimental observation of relativistic nonlinear Thomson scattering," Nature 396, 653–655 (1998).
[CPZ85] E. D. Courant, C. Pellegrini, and W. Zakowicz, "High-energy inverse free-electron-laser accelerator", Phys. Rev. A 32, 2813 (1985).
[CTT+04] C. G. R. Geddes, Cs. Toth, J. van Tilborg, E. Esarey, C. B. Schroeder, D. Bruhwiler, C. Nieter, J. Cary and W. P. Leemans, "High-quality electron beams from a laser wakefield accelerator using plasma-channel guiding," Nature 431, 538–541 (2004).
[EP95] E. Esarey, and Mark Pilloff. "Trapping and acceleration in nonlinear plasma waves," Phys. Plasmas 2, 1432–1436 (1995).
[ERS93] E. Esarey, S. K. Ride and P. Sprangle, "Nonlinear Thomson scattering of intense laser pulses from beams and plasmas," Phys. Rev. E 48, 3003–3021 (1993).
[ESK95] E. Esarey, P. Sprangle, and J. Krall, "Laser acceleration of electrons in vacuum," Phys. Rev. E 52, 5443 (1995).
[ESK+96] E. Esarey, P. Sprangle, J. Krall, and A. Ting, "Overview of Plasma-Based Accelerator Concepts", IEEE Trans. Plasma Sci. 24, 252 (1996).
[ESL09] E. Esarey, C. B. Schroeder, and W. P. Leemans, "Physics of laser-driven plasma-based electron accelerators," Rev. Mod. Phys. 81(3), 1229–1285 (2009).
[FBC+11] D. Filippetto, M. Bellaveglia, M. Castellano, E. Chiadroni, L. Cultrera, G. Di Pirro, M. Ferrario, et al. "Phase Space Analysis of Velocity Bunched Beams." Physical Review Special Topics - Accelerators and Beams 14, 092804 (2011).
[FGP+04] J. Faure, Y. Glinec, A. Pukhov, S. Kiselev, S. Gordienko, E. Lefebvre, J.-P. Rousseau, F. Burgy and V. Malka, "A laser–plasma accelerator producing monoenergetic electron beams," Nature 431, 541–544 (2004).
[FP83] J. R. Fontana, R. H. Pantell, "A high-energy, laser accelerator for electrons using the inverse Cherenkov effect", J. Appl. Phys. 54, 4285 (1983).
[FPA+10] J. A. Fülöp, L. Pálfalvi, G. Almási, and J. Hebling, "Design of high-energy terahertz sources based on optical rectification," Opt. Express 18, 12311–12327 (2010).
[FPV10] P.-L. Fortin, M. Piché, and C. Varin, "Direct-field electron acceleration with ultrafast radially-polarized laser beams: Scaling laws and optimization," J. Phys. B: At. Mol. Opt. Phys. 43 025401 (2010).
[Gao04] J. Gao, "Thomson scattering from ultrashort and ultraintense laser pulses," Phys. Rev. Lett. 93, 243001 (2004).
[GBA+08] T. Grosjean, F. Baida, R. Adam, J.-P. Guillet, L. Billot, P. Nouvel, J. Torres, A. Penarier, D. Charraut, and L. Chusseau. "Linear to radial polarization conversion in the THz domain using a passive system." Opt. Express 16, 18895–18909 (2008).

[GBK+09] W. S. Graves, W. Brown, F. X. Kaertner and D. E. Moncton, "MIT Inverse Compton Source Concept." Nucl. Instrum. Meth. A 1, S103–S105 (2009).

[GJM+00] G. Gallot, S. P. Jamison, R. W. McGowan, and D. Grischkowsky. "Terahertz waveguides." J. Opt. Soc. Am. B **17**, 851–863 (2000).

[GPT] *GPT User Manual*, Pulsar Physics.

[GSC+88] W. Gai, P. Schoessow, B. Cole, R. Konecny, J. Norem, J. Rosenzweig, and J. Simpson, "Experimental demonstration of wake-field effects in dielectric structures," Phys. Rev. Lett. 61, 2756–2758 (1988).

[Haa95] C. M. Haaland, "Laser electron acceleration in vacuum," Opt. Comm. 114, 280-284 (1995).

[Haa96] C. M. Haaland, "Response to comments on laser electron acceleration in vacuum," Opt. Comm. 124, 74-78 (1996).

[Hau84] H. A. Haus, *Waves and Fields in Optoelectronics* (Prentice Hall, 1984).

[HAS+10] F. V. Hartemann, F. Albert, C. W. Siders, and C. P. J. Barty. "Low-intensity nonlinear spectral effects in Compton scattering," Phys. Rev. Lett. 105, 130801 (2010).

[HK07] Z. Huang and K.-J. Kim. "Review of x-ray free-electron laser theory." Phys. Rev. ST Accel. Beams 10, 034801 (2007).

[Hor88] H. Hora, "Particle acceleration by superposition of frequency-controlled laser pulses," Nature 333, 337 (1988).

[HFM+11] J. Hebling, J. A. Fülöp, M. I. Mechler, L. Pálfalvi, C. Tőke and G. Almásik, "Optical manipulation of relativistic electron beams Using THz pulses," arXiv:1109.6852 (2011).

[HFS+95] F. V. Hartemann, S. N. Fochs, G. P. Le Sage, N. C. Luhmann Jr., J. G. Woodworth, M. D. Perry, Y. J. Chen and A. K. Kerman, "Nonlinear ponderomotive scattering of relativistic electrons by an intense laser field at focus," Phys. Rev. E 51, 4833 (1995).

[HLK+03] N. Hafz, H. J. Lee, J. U. Kim, G. H. Kim, H. Suk and J. Lee. "Femtosecond x-ray generation via the Thomson scattering of a terawatt laser from electron bunches produced from the LWFA utilizing a plasma density transition." IEEE Trans. Plasma Sci. 31, 1388–1394 (2003).

[HS02] S. X. Hu and A. F. Starace, "GeV electrons from ultraintense laser interaction with highly charged ions," Phys. Rev. Lett. 88, 245003 (2002).

[HYH+08] J. Hebling, K.-L. Yeh, M. C. Hoffmann, B. Bartal and K. A. Nelson, "Generation of high-power terahertz pulses by tilted-pulse-front excitation and their application possibilities." J. Opt. Soc. Am. B 25, B6–B19 (2008).

[HZT+96] Y. C. Huang, D. Zheng, W. M. Tulloch and R. L. Byer, "Proposed structure for a crossed-laser beam, GeV per meter gradient, vacuum electron linear accelerator," Appl. Phys. Lett. 68, 753-755 (1996).

[Jac75] J. D. Jackson, *Classical Electrodynamics*, 2nd ed. (Wiley, New York 1975).

[JMK+84] C. Joshi, W. B. Mori, T. Katsouleas, J. M. Dawson, J. M. Kindel, and D. M. Forslund, "Ultrahigh gradient particle acceleration by intense laser-driven plasma density waves", Nature 311, 525 (1984).

[Kra04] G. A. Krafft, "Spectral distributions of Thomson-scattered photons from high-intensity pulsed lasers," Phys. Rev. Lett. 92, 204802 (2004).

[Kim89] K.-J. Kim, "Characteristics of synchrotron radiation," AIP Conf. Proc. 184, 565–632 (1989).

[Kub09] V. V. Kubarev, "Optical properties of CVD-diamond in terahertz and infrared ranges," Nucl. Instr. and Meth. A 603, 22–24 (2009).

[KCH+07] V. V. Kulagin, V. A. Cherepenin, M. S. Hur, and H. Suk, "Theoretical investigation of controlled generation of a dense attosecond relativistic electron bunch from the interaction of an ultrashort laser pulse with a nanofilm." Phys. Rev. Lett. 99 (2007).

[KD83] T. Katsouleas and J. M. Dawson, "Unlimited electron acceleration in laser-driven plasma waves", Phys. Rev. Lett. 51, 392 (1983).

[KHY+10] J. H. Kim, J. Han, M. Yoon, and S. Y. Park, "Theory of wakefields in a dielectric-filled cavity," Phys. Rev. ST Accel. Beams 13, 071302 (2010).

[KSB+01] W. D. Kimura, A. van Steenbergen, M. Babzien, I. Ben-Zvi, L. P. Campbell, D. B. Cline, C. E. Dilley, J. C. Gallardo, S. C. Gottschalk, P. He, K. P. Kusche, Y. Liu, R. H. Pantell, I. V. Pogorelsky, D. C. Quimby, J. Skaritka, L. C. Steinhauer and V. Yakimenko, "First Staging of Two Laser Accelerators," Phys. Rev. Lett. **86**, 4041–4043 (2001)..

[KP07] A. Karmakar and A. Pukhov, "Collimated attosecond GeV electron bunches from ionization of high-Z material by radially polarized ultra-relativistic laser pulses," Laser Part. Beams 25, 371-377 (2007).

[L12] "LCLS-II", https://slacportal.slac.stanford.edu/sites/lcls_public/lcls_ii/Pages /default.aspx (Sep 8, 2012).

[Lew04] R. A. Lewis, "Medical phase contrast x-ray imaging: Current status and future prospects," Phys. Med. Biol. 49, 3573–3583 (2004).

[Lin01] X. E. Lin, "Photonic band gap fiber accelerator," Phys. Rev. STAB 4, 051301 (2001).

[LL87] L. D. Landau and E. M. Lifshitz, *The Classical Theory of Fields*, 4th ed. (Oxford 1987).

[LLC06] Lan, Pengfei, Peixiang Lu, and Wei Cao, "Single attosecond pulse generation by nonlinear Thomson scattering in a tightly focused intense laser beam," Phys. Plasmas 13, 013106 (2006).

[LLC+05] Lan, Pengfei, Peixiang Lu, Wei Cao, and Xinlin Wang, "Attosecond and zeptosecond x-ray pulses via nonlinear Thomson backscattering." Phys. Rev. E 72, 066501 (2005).

[LVL+04] O. J. Luiten, S. B. van der Geer, M. J. de Loos, F. B. Kiewiet, and M. J. van der Wiel. "How to realize uniform three-dimensional ellipsoidal electron bunches." Phys. Rev. Lett. 93 (2004).

[LXL+10] Liu, L., C.-Q. Xia, J.-S. Liu, W.-T. Wang, Y. Cai, C. Wang, R.-X. Li, and Z.-Z. Xu, "Generation of attosecond x-ray pulses via Thomson scattering of counter-propagating laser pulses." Laser Part Beams 28 27-34 (2010).

[MVA+12] V. Marceau, A. April and M. Piché. "Electron acceleration driven by ultrashort and nonparaxial radially polarized laser pulses." Opt. Lett. 37, 2442–2444 (2012).

[MVP13] V. Marceau, C. Varin and M. Piché, "Validity of the Paraxial Approximation for Electron Acceleration with Radially Polarized Laser Beams," Opt. Lett. 38, 821–823 (2013).

[Mac00] K. T. MacDonald, "Gaussian laser beams with radial polarization", http://puhep1.princeton.edu/~mcdonald/examples/axicon.pdf (2000).

[MLM97] G. Malka, E. Lefebvre, and J. L. Miquel, "Experimental observation of electrons accelerated in vacuum to relativistic energies by a high-intensity laser," Phys. Rev. Lett. 78, 3314 (1997).

[MMN+04] S. P. D. Mangles, C. D. Murphy, Z. Najmudin, A. G. R. Thomas, J. L. Collier, A. E. Dangor, E. J. Divall, P. S. Foster, J. G. Gallacher, C. J. Hooker, D. A. Jaroszynski, A. J. Langley, W. B. Mori, P. A. Norreys, F. S. Tsung, R. Viskup, B. R. Walton and K. Krushelnick, "Monoenergetic beams of relativistic electrons from intense laser–plasma interactions," Nature 431, 535–538 (2004).

[MS04] A. Mizrahi and L. Schächter, "Optical Bragg Accelerators," Phys. Rev. E 70, 016505 (2004).
[MU92] G. Mourou and D. Umstadter, "Development and applications of compact high-intensity lasers", Phys. Fluids B 4, 2315 (1992).
[MZD+95] A. Modena, Z. Najmudin, A. E. Dangor, C. E. Clayton, K. A. Marsh, C.Joshi, V.Malka, C. B. Darrow, C.Danson, D. Neely & F. N. Walsh, "Electron acceleration from the breaking of relativistic plasma waves", Nature **377**, 606-608 (1995).
[NSK11] R. J. Noble, J. E. Spencer and B. T. Kuhlmey, "Hollow-core photonic band gap fibers for particle acceleration," Phys. Rev. STAB 14, 121303 (2011).
[Pal72] R. B. Palmer, "Interaction of relativistic particles and free electromagnetic waves in the presence of a static helical magnet", J. Appl. Phys. 43, 3014 (1972).
[Pop11] A. Popa, "Periodicity property of relativistic Thomson scattering with application to exact calculations of angular and spectral distributions of the scattered field," Phys. Rev. A 84, 023824 (2011).
[PBC+05] T. Plettner, R. L. Byer, E. Colby, B. Cowan, C. M. S. Sears, J. E. Spencer and R. H. Siemann, "Visible-laser acceleration of relativistic electrons in a semi-finite vacuum," Phys. Rev. Lett. 95, 134801 (2005).
[PBR08] K. I. Popov, V. Yu. Bychenkov, W. Rozmus, and R. D. Sydora, "Electron vacuum acceleration by a tightly focused laser pulse", Phys. Plasmas 15, 013108 (2008).
[PBS05] T. Plettner, R. L. Byer and R. H. Siemann, "The impact of Einstein's theory of special relativity on particle accelerators," J. Phys. B: At. Mol. Opt. Phys. 38, S741 (2005).
[PLB06] T. Plettner, P. P. Lu and R. L. Byer, "Proposed few-optical cycle laser-driven particle accelerator structure," Phys. Rev. STAB 9, 111301 (2006).
[PM94] M. D. Perry and G. Mourou, "Terawatt to petawatt subpicosecond lasers", Science 264, 917 (1994).
[PMK+07] A. S. Pirozhkov, J. Ma, M. Kando, T. Zh Esirkepov, Y. Fukuda, L.-M. Chen, I. Daito, et al. "Frequency multiplication of light back-reflected from a relativistic wake wave," Phys. Plasmas 14 (2007).
[PPS+99] M. D. Perry, D. Pennington, B. C. Stuart, G. Tietbohl, J. A. Britten, C. Brown, S. Herman, B. Golick, M. Kartz, J. Miller, H. T. Powell, M. Vergino, and V. Yanovsky, "Petawatt laser pulses", Opt. Lett. 24, 160 (1999).
[PTV+92] W. H. Press, S. A. Teukolsky, W. T. Vetterling and B. P. Flannery, *Numerical Recipes in C*, 2nd ed. (Cambridge University, 1992, pp. 714-720).
[QM98] B. Quesnel and P. Mora, "Theory and simulation of the interaction of ultraintense laser pulses with electrons in vacuum," Phys. Rev. E 58, 3719 (1998).
[REB95] S. K. Ride, E. Esarey and M. Baine, "Thomson scattering of intense lasers from electron beams at arbitrary interaction angles," Phys. Rev. E 52, 5425–5442 (1995).
[Sal06] Y. I. Salamin, "Electron acceleration from rest in vacuum by an axicon Gaussian laser beam," Phys. Rev. A, 73, 043402 (2006).
[Sal07] Y. I. Salamin, "Mono-energetic GeV electrons from ionization in a radially-polarized laser beam," Opt. Lett. 32, 90-92 (2007).
[SEK+92] P. Sprangle, E. Esarey, J. Krall, and G. Joyce, "Propagation and guiding of intense laser pulses in plasmas", Phys. Rev. Lett. 69, 2200 (1992).
[SEK96] P. Sprangle, E. Esarey, and J. Krall, "Laser driven electron acceleration in vacuum, gases, and plasmas", Phys. Plasmas 3, 2183 (1996).

[SEK+96] P Sprangle, E. Esarey, J. Krall and A. Ting, "Vacuum laser acceleration," Opt. Comm. 124, 69-73 (1996).

[SEM+11] M. M. Seibert, T. Ekeberg, F. R. N. C. Maia, M. Svenda, J. Andreasson, O. Jönsson, D. Odić, et. al., "Single mimivirus particles intercepted and imaged with an x-ray laser," Nature 470, 78–81 (2011).

[SET+88] P. Sprangle, E. Esarey, A. Ting, and G. Joyce, "Laser wakefield acceleration and relativistic optical guiding", Appl. Phys. Lett. 53, 2146 (1988).

[SF01] L. Serafini and M. Ferrario. "Velocity bunching in photo-injectors," AIP Conference Proceedings 581, 87–106 (2001).

[SF96] Y. I. Salamin and F. H. M. Faisal. "Harmonic generation by superintense light scattering from relativistic electrons." Phys. Rev. A 54, 4383–4395 (1996).

[SHK08] Y. I. Salamin, Z. Harman and C. H. Keitel, "Direct high-power laser acceleration of ions for medical applications," Phys. Rev. Lett. 100, 155004 (2008).

[SLS+06] H. Schwoerer, B. Liesfeld, H.-P. Schlenvoigt, K.-U. Amthor, and R. Sauerbrey, "Thomson-backscattered x-rays from laser-accelerated electrons," Phys. Rev. Lett. 96, 014802 (2006).

[SK02] Y. I. Salamin and C. H. Keitel, "Electron acceleration by a tightly focused laser beam," Phys. Rev. Lett. 88, 095005 (2002).

[SK92] L. C. Steinhauer and W. D. Kimura, "A new approach for laser particle acceleration in vacuum," J. Appl. Phys. 72, 3237 (1992).

[SLC+96] R. W. Schoenlein, W. P. Leemans, A. H. Chin, P. Volfbeyn, T. E. Glover, P. Balling, M. Zolotorev, K.-J. Kim, S. Chattopadhyay, and C. V. Shank, "Femtosecond x-ray pulses at 0.4 Å generated by 90° Thomson scattering: A tool for probing the structural dynamics of materials," Science 274, 236–238 (1996).

[SLH08] A. Sell, A. Leitenstorfer and R. Huber, "Phase-locked generation and field-resolved detection of widely tunable terahertz pulses with amplitudes exceeding 100 MV/cm," Opt. Lett. 33, 2767–2769 (2008).

[SM11] G. Sciaini and R. J. D. Miller. "Femtosecond electron diffraction: heralding the era of atomically resolved dynamics," Rep. Prog. Phys. 74 096101 (2011).

[SM85] D. Strickland and G. Mourou, "Compression of amplified chirped optical pulses", Opt. Comm. 56, 219 (1985).

[SMK03] Y. I. Salamin. G. R. Mocken and C. H. Keitel, "Relativistic electron dynamics in intense crossed laser beams: Acceleration and Compton harmonics," Phys. Rev. E 67, 016501 (2003).

[SS70] E. S. Sarachik and G. T. Schappert. "Classical theory of the scattering of intense laser radiation by free electrons," Phys. Rev. D 1, 2738–2753 (1970).

[SZ01] G. V. Stupakov and M. S. Zolotorev, "Ponderomotive laser acceleration and focusing in vacuum for generation of attosecond electron bunches," Phys. Rev. Lett 86, 5274-5277 (2001).

[SZ91] M. O. Scully and M. S. Zubairy, "Simple laser accelerator: Optics and particle dynamics," Phys. Rev. A 44, 2656 (1991).

[TCT+12] K. Ta Phuoc, S. Corde, C. Thaury, V. Malka, A. Tafzi, J. P. Goddet, R. C. Shah, S. Sebban, and A. Rousse, "All-optical Compton gamma-ray source." Nature Photon. 6, 308–311 (2012).

[TD79] T. Tajima and J. M. Dawson, "Laser electron acceleration", Phys. Rev. Lett. 43, 267 (1979).

[TM02] T. Tajima, G. Mourou, "Zettawatt-exawatt lasers and their applications in ultrastrong-field physics", Phys. Rev. ST AB 5, 031301 (2002).

[TRP+03] K. Ta Phuoc, A. Rousse, M. Pittman, J. P. Rousseau, V. Malka, S. Fritzler, D. Umstadter, and D. Hulin. "X-ray radiation from nonlinear Thomson scattering of an intense femtosecond laser on relativistic electrons in a Helium plasma." Phys. Rev. Lett. 91, 195001 (2003).

[Vac62] Vachaspati, "Harmonics in the scattering of light by free electrons." Phys. Rev. 128, 664–666 (1962).

[VPP05] C. Varin, M. Piché, and M. A. Porras, "Acceleration of electrons from rest to GeV energies by ultrashort transverse magnetic laser pulses in free space," Phys. Rev. E 71, 026603 (2005).

[WG12] Y. Wang and N. Gedik, "Electron Pulse Compression With a Practical Reflectron Design for Ultrafast Electron Diffraction," J. Select. Topics Quantum Electron. 18, 140-147 (2012).

[WHY+01] P. X. Wang, Y. K. Ho, X. Q. Yuan, Q. Kong, N. Cao, A. M. Sessler, E. Esarey and Y. Nishida, "Vacuum electron acceleration by an intense laser," Appl. Phys. Lett. 78, 2253 (2001).

[WK10] L. J. Wong and F. X. Kärtner, "Direct acceleration of an electron in infinite vacuum by a pulsed radially polarized laser beam," Opt. Express 18, 25035–25051 (2010). Invited paper, Virtual Journal of Ultrafast Science, 10 (2011).

[WK11a] L. J. Wong and F. X. Kärtner, "Two-color-laser-driven direct electron acceleration in infinite vacuum," Opt. Lett. 36, 957-959 (2011).

[WK11b] L. J. Wong and F. X. Kärtner, "A threshold for laser-driven linear particle acceleration in unbounded vacuum," Appl. Phys. Lett. 99, 211101 (2011). Invited paper, Virtual Journal of Ultrafast Science, 10 (2011).

[WFK13] L. J. Wong, A. Fallahi and F. X. Kärtner, "Compact electron acceleration and bunch compression in terahertz waveguides," Opt. Express 21, 9792–9806 (2013).

[WZP+09] S. Winnerl, B. Zimmermann, F. Peter, H. Schneider, and M. Helm. "Terahertz Bessel-Gauss beams of radial and azimuthal polarization from microstructured photoconductive antennas." Opt. Express 17, 1571–1576 (2009).

[YR05] R. B. Yoder and J. B. Rosenzweig, "Side-coupled slab-symmetric structure for high-gradient acceleration using terahertz power," Phys. Rev. ST Accel. Beams 8, 111301 (2005).

[YTU+01] H. Yoneda, K. Tokuyama, K. Ueda, H. Yamamoto, and K. Baba, "High-power terahertz radiation emitter with a diamond photoconductive switch array," Appl. Optics 40, 6733–6736 (2001).

[YYM78] P. Yeh, A. Yariv, and E. Marom, "Theory of Bragg fiber," J. Opt. Soc. Am. **68,** 1196–1201 (1978).

[Zew00] A. H. Zewail, "Femtochemistry: Atomic-Scale Dynamics of the Chemical Bond," J. Phys. Chem. A 104, 5660–94 (2000).